THE MECHANISMS FOR PASSIVE SUPPRESSION OF FLUCTUATING SURFACE PRESSURE IN A SUPERSONIC CAVITY FLOW

By

JONATHAN G. DUDLEY

A DISSERTATION PRESENTED TO THE GRADUATE SCHOOL
OF THE UNIVERSITY OF FLORIDA IN PARTIAL FULFILLMENT
OF THE REQUIREMENTS FOR THE DEGREE OF
DOCTOR OF PHILOSOPHY

UNIVERSITY OF FLORIDA

2010

© 2010 Jonathan G. Dudley

To Megan and Malia

ACKNOWLEDGMENTS

I would first and foremost like to thank my wife whose constant patience and support have guided me through the ups and downs of the past few years. I would like to extend my gratitude to my family whose uninterrupted and unwavering support, sacrifice and love throughout this arduous journey was not unrecognized or misguided. A special thanks is given to Mr. Robert Ball for his help in design and fabrication of the SWT and test models and anything else I needed yesterday. I am also indebted to all my colleges who have come and gone at the Research and Engineering Education Facility for their time and help with every aspect of the research including (but far from limited to) experimental setup, facility maintenance/operation and discussions.

I would like to acknowledge Dr. Lawrence Ukeiley for providing guidance throughout my research at the University of Florida. I would like to thank the other members of my committee, Dr. Andreas Haselbacher, Dr. Louis Cattafesta III, Dr. Jason Butler and Dr. Srinivasan Arunajatesan for providing insight, reviewing my research and providing valuable feedback.

Additionally, thanks go out to the members of the Air Force SEEK EAGLE Office and Air Force Research Lab not only for funding but for providing resource and true center(s) of expertise. Specifically, I would like to extend my gratitude to Dr. John Martel, Dr. Magdi Rizk, Mr. Sergey Kernazhitskiy and Mr. Jason Torres for the many hours of discussion and trouble shooting the numerics. I think I finally have time to join all of you Friday afternoon on the boat.

TABLE OF CONTENTS

page

ACKNOWLEDGMENTS 4

LIST OF TABLES 8

LIST OF FIGURES 9

ABSTRACT 14

CHAPTER

1 INTRODUCTION 16

1.1 Background 16
1.1.1 Dissertation Outline 16
1.1.2 Objectives 17
1.2 Fundamentals of Cavity Flow 18
1.3 Cavity Flow with Control 23

2 STATISTICAL ANALYSIS TECHNIQUES 32

2.1 Unsteady Pressure Measurements 32
2.1.1 Spectral Calculations 33
2.1.2 Joint Time-Frequency Analysis 34
2.1.3 Correlation Analysis 35
2.2 Turbulent Statistics and Flowfield Measurements 36
2.3 Proper Orthogonal Decomposition 39
2.4 Non-Dimensionalization 42

3 THE FACILITY AND EXPERIMENTAL TECHNIQUES 45

3.1 Facility Overview 45
3.2 Cavity Design 48
3.3 SWT Characterization 50
3.4 Instrumentation 53
3.4.1 Wind Tunnel Control 53
3.4.2 Unsteady Pressure Measurements 55
3.5 Flow Visualization 56
3.5.1 Schlieren 56
3.5.2 Particle Image Velocimetry 59
3.6 Experimental Setup 62
3.7 Measurement Uncertainty 63
3.7.1 Unsteady Pressure Measurement 64
3.7.2 PIV Measurement 64

4 NUMERICAL SIMULATION APPROACH . . . 68
4.1 Turbulence . . . 68
4.1.1 Compressible Navier-Stokes Equations . . . 74
4.1.2 Spalart-Allmaras DES . . . 76
4.2 Flow Solver . . . 78
5 CYLINDER IMMERSED IN A SUPERSONIC BOUNDARY LAYER . . . 80
5.1 Computational Grids . . . 83
5.2 Results . . . 87
5.2.1 Mean Flowfield . . . 88
5.2.2 Instantaneous Vorticity Flowfield . . . 96
5.2.3 Turbulent Statistics . . . 103
5.3 Summary . . . 106
6 UNSTEADY PRESSURE MEASUREMENTS . . . 108
6.1 Full and Finite Span Baseline Cavity Comparison . . . 108
6.2 Finite Span Cavity with Suppression . . . 113
6.2.1 Effects of Rod Mounts . . . 114
6.2.2 Effects of Rod Diameter and Gap Height . . . 116
6.3 Full Span Cavity with Suppression . . . 123
6.4 Summary . . . 128
7 FLOWFIELD MEASUREMENTS . . . 131
7.1 Full Span Cavity . . . 131
7.1.1 Mean Flowfield . . . 131
7.1.2 Turbulent Flowfield . . . 137
7.1.3 Evolution of Two-Point Statistics . . . 144
7.1.4 Proper Orthogonal Decomposition . . . 148
7.2 Finite Span Cavity . . . 157
7.2.1 Full and Finite Span Flowfield Comparison . . . 157
7.2.2 Mean Flowfield . . . 159
7.2.3 Turbulent Flowfield . . . 160
7.3 Summary . . . 162
8 SIMULATION OF BASELINE AND CONTROLLED CAVITY . . . 166
8.1 Validation of Cavity Simulations . . . 168
8.2 Instantaneous Flowfield and Pressure Measurement . . . 173
8.3 Mean Flowfield . . . 177
8.4 Mean Turbulent Flowfield . . . 183
8.4.1 Evolution of Two-Point Velocity Correlations . . . 184
8.4.2 POD . . . 188
8.5 Summary . . . 192

9 CONCLUSIONS AND FUTURE WORK 196

9.1 Finite and Full Span Cavities 197
9.2 Demonstration of DES 197
9.3 Cavity Control 198
9.4 Future Work 201
9.4.1 Computational Fluid Dynamics 201
9.4.2 Experimental 202
9.4.3 Future Consideration 203

APPENDIX

A TURBULENCE MODEL FORMULATION 204

A.1 Compressible Navier-Stokes Equations 204
A.2 Compressible Reynolds Averaged Navier-Stokes Equations 206
A.3 Spalart-Allmaras Turbulence Model 208

B VIBRATION AND DEFLECTION OF SELECTED RODS 212

B.1 Rod Fundamental Frequency 212
B.2 Deflection of Rod 213

REFERENCES 215

BIOGRAPHICAL SKETCH 225

LIST OF TABLES

Table		page
3-1	Standard operating conditions.	62
3-2	Cavity floor pressure sensor locations.	63
4-1	Summary of numerical strategies and cost.	71
5-1	Summary of computational details	88
6-1	Rossiter resonant tone predictions.	109
6-2	Finite span cavity configurations.	114
8-1	List of variable dimensions	167
8-2	Computational grid sizes for the baseline cavity.	168
8-3	Cavity wave speed, time lags and distances.	175
A-1	SA-DES turbulence model coefficients	211
B-1	Rod geometry	212
B-2	Transverse fundamental vibration of rod	213

LIST OF FIGURES

Figure page

1-1 Schematic and common nomenclature of typical cavity configurations. 18

1-2 Open cavity flow illustrating acoustic feedback loop. 19

1-3 Adapted flow control classification. 23

1-4 Passive rod spoiler suppression mechanism 27

3-1 The supersonic wind tunnel. 45

3-2 RANS solution of the supersonic wind tunnel nozzle. 46

3-3 Test-section with analytical wave reflection. 47

3-4 Test-section with flat plate. 47

3-5 Finite span cavity with closeup of rod mounted on leading edge block 48

3-6 Simulation of flow around rod mounting structure. 49

3-7 Rod mounting location relative to cavity leading edge 50

3-8 Experimental and numerical boundary layer profile comparison. 51

3-9 Flow visualization using Schlieren for the SWT test-section. 53

3-11 Bending of light due to density gradient of two mediums. 57

3-12 Z-type Schlieren arrangement for qualitative flow assessment. 58

3-13 Schlieren imaging of a bullet 58

3-14 Particle Image Velocimetry (PIV). 59

3-15 PIV and pressure synchronization. 61

3-16 Pressure sensor locations 63

3-17 PIV uncertainty for turbulent intensities that are less than 30%. 65

3-18 DEHS particle size frequency distribution 67

4-1 Transition of a turbulent boundary layer over a flat plate 69

4-2 Turbulence energy spectrum depicting RANS through DNS simulation scales . . 72

4-3 Numerical Schlieren of supersonic cavity flow 74

5-1 Sketch of cylinder immersed in a supersonic boundary layer. 84

5-2 Grid topology. 85
5-3 Grid and time-step sensitivity on spectral results for $d^* = 0.40$. 86
5-4 Mean streamwise velocity contours. 89
5-5 Mean streamwise velocity profiles at given axial locations. 91
5-6 Time averaged pressure distribution on cylinder surface. 93
5-7 Cylinder PSD as a function of frequency and Strouhal taken at $\left(\frac{x}{d}, \frac{y}{\delta}\right) = (1, 0)$. . 94
5-8 Strouhal number based on U_∞ and U_c 95
5-9 Small diameter rod mean flowfield contours for $G^* = 0.11$. 97
5-10 Instantaneous z-vorticity for $G^* = 0.11$. 98
5-11 Instantaneous z-vorticity for $G^* = 0.21$. 99
5-12 Instantaneous z-vorticity for top of rod near the top of boundary layer. 100
5-13 Instantaneous z-vorticity for rod outside boundary layer. 101
5-14 $d^* = 0.20$ Instantaneous iso-vorticity colored by velocity magnitude. 103
5-15 $d^* = 0.40$ Instantaneous iso-vorticity colored by velocity magnitude. 104
5-16 Mean resolved $RSS = \frac{u'v'}{U_\infty{}^2}$ on z=0 plane. 105
5-17 Mean resolved TKE profiles at given $\frac{x}{d}$ locations. 106
6-1 Full and finite span baseline PSD comparison 110
6-2 Full and finite span baseline p_{rms} on the cavity floor. 111
6-3 Baseline cavity surface pressure correlation. 112
6-4 Full and finite span spectrograms measured on the aft wall. 113
6-5 Finite span cavity rod mounting effects 115
6-6 Mean Schlieren gradients for isolated rod mounts as suppression devices. 116
6-7 Fluctuating surface pressures based on d^* 117
6-7 Fluctuating surface pressures based on d^* and G^*. 120
6-8 Cross-correlation coefficient for top of rod near top of boundary layer. 121
6-9 Cross-coherence coefficient for top of rod near top of boundary layer 122
6-10 Finite span spectrogram for $d^* = 0.43$. 124

6-11 Full span baseline and controlled fluctuating surface pressure 125
6-12 Full span cavity cross-correlation 126
6-13 Full span cavity cross-coherence 127
6-14 Full span cavity aft wall spectrogram for given d^* and G^* values. 129
6-15 Percent reduction of p_{rms} 130
7-1 Full span mean streamwise velocity contours with vectors. 132
7-2 Zoomed cavity streamwise mean velocity contours with vectors. 134
7-3 Full span cavity streamlines. 135
7-4 Full span cavity mean streamwise velocity profiles. 136
7-5 Full span cavity mean streamwise turbulent velocity contours. 137
7-6 Full span cavity mean streamwise turbulent velocity profiles. 138
7-7 Full span cavity mean normal turbulent velocity contours. 139
7-8 Zoomed cavity normal turbulent velocity contours. 140
7-9 Mean RSS flow contours for the full span cavity. 141
7-10 Full span mean RSS profiles. 142
7-11 Full span cavity vorticity thickness. 145
7-12 Evolution of two-point spatial axial velocity correlation for varying $\frac{y}{D}$ and $\frac{x}{L}$. . . 146
7-13 Evolution of two-point spatial normal velocity correlation for varying $\frac{y}{D}$ and $\frac{x}{L}$. . 147
7-14 Evolution of two-point spatial axial velocity correlation for fixed $\frac{y}{D} = 0$. 149
7-15 Evolution of two-point spatial normal velocity correlation for fixed $\frac{y}{D} = 0$. . . . 150
7-16 Convergence of POD Modes 152
7-17 Convergence of POD Energy 153
7-18 Full span cavity POD temporal convergence and energy distribution. 153
7-19 Streamwise POD modes for the full span cavity 155
7-20 Normal POD modes for the full span cavity 156
7-21 Full span POD spatial correlation map for the first 20 modes. 157
7-22 Example of seeded flowfield illustrating edge of cavity sidewall. 158

7-23 Comparison of full and finite span cavity streamwise velocity contours. 158
7-24 Finite span cavity mean streamwise velocity contours and profiles. 160
7-25 Full span cavity mean streamlines. 161
7-26 Finite span mean streamwise turbulent velocity contours. 162
7-27 Finite span mean normal turbulent velocity contours. 163
7-28 Finite span mean streamwise RSS contours. 164
7-29 Random instantaneous Schlieren images 165
8-1 Geometry and boundary conditions for the numerical simulations. 166
8-2 Structured overset grid. 167
8-3 Effect of grid refinement on ω_z vorticity contours. 169
8-4 Effect of grid refinement on cavity fluctuating surface pressures. 170
8-5 Instantaneous snapshot of tracer particle in cylinder near field 170
8-6 CFD and experiment mean axial velocity comparison. 171
8-7 CFD and experiment mean streamwise velocity comparison. 172
8-8 Aft wall experimental and numerical spectra. 173
8-9 Baseline and suppressed cavity fluctuating surface pressures. 174
8-10 Baseline and controlled cavity auto and cross correlations. 175
8-11 Instantaneous non-dimensional vorticity contours. 176
8-12 Baseline and controlled mean streamlines. 177
8-13 Mean velocity flowfield contours. 179
8-14 Mean streamwise and normal velocity profiles at various axial locations. 180
8-15 Baseline cavity yz plane recirculation 181
8-16 Suppressed cavity yz plane recirculation 182
8-17 Computational vorticity thickness 183
8-18 Mean vorticity contours. 183
8-19 Mean turbulent flowfield contours. 185
8-20 Mean flowfield and mean turbulent flowfield profiles. 186

8-21 Evolution of streamwise spatial velocity correlation. 187
8-22 Evolution of normal spatial velocity correlation. 189
8-23 Fluctuating surface pressure correlation 190
8-24 Energy distribution of POD modes. 190
8-25 POD modes based on the normal fluctuating velocity. 193
B-1 Suppression device properties. 213
B-2 Estimated rod deflection based on diameter and L for a given U_∞. 214

Abstract of Dissertation Presented to the Graduate School
of the University of Florida in Partial Fulfillment of the
Requirements for the Degree of Doctor of Philosophy

THE MECHANISMS FOR PASSIVE SUPPRESSION OF FLUCTUATING SURFACE PRESSURE IN A SUPERSONIC CAVITY FLOW

By

Jonathan G. Dudley

December 2010

Chair: Lawrence Ukeiley
Major: Mechanical Engineering

The study of the passive suppression of supersonic cavity flow using a rod immersed in the upstream boundary layer is a unique and challenging fluid mechanics problem. The flowfield includes a compressible shear layer interacting with a complex pattern of compression and expansion waves. The turbulent fluctuations inside the shear layer may be amplified through a feedback-receptivity cycle resulting in increased pressure loading on the surfaces of the cavity. Studying the mechanisms dictating the suppression of these amplified turbulent fluctuations when control is present makes for an enlightening and challenging problem. A combined experimental and time accurate numerical study using detached-eddy simulation was conducted to study the suppression of pressure fluctuations due to supersonic cavity flow at $M_\infty = 1.4$ over an open rectangular cavity with a length-to-depth ratio of six. In this study, the focus is confined to suppression due to a rod spoiler. The experimental measurements included temporally resolved fluctuating surface pressure measurements coupled with spatially resolved particle image velocimetry.

Analysis of the fluctuating pressures on the cavity surfaces included investigations of the root-mean-square fluctuating pressure, spectral analysis, correlation and coherence analysis and joint time-frequency spectrograms. The shear layer flowfield and turbulence was studied using ensemble averaged turbulent statistics including two-point spatial turbulent velocity correlations and Proper Orthogonal Decomposition. Results indicate that the most effective suppression of the fluctuating pressures was achieved when a rod

sized roughly 40% of the boundary layer was placed such that the top of the rod was near the top edge of the boundary layer. It was shown that the rod leads to a thicker shear layer that initially spreads more rapidly. The turbulent structures in the wake of the rod interact with the cavity shear layer with a time periodic excitation which lifts the shear layer near the cavity leading edge. The structures are smaller and less organized which is believed to lead to a shear layer that is less receptive to the disturbances propagating upstream inside the cavity. The controlled cavity exhibits an altered aft wall impingement point which is due to the lifting and altered flapping nature of the shear layer. The upstream propagating disturbance emanating from the aft wall is thus weakened due in part to the lower speed flow impinging on the aft wall. These coupled events lead to drastically reduced tonal components (which are lowered to near broadband levels) and notable lowering of the broadband levels of the fluctuating pressure measured on the cavity surfaces.

CHAPTER 1
INTRODUCTION

1.1 Background

The grazing flow past a cavity, as described in Rockwell & Naudascher (1979), can generate an intense aeroacoustic resonant phenomena due to the interaction of the shear layer with the aft wall. This type of fundamental fluid flow problem has many practical applications ranging from automotive flows over sunroofs and windows to aerospace flows of open wheel wells and weapons bays. Studies of the aeroacoustic environment encountered in these bays have been ongoing since the early 1950's initiated by the works of Krishnamurty (1955) and Roshko (1955).

Modern military aircraft have resorted to internal weapons carriages and jettisons at supersonic freestream conditions which present many challenges due to the presence of complex unsteady flowfields. Technological developments are improving the accuracy and reducing the size and mass of munitions. This dictates the need to understand and control the intense pressure fluctuations observed in cavity flow scenarios. Further, the delicate electronics that might exist in the environment of real aircraft also predicate the necessity to reduce these fluctuating pressures. To achieve maximum and effective suppression of these loads it is vital to understand the inherent fundamental mechanisms driving the flow and how to couple it with the desired control.

1.1.1 Dissertation Outline

This dissertation is organized into nine chapters. Chapter 1 presents the motivation for the research and literature review. The statistical analysis techniques and plotting conventions for this work will be described in Chapter 2. Chapter 3 will lay the foundations for the experimental investigation of the research including the design and fabrication of the Supersonic Wind Tunnel (SWT) at the University of Florida Research and Engineering Education Facility (REEF). Chapter 4 introduces the numerical modeling techniques to be used throughout the research including a detailed look at the selected

methods and closure models. Chapter 5 presents the initial computational results of a rod immersed in a supersonic boundary layer which lays the groundwork for the passive cavity control which will be used in this study. Chapter 6 focuses on discussing the results of the experimentally obtained fluctuating surface pressure measurements. Chapter 7 presents the flowfield measurements and visualization using Schlieren imaging and particle image velocimetry. Chapter 8 will detail the numerical simulation results for the baseline and suppressed cavity configurations. Chapter 9 concludes with a review of the results and future work. Lastly, appendices are included that discuss the intricate details of the turbulence model and the physical and material properties of the rods used in the experimental effort.

1.1.2 Objectives

The primary objective of this research is to gain a better understanding of the physical mechanisms dictating the suppression of a low freestream supersonic Mach number on open cavity flow when a rod is immersed in the upstream boundary layer prior to the cavity leading edge. Intuitively, the flow phenomena in the wake of the rod will interact with the shear layer above the cavity causing changes in its properties. To date, there is little specific understanding of the effects of this on the mean or turbulent velocities for supersonic freestream conditions. In this effort details of the cylinder diameter and placement on the fluctuating surface pressure will first be evaluated to determine the most effective configuration. Detailed measurements and Computational Fluid Dynamic (CFD) simulations will be conducted in an attempt to quantify the effects of the passive flow control device on the flow. Specifically, quantities associated with the growth of the cavity shear layer along with the amplitude and scale of the turbulence will be examined. Through a detailed comparison between the baseline and controlled cases a quantitative assessment of the control on the flow can be established and hypotheses for the mechanisms will be put forth. A secondary objective is to demonstrate that numerical

simulations of this highly unsteady flow can be reasonably accurately captured using Detached Eddy Simulation (DES) techniques.

1.2 Fundamentals of Cavity Flow

The basic flowfield structure of cavities are typically classified as either open or closed based on the geometrical length (L) to depth (D) ratio $\left(\frac{L}{D}\right)$. A schematic of typical open and closed cavity flow are illustrated in Figure 1-1. Cavities with an $\frac{L}{D} \leq 10$ are designated as open, $\frac{L}{D} \geq 13$ are considered closed (shallow) and cavities where the $\frac{L}{D} \leq 2$ are commonly referred to as deep cavities. In closed cavity flows the leading edge

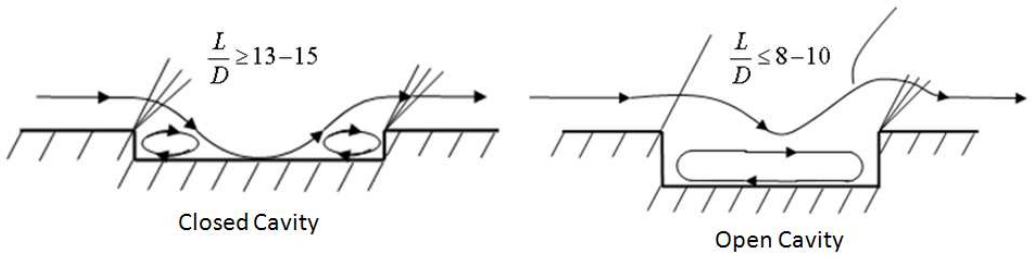

Figure 1-1. Schematic and common nomenclature of typical cavity configurations.

boundary layer separates and forms a shear layer that tends to reattach itself on the cavity floor. The flow separates again upstream of the cavity trailing edge which leads to two recirculation zones inside the cavity. Closed cavities tend to be associated with higher drag and heat transfer properties as reported by Dusing *et al.* (1994) when compared to open cavities and are thus less desirable for most practical engineering purposes. Since the study here is aimed at open cavities the following discussion will focus more closely on this class of cavity flows.

The primary parameters dictating the nature of cavity flows as listed by Cattafesta III *et al.* (2003) are the length to depth ratio $\left(\frac{L}{D}\right)$, length to width ratio $\left(\frac{L}{W}\right)$, Reynolds number (Re), boundary layer thickness (δ), displacement thickness (δ^*), momentum thickness (θ) and the freestream dynamic pressure (Q_∞). Discrete tones are generated by both laminar and turbulent boundary layers though laminar boundary layers tend to be thicker resulting in a thicker initial shear layer and higher tones Tam & Block (1978).

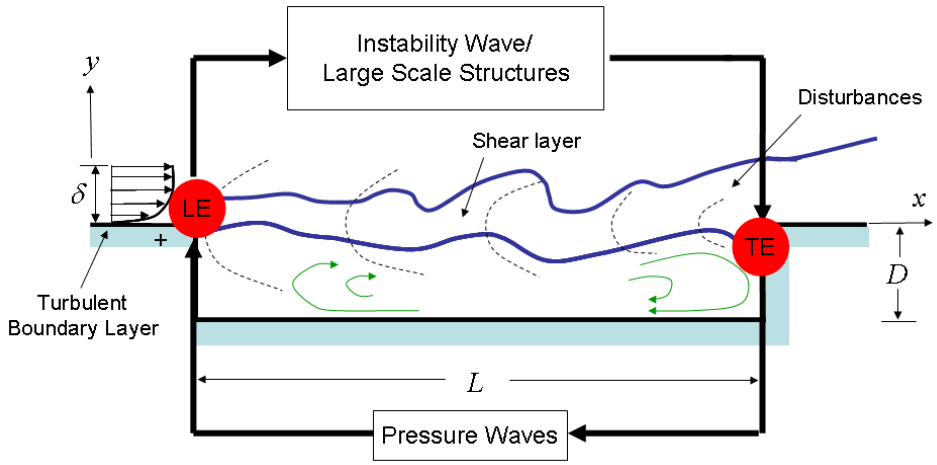

Figure 1-2. Open cavity flow illustrating acoustic feedback loop.

Using the framework for an acoustic feedback loop similar to that illustrated in Figure 1-2 for open cavity flow. Powell (1961) explained the mechanism of self sustained acoustic resonance for edge tones which is analogous to a resonant cavity. He argued the time for large scale structures to reach the trailing edge of the cavity and the time required for acoustic waves to propagate back to the receptivity point, should be an integral multiple of the resonant time scale. The addition of a term to account for the phase shift between these velocities would satisfy any time lag noticed between the hydrodynamic and acoustic waves.

Rossiter (1964) was the first to develop a semi-empirical model based on subsonic and transonic experimental data using this feedback loop concept. He believed the pressure was higher near the trailing edge of the cavity due to the acceleration of the shear layer caused by the flow entering the cavity. This pressure gradient allowed for the formation of large scale structures within the expanding shear layer. He also believed that vortex shedding from the separating region of the shear layer contributed to the acoustic feedback. He postulated that when the frequency of these events approached the natural frequency of the cavity the conditions were met which allow resonance to occur. The frequency with the highest peak magnitude is known as the dominant or fundamental

cavity tone. The frequencies could therefore be represented empirically by

$$f = \frac{U_\infty}{L} \frac{(m - \alpha)}{\left(\frac{1}{k} + M_\infty\right)} \tag{1–1}$$

where the ratio of the convection speed to the freestream velocity is given by the constant k and the freestream velocity is U_∞. The integer mode number is given by m and α is the phase delay constant.

Rossiter's formula is based on the existence of a feedback-receptivity loop and an integer number of phase shifts as previously discussed where disturbances are propagated in the form of an acoustic wave inside the cavity. Cattafesta III *et al.* (1999) has previously noted that this phase shift is required for self-sustaining oscillations. Rossiter's equation is limited in that it does not account for three dimensionality of the flowfield. Specifically, it is only capable of predicting the longitudinal cavity modes and the empirical constants are only valid up to moderate Mach numbers typically $M_\infty \leq 2$. Many researchers, such as Unalmis *et al.* (2004), have refit the constants to extend the region of validity.

Rossiter's original equation was slightly modified by Heller & Bliss (1975) who assumed the temperature in the cavity is the same as the freestream stagnation temperature thus correcting the ratio of the speeds of sound $\frac{a_e}{a_c}$. Equation 1–2 is commonly referred to as the modified Rossiter equation

$$St = \frac{fL}{U_\infty} = \frac{m - \alpha}{\frac{M_\infty}{\sqrt{1 + \frac{\gamma - 1}{2} M_\infty^2}} + \frac{1}{k}} \tag{1–2}$$

where the integer mode number m, α and k are as defined above. The constants k and α have dependence on the freestream conditions and boundary layer shape factor. The constant k has been shown to range from $0.5 - 0.75$ for freestream Mach numbers ranging from $0.4 - 2.5$ as reported by Unalmis *et al.* (2004). For thin boundary layers with $M_\infty \leq 2.0$ the accepted values are $\alpha = 0.25$ and $k = 0.57$ as reported by Dix & Bauer (2004) and Unalmis *et al.* (2004). Under these conditions, the modified Rossiter equation

has demonstrated considerable success in predicting the possible frequencies or modes that are likely to appear in supersonic flows. Although these semi-empirical models have proven quite effective at predicting the frequencies of the tones there is no means by which to predict their amplitudes or which tones will exist hence the need for continued study.

Cavity flow has been previously modeled by assuming an inviscid flow and splitting the fluid domain into an interior and exterior region separated by a thin mixing layer as proposed by Bilanin & Covert (1973). The thin mixing layer was approximated by a vortex sheet with the dominant pressure oscillations occurring at the trailing edge. These pressure oscillations were modeled by a periodic acoustic monopole. They assumed the driving disturbance of the flow emanated from the leading edge and was later verified by control sensitivity experiments conducted by Kegerise *et al.* (2004). Though this model is an improvement to Rossiter's equation as it eliminates the need for empirical constants, it falters if the vortex sheet becomes stable which typically occurs near $M_\infty \approx 2.5$.

Tam & Block (1978) performed experimental investigations of subsonic cavity flow for $M_\infty \leq 0.4$. From these investigations they postulated that the cavity formed flow induced oscillations by means of the shear layer rolling up and generating acoustic waves analogous to Figure 1-2. Two assumptions were required for this proposal which were the cavity flow was dominantly two dimensional and the mean flow interior to the cavity is zero. It has been postulated that three dimensional effects of cavity flow, or the coupling of the longitudinal and vertical modes, are likely of secondary importance as long as the width is small so that higher order spanwise modes are not generated as noted by Bilanin & Covert (1973) and Zhuang (2007). Rossiter (1964) noted the width of the cavity does affect the amplitude of the oscillations and Cain *et al.* (1999) again noted it is of secondary importance. Tam and Block argued that the shear layer flaps into and out of the cavity near the trailing edge. They further postulated that the upward motion of the shear layer must be uncorrelated with the generation of acoustic waves. This was justified based on the notion that for the acoustic waves to be emitted, impingement on the aft wall of the

cavity must occur. If the shear layer only oscillated above the cavity, in essence covering the trailing edge of the cavity, there would be no means for acoustic wave generation as the shear layer would flow freely above the cavity. They then argued that only the downward motion of the shear layer could generate significant disturbances and radiation of acoustic waves throughout the interior of the cavity.

Following the model of Tam and Block a cavity exposed to uniform freestream supersonic flow typically exhibits a fully developed turbulent boundary layer upstream of the cavity leading edge. The boundary layer separates off the leading edge and forms a shear layer. The Kelvin-Helmholtz instability is driven by the mean shear in the velocity profile. This mean shear results in shear layer growth and the organization of the underlying vortical structures. These small scale structures convect downstream and evolve into large scale coherent structures. Consequently, the shear layer rolls-up and impinges on the aft wall of the cavity. This impingement generates resonant conditions which influence the shear layer through complex interactions with the upstream advancing acoustic waves and the shear layer. A subsonic incompressible flow theoretically senses this feedback instantaneously whereas for a compressible flow there exists a time-lag before the reflecting waves constructively (are in phase and thus synchronized with the shear layer) interfere with the shear layer disturbances as discussed in Boydston *et al.* (2008).

Rowley *et al.* (2002*a*); Rowley & Williams (2006); Rowley *et al.* (2006) suggested that the dominant tones in cavity flow are due to the instabilities in the shear layer and its coupled interaction with the acoustic field and flow. The strength of these oscillations were determined by nonlinear saturation and driven by external disturbances. They used a second order system with a one dimensional standing wave model to estimate the acoustical effects and they derived their own version of Rossiter's equation whose derivation is nicely laid out in the appendices of Song (2008).

1.3 Cavity Flow with Control

Flow control attempts to alter the natural state of a particular flow into a more desired state. Flow control strategies are classically categorized as active or passive yet they do not have clearly accepted rigorous definitions. For the purposes of this research the classification chosen is outlined in Figure 1-3. This classification is based on whether external energy is used to control an actuator, whether there exist parameters that can be modified (such as system gain or oscillation frequencies) after the control system is designed or whether the control is steady or unsteady. Active control provides energy to the flow but requires external energy to operate whereas passive control approaches do not require external energy but still may provide energy to the flow. Passive flow control approaches have been implemented with varying degrees of success. Examples of passive flow control techniques are vortex generators, geometrical modifications such as slanted aft walls or devices placed at the cavity leading such as ramps, spoilers or a rod in crossflow.

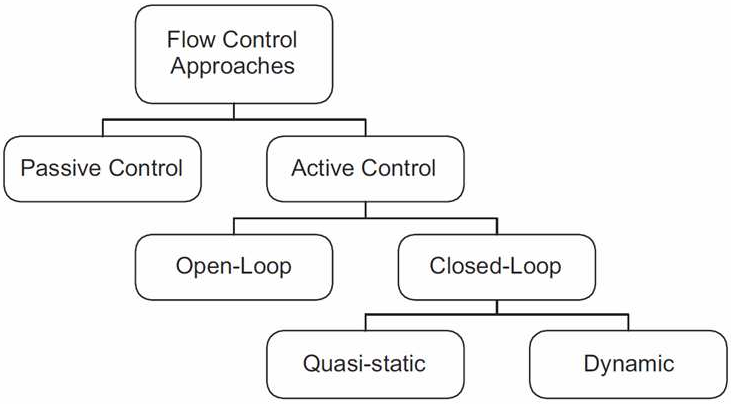

Figure 1-3. Adapted flow control classification. Reprinted with permission from Cattafesta III *et al.* (2008).

Active flow control may be further divided into open and closed-loop approaches. A closed-loop system has a well defined feedback loop where a sensor is used to change the output of an actuator which in turn effects the sensor closing the loop. In the case

of a cavity, the pressures are typically monitored on the cavity walls and processing of the data occurs before the signal is received by the actuator. Closed-loop systems can further be categorized on the basis of time scales. If the control parameters are adjusted slowly compared to the dynamics of the flow it is referred to as quasi-steady flow control. If the control parameters are adjusted on a time scale on the order of that with the flow dynamics the control is commonly referred to as dynamic control. If no such closed-loop exists the system is considered open-loop where flow control strategies are typically predetermined with no sensor measurement and are typically feed-forward systems.

Active flow control is attractive due to the ability to adapt to varying freestream conditions. Active control techniques have been successful at reducing noise levels in a wide range of operating conditions some of which will be briefly discussed next. Detailed reviews of studies on the control of cavity flows can found in the reviews by Cattafesta III *et al.* (2008), Williams *et al.* (2007) and Colonius (2001). The discussion below will discuss some highlights to set up the studies of this dissertation.

Cattafesta III *et al.* (1997) demonstrated dynamic closed-loop control in subsonic cavity flow. They were able to obtain a time transfer function to model the system which is realizable for real-time control hardware. Cattafesta et al. were able to reduce key tones on the order of 20dB with up to 20 times less power than required for open-loop control. Cattafesta III *et al.* (2001) used adaptive piezoelectric flap actuators for Mach 0.74 subsonic flow successfully suppressing the first mode by more than 10dB. Improvements to these original studies were reported in Kegerise *et al.* (2007*a*,*b*) where they developed a real-time adaptive controller using a generalized predictive control (GPC) algorithm which was successful for freestream Mach numbers ranging from 0.275 to 0.38.

Rowley *et al.* (2000*a*,*b*) applied POD based Galerkin methods that attempt to obtain low-order models of the flow. POD based methods all require the basis functions to change once the controller is turned on and the challenge is deriving a methodology to account for this. In an attempt to gain more insight into the behavior of the controlled cavity,

Rowley & Williams (2006); Rowley *et al.* (2002*b*) have also considered a linear model for cavity oscillations which incorporates the effect of external disturbances. They found the system to be unstable under some conditions where perturbations grow until nonlinearities become important and the linear model is no longer valid. For other conditions, the system is found to be stable but lightly damped and acts as a noise amplifier. They note the nonlinearities may be important for cavity oscillations in other parameter ranges. They hope the controlled system will always be stable implying the linear models presented in their work should always be useful for understanding the controlled system.

Open-loop control, on the other hand, does not use the above mentioned feedback mechanism. Some of the techniques used include upstream steady mass injection as studied by Alvi *et al.* (2003) and Vakili & Gauthier (2004). The effectiveness of piezoelectric actuators were investigated by Kegerise *et al.* (2003) and Cattafesta III *et al.* (2001). Suppression characteristics of harmonic blowing were studied by Shaw & Northcraft (1999) and Smith *et al.* (2000). Oscillating flaps were detailed in Smith & Shaw (1975) while powered resonance tubes were investigated by Kastner & Samimy (2003) and Stanek (2005). Stanek *et al.* (2000) studied four high frequency actuators in subsonic and supersonic flow: rod in cross flow, resonance tube, spoiler (saw-tooth) and piezo-ceramic wedges. They reported the most effective device for reducing tones at peak frequencies was the resonant tube. Ukeiley *et al.* (2003) investigated powered whistles to impose steady mass (nitrogen and helium) blowing at the leading edge of a supersonic cavity and reported dominant peak reductions of nearly 85% with apparent broadband suppression. Zhuang (2007) and Zhuang *et al.* (2003, 2006) have reported up to 10dB reduction in the broadband spectrum and 20dB reductions at tonal frequencies using mass injection through leading edge micro jets with the cavity flow at supersonic speeds. Williams *et al.* (2007) conducted experiments and studied the effects of open-loop forcing on the acoustic tones generated in a supersonic cavity flow and the ability of a closed-loop controller to suppress the tones. They found the amplitude of the disturbances scaled with the

freestream dynamic pressure and the acoustic tones were linearly proportional to the actuator input and were able to effectively reduce tones by roughly 10dB.

Common limitations realized for open-loop active control are the requirement for large mass-flux injection into the base flow, the physical structure (piezoelectric) tend to be prone to fatigue failures or come with the trade-off of added drag to the flow. The interested reader is directed to the more exhaustive list of references from Cattafesta III *et al.* (2008) and Colonius (2001) for more details and examples regarding open and closed loop active control.

In contrast, passive flow control does not directly provide energy input to the flow and is typically implemented by means of geometric modifications. While these methods reduce the complexity of the control systems their biggest drawbacks are they tend to be a point design and are sometimes detrimental at off design conditions. However, they are still the source of a great wealth of studies and have proven useful in many practical situations.

One example of passive studies is the numerical study of slanted leading and trailing edge walls were performed by Nayyar *et al.* (2005). Vikramaditya & Kurian (2009) conducted an experimental investigation of supersonic flow over wall mounted cavities with aft wall angles of 15 to 90 degrees. The strength of the upstream traveling acoustic wave was weakened with decreasing aft wall angles. Further investigation of passive techniques can be found in the Weapons Internal Carriage and Separation (WICS) report by Dix & Bauer (2004) which provides an immense database of experimental results for fluctuating pressure suppression at various freestream Mach numbers using different leading edge spoilers including fences and sawtooth spoilers.

A rod spoiler, as illustrated in Figure 1-4, immersed in a leading edge boundary layer has been studied in detail for the past decade with various degrees of success. In this technique to suppress the fluctuating surface pressure within the cavity a cylinder is immersed some distance (G) off the wall but still at least partially immersed inside the

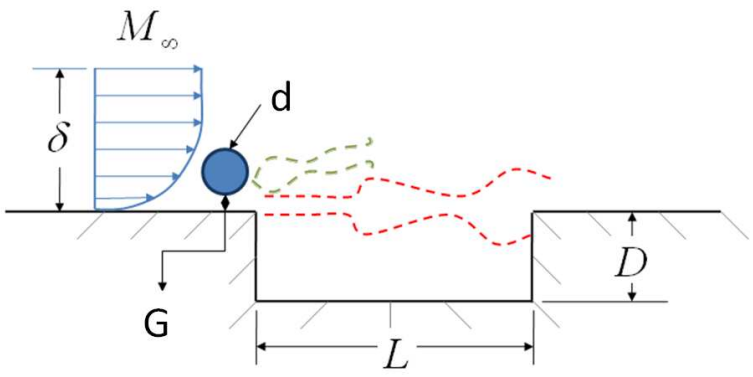

Figure 1-4. Supersonic deep cavity with a passive rod spoiler suppression mechanism.

boundary layer ahead of the cavity leading edge. This changes the flow feeding into the cavity shear layer resulting in an altered interaction of the shear layer with the cavity trailing edge. Shaw (1998) appears to be the first documented study to use the rod in cross-flow as a tone suppression device in cavity flows. Stanek (2005) and Stanek *et al.* (2002*a*, 2003) continued and expanded Shaw et al.'s experiments investigating flows in the Mach number range of $M_\infty = 0.5 - 1.2$. They elaborated on the significance of rod end effects in supersonic flow to achieve adequate shedding characteristics. Some supersonic experiments failed and Stanek et al. have attempted to link this to missing or inappropriate end conditions on the rod where the effectiveness of the rod was greatly reduced for supersonic free stream conditions. That work further showed that the lack of end caps lead to significant alterations in the vortex shedding characteristics of the rods. With this claim, it was also suggested design criteria for rods used for tone suppression in supersonic flows. He suggested a good starting point to achieve reliable optimum suppression was to use large diameter rods at least 50% of the boundary layer thickness immersed roughly $\frac{2}{3}\delta$ into the boundary layer.

Stanek *et al.* (2002*a*) hypothesized that Von-Kármán type vortex shedding by the cylinder at high frequencies supplied the necessary disturbances to the shear layer consistent with high frequency forcing. Stanek *et al.* (2002*b*) also later postulated that the interaction of the rod shedding and shear layer enhanced the shear layer

stability characteristics. This was argued to be accomplished by altering the mean shear layer growth rate. Stanek et al. were justifying their assumptions based on the work of Wiltse & Glezer (1998) who suggested that high frequency forcing (introducing disturbances at frequencies that correspond to the spectra's inertial range) was the driving mechanism behind jet shear layer noise suppression. They noted a drastic increase in the turbulent dissipation rate when the shear layer was excited by frequencies three to four times higher than it's most unstable frequency. Cain *et al.* (2001, 2003) performed numerical simulations which agreed with Wiltse and Glezer but also showed a reduction in turbulence production rates.

Ukeiley *et al.* (2002) demonstrated that a rod fully immersed in the approaching boundary, which is upstream and spans the cavity width, is a more effective suppression device than a typical fence. They showed reduction in the broadband levels as well as the resonant tones for both supersonic and subsonic freestream conditions and reported reductions on the order of 20dB. Consistent findings were discovered numerically with investigations prepared by Arunajatesan *et al.* (2002, 2003). Through the use of CFD, they have shown that control at subsonic conditions is partially achieved by lifting and spreading of the shear layer and thus the turbulent kinetic energy in the shear layer. They postulate this minimizes the impingement on the aft wall and thus the feedback receptivity mechanism for the flow.

Panickar & Raman (2008*a*,*b*) studied surface pressure suppression by high frequency excitation of the shear layer by using the cylinder in crossflow at a Mach number of $M_\infty = 0.60$. The stability characteristics of the shear layer wake profiles were studied with a new model to explain the suppression characteristics. Their claim is that suppression is achieved through the introduction of the high frequency excitation in the shear layer which decays rapidly as it is convected downstream. These introduced frequencies alter the mean velocity profile near the leading edge of the cavity and were shown to be effective at reducing the cavity resonance.

Sarpotdar *et al.* (2009) and Sarpotdar & Raman (2009) studied the cylinder in crossflow configuration for subsonic flow with $M_\infty = 0.50 - 0.80$ in order to understand the mechanism of resonance suppression using linear stability characteristics of the modified mean velocity profile. They assumed the shear layer was nearly parallel (locally), inviscid and compressible and incorporated the modified mean velocity profile. They examined the instability growth rates of experimentally measured mean velocity profiles in an attempt to correlate them to their results for the controlled cases. They found the suppression results vary greatly as the location of the cylinder is changed despite nearly constant shear layer growth rates. It should be stressed, the cylinder used in this study was sized such that $\frac{d}{\delta} \approx 1$ which is much larger than has been recommended in previous research by Stanek (2005) and Smith *et al.* (2002). They suggest that the link between the cavity tone suppression and the influence of the cylinder on the shear layer stability is weak. They state other mechanisms for cavity such as high frequency forcing and shear layer lift-off need to be examined more closely before a conclusive statement can be made.

Both Bastrzyk *et al.* (2009) and Sarpotdar *et al.* (2009) investigated how the streamwise location of the rod effected the fluctuating surface suppression. They reported the most effective placement of the rod was near the leading edge of the cavity. Bastryzk studied two different rod diameters with the rod always lying on the floor leaving questions regarding the ability to enhance suppression at various gap heights for fixed streamwise positions. Sarpotdar *et al.* (2009) reported similar results but did not consider different rod diameters. Interestingly, the optimal suppression reported in these studies was with most of the rod lying outside the boundary layer. The rod diameter was also slightly larger than the measured boundary layer height which is inconsistent with investigations reported previously. However, these are for different freestream conditions than those being examined in this research.

Previous researchers, some of whom are discussed next, have performed CFD computations of subsonic and transonic flow over a cavity using a cylindrical rod as

a passive suppression mechanism. Levasseura *et al.* (2008) reported similar results as Ukeiley *et al.* (2007) when comparing a rod and spoiler as suppression devices. Comte *et al.* (2008) reported a strong sensitivity of the rods performance based on the turbulence levels of the upstream boundary layer. They quantified this by considering two cases for the Reynolds Averaged Navier-Stokes (RANS)-Large Eddy Simulation (LES) coupling. The first simulation utilized a classic coupling of the RANS-LES equations where no upstream turbulence is added to the simulation. The second simulation added turbulence generated by the recycling method proposed by Lund *et al.* (1998). The upstream forcing is limited to the size of the integral scale of the turbulence found in the cylinder wake. They noted suppression cases with the injected turbulent fluctuations agreed more favorably with the experimental data while the baseline cavity simulations remained unsensitive to the added fluctuations. They concluded that the Kelvin-Helmoltz instability impinging on the aft wall of the cavity is reduced but the mean flow profiles between the baseline and suppression case do not show significant differences. They also postulated that the mean upward deflection of the shear layer (lofting) does not seem to play a significant role in the suppression. They further conjecture that small scale vortical structures injected into the flow from the wake of the cylinder seem to enrich the frequency content altering the shear layer profile which is consistent with arguments by Stanek *et al.* (2003).

Smith *et al.* (2002) summarized experiments conducted by Lockheed Martin Aeronautics in their transonic in-draft wind tunnel in Fort Worth Texas. The experiments included the placement of the rod downstream and upstream of the cavity leading edge, low drag model rods incorporating a 20° included angle and a flat-top rod with a 10° included angle. The conclusions were consisted with that reported previously by Stanek and are summarized as follows:

- Larger rods were generally more effective flow control devices.

- Effective suppression required the rod to be immersed roughly 30% of the boundary layer thickness.
- Rods appear to maintain their suppression characteristics for supersonic flows.

To date Williams *et al.* (2007) and Stanek *et al.* (2003) have provided the most complete summary of the mechanisms believed to be at work in reducing and disturbing the acoustic feedback and receptivity of cavity flows:

- The high frequency rod shedding convects downstream and breaks down the coherent structures in the shear layer. The accelerated energy cascades in the inertial range destructively interfere with and starve the lower frequency modes.
- The lofting of the shear layer alters the impingement point on the aft wall and consequently alters the mean shear profile.
- The thickening of the shear layer alters the inviscid instability characteristics of the shear layer.
- The cancelation of the acoustic feedback wave within the cavity due to any combination of the above.

The ultimate goal of this research is to gain an understanding of how the flow is altered when a rod is placed inside the boundary layer at the leading edge of supersonic cavity flow. This will be accomplished by detailed analyses of the acquired quantitative flow field velocity and surface pressure measurements for both baseline and multiple suppressed configurations. The broadband noise levels, key spectra peaks and wall pressure fluctuations will be investigated to determine the effectiveness of the rod as an actuator and the optimal size and positioning based on the supersonic facility at the REEF. Mean flowfield measurements using a compliment of experimental and numerical simulations through the cavity shear layer will be considered to determine the likely suppression mechanism using the rod in crossflow.

CHAPTER 2
STATISTICAL ANALYSIS TECHNIQUES

Throughout this dissertation a time series, defined as an ordered sequence of observations, will be used in the discrete form where a sequence of observations are taken at evenly spaced points in time. The acquired time series is assumed to be weakly stationary implying the mean values and autocorrelations are time invariant. The time series is further assumed to be ergodic implying all of the statistics computed from the single time series are equal to those calculated from an ensemble average.

2.1 Unsteady Pressure Measurements

Several statistical concepts will be used for the analysis of unsteady pressure measurements in this study and are subsequently introduced. The fluctuating component of the pressure will be the primary variable of interest for pressure measurements and are found from a classical Reynolds decomposition. Equation 2–1 gives the fluctuating pressure

$$p'(t) = p(t) - \overline{p}(t) \tag{2–1}$$

where the prime represents the fluctuating component of the variable, the overbar represents the mean and a variable with no demarcation represents the instantaneous value. The mean takes the traditional definition given in Equation 2–2

$$\overline{p}(t) = \frac{1}{N}\sum_{1}^{N} p(t) \tag{2–2}$$

where the number of independent observations is given by N which is sufficiently large to ensure the mean value has converged. The variation of the measured unsteady pressure

$$p_{\text{rms}} = \sqrt{\frac{1}{N-1}\sum_{1}^{N} p'^{2}(t)} = \text{std}\left(p(t)\right) \tag{2–3}$$

is studied using the root-mean-square (rms) of the fluctuating variable and is commonly referred to as the standard deviation in statistical literature. Computed percent reductions

follow

$$\%\text{diff} = \frac{|\text{baseline} - \text{suppressed}|}{\text{baseline}} \times 100\% \tag{2–4}$$

and are found by considering the suppressed and baseline values of the variable of interest.

2.1.1 Spectral Calculations

The Fourier Transform (FT) converts a signal from the time (t) domain to the frequency (f) domain which is the cyclical frequency. The Fourier transform is the basis for much of the pressure signal analysis in this dissertation. A Discrete Fourier Transform (DFT) is applied to the time series $f_n(t)$ and subsequently transformed yielding

$$A_k(n) = \sum_{n=0}^{N-1} f_n(t)\, e^{-\frac{i2\pi}{N}kn}, k = 0, 1, 2, ..., N-1 \tag{2–5}$$

where the discrete signal is assumed to repeat in a periodic fashion. The Fast Fourier Transform (FFT) is simply a class of special algorithms which implement the DFT with considerable savings in computational time and is thus used extensively in this dissertation.

Power spectral density functions (PSD) show the strength of power variations as a function of frequency normalized to a 1Hz bin. Simply stated, it shows at which frequencies variations are strong and at which frequencies variations are weak. Throughout this work the use of the periodogram method will be implemented for estimating power spectra. Following the work of Welch (1967) let a sample from a stationary stochastic sequence be given by $X(j)$ where $j = 0, 1, 2...N-1$. The sequence may be split into segments of length L, that may use overlapping, with the starting points separated by distance D. There are then K segments of $X_k(j)$ such that they cover the entire record (N) and $(K-1)D + L = N$. A modified periodogram is computed for each segment of length L where a window is selected $W(j)$ for $j = 0, 1, 2...L-1$. The sequences $X_k(j)W(j)$ are formed and the finite Fourier transforms are computed on each segment

$$A_k(n) = \frac{1}{L}\sum_{j=0}^{L-1} X_k(j)\, W(j)\, e^{\frac{-2kijn}{L}} \tag{2–6}$$

where $i = \sqrt{(-1)}$. The K periodograms are then computed

$$I_k(f_n) = \frac{L}{U} |A_k(n)|^2 \tag{2–7}$$

where $k = 1, 2, ...K$, $f_n = \frac{n}{L}$ for $n = 0, 1, ..\frac{L}{2}$ and $U = \frac{1}{L} \sum_{j=0}^{L=1} W^2(j)$. The spectral estimate, given by $\hat{P}(f_n)$, is the mean of these periodograms

$$\hat{P}(f_n) = \frac{1}{K} \sum_{k=1}^{K} I_k(f_n) \tag{2–8}$$

with a resulting spectral window whose area is unity and whose width is of order $\frac{1}{L}$. The frequency resolution of the PSD estimate is given by $f_r = \frac{f_s}{\text{nfft}}$ where f_s is the sampling frequency and nfft is the length of an individual block of the PSD estimate.

2.1.2 Joint Time-Frequency Analysis

One limitation of time averaged frequency spectra is that it is not capable of distinguishing whether the resonant modes coexist or experience mode switching. Mode switching occurs when the peak with the dominant amplitude switches modes as a function of time. Joint time-frequency analysis provides information containing frequency, time and amplitude allowing one to visualize the time-evolution of the frequency content. The spectrograms are computed using Short-Time Fourier Transform (STFT)

$$STFT(t, f) = \int_{-\infty}^{\infty} z(t) w^*(t - \tau) e^{-i2\pi f\tau} d\tau \tag{2–9}$$

where $z(t)$ is a window function with a short time duration. The time dependent input signal is partitioned into several disjointed or overlapped blocks by multiplying the signal with a Hanning window. The Fast Fourier Transform is then applied to each block. The blocks occupy different time periods so the resulting STFT computes the spectral content of the input signal at each period. The STFT therefore represents the time-dependent power spectrum of the input signal.

A well known property of the Fourier transform pair $s(t)$ and $S(\omega)$ is the uncertainty principle described in Qian & Chen (1996). The principle states the time duration Δ_t of

$s(t)$ and the frequency bandwidth Δ_ω are related by $\Delta_t \Delta_\omega \geq \frac{1}{2}$. This implies a longer time duration of the input signal will result in a smaller frequency bandwidth and conversely the larger the frequency bandwidth of the transformed input signal, the shorter the time duration of the input signal. This illustrates the tradeoff between the frequency resolution and time resolution when using this method. The precision of the transform is determined by the size of the selected window and is fixed for all frequencies. It is recognized that this could be a limiting case in the analysis of turbulent flowfields. Joint time frequency analysis using STFT has been used successfully for highly resonant cavity flowfields as evident in the works Kegerise *et al.* (2004) among others.

2.1.3 Correlation Analysis

Cross-correlation and cross-coherence analysis was used to help determine how strongly two signals are related. If the signals are identical the correlation coefficient is unity and if they are unrelated the correlation coefficient is zero. If the signals are identical except that the phase is shifted by exactly 180 degrees then the correlation coefficient is -1. When two independent signals are compared in the time domain the procedure is known as cross-correlation. Autocorrelation is a special case of cross-correlation where the same signal is compared to itself. The auto correlation coefficient of a signal $x(t)$ is given as

$$\hat{R}_{xx}(r\Delta t) = \frac{1}{N-r}\sum_{n=1}^{N-r} x'_n x'_{n+r} \quad r = 0, 1, 2, ..., m \tag{2–10}$$

where the time lag is given by $\tau = r\Delta t$, r is referred to as the lag number and the maximum number of lags is given by m. The cross-correlation of two signals $x(t)$ and $y(t)$ is then

$$\begin{aligned} \hat{R}_{xy}(r\Delta t) &= \frac{1}{N-r}\sum_{n=1}^{N-r} x'_n y'_{n+r} \\ \hat{C}_{xy}(r\Delta t) &= \frac{\hat{R}_{xy}(r\Delta t)}{\sqrt{\hat{R}_{xx}(\tau=0)}\sqrt{\hat{R}_{yy}(\tau=0)}} \quad r = 0, 1, 2, ..., m \end{aligned} \tag{2–11}$$

where $\hat{R}_{xy}$ and $\hat{C}_{xy}$ are is the cross-correlation and normalized cross-correlation coefficient estimates respectively.

The cross-correlation performed in the time domain is a computationally inefficient approach, as described in Papoulis (1962), which may be computed faster by the use of the FFT. The enhanced correlation is written by convolving the first function, $g(t)$, with the time-reverse of the second function given by $h(t)$

$$g(t) \times h(t) = g^*(-t) \star h(t) \tag{2–12}$$

where the $\star$ denotes a convolution, $*$ is the complex conjugate and $\times$ indicates the cross-correlation. The convolution is defined as

$$g \star h = \int_{\infty}^{\infty} g(\tau)\, h(t-\tau)\, d\tau. \tag{2–13}$$

The resulting cross-correlation as demonstrated by Papoulis (1962) is therefore

$$g \times h(t) = \int_{\infty}^{\infty} g^*(\tau)\, h(t-\tau)\, d\tau. \tag{2–14}$$

The ordinary coherence function reveals how well one data set could be explained by a linear fitted version of another data set. The ordinary coherence function, given in Equation 2–15, is a measure of the average correlation between two time series at each frequency

$$\hat{\gamma}_{xy}^2(f) = \frac{|\hat{S}_{xy}(f)|^2}{\hat{S}_{xx}(f)\,\hat{S}_{yy}(f)} \tag{2–15}$$

where $\hat{S}_{xy}(f)$ is the cross spectra between the two sensors and $\hat{S}_{xx}(f)$ and $\hat{S}_{yy}(f)$ are the auto-spectra of those two sensors, detailed in Bendat & Piersol (1986), which are all estimated discretely. Normalization values of one represent perfect correlation between the two sensors at that given frequency.

2.2 Turbulent Statistics and Flowfield Measurements

Particle image velocimetry was used extensively in this research therefore a brief description of the computed variables are presented next. Image pairs were acquired at an interval of 7Hz which for this flowfield makes them appear as randomly sampled independent members of an ensemble. The streamwise and normal components of the

velocity vectors are functions of space and snapshot and the (x, y, N) nomenclature will be dropped for convenience in the definitions below. Velocity components (u, v, w) will be taken as the streamwise, normal and spanwise flow directions which corresponds to fixed coordinate directions (x, y, z) respectively. Tensor notation for the velocity field may be used for conciseness (u_i) where $i = 1, 2, 3$ correspond to u, v, w velocities respectively.

The ensemble average of the velocity is

$$\langle u_i \rangle = \frac{1}{N} \sum_{n=1}^{N} u_{i_n} \tag{2–16}$$

where N is the total number of valid vectors at a given point in the vector flowfield. The fluctuating velocity is found from classical Reynolds decomposition

$$u_i{}' = u_i - \langle u_i \rangle . \tag{2–17}$$

where lower case variables represent the instantaneous velocities, $\langle\rangle$ represent the ensemble averaged quantities and primes mark the fluctuating component of a given variable. The root-mean-square of the velocities are

$$\langle u_{i,\mathrm{rms}} \rangle = \sqrt{\frac{1}{N-1} \sum_{n=1}^{N} \left(u_i{}'\right)_n{}^2} \tag{2–18}$$

where the unbiased estimator of the population variance is used.

Quantitative density measurements could not be measured for the experiments so turbulent stress calculations neglect density as was done for consistency with numerical calculations. The Reynolds stress tensor simplifies accordingly

$$R_{ij} = \langle u_i{}' u_j{}' \rangle \tag{2–19}$$

where the shear stress components are found when $i \neq j$ and normal stresses are computed when $i = j$. The simplified equation for the Turbulent Kinetic Energy (tke) is

$$\mathrm{tke} = \left\langle \frac{1}{2} u_i{}' u_i{}' \right\rangle \tag{2–20}$$

which is simply the trace of the Reynolds stress matrix. It should be noted since all velocities were available for the numerical simulations the turbulent kinetic energy was computed using all three components of the velocity field.

The length scale variations in the shear layer are studied by employing a two point spatial cross-correlation on the components of the fluctuating velocity with an origin defined at some fixed point ($\vec{x}$) with a known separation ($\vec{r}$). The two point spatial tensor is then

$$\rho_{ij}\left(\vec{x},\vec{r}\right)=\frac{\left\langle u_i{}'\left(\vec{x}\right)u_j{}'\left(\vec{x}+\vec{r}\right)\right\rangle}{\sqrt{\left\langle u_i{}'^2\left(\vec{x}\right)\right\rangle}\sqrt{\left\langle u_j{}'^2\left(\vec{x}+\vec{r}\right)\right\rangle}} \tag{2–21}$$

where at zero separation the diagonal elements represent the normal turbulent stresses and the off diagonals represent the turbulent shear stresses. With the spatial separation represented in the correlation, one may look at how the velocity at the defined origin is related to the velocity at another point which inherently defines a length ($\vec{r}$) of how far apart the velocities are related. Similarly, pressure correlations were performed on the cavity surfaces using the expression

$$P\left(\vec{x},\vec{r}\right)=\frac{\left\langle p'\left(\vec{x}\right)p'\left(\vec{x}+\vec{r}\right)\right\rangle}{\sqrt{\left\langle p'^2\left(\vec{x}\right)\right\rangle}\sqrt{\left\langle p'^2\left(\vec{x}+\vec{r}\right)\right\rangle}}. \tag{2–22}$$

The z-vorticity (ω_z) field calculation was based on a circulation (Γ_{ij}) estimate

$$\begin{aligned}\omega_{z_{i,j}}&=\frac{\Gamma_{i,j}}{8\Delta X\Delta Y}\\ \Gamma_{i,j}&=\Delta X\left(u_{i-1,j-1}+2u_{i,j-1}+u_{i+1,j-1}\right)+\\ &\Delta Y\left(v_{i+1,j-1}+2v_{i+1,j}+v_{i+1,j+1}\right)-\\ &\Delta X\left(u_{i+1,j+1}+2u_{i,j+1}+u_{i-1,j+1}\right)-\\ &\Delta Y\left(v_{i-1,j+1}+2v_{i-1,j}+v_{i-1,j-1}\right)\end{aligned} \tag{2–23}$$

with differencing including the neighboring eight points as detailed in Raffel *et al.* (1998). The application of this differentiation scheme is comparable to applying a central difference scheme, which has a truncation error estimate of $0.7\frac{\epsilon_U}{\Delta X}$, to a smoothed velocity

field where the velocity uncertainty is given by ϵ_U. Application of this differencing tends to result in a lower truncation error which may be estimated by $0.61\frac{\epsilon_U}{\Delta X}$.

2.3 Proper Orthogonal Decomposition

The Proper Orthogonal Decomposition (POD) as proposed by Lumley (1967) is a commonly used tool for extracting a basis set from a set of experimental or numerical data which exhibit non-homogeneous conditions. The data is represented as a function of space and time and the POD determines a basis set of orthogonal functions of space which span the data. Given that $u_i(\vec{x},t)$ is a function of space and time the POD determines orthogonal functions $\phi^i(\vec{x}), j = 1, 2, ...,$ where the projection

$$u(\vec{x},t) = \sum_{i=1}^{n} a_i(t)\,\phi_i(\vec{x}) \tag{2–24}$$

is optimized such that the projection onto the first n functions results in the smallest error $E(||u_i - \hat{u_i}||^2)$ where E represents the time average and $(||u_i - \hat{u_i}||^2)$ is the L^2 Euclidian norm on spatial functions.

The POD coefficients given by $a_i(t)$ are uncorrelated. The modes are optimal, in converging on a mean square sense, for reconstructing a signal implying that among all other linear decompositions Equation 2–24 is the most compact. For a given number of POD modes the projection will contain, on average, the most turbulent kinetic energy. The empirical eigenfunctions, commonly referred to as POD modes, are represented by ϕ^i assuming the two point spatial velocity tensor is used as the kernel. The POD modes are computed by solving the following Fredholm integral equation as described in Berkooz *et al.* (1993)

$$\int K(\vec{x},\vec{x}+\vec{r})\,\phi(\vec{x}+\vec{r})\,dy = \lambda\phi(\vec{x}) \tag{2–25}$$

whose kernel $K(\vec{x},\vec{x}+\vec{r})$. The kernel is also referred to as the two-point turbulent velocity correlation tensor and is given in Equation 2–26

$$K(\vec{x},\vec{x}+\vec{r}) = \langle u_i(\vec{x})\,u_i^*(\vec{x}+\vec{r})\rangle \tag{2–26}$$

where the * notation denotes the complex conjugate and x and $\vec{x} + \vec{r}$ are vectors that represent any two points of a cartesian coordinate system. Equation 2–25 may be more compactly written as an eigenvalue problem

$$K\phi = \lambda\phi. \tag{2–27}$$

According to the Hilbert-Schmidt theorem explained in Riesz & Nag (1955) there exists a diagonal decomposition of the kernel given by

$$K\left(\vec{x}, \vec{x} + \vec{r}\right) = \sum_{i=1}^{\infty} \lambda^i \phi^i\left(\vec{x}\right) \phi^{*i}\left(\vec{x} + \vec{r}\right) \tag{2–28}$$

where ϕ^i and λ^i are the eigenvector and eigenvalue pair of the kernel K and $\lambda^i \geq 0$ since K is a positive definite matrix. The ensemble may be reproduced by a modal decomposition using the eigenvalues and eigenvectors as given by Equation 2–24.

Equation 2–27 is commonly solved using the Method of Snapshots developed by Sirovich (1987). This method was introduced as an efficient approach when the resolution of the spatial domain (N) exceeds the number of independent observations (M). The discrete form of the kernel (K) given by

$$\overline{K} = \frac{1}{N} Y Y^T \tag{2–29}$$

where Y is a vector given by $Y = \left[u\left(x_1, t\right), u\left(x_2, t\right) ... u\left(x_N, t_i\right)\right]^T$, Y^T is the transpose of Y and x_j is the jth grid point of Y. The data set can be obtained from either a numerical simulation or experimental observations or a combination of the two. A numerical solution for the POD Modes from Equation 2–27 is typically solved using a singular value decomposition

$$\begin{aligned} \text{svd}\left(\overline{K}\right) &= \Phi \Sigma \Phi^T \\ Y Y^T \Phi &= \Phi \lambda \end{aligned} \tag{2–30}$$

where Φ is an $m \times m$ orthonormal matrix forming left singular vectors with the column vectors who form an orthogonal basis and are the POD modes. $\Sigma = N\lambda$ is an $m \times N$

semi-positive-definite matrix. Φ^T is the transpose of Φ and forms the right singular vectors.

The method of snapshots is applied assuming the POD modes are a linear combination of the snapshots

$$\Phi = YA \tag{2–31}$$

where Y is an $m \times N$ matrix, m is the number of spatial points and N is the number of snapshots. The matrix A is determined by substituting Equation 2–31 into Equation 2–30 which yields the eigenvalue problem

$$\begin{aligned} Y^T Y A &= A\lambda \\ CA &= \lambda A \end{aligned} \tag{2–32}$$

where A represents the eigenvectors of the empirical correlation matrix $C = \left(Y^T Y\right)$. The POD modes may then be determined by normalizing the column vector ϕ^j of Φ by it's L^2 norm

$$\phi^j = \frac{\phi^j}{||\phi^j||}, j = 1, 2, ..., n. \tag{2–33}$$

Statistically speaking, λ^j represents the variance of the data set on the direction of the corresponding POD mode. In the case of this dissertation this implies that since u or v will represent components of a fluctuating velocity field, then λ^j measures the amount of turbulent kinetic energy captured by the corresponding POD mode. The total turbulent kinetic energy captured in a POD may then be represented by

$$E = \sum_{i=1}^{n} \lambda^n. \tag{2–34}$$

The relative energy captured at the nth mode may then be expressed

$$E_n = \frac{\lambda^n}{\sum_{i=1}^{n} \lambda^i}. \tag{2–35}$$

2.4 Non-Dimensionalization

For simplicity, this research attempts to maintain consistent non-dimensional plotting where streamwise ($+x$) lengths will typically be divided by the cavity length (L) and normal heights ($+y$) by the cavity depth (D) which is typical convention for cavity flows. The exception for these guidelines falls in Chapter 5 where the simulation consisted of two rods of different diameter (d) immersed in a flat plate supersonic boundary layer with a height (δ) at various gap heights with no cavity present. The appropriate turbulent length scales for this type of boundary layer flow may be taken as the boundary layer height in the normal direction and the rod diameter in the streamwise direction and therefore the normal and streamwise coordinate directions are non-dimensionalized by δ and d respectively. To attempt to reduce ambiguity, the capital letter D will represent a given cavity depth while the lower case letter d will represent a given cylinder diameter throughout the remainder of this research.

The freestream dynamic pressure (Q_∞) can be shown to be a function of the freestream total pressure (P_0). The freestream density (ρ_∞) may be found from the ideal gas law given in Equation 2–36

$$\rho_\infty = \frac{p_\infty}{RT_\infty} \tag{2–36}$$

where p_∞ is the freestream static pressure, T_∞ is the freestream static temperature and R is the specific gas constant. The compressible flow relation for the freestream velocity (U_∞) is

$$U_\infty = \frac{M_\infty}{a_\infty} = \frac{M_\infty}{\sqrt{\gamma RT_\infty}} \tag{2–37}$$

where a_∞ and M_∞ are the freestream speed of sound and Mach number respectively. Substitution of Equation 2–36 and Equation 2–37 in the equation for dynamic pressure yields

$$Q_\infty = \frac{1}{2}\rho_\infty {U_\infty}^2 = \frac{\gamma}{2} p_\infty {M_\infty}^2. \tag{2–38}$$

The variable γ represents the ratio of specific heats and is calculated from $\gamma = \frac{C_p}{C_v} = 1.4$. The isentropic compressible flow relation for the ratio of the static and stagnation pressures derived in John & Keith (2006) is

$$\frac{p_\infty}{P_0} = \left(1 + \frac{\gamma - 1}{2} {M_\infty}^2\right)^{\frac{\gamma}{\gamma-1}}. \tag{2–39}$$

Substitution of the static pressure as a function of the stagnation pressure into Equation 2–38 yields an expression for the freestream dynamic pressure as a function of the freestream stagnation pressure yielding

$$Q_\infty = \frac{\gamma}{2} P_0 {M_\infty}^2 \left(1 + \frac{\gamma - 1}{2} {M_\infty}^2\right)^{-\frac{\gamma}{\gamma-1}}. \tag{2–40}$$

Power spectral density plots and root-mean-square pressures will be non-dimensionalized by the mean freestream dynamic pressure

$$PSD^* = \frac{\sqrt{PSD \times f_s}}{Q_\infty} \tag{2–41}$$

$$p^*_{\text{rms}} = \frac{p_{\text{rms}}}{Q_\infty} \tag{2–42}$$

following Equations 2–41 and Equation 2–42 respectively.

When a cavity is present the streamwise and normal directions are non-dimensionalized by the cavity length and depth

$$x^* = \frac{x}{L}, \quad y^* = \frac{y}{D}. \tag{2–43}$$

When no cavity is present, as is the case for Chapter 5, the appropriate turbulent length scales are the rod diameter and the boundary layer height. The streamwise and normal directions are therefore non-dimensionalized according to

$$x^* = \frac{x}{d}, \quad y^* = \frac{y}{\delta}. \tag{2–44}$$

The rod key non-dimensional variables are given below

$$d^* = \frac{d}{\delta}, \quad G^* = \frac{G}{\delta} \tag{2–45}$$

where the variable G is the gap height between the bottom of the cylinder and the wall, δ is taken as the boundary layer height and d is the rod diameter.

All velocities (mean, fluctuating or root-mean-square) are non-dimensionalized by the mean freestream velocity given by Equation 2–37 which gives

$$u_i{}^* = \frac{u_i}{U_\infty}, \quad u_{i_{\text{rms}}}{}^* = \frac{u_{i_{\text{rms}}}}{U_\infty}. \tag{2–46}$$

The corresponding Reynolds stresses and turbulent kinetic energy are non-dimensionalized by the freestream velocity squared giving

$$R_{ij}{}^* = \frac{R_{ij}}{{U_\infty}^2}, \quad tke^* = \frac{tke}{{U_\infty}^2}. \tag{2–47}$$

The z-component of the vorticity field is non-dimensionalized by the ratio of the cavity length and freestream velocity yielding

$$\omega_z{}^* = \frac{\omega_z L}{U_\infty}. \tag{2–48}$$

CHAPTER 3
THE FACILITY AND EXPERIMENTAL TECHNIQUES

This chapter will begin with a discussion regarding the design of the supersonic wind tunnel which was designed and installed at the REEF. This discussion is followed by explanations of the experimental data acquisition techniques and the specific cavity geometries studied. The chapter is concluded with a summary of the anticipated uncertainty of the experimental observations.

3.1 Facility Overview

A blowdown SWT as illustrated in Figure 3-1 and detailed in Dudley *et al.* (2008) was recently designed and installed at the REEF. The tunnel emphasized a modular design and includes optical access through the test-section to allow for the use of PIV and Schlieren imaging techniques. The facility uses a 44m^3 storage tank with high pressure air supplied from a rotary screw Quincy Compressor (model QSI 1000 A/C) capable of producing 26.4m^3/min at 1448kPa through 50.8mm diameter piping. From the exit of the compressor the air flows through a desiccant dryer which lowers the dew point of the air to 232.2K before entering the storage tank.

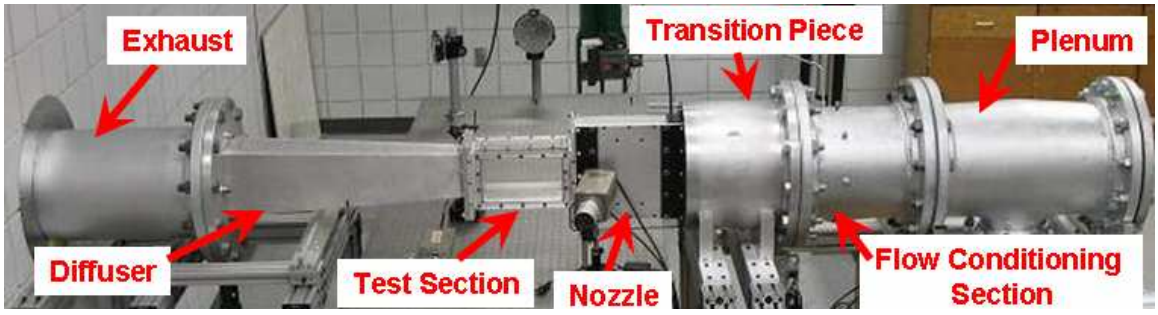

Figure 3-1. The supersonic wind tunnel.

The tunnel generally operates at a stagnation pressure of 172kPa allowing for approximately 180s of run-time. Subsonic air is brought into the plenum and filtered through a honeycomb substrate used to breakdown any remaining organized large scale turbulent motions in the flow conditioning section. The air then passes through the first contraction designed to smoothly transition the cross-section from circular to

rectangular which matches the inlet face of the nozzle. The nozzle is a two dimensional converging-diverging assembly with an exit cross section of 76.2mm wide by 101.6mm tall. The nozzle was designed using classical method of characteristics, found in John & Keith (2006), and further evaluated with RANS numerical simulations resulting in the Mach contours illustrated in Figure 3-2. The air next passes through a constant area

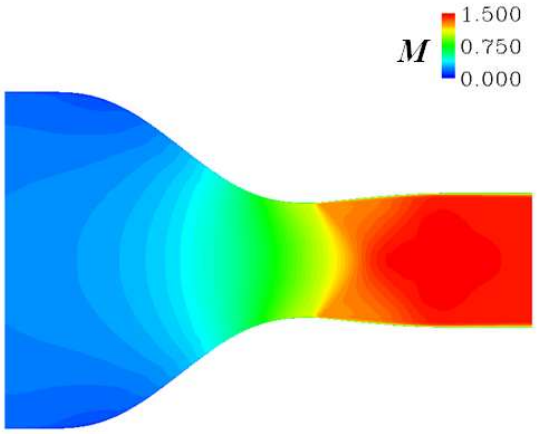

Figure 3-2. RANS solution of the supersonic wind tunnel nozzle.

test-section with a uniform rectangular cross-section. Air then enters the diffuser with diverging angles totaling 5.5° to keep the flow from separating. The air is finally exhausted through 304.8mm piping as shown in Figure 3-1 above. The cross-section of the test-section has a height of 101.6mm and a width of 76.2mm. It should be noted that the aspect ratio of this test-section is somewhat unconventional in supersonic wind tunnel design with the height being greater than the width. The additional vertical height allowed for a maximum length cavity to be inserted by giving the anticipated oblique shock wave at the leading edge of the cavity a longer streamwise distance to traverse before being reflected off the top wall as shown in Figure 3-3. Computational fluid dynamics and analogy from similar experimental studies were used in estimating the oblique shock angle illustrated by α. Assuming a perfect reflection off the top wall, the test-section height was chosen so the reflected shock wave would fall a minimum of 2D downstream of the aft wall of a cavity with a length of 228mm.

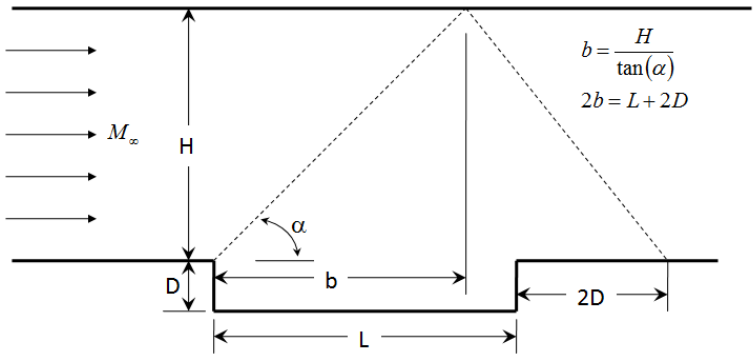

Figure 3-3. Test-section with analytical wave reflection.

The test-section, as illustrated in Figure 3-4, was symmetrically designed so either a top or bottom mounted cavity could be installed. The design consists of a one piece 6061-aluminum frame with four rectangular cutouts for optical access. The primary optical inserts were fabricated with 19mm thick $N-BK-7$ Schott optical grade glass machined and polished to $0.5-1$ waves flatness per 25.4mm 60/40 scratch/dig and a maximum allowable chip of 0.25mm. Plexiglas and aluminum inserts are available when visual access to the tunnel is not required. The assembly is sealed with the use of 1.6mm diameter O-Ring inserts.

Figure 3-4. Test-section with flat plate.

3.2 Cavity Design

Two cavities have been designed and built for this research. The first cavity is a finite span cavity which has been designed with a $\frac{L}{D} = 6$, $\frac{L}{W} = 3$ and a length of 76.2mm. The full span, or two dimensional cavity, is included in the research with an identical $\frac{L}{D}$ ratio and length but spans the entire test-section, ie $W = 76.2$mm. The cavity is a four piece construction as shown in Figure 3-5. A 12.2mm long leading edge block is mounted to the aluminum frame followed by a rectangular floor section. The trailing edge block is constructed of 6061-aluminum where two plugs (pieces that sit flush with trailing edge block front surface to make the full-span cavity) or sidewall blocks (that are illustrated in orange in Figure 3-5) are attached. Depending on the desired application the cavity sidewalls are fabricated with either BK7 glass or plexiglass when optical access is desired or aluminum when it is not. This design allows for easy transition between the full and finite span cavity sharing a floor where the bulk of the pressure transducers were mounted.

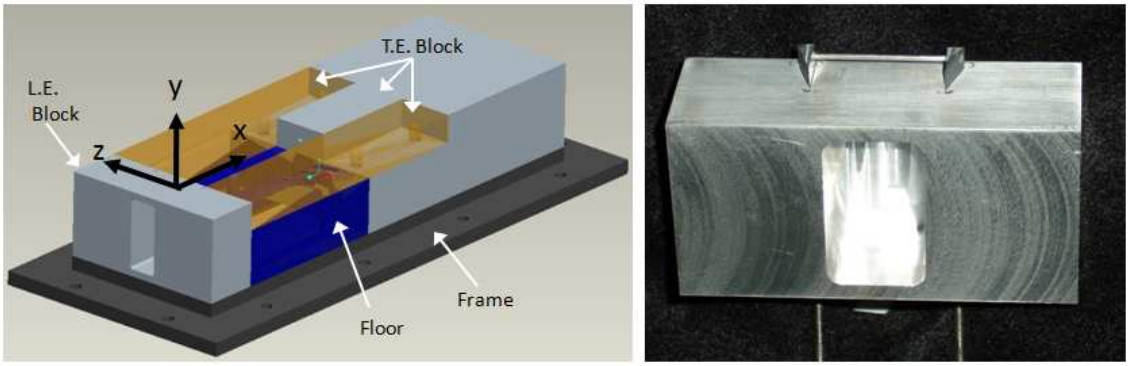

Figure 3-5. Finite span cavity with closeup of rod mounted on leading edge block

The leading edge block of the cavity was fitted with a fixture that supports the rod spoiler whose suppression characteristics were studied with specific details reported in Chapter 6. An oblique triangular cross section mount with an angle of 20° was designed for the cylinder end mounts for shock management. The rod spans the full cavity width for the finite span cavity and details of the mounting structure for the two dimensional

cavity will follow. It is understood the effect of the rod span length may be further parameterized which is beyond the scope of the current research. Figure 3-6 illustrates the mean pressure contours taken from a RANS CFD simulation. The numerical approach for the simulation is presented in depth in Chapter 4. This solution was acquired at a constant y-plane intersecting the support when positioned at a height for the most effective rod placement corresponding to $d^* = 0.43, G^* = 0.57$. The pressure disturbances interfering with the cavity flow due to the expansion waves off the inside corner are evident and unavoidable with the current mount location. The leading edge attached oblique shock reflects off the test-section side wall and subsequently becomes very weak upon reaching the cavity side walls. Suppression studies using the full span cavity had

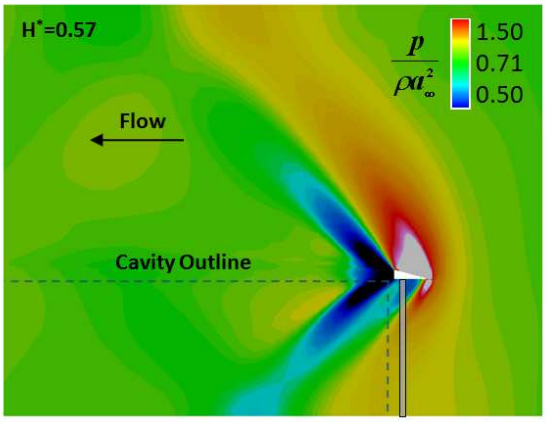

Figure 3-6. Simulation of flow around rod mounting structure.

to ensure there was minimal deflection or bending of the rod because it is not feasible to stretch the rod the whole span of the test-section due to the small scales of the research (the rod would certainly bend). With that in mind, the rod length and wall thickness was selected to minimize rod deflection. The rods selected (for both three dimensional and full span cavities) were hollow cross-section 304 stainless steel with a minimum wall thickness of 0.2mm. The length chosen was 38mm (25.4 mm for the finite span cavity) resulting in deflections of less than 0.90mm for the smallest diameter rod based on the freestream flow and simple beam calculations. It was found that neither the anticipated

longitudinal or transverse natural frequency of the rod were of major concern as the fundamental frequency exceeded the cavity resonant tones and the anticipated shedding frequencies of the rods. Details of the deflection and natural frequency analysis can be found in Appendix B.

Figure 3-7 illustrates a close up of the rod and variables used to define its location relative to the wall and cavity leading edge. The gap distance measured from the wall to the bottom most part of the cylinder is denoted by G. The distance to the cavity leading edge from the most forward part of the rod is denoted by X_2 which is fixed at 3.2mm. The extra distance allows for a pressure transducer to be mounted used to measure the vortex shedding frequency of the rod(s). The mounting structures are pocketed and filled with a small amount of epoxy to hold the cylinder in place. The lower case d defines the rod diameter while G_{cl} and X_{cl} give the vertical and streamwise position of the rod centerline.

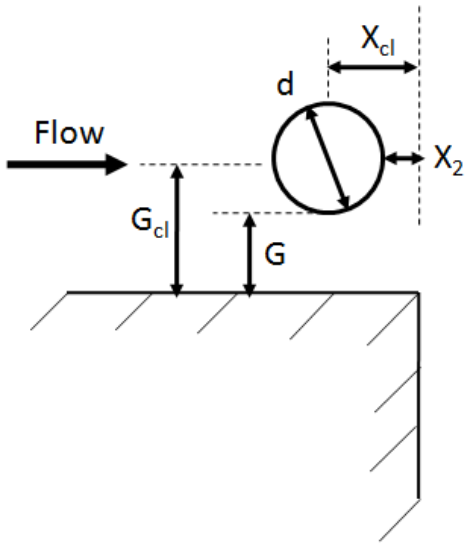

Figure 3-7. Rod mounting location relative to cavity leading edge

3.3 SWT Characterization

Qualitative and quantitative measurements were obtained to ascertain the quality of the flow through the test-section. There was less than 2% spanwise pressure variation

measured at various streamwise positions on the bottom wall. The streamwise pressure distribution measured on the centerline varied by less than 3% over the length of the cavity considered in this study. The measured variation is likely attributable to the growth of the boundary layer with a constant cross-section of area. For a further discussion of the sidewall boundary layer results and pressure variations the interested reader is referred to Dudley *et al.* (2008). A United Sensor stainless steel boundary layer probe with a sensing head diameter of 0.64mm flattened down to 0.20mm was used to measure the boundary layer profiles on the bottom wall. Measurements were taken on the floor 41.3mm downstream of the nozzle exit.

Figure 3-8 overlays the boundary layer as measured in the SWT and the computational boundary layer found at the exit of the nozzle. There is good agreement between the numerical and experimental profiles down to the minimum measurement distance in the experiment of 0.30mm off the wall. The maximum percent difference was on the order of

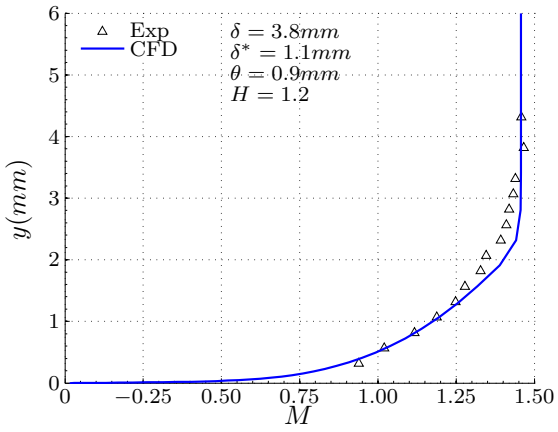

Figure 3-8. Experimental and numerical boundary layer profile comparison.

1.7% and the mean difference across all measurement locations was 0.7%. The boundary layer thickness (δ) in Figure 3-8 at 99% of freestream velocity is 3.8mm. The resulting momentum (θ) and displacement thickness (δ^*) are then 0.9mm and 1.1mm respectively computed as shown in Equation 3–1 and Equation 3–2. These calculations were performed assuming an incompressible flow $\left(\frac{\rho}{\rho_o} = 1\right)$. This assumption is typically valid where

density fluctuations are assumed to be negligible which is commonly the case for boundary layer flows where $M_\infty \leq 2$.

$$\delta^* = \int_0^\delta \left(1 - \frac{u\left(y\right)}{U_\infty}\right) dy \tag{3–1}$$

$$\theta = \int_0^\delta \left[\frac{u\left(y\right)}{U_\infty}\left(1 - \frac{u\left(y\right)}{U_\infty}\right)\right] dy \tag{3–2}$$

$$H = \frac{\delta^*}{\theta} \tag{3–3}$$

The boundary layer calculations reported are in general agreement with previous research conducted by Zhuang (2007) where the approaching boundary layer momentum thickness was found to be 0.80mm for $M_\infty = 2$ freestream flow. The critical Reynolds number for transition from a laminar to turbulent boundary layer for flow over a flat plate is generally believed to occur at $Re = \frac{U_\infty L}{\nu} > 10^5$ which is an order of magnitude lower than the operating Reynolds number for these experiments. The shape factor calculated according to Equation 3–3 was found to equal 1.2. As reported in White (2006) for flow over a flat plate a boundary layer is typically considered laminar if $H \approx 2.6$ and turbulent when $H \approx 1.3$. Based on comparison of the boundary layer shape factor and Reynolds number calculations it was assumed the boundary layer was fully turbulent upstream of the cavity.

It should be noted that a large portion of the boundary layer is supersonic so the introduction of the Pitot tube will induce a bow shock in front of the probe. Due to this, a correction was made for the data presented in Figure 3-8 by relating the measured stagnation pressure to the constant static pressure at the measured cross section after a check to verify the measured pressure ratio resulted in supersonic flow. The correction applied is the well known Rayleigh-Pitot formula found in John & Keith (2006) where an iterative procedure is used to find the Mach number based on the measured pressure ratio

$$\frac{p_{02}}{p_1} = \frac{\gamma+1}{2} M_1^2 \left[\frac{\left(\gamma+1\right)^2 M_1^2}{4\gamma M_1^2 - 2\left(\gamma-1\right)}\right]^{\frac{1}{(\gamma-1)}} \tag{3–4}$$

where p_1 is the freestream static pressure and p_{02} is the stagnation pressure measured on the probe side of the shock. A qualitative assessment of the flow quality in the SWT was

made using the Schlieren imaging technique shown in Figure 3-9. The figure displays an instantaneous Schlieren image through the tunnel test-section midplane with the flow from left to right and the location of the cavity outlined. Waves with an angle of roughly 48° are evident in Figure 3-9 that form at the joint of the nozzle and test-section frame at the upper and lower joints. The oblique shock at the lower joint lands far downstream (out of the image) after reflecting off the top wall. The upper test-section and nozzle joint disturbance hits near the cavity center and reflects off. The joint of the top-panel insert and test-section frame result in an oblique-shock wave that falls downstream off the aft wall of the cavity. The stronger waves reflect downstream of the cavity location of interest and should not influence the flow of the cavity.

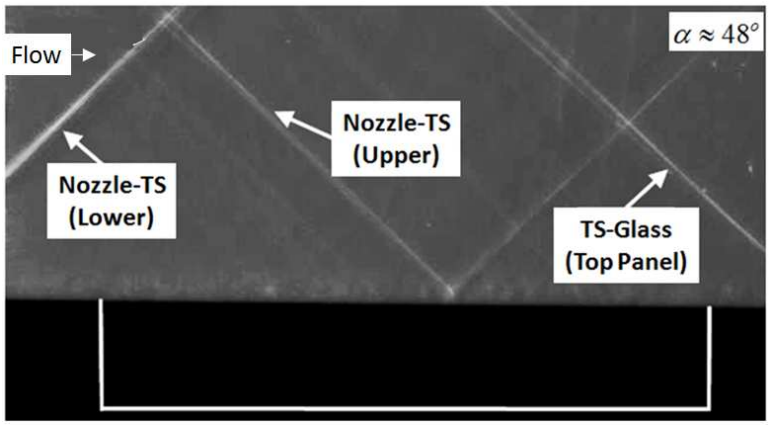

Figure 3-9. Flow visualization using Schlieren for the SWT test-section.

3.4 Instrumentation

3.4.1 Wind Tunnel Control

The wind tunnel is instrumented to monitor static pressure at the nozzle exit, the stagnation temperature in the plenum and the stagnation pressure in the flow conditioning section. A Druck™ PMP4015 pressure transducer is used to monitor the static pressure upstream of the nozzle at the surface of the flow conditioning section where the flow is assumed to be slow enough that static and stagnation pressures are nearly equivalent. The stagnation and static pressure were measured in the flow conditioning section for

varying dynamic pressures in some initial experiments and were all found to be well within the measurement uncertainty. The transducer has a pressure range of 0-345kPa with an accuracy of 0.08% full scale. A second pressure transducer measures the absolute static pressure at the entrance of the test- section and its specifications are identical except the pressure range is from 0-103.4 kPa. A four lead wire 100Ω Resistance Temperature Detector (RTD) is mounted in the plenum end flange to monitor the stagnation temperature. The RTD sensor is 50.8mm long with an exposed platinum element to increase the response time and supplies measurements with +/- 0.06% accuracy of the measured temperature. Additional monitoring of the system stagnation conditions is achieved through a Omega probe mounted in the storage tank which monitors stagnation temperature, relative humidity and dew-point. A Druck 2068kPa pressure transducer monitors the tank pressure allowing for a feed-forward control if desired.

The tunnel is controlled by a 152mm Fisher Control valve operated by an PC-based LabVIEW algorithm implemented on a Field-Programmable Gate Array (FPGA) card. The control valve is operated by a proportional gain control algorithm which samples data at 1kHz and averages at 4Hz to account for system responses and delays. A National Instruments PXI-1033 chassis and PXI-7831R card uses measurements from Druck 103.4kPa and 345kPa pressure transducers to measure the nozzle exit static pressure and the tunnel stagnation pressure in the flow conditioning section. The 7831R has 8 analog inputs and 8 analog outputs, each with a 16 Bit resolution and a direct current input voltage -10 to 10V. It also has a digital input/output interface with 96 channels with a 0 to 5.5Vrange. The SWT is controlled using a LabVIEW virtual instrument (vi). With the assumption of an ideal gas and isentropic flow, the Mach number is controlled by measuring the static and stagnation pressure ratio according to the isentropic compressible flow equation given below where $\gamma = 1.4$.

$$\frac{p_0}{p} = \left(1 + \frac{\gamma - 1}{2} M^2\right)^{\frac{\gamma}{\gamma - 1}} \tag{3–5}$$

3.4.2 Unsteady Pressure Measurements

The fluctuating surface pressures on the cavity walls are measured with Kulite™ pressure sensors. Two model numbers were used for the experiments each of the XCQ series: XCQ-062-5D and XCQ-062-30A. The nomenclature is as follows:

1. 062 - 1.5mm nominal outer diameter
2. 5D - Differential pressure measurement of 0-35kPa
3. 30A - Absolute pressure measurement with a range of 0-207kPa

The transducers are mounted flush with the cavity surfaces and held in place with silicone during measurements. The natural resonance frequency specified by the vendor is 150kHz for XCQ-062-5D and 300kHz for XCQ-062-30A models. Flat frequency responses are expected up to 20% of their natural frequencies with maximum combined non-linearity and hysteresis of ±0.5% of full scale per manufacturer specification. The diameter of each sensor model sensor was nominally 1.67mm while the XCQ-062-5D transducers include a 0.41mm inch outer diameter reference tube for setting the pressure on the back of the diaphragm. The sensor measures the difference between the pressure on the front surface of the sensor diaphragm and the pressure in the reference tube for measuring the pressure differential. The back pressure tubes were hooked to taps which were typically located at a spanwise distance of 6.35mm on centerlines from the desired measurement location.

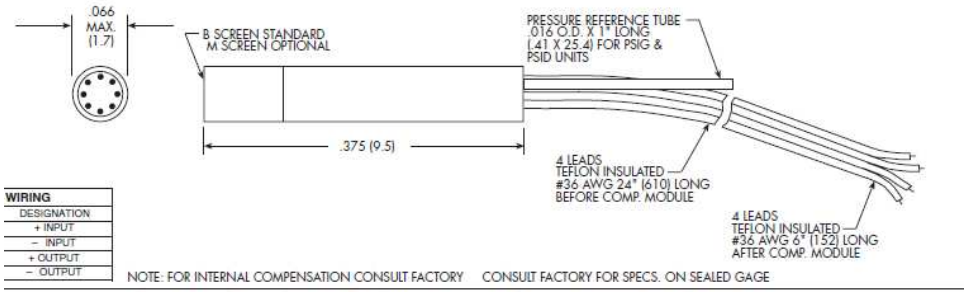

Figure 3-10. Differential pressure transducers. Reprinted from Kulite (2010).

The overpressure is rated as twice the listed operating pressure while the burst pressure is three times the operating pressure. If the overpressure difference is exceeded

the diaphragm in the sensor will experience a plastic deformation and calibration curve would be permanently altered. The use of such transducers to measure time dependent dynamic wall pressure fluctuations has been well documented by Ukeiley *et al.* (2004*a*) for subsonic and by Dix & Bauer (2004) and Ukeiley *et al.* (2004*a*) for high speed cavity flows.

3.5 Flow Visualization

The following section will discuss the optical capabilities for the SWT measurement techniques that will be used in this study. The section will first discuss the instrumentation and setup for the qualitative Schlieren measurements in the tunnel. This will be followed by a discussion of the Particle Image Velocimetry system and its setup for use in the SWT.

3.5.1 Schlieren

Schlieren imaging can be made using any one of several different setups. The common driving principle of each method is that the speed of light will change in mediums of different density. This speed change is referred to as the refractive index of the medium and is a non-dimensional number given in Equation 3–6. The refractive index for air has a linear relation based on the speed of light in a vacuum (c) and the phase velocity (v_p) in the medium the light is passing through.

$$n = \frac{c}{v_p} = \sqrt{\epsilon_\tau \mu_\tau} \tag{3–6}$$

The value ϵ_τ refers to the material's relative permittivity and μ_τ is the relative permeability. This implies light will travel slower with increasing medium density. When this is applied to a density variation in an air flow such as compressible flows, the path of the wave front is forced to change or bend. Figure 3-11 illustrates this phenomena of a bent wavefront passing through a medium of different densities. The light will travel faster in the region of low density forcing the light to bend with the angle of refraction θ_2 less than the angle of incidence θ_1.

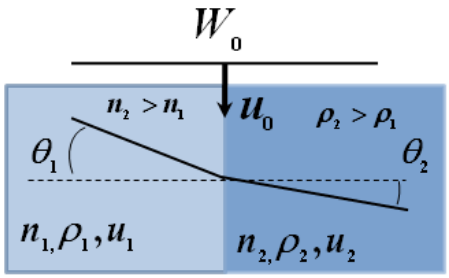

Figure 3-11. Bending of light due to density gradient of two mediums.

The object used to block the light rays is typically called a 'knife edge' because the Schlieren test originated with the Foucault Knife Test. Equation 3–7 relates the relative displacement of the image to the relative change in light intensity as explained by Settles (2001)

$$\frac{\Delta I}{I} = \frac{\Delta h}{h} \tag{3–7}$$

where the right hand side is referred to as the relative displacement of the image and the left hand side is referred to as the relative change in light intensity. Gladstone & Dale (1864) introduced the Gladstone-Dale equation which is used to calculate the deflection angle of the light due to the density gradients. With the use of the Gladstone-Dale equation it can be shown that the Schlieren system depends upon the first derivative of the density in a direction normal to the light path.

Figure 3-12 illustrates the typical Z-type Schlieren arrangement used in the supersonic wind tunnel laboratory at the REEF. The point source light is reflected off of a parabolic mirror (M_1) which columnates the light providing parallel beams through the test-section. The parallel light beams are then refocused by a second parabolic mirror (M_2). A razor blade is used in the focal plane of the second mirror with capability to be vertically adjusted. The knife edge is positioned to block approximately one-half of the incident light allowing a uniformly illuminated darker image. The light is then focused using a simple lens and projected directly onto a digital camera charge-couple device (CCD). The CCD is connected to a PC through a fire-wire port for digital image acquisition.

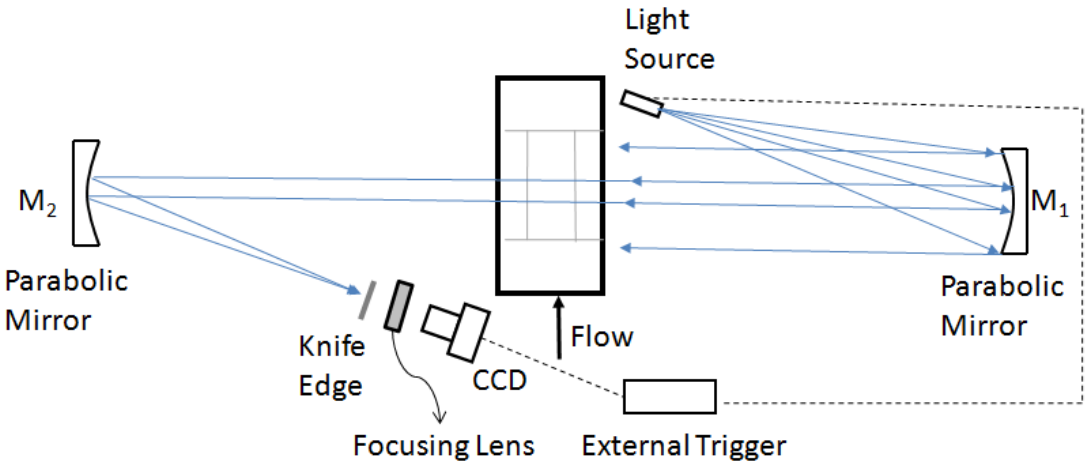

Figure 3-12. Z-type Schlieren arrangement for qualitative flow assessment.

If there are no density variations in the flow the knife edge will uniformly reduce the intensity of the image. If there is a density variation between the first mirror and second mirror, the light leaving the second mirror that passed through the density variation will not follow the parallel path to the focusing lens, it will be bent as described above. Due to the divergent path of the light the light is either diverted towards or away from the knife edge. This produces the alternating light spots and dark spots seen in Schlieren image given in Figure 3-13 which is an example of a bullet during supersonic flight.

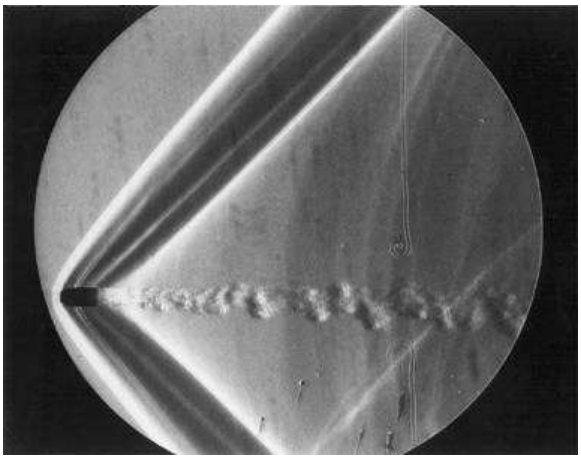

Figure 3-13. Schlieren imaging of a bullet in mid-flight. Reprinted with permission from Davidhazy (2009).

The Schlieren system in this research consists of two 152.4mm parabolic mirrors with a 1232mm focal length. Light is supplied from a 3mm arc-length Xenon pulsed flash lamp with a 2μs pulse duration controlled by an external trigger. A Sony XCD-V60 digital video camera (640×480 VGA Resolution) is used for image acquisition and is capable of a sampling rate of 90Hz.

3.5.2 Particle Image Velocimetry

PIV is a non-intrusive optical technique used to measure the velocity field in a plane. The flow is seeded with tracer particles and illuminated periodically by a light source that is spread into a thin sheet which is generated through the use of a cylindrical lens as shown in Figure 3-14. The light is scattered from the particles in two successive laser

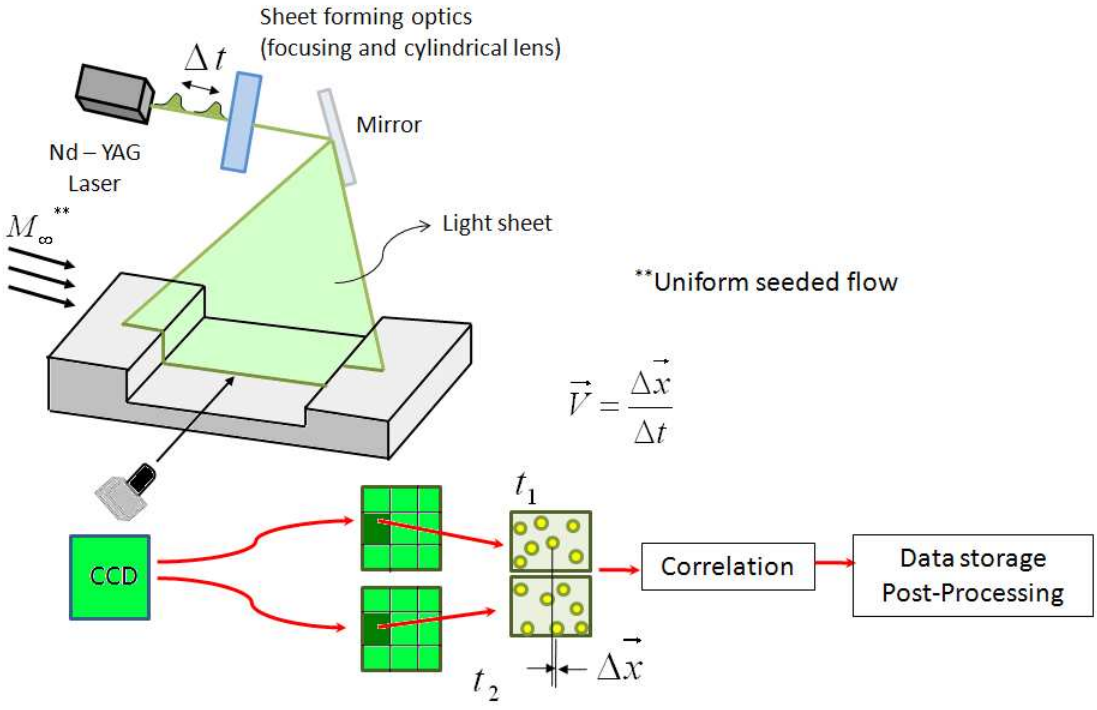

Figure 3-14. Particle Image Velocimetry (PIV).

pulses and are acquired on a digital camera. The lag of the two laser pulses gives the system a change of time for successive digital images to be acquired from the CCD. Each image in the pair pair is then divided into small subsections called interrogation areas

(IA). The interrogation areas from each image frame are then cross-correlated on a pixel by pixel basis to obtain a instantaneous snapshot of the velocity field.

PIV in compressible flows was pioneered by Kompenhans & Hőcker (1988) and Adrian (1991) who used photographic recording and image-shifting techniques. Investigations range from supersonic jets by Krothapalli *et al.* (1994) to turbulence measurements in compressible mixing layers by Vakili & Gauthier (2001). They were able to obtain instantaneous snapshots of planar velocity to compute vorticity thus allowing planar maps of turbulence statistics to be computed from ensemble averages. Recently Zhuang (2007) successfully applied PIV to cavity flow with $M_\infty = 2$ to investigate the suppression of pressure fluctuations using leading edge microjets.

The PIV system used in this research is supplied from LaVision using the 32-bit DaVis Version 7.x software package for image acquisition, processing and control of all hardware components. The 2D PIV software package includes cross-and auto-correlation image processing algorithms with high spatial resolution, second-order correlation including deformed window correlation and multi-pass correlations for vector field displays.

Two component PIV is implemented for the measurement of the instantaneous velocity flowfield on the cavity centerline-plane ($z = 0$) and used concurrently with the unsteady pressure measurements throughout this research. An aerosol of Di-ethyl hexyl sebacate (DEHS) oil is used for seed with a mean particle diameter of 1μm as reported by Kähler (2003). The flow seed is introduced by the use of a LaVision FlowMaster four nozzle head submicron droplet generator capable of a 7000 particle per second generation rate. A Nd:YAG Litron Nano dual head 135MJ per pulse laser system was used to illuminate the seed particles. The laser light was converted from infrared light at a wavelength of 1024nm to green visible light at a wavelength of 532nm using harmonic generators and emitted with 135MJ of energy per pulse. The nominal pulse duration of the laser was approximately 5-10ns. The focused point energy source was converted into a diverging laser sheet using LaVision supplied all quartz adjustable light sheet optics

with anti-reflecting coating for wavelengths of 532nm. The laser pulses are relayed to the test-section at a rate of 7Hz with the use of a mirror to reflect the laser 90°.

Images were captured with a high resolution 14-bit Imager ProX camera with 2048 × 2048 pixel resolution and 512MB of on-board memory supplied by LaVision. The vendor listed minimum interframe time is 115ns which is much lower than required for these studies. The scattered light pattern relative to each time instant is stored onto separate recordings which allows analyzing the images with the cross-correlation-based algorithms. Cross-correlation has the major advantage of resolving the directional ambiguity and has a higher signal-to-noise ratio of the correlation signal resulting in higher accuracy and resolution. Figure 3-15 illustrates the synchronization between the laser, camera and

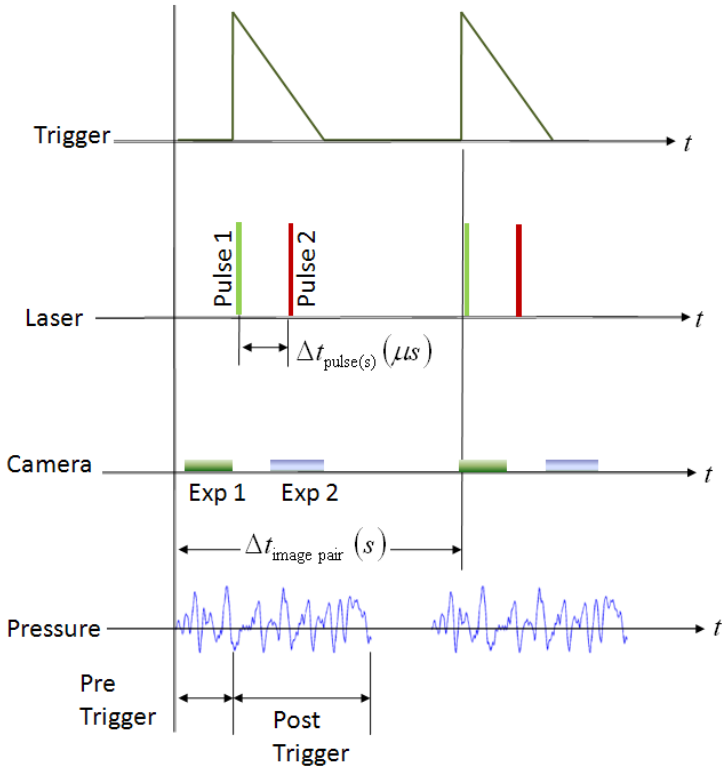

Figure 3-15. PIV and pressure synchronization.

pressure signal for a given PIV image pair. The anticipated number of image pairs per run will be limited by condensation effects and poor-visualization due to the seeding particle clinging to the windows and not the run time of the tunnel. The minimum transfer rate

is the time required to transfer one image from the photo diode array (pixel array) to a storage cell array. If the minimum time is not allowed to clear the charges from the pixel array there could be degradation in image quality. Vectors were computed using a cross correlation algorithm using 50% overlap and a multi-pass 64×64 pixel (first sweep) and 16×16 pixel 2-sweep interrogation region to enhance spatial resolution for vector field displays.

3.6 Experimental Setup

All of the experiments were conducted at a freestream Mach number of 1.44 with the standard operating conditions given in Table 3-1. Two cavities, full and finite span as previously discussed, were considered in the study. The rod centerline location (X_{cl}) in the streamwise direction was fixed for each cavity model and was 3.2mm from the leading edge for each controlled cavity configuration.

Table 3-1. Standard operating conditions.

	P_0	Mach	$Re = \frac{U_\infty L}{\nu}$	$Q_\infty = \frac{1}{2}\rho_\infty U_\infty^2$	U_∞
Typical Values	172kPa	1.44	1.29×10^6	74.4kPa	415m/s

The pressure transducers were located on the cavity floor and aft wall centerline as shown in Figure 3-16 with streamwise locations tabulated in Table 3-2. The aft wall sensor was mounted on the center point of the aft wall. The sensors were powered and their output signals were conditioned using Endevco136™ DC differential voltage amplifiers. All sensors were sampled simultaneously at 90kHz with high pass filtering at 100Hz and low pass filtering at 30kHz. All data were digitized using a National Instruments (NI) PXI4472 24-bit 8-channel Data Acquisition Card (DAQ) through a LabView interface. The spectra for the experimental data uses a record length of 8192 points giving a frequency resolution of 11Hz.

For the full view cavity particle image velocimetry cases the camera resolution based on the field of view for the experiment was roughly 18 pixels per millimeter. Considering a freestream flow velocity of 420m/s the separation time between two exposures was set

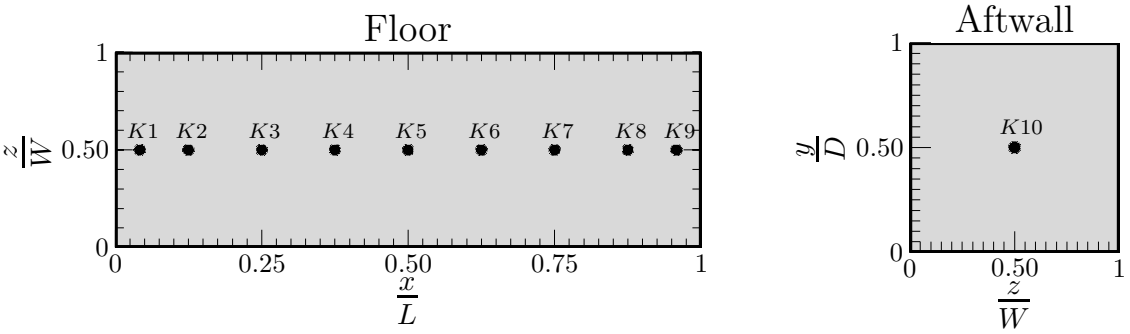

Figure 3-16. Pressure sensor locations

Table 3-2. Cavity floor pressure sensor locations.

No	$\frac{x}{L}$	$\frac{y}{D}$
K1	0.042	0
K2	0.125	0
K3	0.250	0
K4	0.375	0
K5	0.500	0
K6	0.625	0
K7	0.750	0
K8	0.875	0
K9	0.958	0
K10	0.500	0.5

to 1.5μs to allow a particle to travel at least 10 pixels (in the freestream and immediately around the shear layer) between successive image pairs. A set of data was collected where the field of view was roughly cut in half focused on the leading edge of the cavity by the use of a 2X teleconverter. For these experiments the time between laser pulses was adjusted to 0.75μs as the spatial resolution was doubled and the flow velocity immediately around the cylinder was accelerated beyond freestream values.

3.7 Measurement Uncertainty

An analysis of the anticipated measurement uncertainty will be discussed in this section. The section will first discuss uncertainties coupled with measurements of the unsteady pressures and will conclude with a discussion of uncertainty analysis for particle image velocimetry measurements.

3.7.1 Unsteady Pressure Measurement

The experimental uncertainty for the spectral power density of the surface pressure fluctuations is primarily due to the statistical convergence uncertainty. The signals are acquired through the use of 16 and 24-bit digital acquisition cards. The accuracy specified by the vendor of the transducers is on the order of 0.5% of full scale or 0.17kPa and 1.03kPa. Following the analysis found in Bendat & Piersol (1986) the normalized statistical convergence uncertainty, or random error, is found to be inversely proportional to the square root of the number of ensembles. The sampling rate in the experiments is 90kHz for a period of approximately 11.6s. The resulting blocks of data are split into independent data records of 8192 points resulting in 256 ensembles. These blocks are analyzed and ensemble averaged to obtain an estimate for quantities such as p_{rms} or the peak tones found in the PSD plots. The resulting convergence uncertainty may therefore be expressed as a function of the independent samples and calculated as shown below.

$$\epsilon_{\text{convergence}} = \frac{1}{\sqrt{\#\text{ of Ensembles}}} = \frac{1}{\sqrt{256}} = 6.25\% \tag{3–8}$$

Propagating the measurement error due to selected instrumentation using the least accurate pressure transducer and employing a root square sum (RSS) method yields a complete error given by E below.

$$E = \sqrt{(6.3^2 + 0.5^2)} = 6.3\% \tag{3–9}$$

3.7.2 PIV Measurement

The uncertainty in the PIV measurements is largely dominated by three events:

1. bias error introduced by software correlations
2. statistical error due to the flowfield turbulence
3. error due to the introduction and tracking of seed particle

The bias error due to software computations as supplied by the vendor is roughly 3% meaning the mapping of the velocity vectors is typically within 0.03 pixels. The statistical

error is largely controllable by ensuring enough image pairs are acquired for data analysis. The error is estimated accurately for flowfields with moderate to low turbulent intensities that are under 30% as explained in Grant & Owens (1990). Equation 3–10 illustrates this by considering the relative error of the standard deviation where Z_c is the anticipated confidence interval and N is the number of samples or image pairs.

$$\epsilon_\sigma = \frac{Z_c}{\sqrt{2N}} \tag{3–10}$$

Due to the randomness inherent in turbulence, multiple measurements are required to adequately obtain the mean flow properties. The required number of ensembles is related directly to the turbulent intensity of the flowfield with higher turbulent levels requiring a greater number of averages. Figure 3-17 illustrates a rapid convergence of the error for a 95% confidence interval over the first 1000 ensembles. Thereafter improved accuracy becomes exceedingly expensive nearing the limit of diminishing returns.

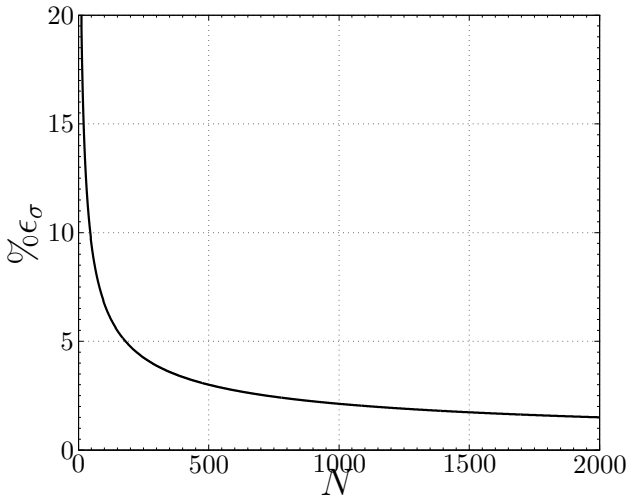

Figure 3-17. PIV uncertainty for turbulent intensities that are less than 30%.

The error introduced by the ability to track the seeding particle is more difficult to quantify. A particles ability to stay true to and track the flowfield will depend largely on its mass and size with smaller and lighter particles preferred. As the particle size decreases the ability of the camera to adequately visualize and track the particle motions begins to

drop off due to the fixed spatial resolution. Samimy & Lele (1991) discovered the ratio of the aerodynamic and turbulent characteristic time scales predicts the ability of the particle to track compressible shear layers within roughly 2% error if the ratio is maintained under 20%.

$$\frac{\tau_a}{\tau_t} \leq 0.20 \tag{3–11}$$

The aerodynamic time scale is estimated using Oseen's corrections for drag over a sphere in Stokes flow where:

$$\tau_a = \frac{f\left(u_i - v_i\right)}{\frac{\partial v_i}{\partial t}} \tag{3–12}$$

v_i is a three component tensor for the particle velocity, u_i is the flow velocity, the correlation factor is typically taken as $f = 1 + 0.15{Re_p}^{\frac{2}{3}}$ and $Re_p = |u_i - v_i| \frac{d_p}{\nu}$ where d_p is the mean particle diameter reported by Chung & Troutt (1988). The aerodynamic time constant may also be estimated using:

$$\tau_a = \frac{\rho_p {d_p}^2}{18\mu} \tag{3–13}$$

where μ_p = is the fluid viscosity and ρ_p is the particle density. The largest turbulent characteristic time scale, τ_t, is typically taken by the dominant frequency or turbulent velocity of the flowfield which for this research can be taken as $\tau_t = \frac{1}{3100hz}$ =32ms. τ_t may also be estimated by dimensional analysis $\tau_t = \frac{\delta}{u'}$ as shown in Tennekes & Lumley (1972) where u' is the characteristic turbulent velocity taken as $25\%U_\infty$ for this research. A third way to estimate the characteristic turbulent time scale was proposed by Samimy & Lele (1991) $\tau_t = \frac{10\delta_{\omega 0}}{U_\infty - U_2}$ which uses the initial vorticity thickness $\delta_{\omega 0}$ of the shear layer. Using any of these calculations for τ_t the ratio $\frac{\tau_a}{\tau_t} << 0.2$ indicating the seed should adequately track the flow.

The effect of temperature and pressure on the DEHS oil particle size frequency distribution is illustrated in 3-18. The dependence of the particle size distribution on the viscosity of the oil is apparent. When the temperature is low (the stagnation temperature is expected to vary from anywhere between (0°C $\leq T_\infty \leq$ 30°C) DEHS oil is well suited

to generate a small-band particle size distribution with a cut-off diameter at 2µm which is within the desired range to ensure sufficient flow tracking.

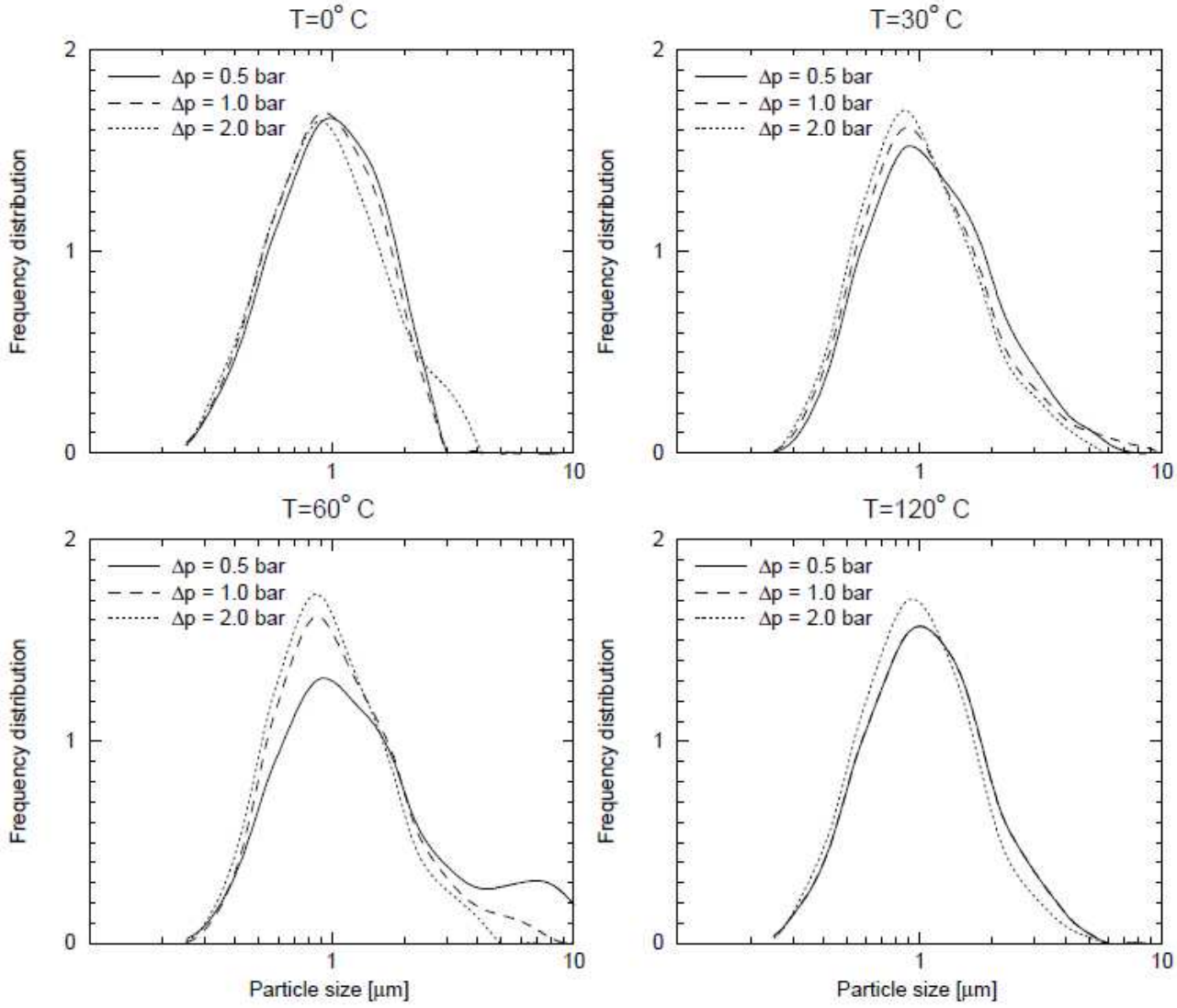

Figure 3-18. DEHS particle size frequency distribution reprinted from Kähler (2003).

The PIV error, based on these three components, and using the RSS method assuming the acquired number of image pairs is greater than 1000 and 2% error from seeding is given below.

$$E = \sqrt{(4.25^2 + 2^2 + 3^2)} = 5.6\% \tag{3–14}$$

CHAPTER 4
NUMERICAL SIMULATION APPROACH

This chapter will present the background for the numerical simulations performed throughout this dissertation. Numerical investigations of flow over open cavities have been conducted for over two decades. A complete list of numerical references is not the goal here but comprehensive reviews can be found in Grace (2001) and Colonius (2001) which demonstrate the numerical work which dates back to Komerath *et al.* (1987).

Application of CFD allows researchers to examine instantaneous features of a fully three-dimensional supersonic flow in a time resolved manner, whereas this information is difficult if not impossible to obtain from experimental observations. Additionally, application of CFD has the ability to demonstrate sensitivity to turbulence not capable of being explicitly measured in experiments. The major drawback of computational modeling of cavity flows revolves around accuracy of the appropriate closure models, physical wall clock time required for solutions, storage and post-processing large quantities of data.

4.1 Turbulence

A brief introduction into the topic of turbulence is appropriate before tackling the intricacies of turbulence modeling and computational fluid dynamics. For a more comprehensive review the interested reader is directed to the works of Launder (1991), Pope (2000) and Tennekes & Lumley (1972). Figure 4-1 illustrates the transition from laminar to turbulent conditions for flow over a flat plate. The actual laminar-turbulent transition is a complicated process and is beyond the scope of this research as the flows in this effort are fully developed turbulent flows. Launder (1991) summarizes the transition to turbulence nicely by saying: "At moderate Reynolds numbers the restraining effects of viscosity are too weak to prevent small, random disturbances in a shear flow from amplifying. The disturbances grow, become non-linear and interact with neighboring disturbances. This mutual interaction leads to a tangling of vorticity filaments. Eventually the flow reaches an apparent chaotic state non-repeating form described best only in

statistical terms." Turbulence is inherently an unsteady three dimensional viscous phenomena associated with moderate to high Reynolds number flows. It should be stressed that turbulence is a not a property of the fluid but a property inherent to the flow.

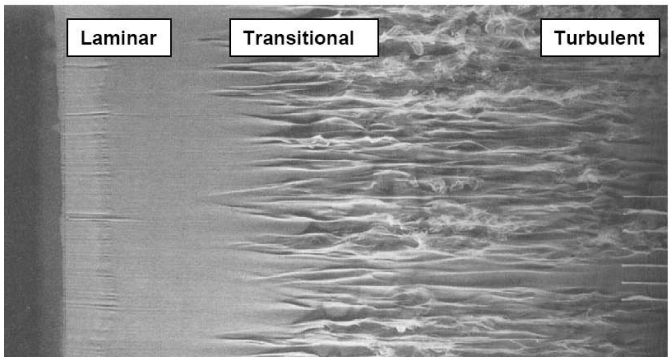

Figure 4-1. Transition of a turbulent boundary layer over a flat plate. Reprinted with permission from Nichols (2005).

Figure 4-2 presents an idealized turbulence energy spectrum which details the average energy per eddy in a turbulent flow. Throughout this dissertation the use of the concept of eddies commonly used in turbulence text books is adopted which are meant to describe whirls in the flow of a given scale.

By convention, the energy is plotted against wave number which is proportional to the inverse of the turbulent eddy size. It is easily noted that large eddies contribute to the left side of the plot and small eddies to the right side. The energy spectrum can be broken into three distinguishable regions as follows:

1. Energy Containing Range (ECR) whose turbulent behaviors accounts for the majority of the turbulent kinetic energy
2. Inertial Range whose turbulent motions are responsible for the transfer of energy from large to small scales through dissipation
3. Dissipation Range where the turbulent energy is removed from the flow

The smallest scale structures have no significant transferable energy because viscous dissipation dominates by converting kinetic energy into heat. Large scale structures,

represented on the left side of the plot, extract energy from the mean flow in the energy production region of the spectrum. In the inertial range, where smaller eddies feed off larger structures, turbulence is in essence in equilibrium. The peak contribution in the energy spectrum occurs with the larger scale structures generally induced from the geometry of the flowfield, i.e., the mean flow gradients.

When considering the appropriate discretization to be used in a numerical analysis it is useful to quantify the length and time scales associated with the turbulent flow. Turbulent scales are typically defined in terms of turbulent kinetic energy, turbulent dissipation and the fluid viscosity. The large scale eddies attributed to turbulent production have length scales characterized by

$$L = \frac{k^{\frac{3}{2}}}{\epsilon} \tag{4–1}$$

where k is the turbulent kinetic energy and ϵ is the turbulent dissipation. The turbulent time scale for these large scale structures may be characterized by the ratio of the turbulent kinetic energy and turbulent dissipation

$$T = \frac{k}{\epsilon}. \tag{4–2}$$

On the other hand, the smallest scale disturbances are associated with the Komlogorov scale given in Tennekes & Lumley (1972) as

$$\eta = \left(\frac{\nu^3}{\epsilon}\right)^{\frac{1}{4}} \tag{4–3}$$

where ν is the kinematic viscosity. Equation 4–4 gives the relationship for the smallest turbulent time scale as

$$\tau = \left(\frac{\nu}{\epsilon}\right)^{\frac{1}{2}} \tag{4–4}$$

where the the turbulent Reynolds number may be given by

$$\mathrm{Re}_t = \frac{k^2}{\nu\epsilon}. \tag{4–5}$$

Considering the ratio of these scales, given below for clarity,

$$\frac{\eta}{L} = \mathrm{Re}_t^{\frac{3}{4}} \tag{4–6}$$

$$\frac{\tau}{T} = \mathrm{Re}_t^{-\frac{1}{2}} \tag{4–7}$$

it is easy to see that range of turbulent scales may span many orders of magnitude for increasingly high Reynolds number flows. The smallest turbulent structures are much smaller than the physical scales of interest, in this case dimensions of the cavity. Therefore it is easily realized that an enormous spatial discretization is required to adequately resolve the complete turbulent spectrum even for moderately high Reynolds numbers.

Computational fluid dynamics can be classified based on their approach to resolve the turbulence in the turbulence energy spectrum depicted in Figure 4-2. If a CFD model resolves all fluid motions through the dissipation region they are referred to as DNS which yields exact results assuming sufficient accuracy of the discretization scheme. Estimates of DNS simulations suggest the required resolution scales by Equation 4–7. The total computational cost (number of operations) may be estimated by considering the factor of spatial and temporal resolutions required. Table 4-1 summarizes the anticipated number of grid points and time-steps required to employ the given method and the estimated date the given method will be ready considering high Reynolds number flow over a complex geometry such as an airplane. The interested reader is pointed to the work of Spalart (2000) where this table was summarized from. It is understood the geometry in this research is more simple than that considered in Table 4-1, though it still illustrates the potential bottleneck in computational resources required for full LES simulations of high Reynolds number three dimensional flows. If the largest turbulent structures are

Table 4-1. Summary of numerical strategies and cost.

Method	Grid Points	Time Steps	Date Ready
DES	10^8	10^4	Now
LES	$10^{11.5}$	$10^{6.7}$	2045
DNS	10^{16}	$10^{7.7}$	2080

resolved, placing the cutoff in the dissipation range, the technique is considered to be a LES method. Large eddy simulation is an attractive solution method as it provides a more accurate solution for the most energetic turbulent structures in the flow. LES only models (does not directly compute) the less energetic, more universal smaller scale structures. This technique is only realizable for moderately high Reynolds numbers if using the same type of analysis as above. LES also is faced with the challenge of near wall modeling explained by Radhakrishnan (2007) where the turbulent eddy sizes are limited by the distance to the wall so the inertial range of near wall turbulence is forced into smaller scales requiring special wall models to be enforced.

CFD techniques using RANS methodologies represent the other side of the spectrum of techniques from DNS. The cutoff scale for RANS is at the far left of the energy spectrum because RANS does not resolve any turbulence directly instead represents turbulence effects in its subgrid turbulence model. The computational overhead and

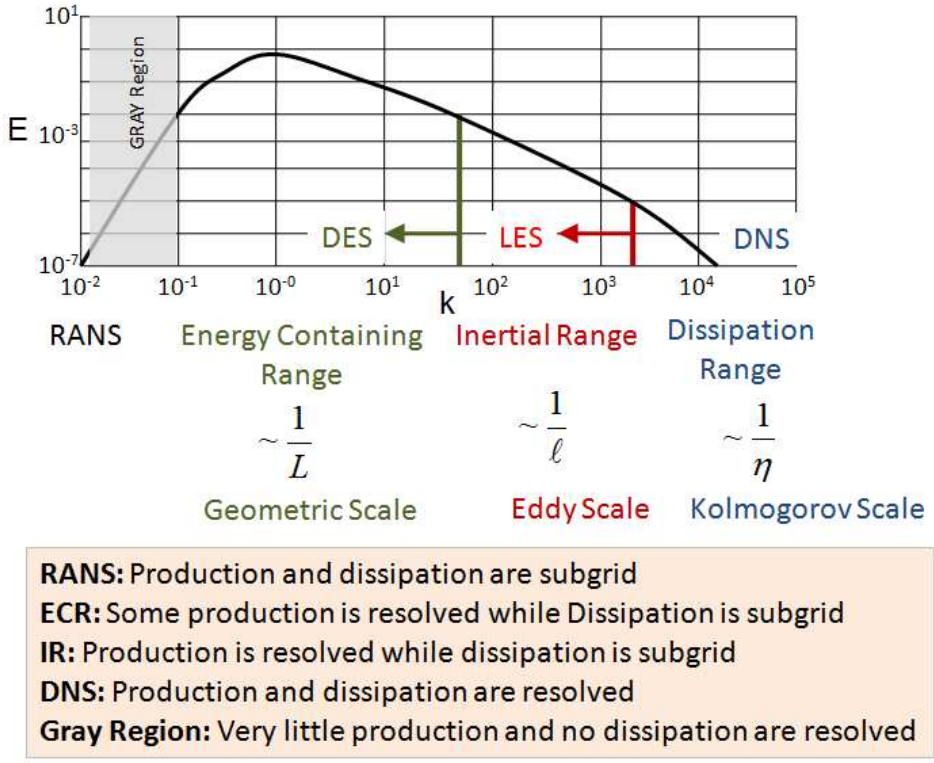

Figure 4-2. Turbulence energy spectrum depicting RANS through DNS simulation scales

difficulties associated with the use of the standard LES models, particularly in near-wall regions, coupled with the shortcomings of unsteady RANS has lead to the development of hybrid models. These models attempt to combine the best aspects of RANS and LES methodologies in a single solution strategy commonly referred to as Detached-Eddy Simulation (DES) detailed in Radhakrishnan (2007). DES techniques place the cutoff in the energy-containing range somewhere in the modeled volume and attempts to treat near-wall regions in a RANS-like manner while treating the rest of the flow in an LES-like manner.

Grace (2001) has compiled a detailed list of publications which have illustrated that time dependent RANS simulations are typically unable to capture the essential features of cavity flow fields. Rizzetta & Visbal (1988) and Shih *et al.* (1994) have even reported RANS simulations may be overly dissipative in the turbulence models driving the solution to steady state conditions. Hence it is fairly well established that RANS simulations are not capable of adequately resolving the acoustic turbulence coupling effects accompanied in cavity flows. On the other hand, DNS offers a solution for resolving the full range of length scales in turbulent flow therefore requiring no turbulence model. However, the computational resources requirement has limited its application to low Reynolds numbers and two dimensional flows as shown in Colonius *et al.* (1999). The Hybrid RANS-LES approach, being utilized for this research, has been shown to be capable of providing a more thorough insight into the physics of cavity flows and the role of turbulence as discussed by Lawson & Barakos (2010). In theory it explicitly resolves the most relevant and highest energy containing structures of the flow. For high Reynolds number flows the hybrid RANS-LES formulation, commonly referred to as DES, is currently accepted as the most practical method. An example of an instantaneous snapshot illustrating the density gradient from such a simulation is illustrated in Figure 4-3. More details of these research areas may be found in Rizzetta & Visbal (2003), Hamed *et al.* (2003, 2004) and Larcheveque *et al.* (2003) among others.

Figure 4-3. Instantaneous snapshot of illustrating numerical Schlieren of supersonic cavity flow in an L/D=6, L/W=1 cavity.

4.1.1 Compressible Navier-Stokes Equations

The basic governing equations for the numerical simulations in this research are the three dimensional compressible Navier-Stokes equations. The equations are written in dimensionless form to give better numerical conditioning by decreasing the number of parameters and keeping them tightly bounded and are given below

$$\frac{\partial \mathbf{Q}}{\partial t} + \frac{\partial\left(\mathbf{F^i} + \mathbf{F^v}\right)}{\partial x} + \frac{\partial\left(\mathbf{G^i} + \mathbf{G^v}\right)}{\partial y} + \frac{\partial\left(\mathbf{H^i} + \mathbf{H^v}\right)}{\partial z} \tag{4–8}$$

where the superscripts i, v denote the inviscid and viscous components of the flux vectors and x, y, z, t represent spatial coordinates and time respectively. Q is the vector of conserved variables defined as

$$Q = (\rho, \rho u, \rho v, \rho w, e)' \tag{4–9}$$

where u, v, w are velocities and rho is the fluid density non-dimensionalized by the freestream speed of sound and density respectively. The prime denotes the transpose matrix operation. The inviscid and viscous flux vectors are given in Equation 4–10 and

Equation 4–11 respectively

$$\begin{aligned}
\mathbf{F^i} &= \begin{bmatrix} \rho u & \rho u^2 + p & \rho uv & \rho uw & (e+p)\,u \end{bmatrix}' \\
\mathbf{G^i} &= \begin{bmatrix} \rho v & \rho uv & \rho v^2 + p & \rho vw & (e+p)\,v \end{bmatrix}' \\
\mathbf{H^i} &= \begin{bmatrix} \rho w & \rho uw & \rho vw & \rho w^2 + p & (e+p)\,w \end{bmatrix}'
\end{aligned} \tag{4–10}$$

$$\begin{aligned}
\mathbf{F^v} &= \begin{bmatrix} 0 & \tau_{xx} & \tau_{xy} & \tau_{zx} & u\tau_{xx} + v\tau_{xy} + w\tau_{xz} + \frac{\mu c_p}{P_r} T_x \end{bmatrix}' \\
\mathbf{G^v} &= \begin{bmatrix} 0 & \tau_{xy} & \tau_{yy} & \tau_{yz} & u\tau_{xy} + v\tau_{yy} + w\tau_{yz} + \frac{\mu c_p}{P_r} T_y \end{bmatrix}' \\
\mathbf{H^v} &= \begin{bmatrix} 0 & \tau_{xz} & \tau_{yz} & \tau_{zz} & u\tau_{xz} + v\tau_{yz} + w\tau_{zz} + \frac{\mu c_p}{P_r} T_z \end{bmatrix}'
\end{aligned} \tag{4–11}$$

where the fluid pressure is given by p, the absolute viscosity is given by μ and P_r is the Prandtl number. The total energy is given by

$$e = \frac{p}{\gamma - 1} + \frac{\rho}{2}\left(u^2 + v^2 + w^2\right) \tag{4–12}$$

where $\gamma = \frac{c_p}{c_v} = 1.4$. The temperature is given by T and can be derived from the perfect gas relation $p = \rho RT$. For a calorically perfect gas this may be rewritten as

$$p = (\gamma - 1)\left[e - \frac{1}{2}\rho\left(u^2 + v^2 + w^2\right)\right] \tag{4–13}$$

where Sutherland's law is used to determine viscosity in terms of local temperatures of the fluid under consideration. The bulk modulus $\lambda = -\frac{2}{3}\mu$ is set according to Stokes

hypothesis. The viscous stresses may then be calculated by

$$\begin{aligned}
\tau_{xy} &= \tau_{yx} = \mu\left(v_x + u_y\right) \\
\tau_{xz} &= \tau_{zx} = \mu\left(w_x + u_z\right) \\
\tau_{yz} &= \tau_{zy} = \mu\left(w_y + v_z\right) \\
\tau_{xx} &= 2\mu\left(u_x - \frac{u_x + v_y + w_z}{3}\right) \\
\tau_{yy} &= 2\mu\left(v_y - \frac{u_x + v_y + w_z}{3}\right) \\
\tau_{zz} &= 2\mu\left(w_z - \frac{u_x + v_y + w_z}{3}\right).
\end{aligned} \tag{4–14}$$

The Navier-Stokes equations are rewritten in curvilinear form employing a space transformation from the cartesian system to the local system. The details are left out here but can be found in Tannehill & Anderson (1984).

4.1.2 Spalart-Allmaras DES

Examination of the set of equations derived for RANS and LES one notes they are very similar in form. The fundamental difference lies in the spatial filtering of the LES formulation not found by definition in the RANS equations. The obvious next step in the evolution of CFD modeling was to take the best of both worlds and apply spatial filtering to the RANS equations and develop another set of equations, now commonly referred to as DES or Hybrid RANS-LES modeling. These filtered equations may be thought of as a subgrid model for large vortical eddies in the flow. The most common approach, and the approach used throughout this research, involves the modification of the production and dissipation terms inside the existing RANS turbulence model. The modified terms add a local scaling factor to destroy or produce the turbulent eddy viscosity based on local grid density.

Zero-equation turbulence models such as the Baldwin-Lowmax are commonly referred to as algebraic models. They are calculated directly from the computed flow variables and thus require no transport equations for closure. These models cannot handle key

turbulent parameters such as convection and diffusion of turbulence and are typically overly simplistic for most problems of engineering interest. One equation models offer one transport equation typically for turbulent kinetic energy but often eddy-viscosities models are used as well. There are more advanced turbulence models available today, such as Menter's Shear Stress Transport model introduced by Menter (1994) which combines the best aspects of the two equation models $k-\omega$ and $k-\epsilon$ models through trigonometric blending functions. Reynolds Stress Models (RSM) discard a transport equation for the eddy viscosity all together and attempts to directly model the Reynolds stress terms. For more elaborate discussions of turbulence modeling the interested reader is directed to Wilcox (2006).

The one equation turbulence model considered in this research was born from the RANS implementation of the Spalart Allmaras turbulence model introduced by Spalart & Allmaras (1994). The author acknowledges the limitations, especially due to the lack of a closure model for the turbulent kinetic energy. It should be noted though, there are a growing number of papers citing fairly successful use of the SA (with the DES implementation to be discussed below) model to simulate cavity flows examples of which are shown in Nichols (2006) and Boydston *et al.* (2008). The hybrid SA-DES model was originally formulated by Spalart *et al.* (1997) and further demonstrated by Strelets (2001) by replacing the wall distance function, d, in the original SA model with a modified distance function, $\tilde{l}$, as illustrated in Equation 4–15. The Spalart-Allmaras turbulence model was derived using empirical relationships with the aim of developing a turbulent transport model that was fast, robust, and accurate for both shear layers and boundary layers. The transported viscosity is given by $\tilde{\nu}$ and a full description of the turbulence

model and associated constants can be found in Appendix-A.

$$\underbrace{\frac{\partial\tilde{\nu}}{\partial t}+U_j\frac{\partial\tilde{\nu}}{\partial x_j}}_{\text{Convection}}=\underbrace{C_{b1}\left(1-f_{t2}\right)\tilde{S}\tilde{\nu}}_{\text{Production}}-\underbrace{\left[C_{w1}f_w-\frac{C_{b1}}{k^2}f_{t2}\right]\left(\frac{\tilde{\nu}}{d}\right)^2}_{\text{Destruction}}+ \underbrace{\frac{1}{\sigma}\frac{\partial}{\partial x_k}\left[\left(\nu+\tilde{\nu}\right)\frac{\partial\tilde{\nu}}{\partial x_k}\right]}_{\text{Dissipation}}+\underbrace{\frac{C_{b2}}{\sigma}\frac{\partial^2\tilde{\nu}}{\partial x_k^2}}_{\text{Diffusion}} \tag{4–15}$$

The modified length scale for the SA-DES simulations is

$$\begin{aligned}\tilde{l}&=\min\left(d,C_{DES}\Delta\right)\\ \Delta&=\max\left(\delta_x,\delta_y,\delta_z\right)\end{aligned} \tag{4–16}$$

where only the production and destruction terms of the original Spalart-Allmaras turbulence model are scaled. The constant C_{DES} is typically set to 0.65 and Δ is the maximum length of the cell edge. This formulation ensures that for wall bounded separated flows the standard RANS SA model is used in the attached boundary layer and the subgrid scale model is used where $(d > C_{DES}\Delta)$ away from the wall where the flow separation occurs.

4.2 Flow Solver

The Beggar CFD code has been developed and maintained at the Air Force Seek Eagle Office (AFSEO) since the early 1990's by Rizk *et al.* (2002) and was the solver chosen for this research. The code is based on the conservative form of the compressible RANS equations as presented in Appendix-A. The code uses blocked and overset grid techniques to allow for mapping complex geometrical configurations. Beggar employs a second order flow solution scheme which requires a two layer interpolation fringe at each overlapping boundary. Beggar's flow solver provides time-accurate inviscid and viscous flow field solutions using a finite volume cell centered discretization. The hybrid SA-DES model as described above was chosen for unsteady simulations using this code because it is the most appropriate turbulence model to study unsteady shear layer flow available in the code.

The turbulence model and the governing flow equations are weakly coupled. At each time step the turbulent equations are solved and then the remaining five governing flow equations are solved. A first order Euler implicit time discretization is employed where the numerical fluxes are obtained using the Roe flux numerical scheme as detailed in Rizk *et al.* (2002). For time accuracy at each time-step Newton's method is applied to satisfy convergence criteria. The left hand side of the resulting discretized flow equations at each cell is derived using first order Steger-Warming fluxes for stability as explained by Rizk *et al.* (2002). The incremental correction to the flow variable is calculated iteratively by using a symmetric Gauss-Seidel relaxation iterative procedure.

The numerical simulations presented in this research were selected to match the flow conditions of the REEF supersonic wind tunnel as described in Dudley *et al.* (2008). To reduce the grid points and alleviate issues arising due to the nozzle start-up shock, the nozzle was not modeled in each simulation. A separate RANS solution of the nozzle was performed where the steady boundary layer profiles for $\rho u, \rho v, \rho w, \rho, e, p$ were extracted at the nozzle exit. The one dimensional profiles from the RANS simulations were then interpolated onto the desired grid inlet flow domain for a prescribed inlet boundary condition. The solution was slowly time ramped for stability purposes to the final prescribed values. The inlet face solution was subsequently frozen to achieve the desired boundary condition.

In the subsequent chapters where the results of the numerical simulations will be presented more details will be included such as applied boundary conditions, spatial and temporal resolution and details relevant to the post-processing of the data.

CHAPTER 5
CYLINDER IMMERSED IN A SUPERSONIC BOUNDARY LAYER

Flow around a circular cylinder has been studied extensively as it represents a canonical flow of significant engineering importance. At sufficiently high enough Reynolds numbers, the boundary layer separates from the surface along the cylinder and forms an unstable free shear layer. The shear layer detaches from the cylinder upper and lower surface and rolls into discrete vortices in a process referred to as vortex shedding. A regular vortex pattern in the cylinder wake emerges as the shear layer vortices shed alternately from the top and bottom of the cylinder surface and interact. The behavior and flow patterns of these recirculation regions are known to be well correlated with the freestream Reynolds number. Above the critical Reynolds number, an asymmetry develops in the wake that leads to growth of the recirculation region and eventual shedding forming the well known Von-Kármán vortex street. In general the above description is valid for cylinders immersed in subsonic flows. Previous experimental investigations cited by Bashkin *et al.* (2002) showed qualitatively that flows at subsonic and transonic speeds the flow pattern in the neighborhood of a circular cylinder changes with the Reynolds number much in the same way as with an incompressible flowfield. When Mach numbers exceed $M_\infty > 0.9$ a fairly extensive supersonic flow zone is formed near the cylinder body. This leads to a shortened separation zone and and a lack of unsteady near-wake flow regimes.

The flow structure which forms around a cylinder and the cylinder wake vary dramatically when the cylinder is placed in close proximity to planar walls as reported by Buresti & Lanciotti (1979), Götkun (1975) and Roshko *et al.* (1975). The presence of the wall boundary layer influences the cylinder wake and the flow behavior is sensitive to factors such as: (1) the boundary layer shape factor (H), (2) the Reynolds number based on rod diameter $\left(Re_d = \frac{U_\infty d}{\nu}\right)$, (3) the scaling of the rod diameter (d^*) relative to the boundary layer height (δ), (4) the gap height (G^*) between the rod and the wall.

Bearman & Zdravkovich (1978) suggested that vortex shedding is suppressed for small gap ratios ($\frac{G}{d}$). They also noticed that separation bubbles were formed on the wall both upstream and downstream of the cylinder whose size is dependent on the gap ratio. This trend is consistent throughout much of the published literature and has been verified in the experimental measurements conducted by Buresti & Lanciotti (1979, 1980) and Zdravkovich (1985, 1986). They measured the mean forces and velocity fluctuations detailing the interference of a plane wall on a cylinder. They each indicate vortex shedding persists almost unaltered down to gap heights where $0.3 \leq \frac{G}{d} \leq 0.4$.

Buresti & Lanciotti (2003) measured the mean and fluctuating forces acting on a cylinder in cross-flow placed near a wall with boundary layer to rod diameter ratio $\left(\frac{\delta}{d}\right)$ between $0.1 \leq \frac{\delta}{d} \leq 1.1$. The Reynolds number based on the rod diameter ranged from $0.86 - 2.77 \times 10^5$. The authors indicate that this is representative of the Reynolds number range where the regular vortex shedding of an isolated cylinder in freestream progressively disappears. The results indicate a periodic lifting force was induced by the vortex shedding irrespective of the boundary layer thickness for gap heights down to $\frac{G}{d} \leq 0.4$. They noted the mean lift coefficient rapidly decreased for increasing gap heights. They also found the Strouhal number decreased for increasing gap heights from $0.20 \leq \frac{G}{d} \leq 0.80$ with thin boundary layers and conversely, increased for thick boundary layers with increasing gap heights between the same range. For ranges outside of $\frac{G}{d} > 0.80$ the variation in Strouhal number was negligible. It should be noted, the maximum variation in the measured Strouhal number did not exceed 5%.

Price *et al.* (2002) conducted Particle Image Velocimetry (PIV) and hot film anemometry experiments for cylinders near a plane wall with $1200 \leq \mathrm{Re}_d \leq 4960$. They found for small gap ratios, where $\frac{G}{d} \leq 0.125$, the flow is virtually suppressed between the cylinder and wall and no vortex shedding of the cylinder occurred. Larger gap heights where $0.25 \leq \frac{G}{d} \leq 0.375$ the interaction between the cylinder inner shear layer and separated wall boundary layer increase with limited vortex shedding. Vortex shedding was

initiated when $0.5 \leq \frac{G}{d} \leq 0.75$ and the upstream separated boundary layer was shown to reduce in size. For the larger gap ratios, where $\frac{G}{d} \geq 1$, there was no separation of the wall boundary layer and the flow around the cylinder was essentially equivalent to the flow of an isolated cylinder.

The flow around a circular cylinder for $Re_d \approx 10^4$ or greater is still a challenging problem for modern computational fluid dynamics. RANS simulations cannot accurately reproduce the small scale structures found in the cylinder wake and tend to be overly dissipative. The application of DNS is limited due to the overbearing computational cost as explained in Chapter 4. Some promising LES results have been obtained for similar flows but are predominately found at lower Reynolds numbers. An example of such is found in the work of Sarkar & Sarkar (2010) who performed LES for low Reynolds number subsonic flow around a cylinder near a plane wall following the experiment of Price *et al.* (2002). They found the gap ratio has a strong influence on the cylinder shear layer instability and thus the dynamics of the cylinder wake. When the inner shear layer lies within the boundary layer ($G \leq \delta$) they note a strong coupling between the cylinder inner shear layer and approaching boundary layer with suppression of vortex shedding. They also report that the front stagnation point shifts towards the wall as the gap ratio is decreased and a lifting force is generated by the flow accelerating underneath cylinder and asymmetry of the base pressure coefficient.

Nishino *et al.* (2008) performed unsteady RANS and DES simulations using the SA-DES closure model for a cylinder near a plane wall at $Re_d = 4 \times 10^4$. The detached-eddy simulations correctly captured the cessation of the vortex shedding whereas the RANS simulations predicted the cessation at much smaller gap ratios when compared with experimental results. The wake structures predicted by the simulations were in good agreement with experiments for both small and large gap ratios. Travin *et al.* (2000) also performed detached-eddy simulations of flow around a cylinder including the sub-critical (characterized by laminar separation) and post-critical (characterized by turbulent

separation) flow regimes. The results were in good agreement with large-eddy simulations and available experimental data.

There exists a wealth of research focusing on subsonic flows with cylinders near plane walls but there lacks a substantial effort to study this geometry for approaching supersonic freestream flows. Though not explicitly detailed in all of the above mentioned works, it should be noted that $\left(\frac{\delta}{d}\right) \leq 1$. This geometrical limit restricts the cylinder from being fully immersed into the boundary layer when $\frac{G}{\delta} \geq 0$. In contrast, the results presented in this work includes compressibility through a supersonic boundary layer and the sizing of the cylinder relative to δ is between $2 \leq \frac{\delta}{d} \leq 5$. The cylinder is therefore exposed to a upstream non-uniform velocity gradient $\Delta\frac{U}{u}$ over its entire surface and the local velocity typically exceeds the local speed of sound. This condition leads to the formation of a leading edge bow-shock whose strength depends on the gap height and thus the approaching Mach number. There also exists a complex wave pattern due to the alternating expansion and contractions of the flow in the wake of the cylinder. The interaction of these waves leads to adverse pressure gradients that the flow cannot negotiate and the flow separates both upstream and immediately downstream of the cylinder. These asymmetric conditions coupled with the tendency of the flow to accelerate in the gap between the cylinder and wall leads toward a mean force directed away from the wall. The interaction of the vortical structures shed by the cylinder and the separated floor boundary layer decrease with larger gap heights indicating for close wall proximity the interaction excites the cylinder wake.

5.1 Computational Grids

Green *et al.* (2008) have demonstrated the selected solver has the ability to accurately predict the shedding characteristics of an isolated rod at lower speed uniform flow and has been compared successfully with publications by Nichols & Heikkinen (2005). This is an important consideration due to the lack of available experimental data with the current investigation described next. The simulations were selected to match the flow conditions of

the REEF SWT as described in Chapter 4 and in Dudley *et al.* (2008). Two rod diameters (d^*) were placed at various gap heights (G^*) above the wall to study the boundary layer and cylinder shedding interaction. The rod dimensions and gap heights were selected based upon a literature review concerning the suppression of supersonic cavity flow using a rod-spoiler device as illustrated in Stanek (2005) and Ukeiley *et al.* (2004*a*).

The leading and trailing streamwise lengths of the computational domain extended at least 20 diameters from the cylinder centerline as illustrated in Figure 5-1. The wall normal boundaries extended a minimum of 20 diameters above the cylinder while the spanwise computational boundaries extended a minimum of 2 diameters. The simulations utilized a three dimensional structured block to block grid system as illustrated in Figure 5-2. The floor and cylinder used a no-slip boundary condition. The outer extents of the Z-planes were defined using symmetry boundary conditions with a non-reflective characteristic boundary condition located on the upper and outer streamwise domains.

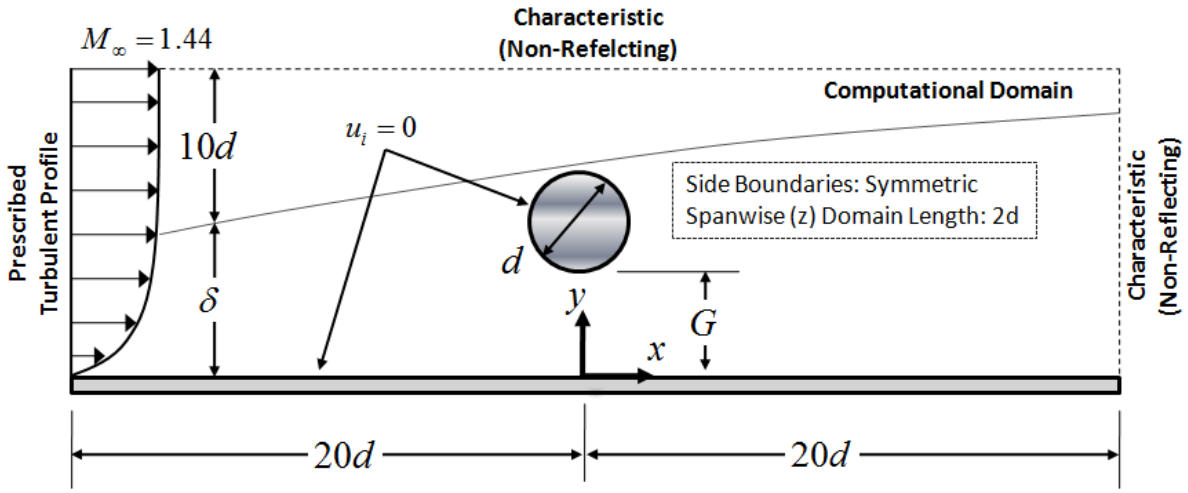

Figure 5-1. Sketch of cylinder immersed in a supersonic boundary layer.

Nishino *et al.* (2008) conducted a relatively thorough grid sensitivity study for $Re_d = 4 \times 10^4$ detached-eddy simulation using the SA-DES closure model for flow around cylinder near a plane wall. In order to resolve the viscous sublayer the grid must be

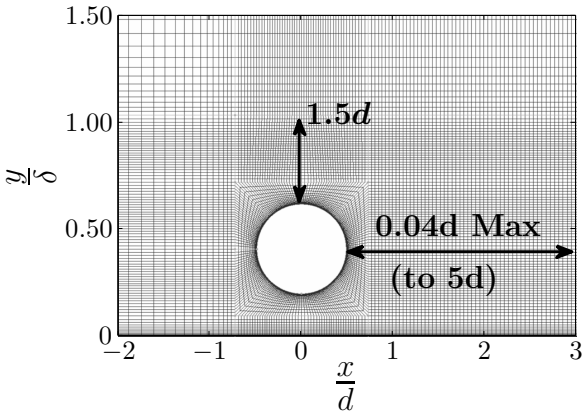

Figure 5-2. Grid topology.

appropriately resolved in the near wall region. The y-plus (y^+) value is commonly used to determine the first grid spacing normal to the wall and is given by

$$y^+ = \frac{u_\star y}{\nu} \tag{5–1}$$

where u_* is the friction velocity calculated by $u_\star = \sqrt{\frac{\tau_w}{\rho}}$. The shear stress at the wall for three dimensional flows is given by

$$\tau_w = \mu\sqrt{\left(\frac{du}{dy}\right)^2 + \left(\frac{dw}{dy}\right)^2} \tag{5–2}$$

which is the magnitude of the surface stress vector. Nishino *et al.* (2008) found the cylinder wake was captured well when $y^+ \leq 1$ at the wall and the maximum grid spacing in the wake region of the cylinder was no greater the $0.05d$.

The primary region of interest in the current study is up to $\pm 5d$ from the cylinder centerline in the streamwise and wall normal directions. Following the efforts of Nishino *et al.* (2008), a similar grid refinement and time-step study with $\Delta = 0.080d, 0.040d, 0.025d$ was conducted. The variable Δ depicts the maximum cell edge length in the x, y and z coordinate directions. The effect of the grid resolution on the pressure spectra as measured one diameter downstream of the rod is illustrated in Figure

5-3. The findings are in good agreement with Nishino *et al.* (2008) who studied grid refinement based on the convergence of separation angles and the drag coefficient. The spectra

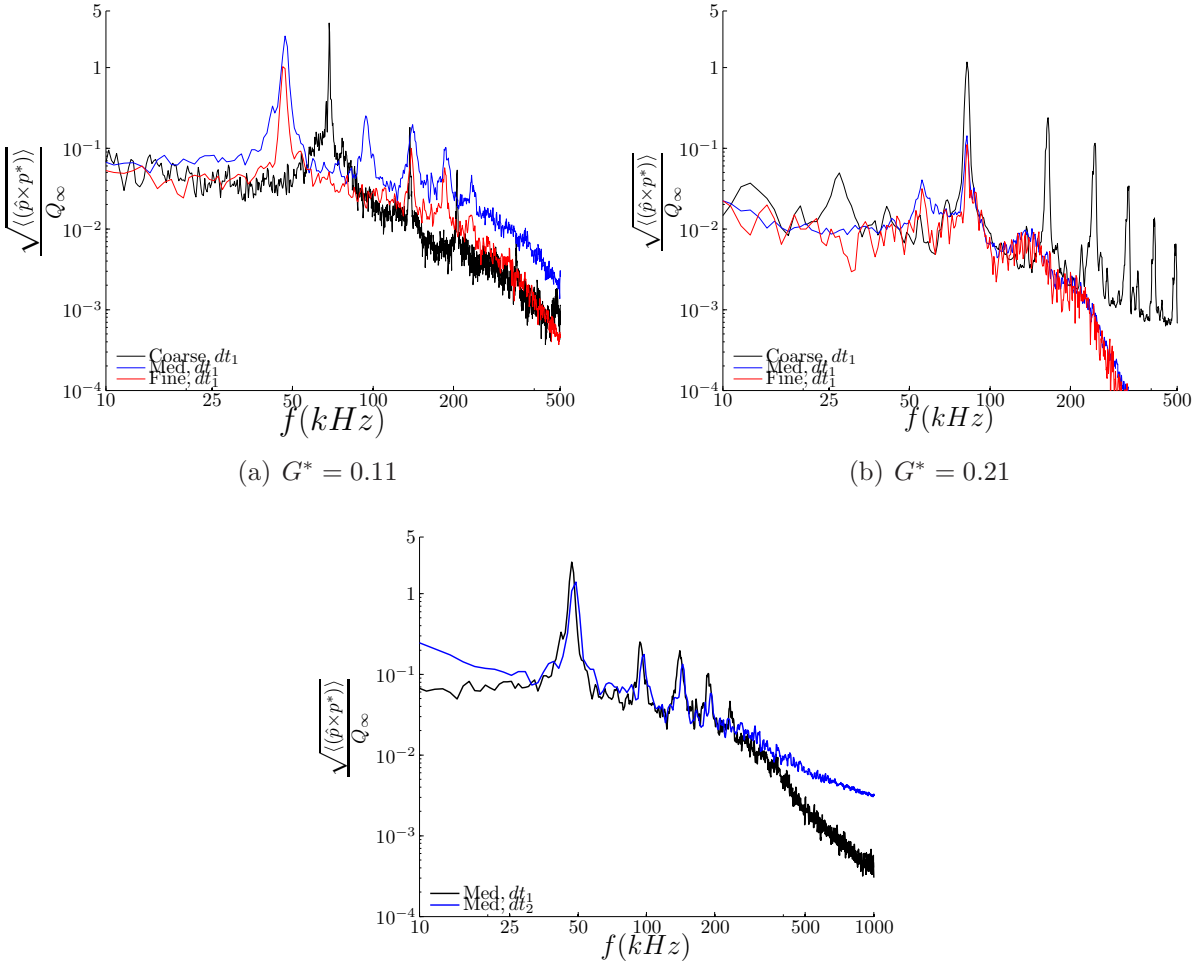

(a) $G^* = 0.11$

(b) $G^* = 0.21$

(c) $G^* = 0.11$

Figure 5-3. Grid and time-step sensitivity on spectral results for $d^* = 0.40$.

were computed with a minimum of 10 (fine grid) averaged ensembles with a length 50 periods as suggested by Cummings *et al.* (2008) using 75% overlapping which resulted in a frequency resolution of 976 hertz. In Figure 5-3 it is apparent that the solution is highly grid dependent at $G^* = 0.11$. At this location both the amplitudes and frequency content, most notably at higher frequencies, are sensitive to the grid refinement. The medium and fine grids converged nicely as the gap ratio is increased as shown where $G^* = 0.21$. The time-step study was conducted after selection of the medium grid and conducted

at $G^* = 0.43$ where the strength of the vortex shedding peaked. It was concluded that the larger time-step adequately resolved the spectra of interest for the problem at hand where less than 5% deviation is noted in the frequency or amplitudes of the spectra plots. It should be noted the frequency resolution of each plot was identical but the number of ensembles were less for the fine resolution grid and smaller time-step simulations. The variation on broadband levels at higher frequencies points to the ability of the smaller time-step to adequately resolve higher frequencies as expected.

The viscous walls used a first point wall spacing $4 \times 10^{-4}d$ resulting in a $y^+ \leq 1$. The cell growth, measured from the first to the adjacent cell-center, in the normal direction was less than 20% inside the boundary layer. The computational grid(s) consisted of roughly 2×10^6 points with 201 equidistant points around the cylinder. The mean velocity flowfield and mean turbulent velocity flowfields deviated less than 5% in approximately 50 periods considering the dominant shedding frequency of each configuration but the solution was typically run an additional 300 periods to increase the accuracy of the spectral analysis.

Table 5-1 outlines the geometry and computational details considered during this study. The Reynolds number based on the rod diameter is tabulated considering the velocity at the rod centerline (U_c) and the freestream velocity (U_∞). Based on the findings of the spatial and temporal resolution studies, the medium grid consisting of approximately 2×10^6 cell-centered grid points and a time-step of 5×10^{-07}s were selected.

5.2 Results

The results of the mean flowfield velocities and the instantaneous vorticity flowfield are discussed next. Mean pressure fields and mean turbulent statistics are also presented to determine the effect the rod diameter and gap height have on the cylinder near body flow dynamics.

Table 5-1. Summary of computational details

d^*	G^*	$\Delta \times d$	$Re_d \times 10^4\,(U_\infty, U_c)$	$dt \times 10^{-7}$ (s)	Notation
0.20	0.11	0.040	1.9,1.45	5	d1G1,dt_1
	0.21	0.040	1.9,1.60	5	d1G2,dt_1
	0.53^+	0.040	1.9,1.75	5	d1G3,dt_1
	$1.00*$	0.040	1.9,1.85	5	d1G4,dt_1
0.40	0.11	0.080	3.8,2.9	5	d2G1, Coarse,dt_1
	0.11	0.040	3.8,2.9	5,2.5	d2G1, Med,dt_1,dt_2
	0.11	0.025	3.8,2.9	5	d2G1, Fine,dt_1
	0.21	0.040	3.8,3.2	5	d2G2,dt_1
	0.64^+	0.040	3.8,3.5	5	d2G3,dt_1
	1.29^*	0.040	3.8,3.7	5	d2G4,dt_1

$^+$ top of rod near top of δ
* bottom of rod near top of δ

5.2.1 Mean Flowfield

The time averaged results pertaining to the cylinder wake are discussed in this section. Figure 5-4 presents the time averaged streamwise velocity contours for all of the configurations being studied in this effort. In general, as the cylinder is moved away from the wall (looking top to bottom in the figure) the length of the cylinder wake increases in the streamwise direction due to the accelerated flow in the gap. This also leads to the wake being more significantly deflected towards the wall. The separation bubble on the floor aft of the cylinder also becomes larger in both streamwise and wall normal directions. A strong coupling exists between the side of the shear layer closest to the wall, which will be referred to as the inner shear layer hereafter, and the boundary layer when the gap ratio is very small. As the gap height is increased the cylinder wake accentuates the deflection of the boundary layer away from the wall forming a large downstream separation bubble for both rod diameters. The location of this separated region appears to be correlated with the location of the cylinder. This region moves downstream as the rod is moved further away from the wall and as the rod wake lengthens in the streamwise direction. The mean contours also depict the formation of a separation bubble upstream of the cylinder for all cases.

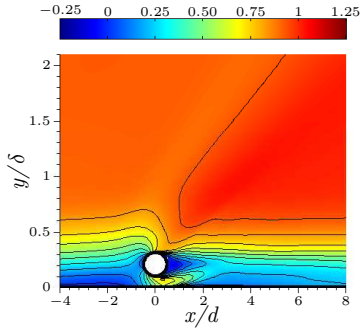

(a) $d^* = 0.21, G^* = 0.11$

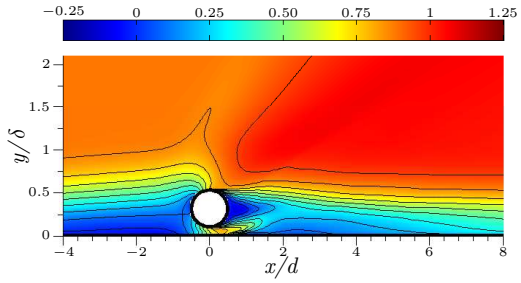

(b) $d^* = 0.41, G^* = 0.11$

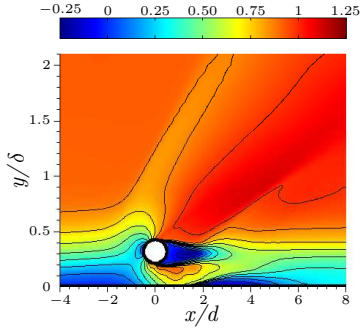

(c) $d^* = 0.21, G^* = 0.21$

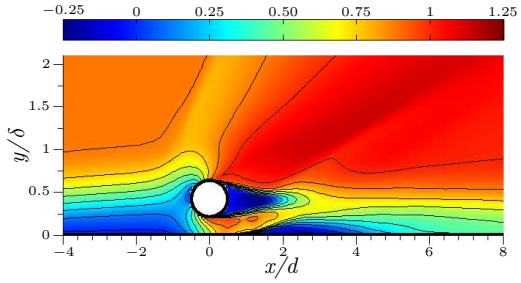

(d) $d^* = 0.41, G^* = 0.21$

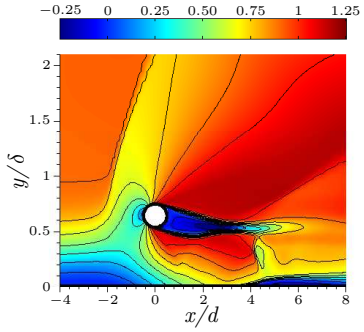

(e) $d^* = 0.21, G^* = 0.53$

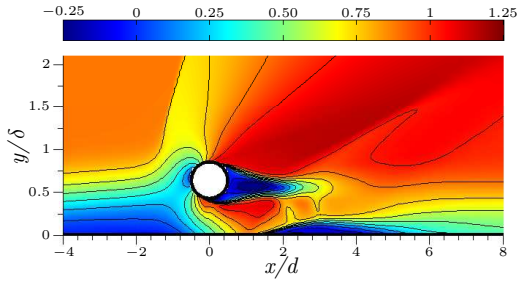

(f) $d^* = 0.41, G^* = 0.64$

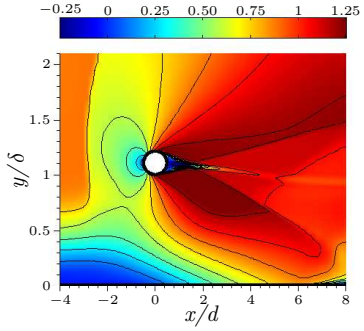

(g) $d^* = 0.21, G^* = 1$

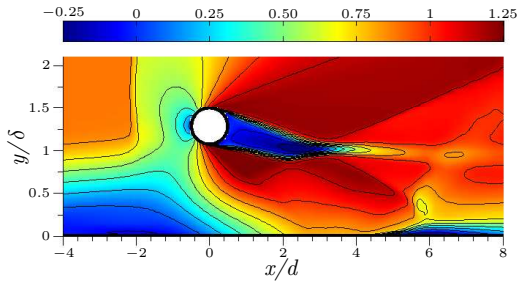

(h) $d^* = 0.41, G^* = 0.1.29$

Figure 5-4. Mean streamwise velocity contours.

The evolution of the mean streamwise velocity profiles for each rod is illustrated in Figure 5-5. Each $\frac{\langle u \rangle}{U_\infty}$ profile on the x-axis is constantly offset for clarity. The velocity deficit due to the presence of the cylinder is fairly short lived for each rod diameter and appears to be independent of gap ratio. For each case the maximum inflected velocity is roughly 50% of the original value after traveling five cylinder diameters downstream. The separated boundary layer aft of the cylinder becomes more prominent as the rods are moved away from the wall up to the point where the rod is still fully immersed in the boundary layer as evident by $d^* = 0.40, G^* = 0.64$ and $d^* = 0.20, G^* = 0.53$. The larger rod diameter produces a larger separated flow in the cylinder wake. The size of the separated region in the streamwise and normal directions are also enhanced for the larger diameter rod. The streamwise velocity increases as the gap of the cylinder is increased (up to the point where the rod is still fully immersed) the flow accelerates around the body of the cylinder generating a larger adverse pressure gradient which results in the flow being turned more aggressively away from the wall. As the rod is moved away from the wall the leading edge bow shock is strengthened and the flow speed in the cylinder gap is increased due to the cylinder's exposure to increased approaching boundary layer flow velocities. The flow expands more on the upper portion of the cylinder as the gap height is increased. This combined behavior forces the wake of the cylinder to deflect downward eventually leading to a series of expansions (as evidenced by the accelerated flow seen in 5-4) and shocks (not clearly visible but appear as the tail deflects upwards causing a compression corner) near the trailing edge of the wake which turns the wake more parallel with the floor. The velocity deficit recovers quicker (in terms of physical downstream distance) for the small diameter rod than the larger cylinder. This in turn weakens the interaction between the cylinder wake and the surface of the planar wall. It should also be noted that when used as a suppression device in cavity flows, rods have typically been placed very near the leading edge of the cavity. As the rod is raised above the floor the cylinder wake becomes elongated in the streamwise direction and the region

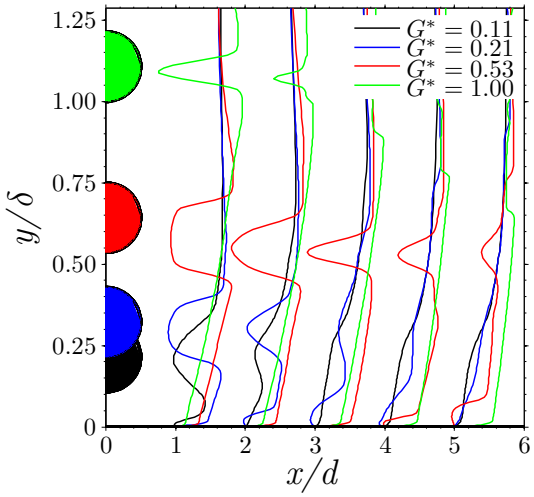

(a) $d^* = 0.20$

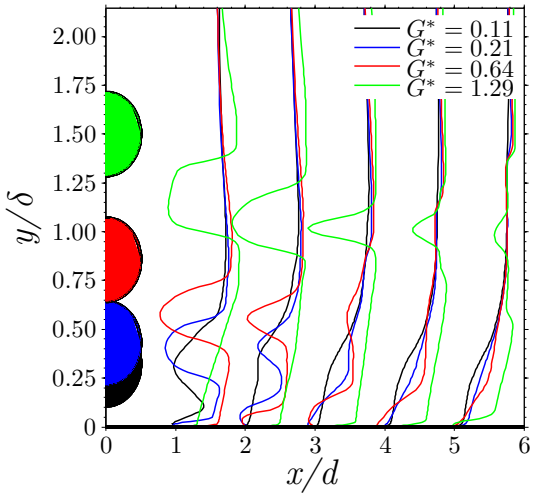

(b) $d^* = 0.40$

Figure 5-5. Mean streamwise velocity profiles at given axial locations.

of separated flow on the floor is pushed further downstream. The separated region on the floor is moved downstream of the cavity leading edge as the rod is raised above the wall and the wake lengthens. This may help explain the reduced effectiveness of the rods to suppress the pressure fluctuations of supersonic cavity flows when the rod is placed outside the boundary layer as reported in Ukeiley *et al.* (2004*a*).

Figure 5-6 illustrates the mean pressure distribution on the cylinder surface as a function of theta and gap height. The angle theta is measured with zero at the forward

most streamwise location and continually increasing on the surface of the cylinder in the clockwise direction up to 360 degrees. When the rod is close to the wall the pressure initially rises on the cylinder and after the flow stagnates the pressure falls as the air accelerates over the top of the body until the separation point is reached for each case. When either rod is moved further away from the wall the pressure drastically falls until the separation point. From 90 to 270 degrees the pressure distribution exhibits noticeable valleys that are strongly evident for small gap ratios indicative of the upper and lower shear layer regions of the cylinder wake. For higher gap ratios these valleys occur at substantially lower pressures indicating the presence of stronger recirculation zones.

For each rod the forward stagnation point on the cylinder shifts towards the wall for $G^* \leq 0.21$ as the gap height is increased but remains on upper half (where $\theta \geq 0$) of the rod. For higher gap ratios, with the rod still fully immersed in the boundary layer, the forward stagnation point shifts to the lower half of the cylinder. The lower surface separation point shifts towards the wall as the gap height is increased and levels off when the top of the rod is brought near the top of the boundary layer. The top separation point is sensitive to the position of the rod inside the boundary layer and appears to shift towards the wall for increasing gap height. As the rod remains immersed inside the boundary layer the flow separates at angles of 120° and 90° for the small and large diameter rod respectively.

The intricate details of the vortex shedding are difficult to interpret from the aforementioned time averaged flow fields. There exists a strong periodicity to the pressure signal associated with the shedding of the cylinder shear layer most noticeably at low gap ratios. A spectral analysis was performed after collecting the pressure signal on the floor at one diameter downstream from the cylinder centerline. Each ensemble was collected over a time period of 300T where the period (T) corresponds to the dominant vortex shedding frequency. There were a minimum of 8 averaged ensembles in the resulting power spectra illustrated in Figure 5-7 which are non-dimensionalized by the freestream dynamic

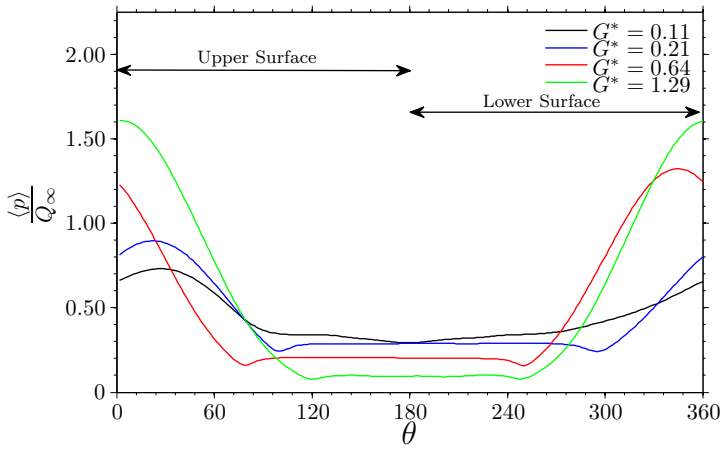

(a) $d^* = 0.20$

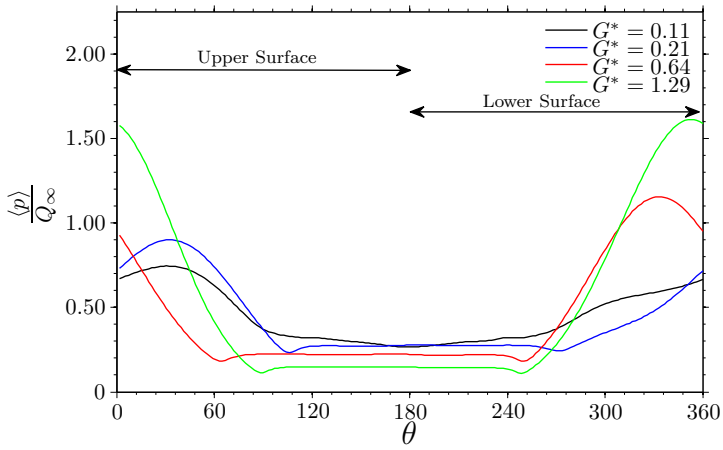

(b) $d^* = 0.40$

Figure 5-6. Time averaged pressure distribution on cylinder surface.

pressure. The rod placed at the top edge of the boundary layer was omitted from each plot as the flow solution converged to a non-oscillatory steady state.

Placing the rod in close proximity to the wall produced the highest peak levels observed in the fluctuating pressure spectra. The dominant peak for the vortex shedding shifted to a higher frequency (near 100kHz for each rod) when the gap height was raised to $G^* = 0.21$ though a first lower frequency peak was still evident in some of the spectra. When the top of the rod was brought near the top of the boundary layer the first peak in the spectra was nearly completely dissipated for the small diameter rod. It should be noted for the either rod the cessation of the vortex shedding occurred when the rod was

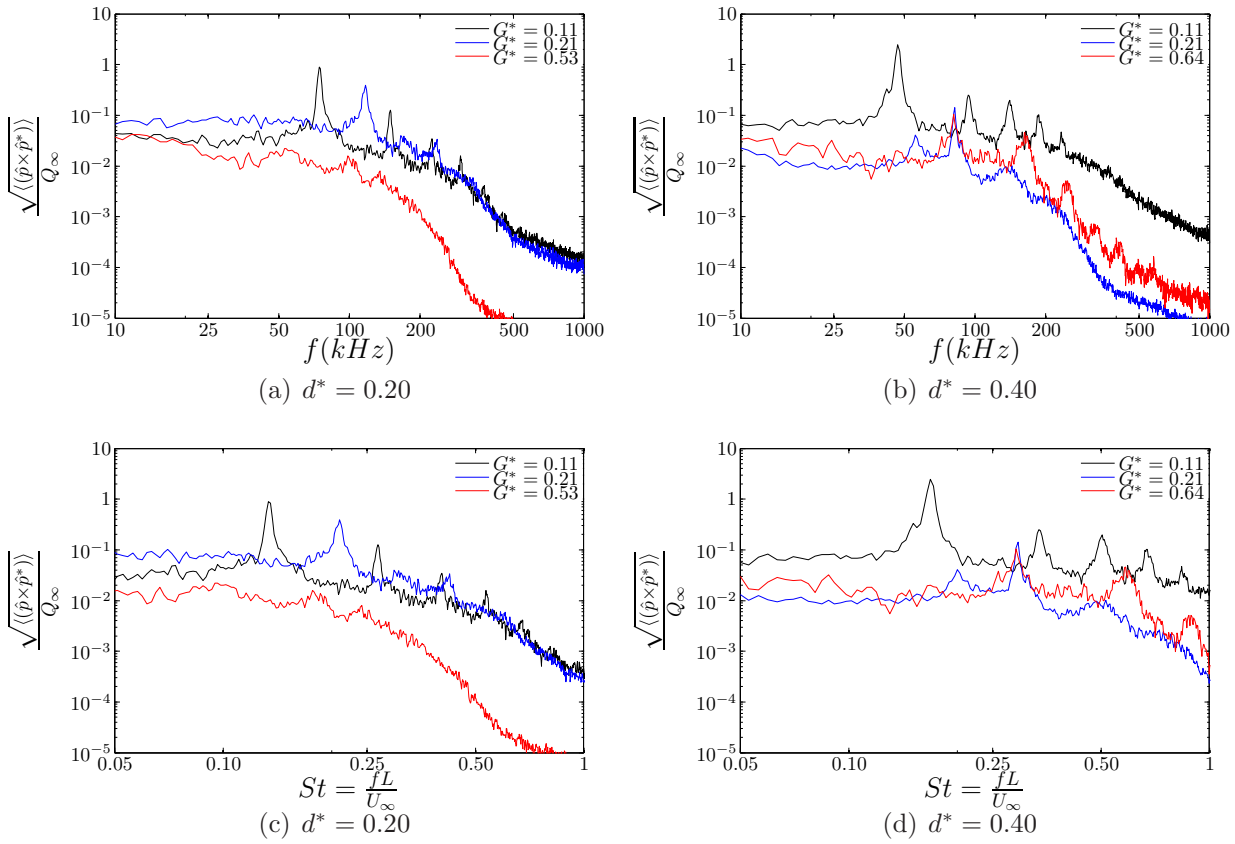

(a) $d^* = 0.20$ (b) $d^* = 0.40$

(c) $d^* = 0.20$ (d) $d^* = 0.40$

Figure 5-7. Cylinder PSD as a function of frequency and Strouhal taken at $\left(\frac{x}{d}, \frac{y}{\delta}\right) = (1, 0)$.

brought outside of the boundary layer consistent with what one would expect based on the visualizations presented in Van-Dyke (1982).

Each rod exhibited pressure fluctuations with dominant peaks for each gap ratio where the rod was fully immersed in the boundary layer. A slight increase in shedding frequency was apparent with increased gap height that is associated with the increased velocity of the exposed rod. The small diameter rod only exhibited strong coherent shedding when the gap ratio was very small albeit at a much reduced overall power when compared with the large diameter rod. The Von-Kármán type of vortex shedding for each rod became less apparent when the rod was moved further away from the wall. Gap heights where $\frac{G}{\delta} > 0.21$, where $M_\infty \approx 1.2$ appears to be the critical gap height where the organized cylinder shedding becomes weak. At this position, the bottom of the rod was brought to the top of the transonic regime, i.e. where $M_\infty \approx 1.2$, and each rod diameter

showed significant drop off in the broadband levels and only the presence of small peaks were evident in the frequency spectra. It should be noted that peaks are still present in the spectra at higher gap ratios, most notably for the large diameter rod, but is likely due to the oscillating nature of the separated region on the floor. This is further demonstrated with instantaneous vorticity contours shown in Figure 5-10 through Figure 5-13.

Figure 5-8 represents the Strouhal number for the dominant peak of the power spectra plotted with both the freestream velocity and cylinder centerline velocity (boundary layer velocity at cylinder centerline with no rod present) being used as the velocity scale. Buresti & Lanciotti (1979, 1980) found that for $Re_d = 0.86 \times 10^5$ the Strouhal number converges to approximately 0.19 for $\frac{G}{\delta}$ greater than 0.45. When plotted as a function of the freestream velocity the current simulations agree reasonably well with the results of the previous authors, at least for the smaller rod diameter tested. Some care needs to be taken with this comparison as one should note there are significant differences in the experiments. Buresti and Lanciotti used rods that where $0.1 < \frac{d}{\delta} < 1.1$ and the flow was purely subsonic with velocities less than 30m/s (compared to 400^{+}m/s in the current study). The Reynolds number ranges were achieved primarily by modification of the tunnel velocity and altering the rod diameter. It is believed, for supersonic

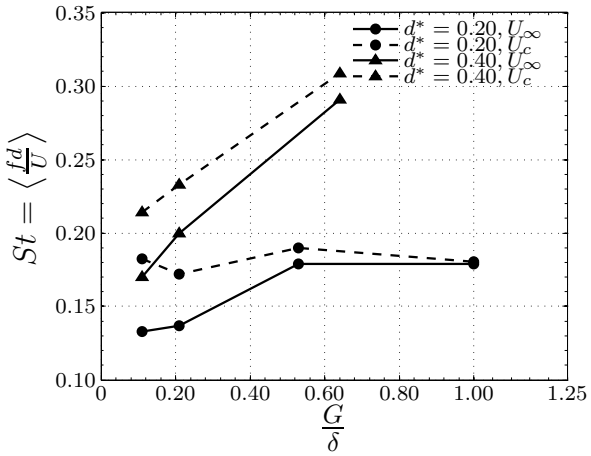

Figure 5-8. Strouhal number based on the freestream velocity U_∞ and the cylinder centerline velocity U_c

boundary layers that exhibit high velocity gradients and with a rod sized so that $\frac{\delta}{d} > 1$ fully immersed inside the boundary layer, the cylinder freestream velocity is still the appropriate velocity to be used in the Strouhal number calculation. The centerline velocity tends to be significantly lower than the approaching boundary layer velocity leading to overestimated Strouhal values.

Figure 5-9 illustrates the mean normal velocity, mean normal turbulent velocity and mean pressure fields for selected gap heights. The larger diameter rod placed near the top edge of the boundary layer shows a stronger mean normal velocity with similar normal turbulent fluctuations. The mean normal velocity for the large diameter rod was more pronounced when compared to the small diameter rod. The larger diameter rod with top of the rod placed near the top of the boundary layer exhibited the lowest pressures aft of the cylinder resulting in a larger separated region downstream of the cylinder which in turn turns the flow more aggressively away from the wall. It should be noted that the geometry considered here is not ideal as in application the rod will be placed just ahead of backward facing step. One would tend to believe the flat plate geometry would be more restrictive and may lead to discrepancies when compared to the actual cavity geometry considered later though trends are expected to be quite similar.

5.2.2 Instantaneous Vorticity Flowfield

A brief description of the vortex formation and cessation, interaction with the boundary layer and eventual break down to smaller eddies are described in this section. To visualize the vortex dynamics in proximity to a wall during the shedding cycle, instantaneous contours of spanwise vorticity (ω_z) on the centerline are presented in Figure 5-10 through Figure 5-13 for each gap ratio. The instantaneous figures are drawn at four different points over time-period T of vortex shedding that has been calculated assuming shedding at a Strouhal number of 0.20 which represents an approximate average value over the range of $\frac{G}{\delta}$ considered in the present study. It should be noted in these figures that the phase of the initiation of this cycle is not the same for each case presented.

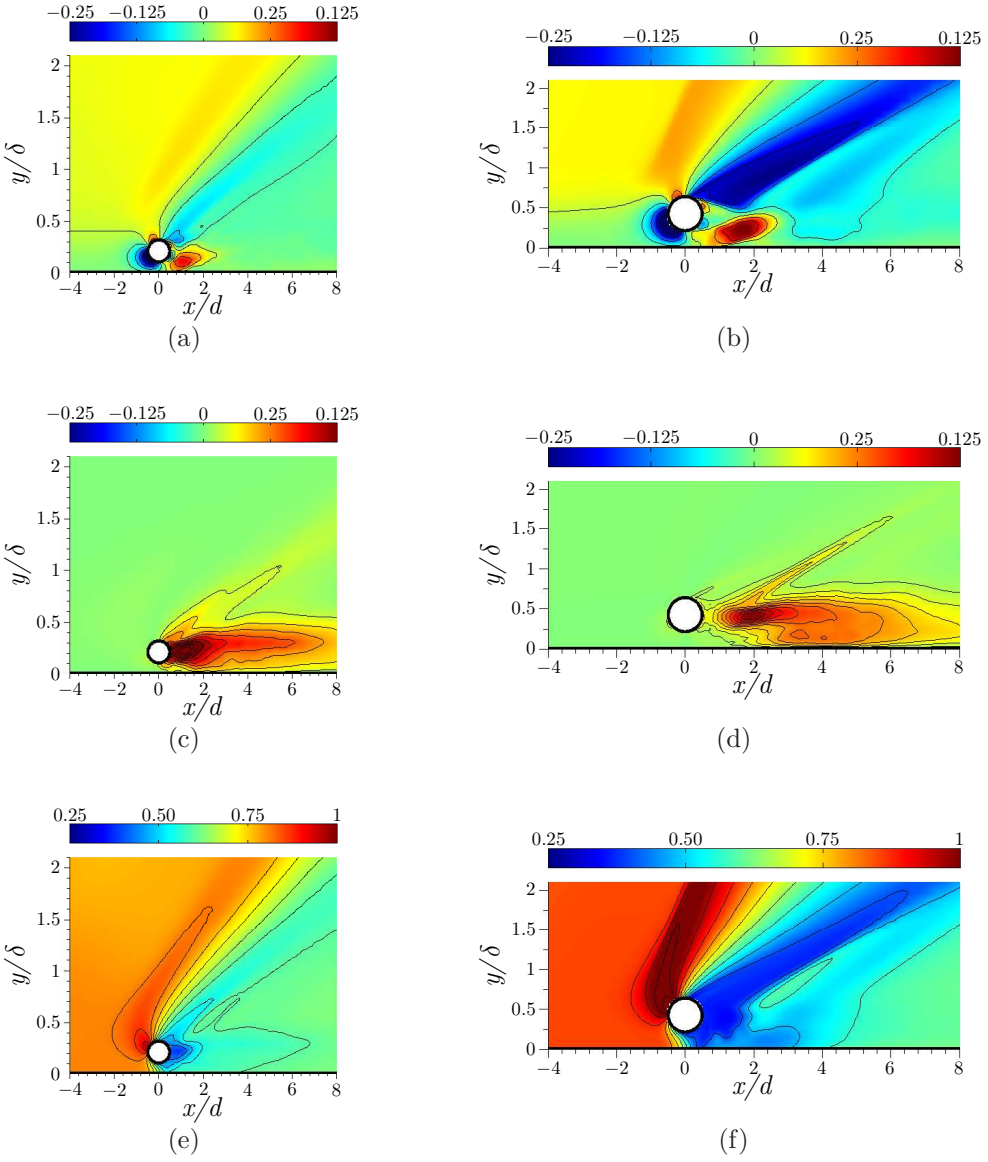

Figure 5-9. Small diameter rod mean flowfield contours for $G^* = 0.11$. Column (a) is $d^* = 0.20, G^* = 0.11$ and Column (b) $d^* = 0.40, G^* = 0.64$. Row (a) is mean normal velocity, Row (c) mean normal turbulent velocity, Row (d) mean pressure flowfield.

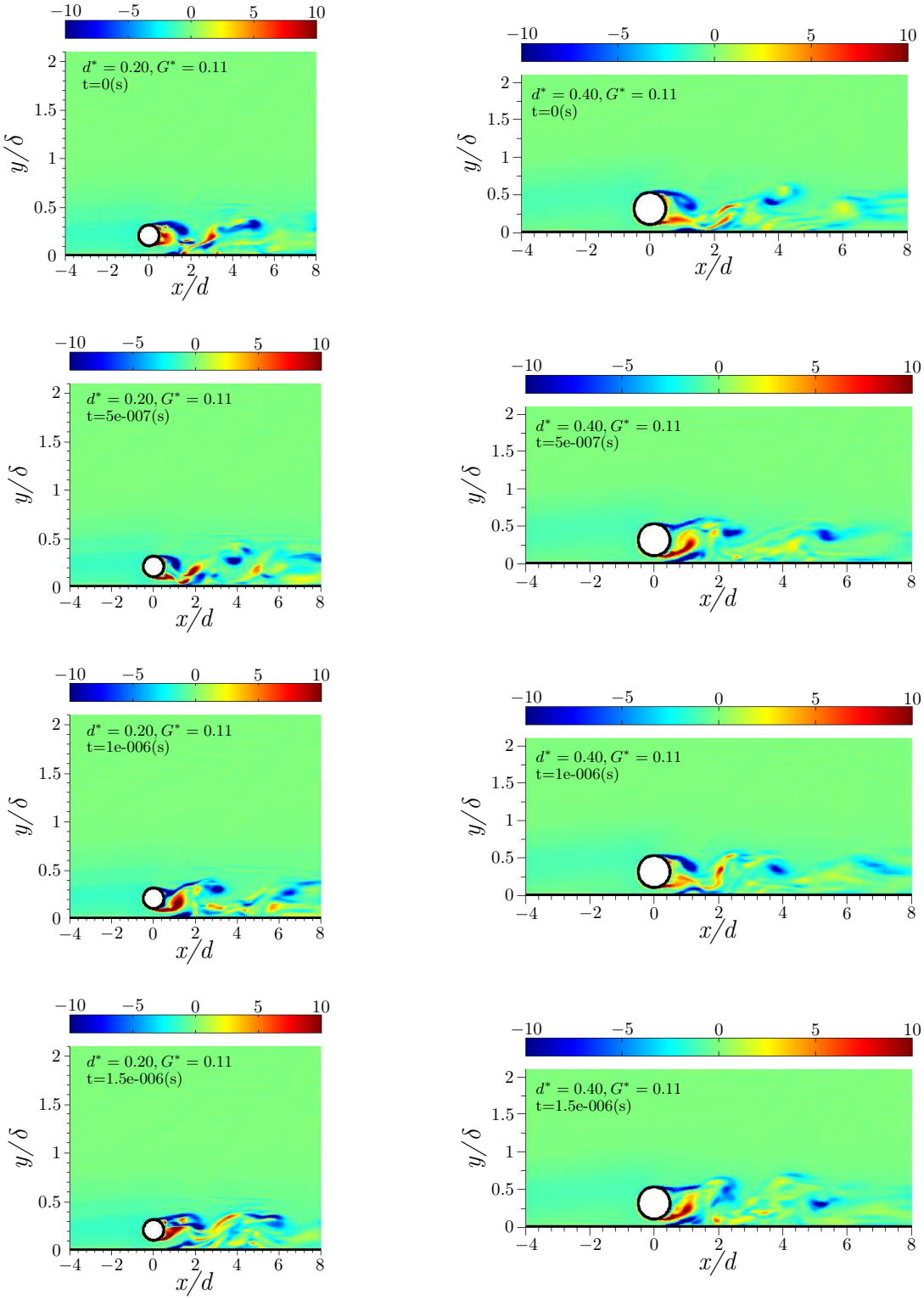

Figure 5-10. Instantaneous z-vorticity for $G^* = 0.11$.

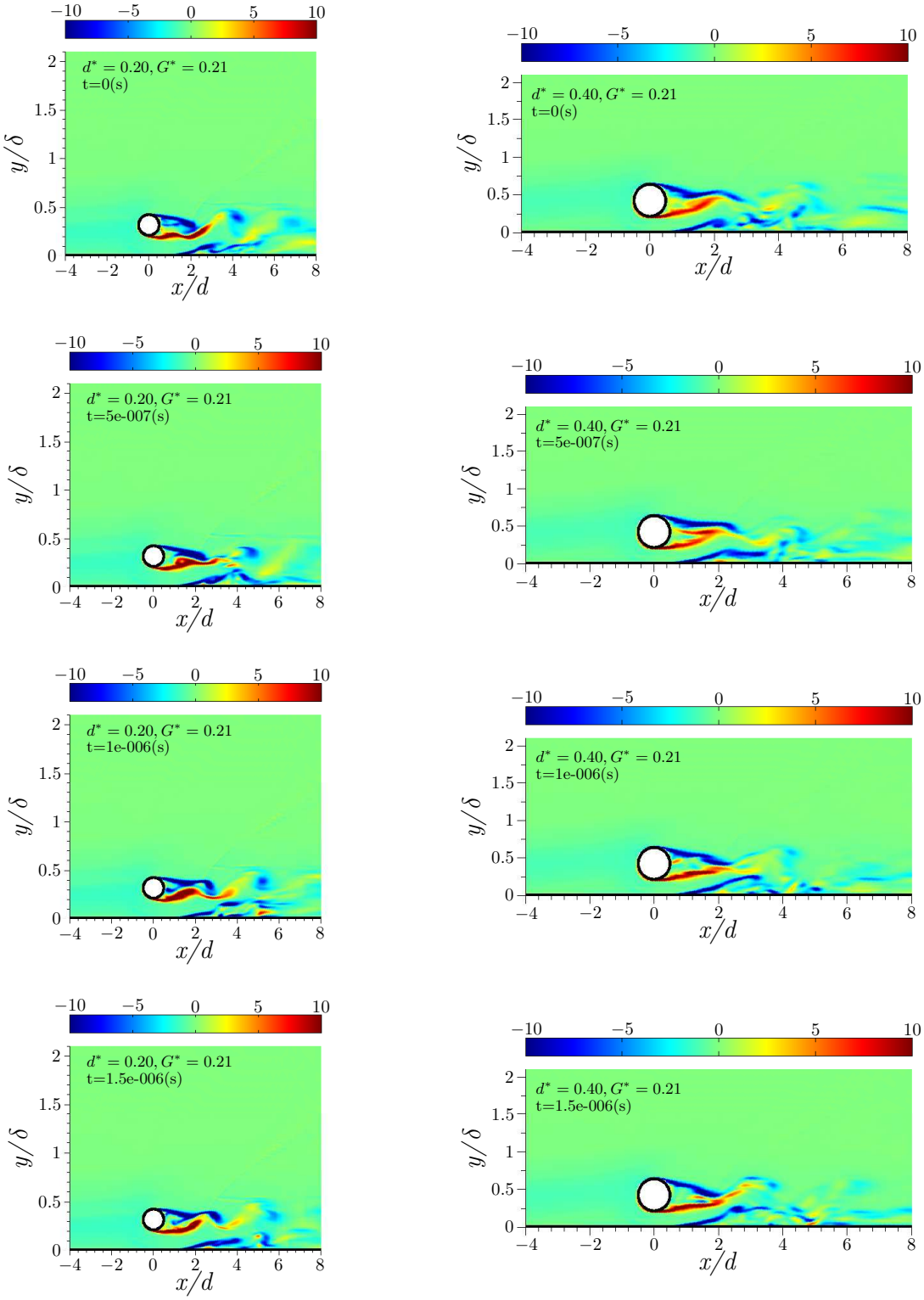

Figure 5-11. Instantaneous z-vorticity for $G^* = 0.21$.

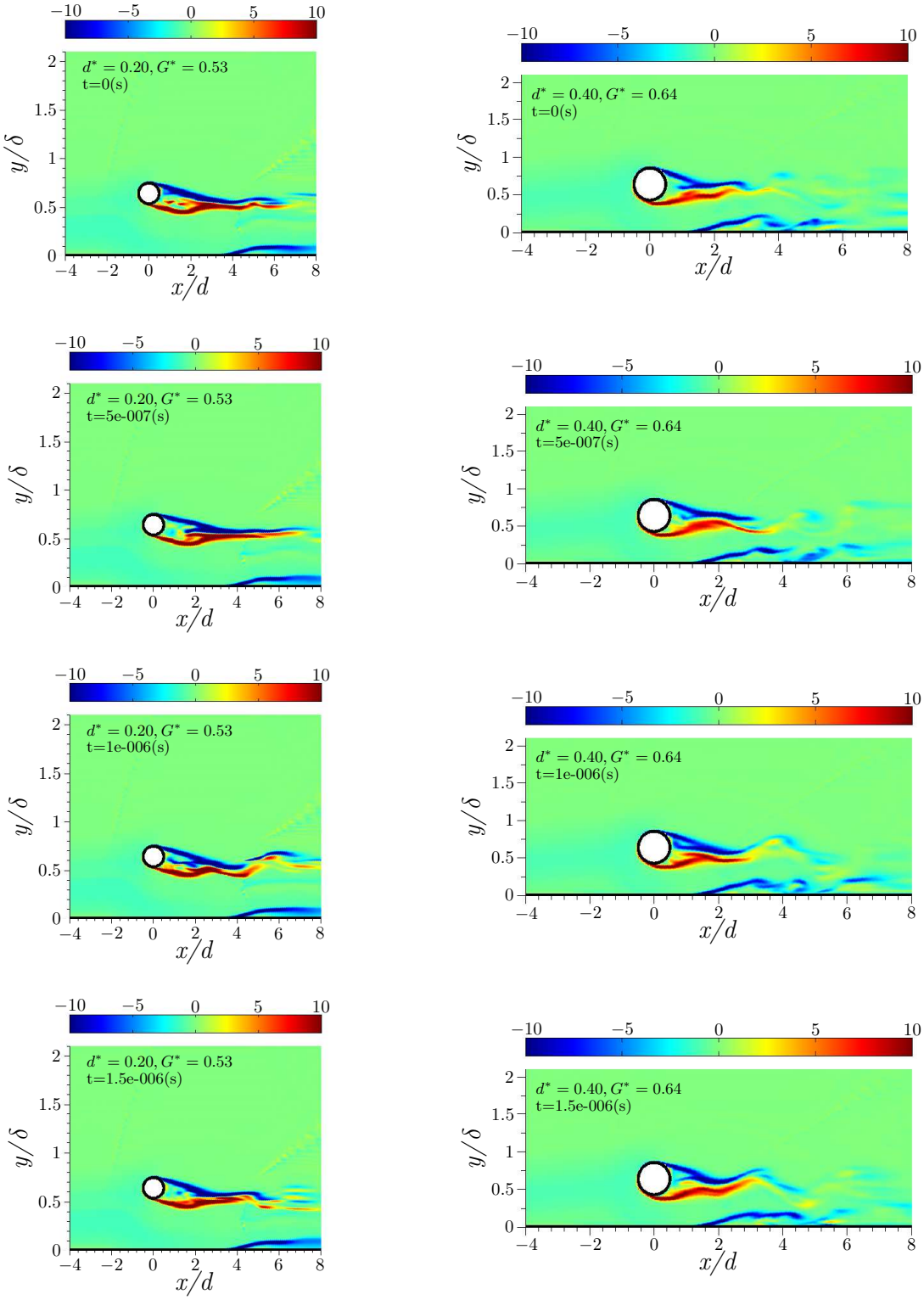

Figure 5-12. Instantaneous z-vorticity for top of rod near the top of boundary layer.

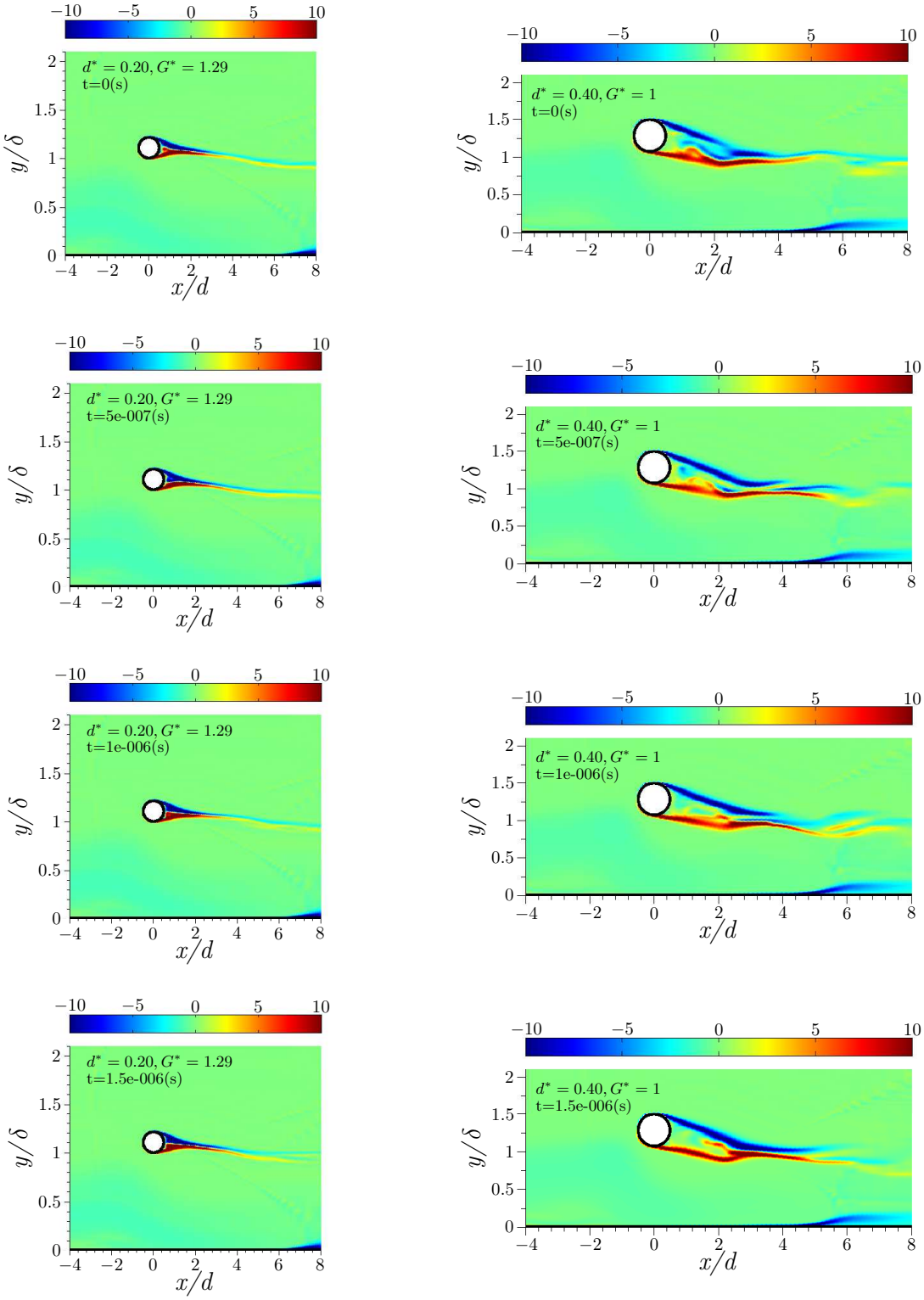

Figure 5-13. Instantaneous z-vorticity for rod outside boundary layer.

Strong vortical features are present when substantial mixing with the floor boundary layer is present. This generally occurs for $\frac{G}{\delta} \leq 0.25$ with each rod. Cessation of Von-Kármán type shedding was observed when the rod centerline velocity neared the sonic velocity for each diameter indicating the presence of a critical gap ratio linked to the boundary layer sonic line. When the rods are near the wall the positive vortex street is deflected away from the wall due to the interaction with the separated floor boundary layer as shown in Figure 5-10 and Figure 5-11. The negative vortex street, which is located on the top of the rod, rolls up in a classical Von-Kármán style resulting in large vortical features that are convected downstream.

As $\frac{G}{\delta}$ is increased above 0.5 for each rod diameter the cylinder wake is deflected towards the wall. The inner and outer shear layers of the cylinder wake remain essentially steady up to the separation bubble aft of the cylinder. The interaction with the floor boundary layer allows the semi-periodic motion noticed in the aft-end of the cylinder wake. As the cylinder is brought outside the boundary layer there is no appreciable motion evident in the cylinder wake and the separated floor boundary layer is pushed further downstream. When the rod is completely outside the approaching boundary layer the separated region aft of the cylinder on the floor experiences negligible turbulent fluctuations.

Figure 5-14 and Figure 5-15 illustrate an instantaneous iso-surface of the spanwise vorticity component colored by velocity magnitude and are intended to demonstrate the three dimensional characteristics of the cylinder wake. The flow tends to exhibit an elongated vortical structure in the spanwise direction for $\frac{G}{\delta} = 0.50$ for both rod diameters. The outer part of the shear layer shed from the top of the cylinder appears to remain smooth much further downstream as the gap ratio is increased as evident in Figure 5-14 and Figure 5-15. For lower gap ratios for each rod, the shear layer instability arises and quickly breaks down the coherent spanwise type structure. As previously stated, the deflection of the boundary layer is highly evident for each gap ratio and each cylinder.

Examining each figure it is evident that the strong coupling of this separated boundary layer with the cylinder wake diminishes quickly as the gap ratio is increased.

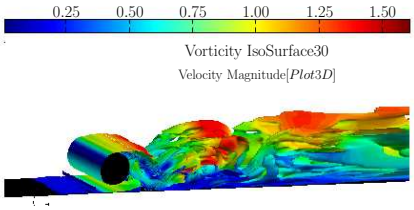

(a) $G^* = 0.11$

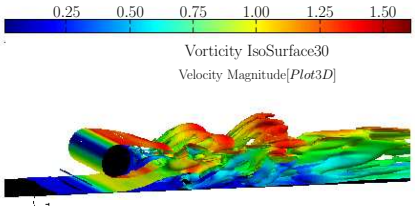

(b) $G^* = 0.21$

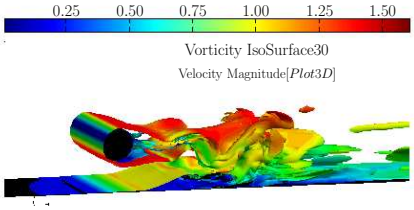

(c) $G^* = 0.53$

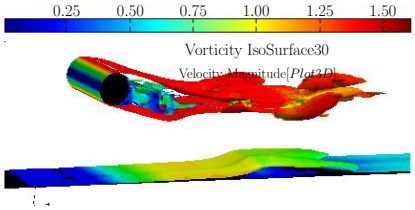

(d) $G^* = 1.00$

Figure 5-14. $d^* = 0.20$ Instantaneous iso-vorticity colored by velocity magnitude.

5.2.3 Turbulent Statistics

To understand the relative effects of the gap ratio on the wake and boundary layer interaction contours of the resolved Reynolds shear stress and line profiles illustrating the evolution of the resolved turbulent kinetic energy are presented in Figure 5-16 and Figure 5-17. A cylinder in subsonic freestream flow is known to exhibit symmetric turbulent stresses about the cylinder centerline in its wake with peak values in the center of both the upper and lower shear layers which is not evident for either rod diameter in this study. The turbulent kinetic energy profiles exhibit peaks at the inner and outer shear layer most notably at elevated gap heights where $G^* \geq 0.21$. The profiles remain largely asymmetrical even when the rod is placed completely outside the boundary layer. The compression and downward deflection of the cylinder wake due the presence of a well established shock on the free stream side of the wake are evident as the gap ratio is increased which changes the wakes development as discussed above. It is also worthwhile noting, the enhancement of

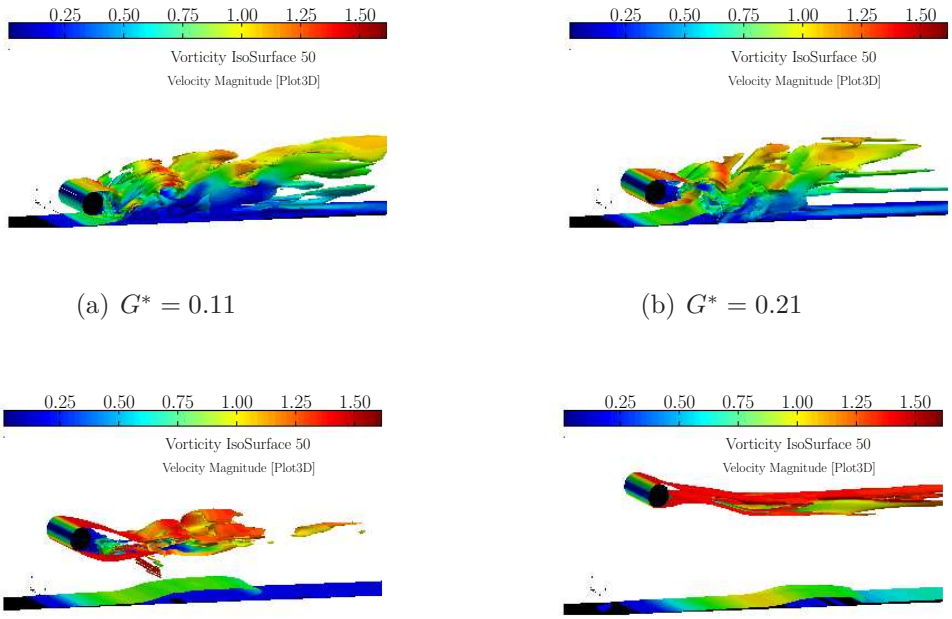

(a) $G^* = 0.11$ (b) $G^* = 0.21$

(c) $G^* = 0.64$ (d) $G^* = 1.29$

Figure 5-15. $d^* = 0.40$ Instantaneous iso-vorticity colored by velocity magnitude.

the turbulent stresses occurs along the trajectories of the inner and outer cylinder shear layer. As the gap ratio is increased above $G^* = 0.21$ for the small diameter rod this leaves relatively low values of shear at the wall. The large diameter rod wake results in elevated shear stress levels at the wall for gap heights as high as $G^* = 0.64$.

The evolution of the turbulent kinetic energy is illustrated in Figure 5-17 to highlight the influence of rod diameter and gap ratio. The enhancement of the turbulent fluctuations occurs along the trajectories of the wake of the cylinder as expected. The peak levels for all G^* values are similar comparing each rod diameter. The profiles mix out quickly for lower G^* values and the double hump survives longer for cases where the rod is moved further away from the wall. When either rod is placed near the wall the turbulent energy tends to be quickly spread out indicating the small turbulent structures induced from the rod shedding may be short lived.

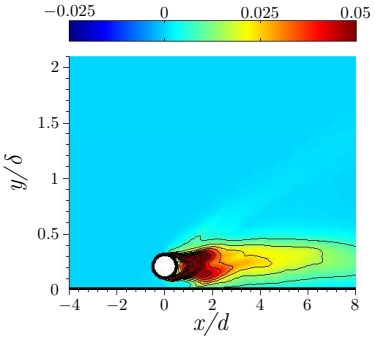

(a) $d^* = 0.20, G^* = 0.11$

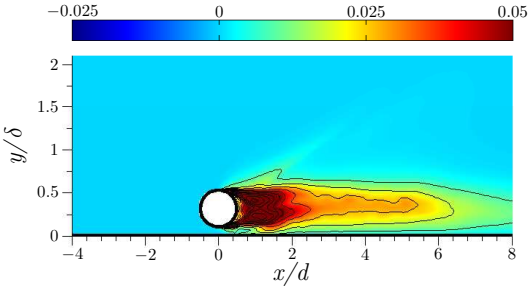

(b) $d^* = 0.40, G^* = 0.11$

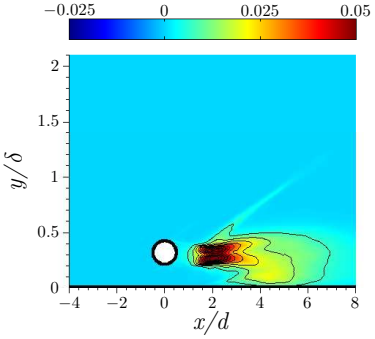

(c) $d^* = 0.20, G^* = 0.21$

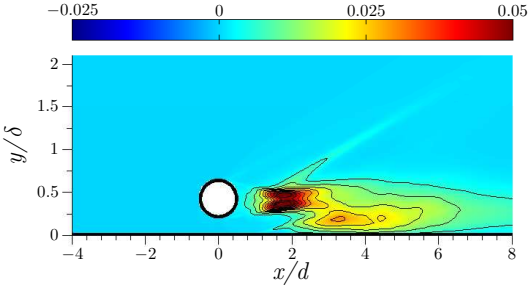

(d) $d^* = 0.40, G^* = 0.21$

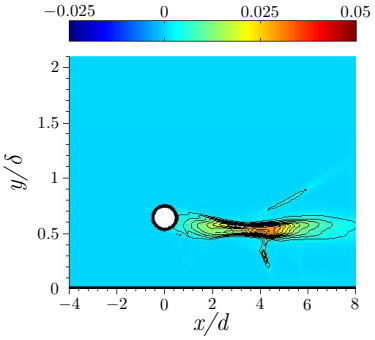

(e) $d^* = 0.20, G^* = 0.53$

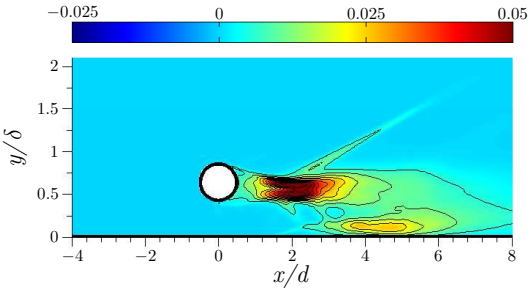

(f) $d^* = 0.40, G^* = 0.64$

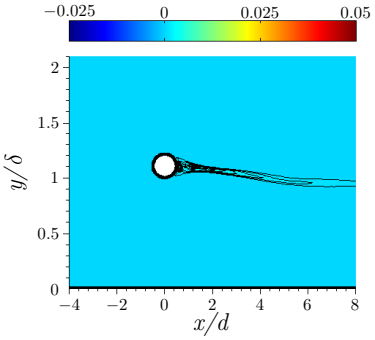

(g) $d^* = 0.20, G^* = 1.29$

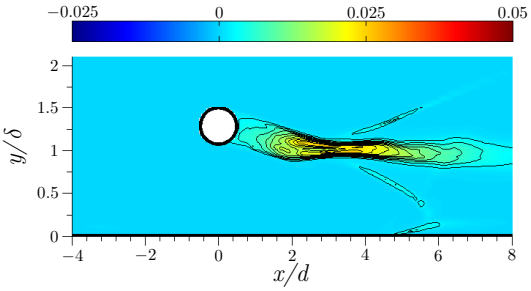

(h) $d^* = 0.40, G^* = 1$

Figure 5-16. Mean resolved $RSS = \frac{u'v'}{U_\infty{}^2}$ on z=0 plane.

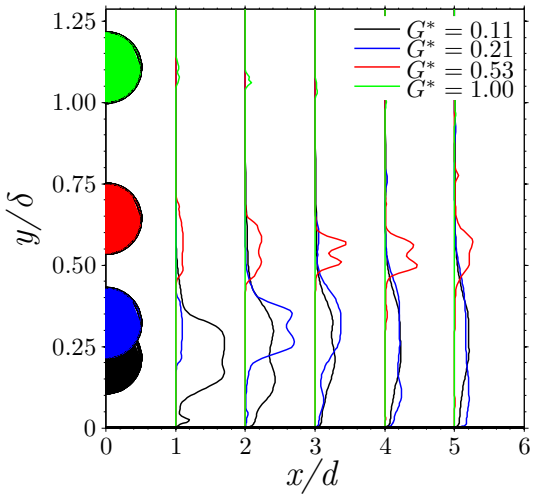

(a) $d^* = 0.20$

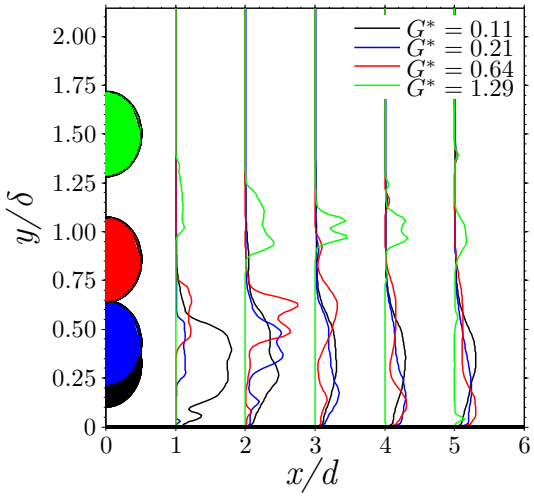

(b) $d^* = 0.40$

Figure 5-17. Mean resolved TKE profiles at given $\frac{x}{d}$ locations.

5.3 Summary

The numerical simulations presented in this chapter indicated that as the rod was raised above $G^* = 0.21$ there appeared to be cessation of the vortex shedding. Evidence was presented concurrently that the separated region of the cylinder increased in the streamwise and vertical direction as the rod is placed near the top of the boundary layer forcing the flow to turn more aggressively away from the wall. This suggests the rod may more effectively loft the near body flowfield of a cavity flow. The turbulent kinetic energy

profiles mix out quickly when the rod is near the wall. The turbulent velocity fluctuations survive longer for the large diameter rod when the rod is moved further away from the wall. When either rod is placed near the wall the turbulent energy tends to be quickly spread out. Coupling this with snapshots of the instantaneous vorticity contours it is believed the small turbulent structures induced from the rod shedding at low gap heights are short lived.

Strong vortical features are present when substantial mixing with the floor boundary layer is present which generally occurs for $\frac{G}{\delta} \leq 0.25$ with each rod. Cessation of well organized Von-Kármán type shedding was observed when the bottom of the rod neared the boundary layer sonic line which indicates the presence of a critical gap ratio.

CHAPTER 6
UNSTEADY PRESSURE MEASUREMENTS

In this chapter a detailed analysis of the experimentally measured surface pressure for both the full and finite span cavity will be performed using techniques outlined in Chapter 2. The streamwise direction is taken to be the x-direction while the y-direction is normal to the floor of the wind tunnel for all of the discussions. The zero point in the coordinate system is located on the leading edge of the cavity at the span midpoint. The free stream Mach number was 1.44 for all cases and the pertinent flow conditions are listed in Table 3-2.

6.1 Full and Finite Span Baseline Cavity Comparison

The full and finite span cavity unsteady pressure measurements are compared in this section. The major advantage of the full span cavity was the ability to acquire higher fidelity PIV measurements and may therefore be very useful to study if the suppression mechanisms are the same. Previous research by Ahuja & Mendoza (1995) and Block (1976) have suggested that the flowfield for cavities whose length to width ratio is less than one is predominately two dimensional in nature. The length to width ratio for the finite span cavity in this research is three so one expects the flow to be highly three dimensional. Ahuja & Mendoza (1995) have reported that the length to width ratio has little effect on the resonant frequencies even though the flow patterns might be different. They further demonstrated up to a 15dB decrease in the overall sound pressure levels on the finite span cavities when compared to the full span models. They concluded it is possible to compare two dimensional computational aeroacoustic analysis with experiments conducted on a three dimensional cavity.

The baseline spectra of the fluctuating surface pressure measured on the aft wall and floor of each cavity are presented in Figure 6-1(a) through Figure 6-1(d). The PSD is plotted as a function of frequency and Strouhal number respectively for the aft wall measurements. The spectra exhibit multiple peaks which are reasonably well estimated

using the modified Rossiter equation with default constants $k_c = 0.57$ and $\alpha = 0.25$ and are tabulated in Table 6-1. The largest difference between the observed resonant tones and estimated frequencies using the modified Rossiter equation was 8.6% found at the first resonant tone. The differences are not alarming due to the somewhat generic nature of the constants in the empirical equation that were derived from subsonic experiments and may need to be slightly readjusted to precisely estimate the frequencies for these flow conditions. The spectra are also plotted against Strouhal number where the first resonant peak occurs at $St = 0.28$ for each cavity. The dominant peak occurs at $St \approx 0.60$ for the three dimensional cavity and at $St \approx 0.97$ for the full span cavity which correspond to the second and third resonant tones respectively.

Table 6-1. Rossiter resonant tone predictions.

Tone(kHz)	1	2	3	4	5
Experiment	1.51	3.29	5.27	7.21	8.56
Rossiter	1.38	3.22	5.06	6.90	8.73

The RMS values of the fluctuating surface pressure on the cavity floor are plotted in Figure 6-2 and is representative of the fluctuating pressure levels integrated over all frequencies. The unsteady surface pressures behave as expected with the highest fluctuating pressures on or near the aft wall and constantly tapering off to a until $\frac{x}{L} = 0.25$. The pressures rise again near the forward wall. The observed reduction in pressure fluctuations between the finite and full span cavity is consistent with the findings reported by Ahuja & Mendoza (1995) and Block (1976).

Figure 6-3(a) and Figure 6-3(b) show the correlation coefficients plotted against time lag for the aft wall sensor (the reference signal) correlated with itself and locations $\frac{x}{L} = 0.25, 0.50, 0.75$ on the cavity floor for both baseline cavities. The plots have been truncated to investigate small time separations. The full time history plot would show steadily decaying oscillations. These plots show increased correlation magnitudes for the full span cavity at each position inside the cavity with little damping of the peaks. The

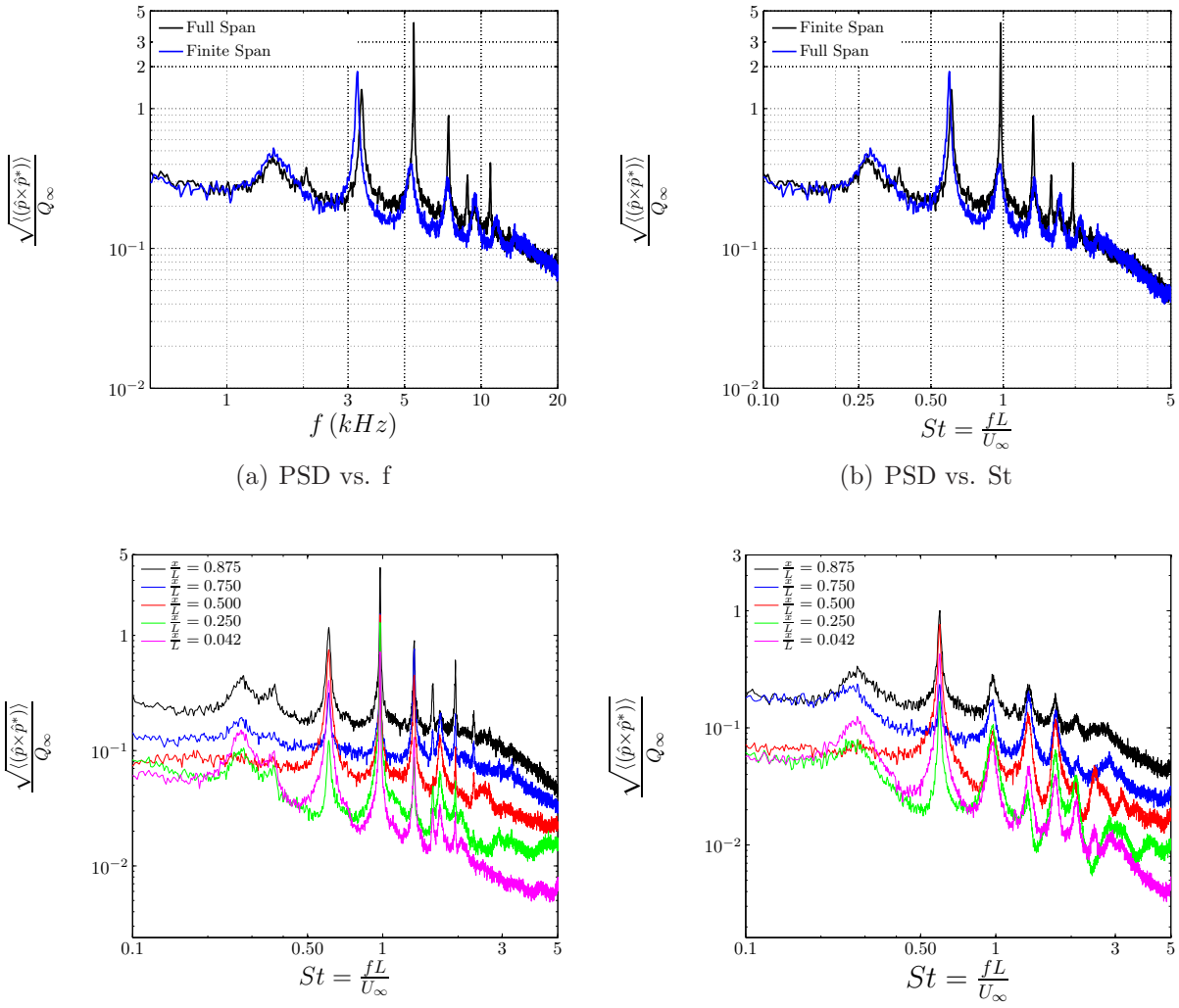

(a) PSD vs. f

(b) PSD vs. St

(c) Full Span

(d) Finite Span

Figure 6-1. Full and finite span baseline PSD comparison. Aft wall measurements are given in the first row taken at $\frac{y}{D} = -0.5$ as a function of frequency and Strouhal number respectively. The second row gives the PSD measured on each cavity floor at various axial locations plotted against Strouhal number.

increased damping observed in the finite span cavity is likely due to the increased cross-flow found in the downstream portion of the cavity which will be further demonstrated in Chapter 7 and Chapter 8. The highly resonant phenomena of the cavity which manifests itself as the nearly sinusoidal oscillations are also apparent in these plots. The coherence function, as defined by Equation 2–15, is illustrated in Figure 6-3(c) and 6-3(d) for both baseline cavities. The plots indicate a highly correlated pressure signal near the trailing

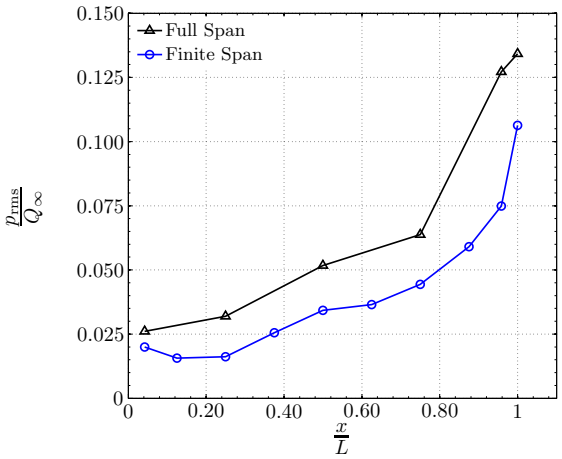

Figure 6-2. Full and finite span baseline p_{rms} on the cavity floor.

edge of the cavity floor with the reference signal taken from the aft sensor. The large amplitudes of the coherence function occur identically to the frequencies associated with the peaks observed in the aft wall spectra, i.e., the Rossiter resonant frequencies. This would indicate that the generation of the disturbance inside the cavity and the resonant tones observed in the cavity evolve as the result of disturbances propagating upstream from the aft wall. The signals become slightly less correlated, as noticed by the decreasing peaks, moving further upstream on the cavity floor. The low coherence observed at off peak frequencies suggest the broadband levels may be insensitive to the resonance-coupling phenomena. The distinct resonant tones observed in the cavity are tightly coupled with the resonant conditions created by the shear layers interaction with the aft wall. The broadband levels exhibit poor correlation which is likely due to the random turbulent features of the supersonic flowfield.

It is evident from the presented spectra and coherence functions that the resonant tones exist at different frequencies and the distribution of the power across the frequencies differs. One limitation of time averaged frequency spectra is it is not capable of distinguishing whether the resonant tones coexist or experience mode switching where the dominant tone shifts in frequency with time. Joint time-frequency analysis provides information containing frequency, time and amplitude. This allows one to visualize the

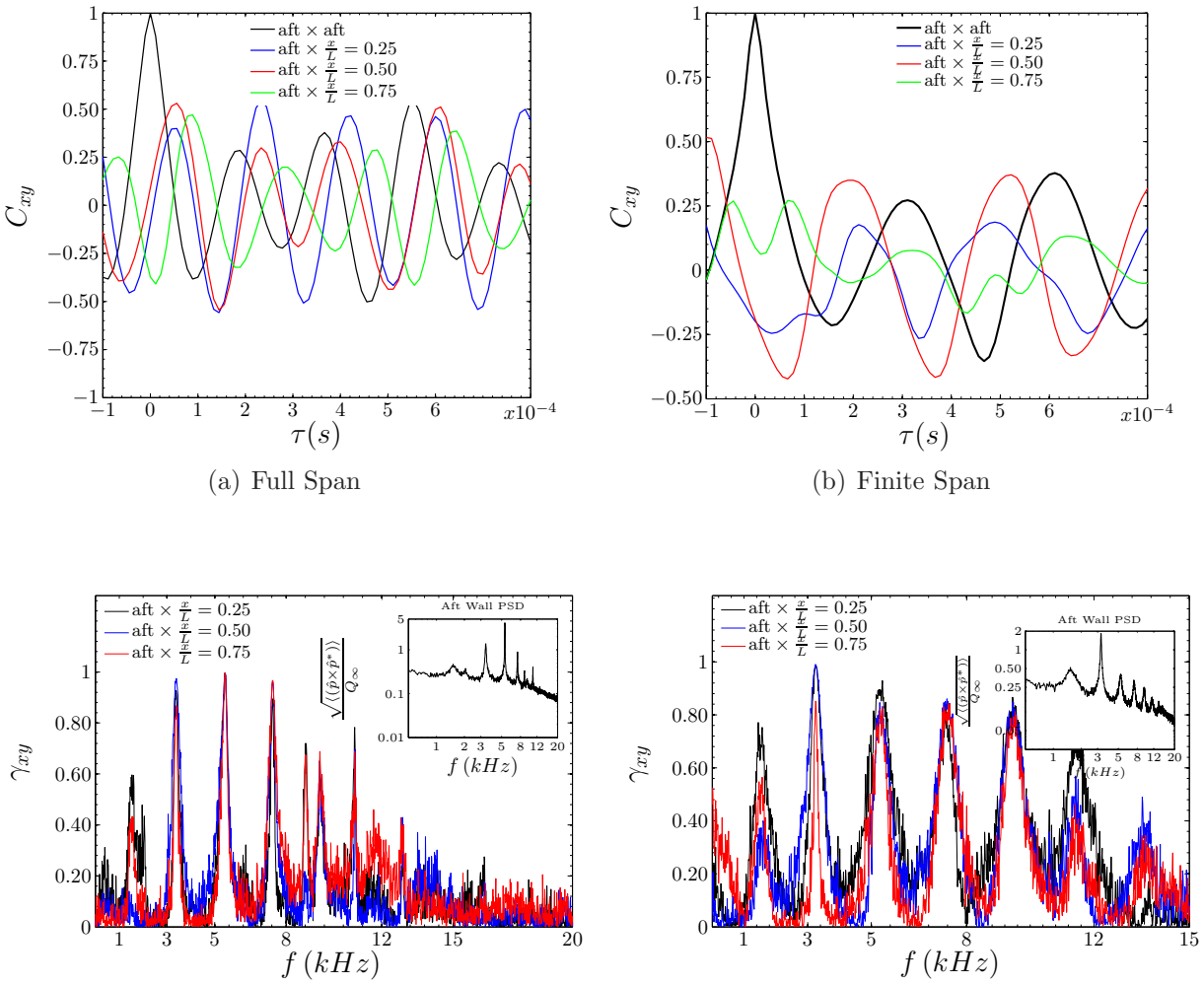

(a) Full Span

(b) Finite Span

(c) Full Span

(d) Finite Span

Figure 6-3. Baseline cavity surface pressure cross-correlation and cross-coherence coefficients. The aft wall sensor is the reference signal.

time-evolution of the frequency content and has been used successfully by Kegerise *et al.* (2004) and Murray & Ukeiley (2007) for subsonic cavity flow. The resulting spectrograms for the unsteady aft wall pressures acquired from the full and finite span cavity are plotted in Figure 6-4(a) and 6-4(b) respectively.

The spectrograms are illustrated in Figure 6-4 where the magnitude is normalized by $PSD^* = \frac{PSD}{\max(PSD)}$. Examining the figure it is noticed that six resonant tones exist for each cavity. The dominant tone shifts between the second and third tone when

comparing the finite and full span cavity respectively. The first resonant tone of each cavity appears intermittently. The second tone's presence is strong during the complete time history while the third is present for the whole time history in the full span cavity only and appears intermittently for the finite span cavity. The fourth tone exhibits a strong presence for the majority of the time history for the full span cavity only. The fifth and sixth resonant tones show a weak intermittent presence for each cavity. There is no evidence of mode switching of the dominant tone when examining the time history of each cavity as it is always present. All other resonant tones appear to be present with varying degrees of intensity with time.

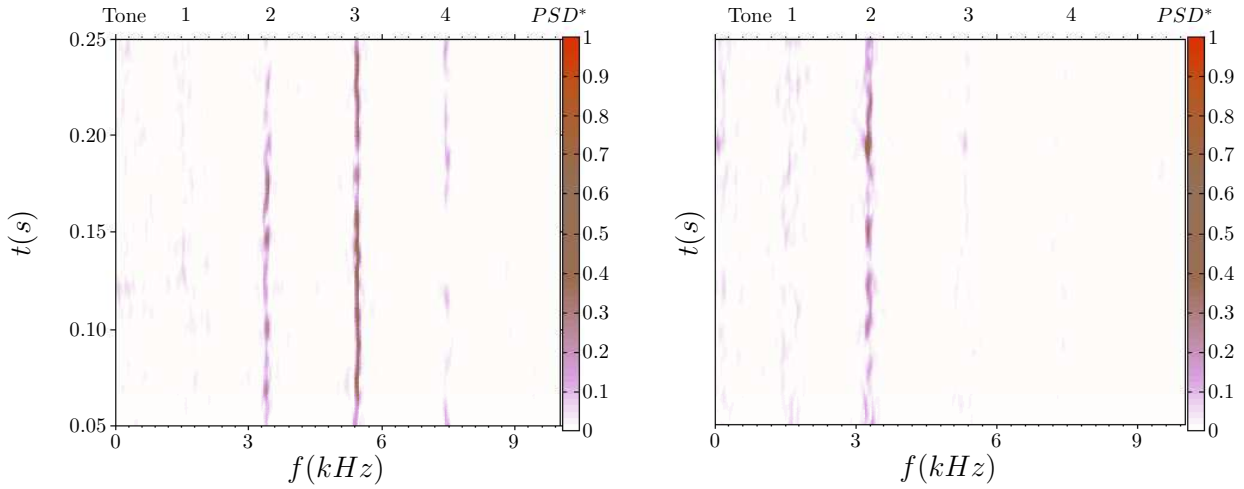

(a) Full Span (b) Finite Span

Figure 6-4. Full and finite span spectrograms measured on the aft wall.

6.2 Finite Span Cavity with Suppression

The experiments to suppress the fluctuating surface pressure inside the finite span cavity were run with five rod diameters and multiple heights off the wall as illustrated in Table 6-2. A thick wall 25.4mm long hollow cylinder made of 304 stainless steel was selected for each rod diameter. The hollow cross section was selected to ensure the natural frequency of the rods were above the dominant peaks realized in the baseline spectra. The detailed calculations and geometric and material properties of the rod can be found in Appendix-B.

Table 6-2. Finite span cavity configurations.

d^*	G^*
0.21	0, 0.18, 0.36, 0.54, 0.71, 0.86^{++}, 0.96^{**}
0.43	0, 0.18, 0.36, 0.54, 0.64^{++}, 0.86^{**}
0.57	0, 0.18, 0.36, 0.54^{++}, 0.79^{**}
0.79	0, 0.18, 0.29^{++}, 0.68^{**}
0.89	0, 0.18^{++}, 0.63^{**}

$^{++}$ top of rod at top of boundary layer
$**$ centerline of rod at top of boundary layer

6.2.1 Effects of Rod Mounts

In order to isolate the effects of the physical hardware necessary to hold the rod in place a series of experiments were conducted with only the rod mounts in place, i.e., no circular rod present. The mounting structures were placed in the tunnel with the cavity and two cases were considered. In the first case the top of the mounting structure was placed as close to the floor as possible, corresponding to a rod with $d^* = 0.21$ and $G^* = 0$. The second case was run where the structure was fully extended leading to a maximum gap height with a rod of diameter $d^* = 0.43$. Figure 6-5 illustrates the aft wall PSD and floor p_{rms} for the baseline cavity and the cavity with only the mounting structure present.

Examining Figure 6-5 it is clear that the ability of the isolated rod mounts to suppress the cavity pressure fluctuations does not exist. At each position the rod mounts actually increased both the peak and broadband levels in these spectra. When the mounts were located near the floor the broadband levels were slightly higher with a noticeable jump in the dominant peak tone while the higher frequency peaks remained largely unaffected. When the mounts were fully extended the peaks at the higher frequencies were increased and the broadband levels were significantly raised.

Examining the p_{rms} profiles on the cavity floor from Figure 6-5(c) there was little evidence supporting the mounts alone had the capability to reduce the average fluctuating surface pressures and actually tended to increase the fluctuations for each position.

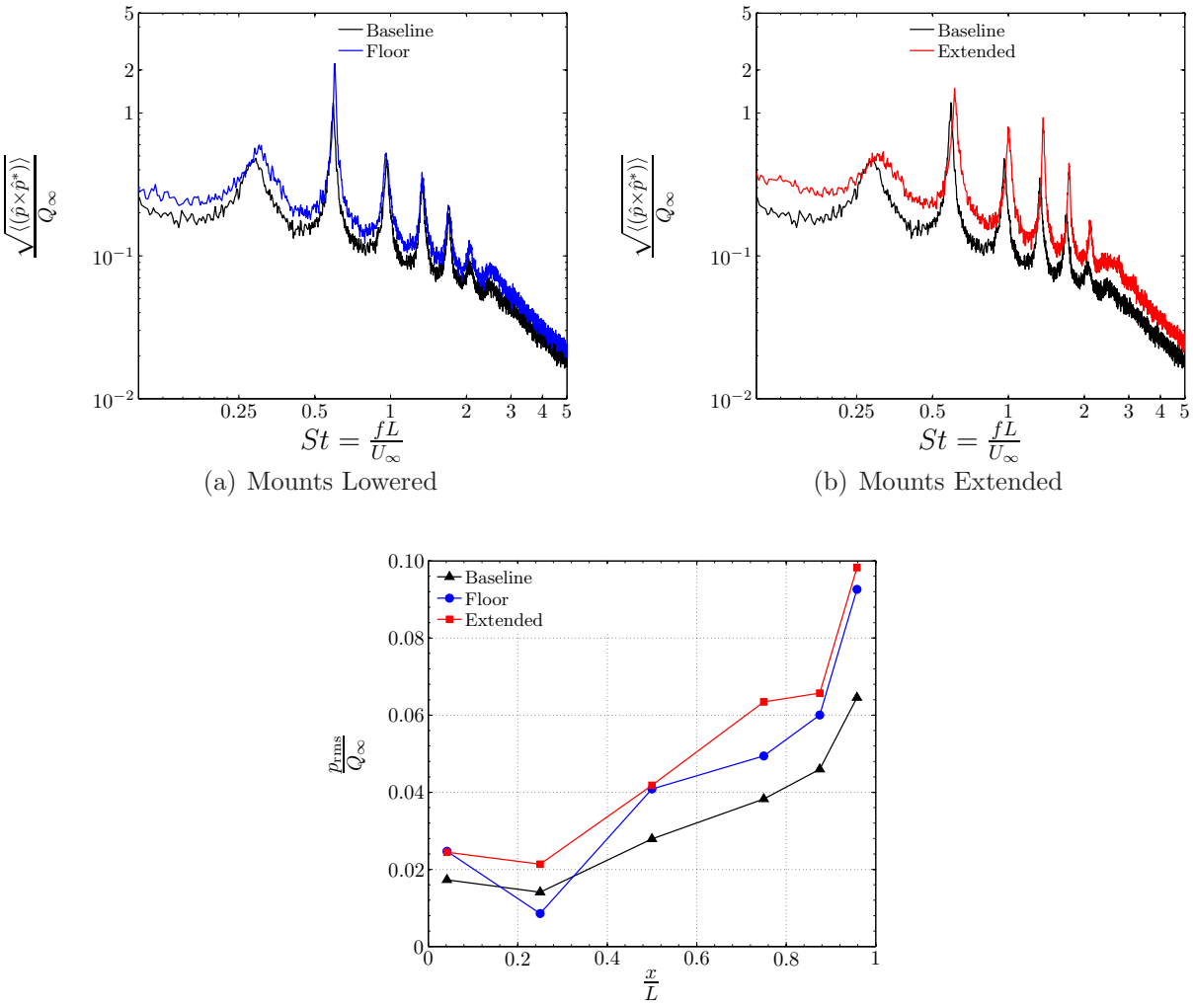

(a) Mounts Lowered

(b) Mounts Extended

(c) Floor

Figure 6-5. Effect of rod mount position with no rod present on the finite span cavity fluctuating surface pressures. Aft wall PSD taken at $\frac{y}{D} = -0.5$ and floor $p_{\rm rms}$ at various streamwise locations.

Figure 6-6 illustrates the mean Schlieren image for each case presented and qualitatively demonstrates that there is little difference on the broadening of the shear layer over the cavity. Noting the excitation of the peak tones and increase in broadband levels with only the mounts present, the suppression levels and efficacy of the rod appear to be even more impressive.

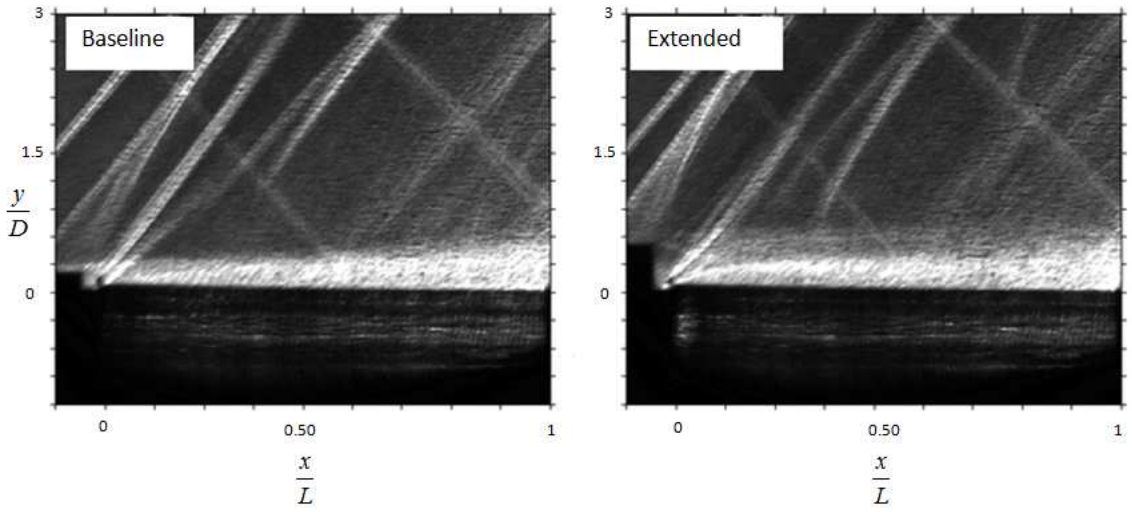

Figure 6-6. Qualitative assessment of the effect of the rod mount position on the mean shear layer thickness using mean Schlieren gradients.

6.2.2 Effects of Rod Diameter and Gap Height

The effects of rod diameter and gap height on the fluctuating surface pressures which include power spectral density measurement, p_{rms} profiles and correlation analysis are presented in this section. Figure 6-7(a) and 6-7(b) illustrates the effect of the rod diameter on the fluctuating surface pressures measured on the aft wall. Each diameter is plotted with the top of the rod placed near the top of the boundary layer which was found to be the most effective rod placement.

With rods sized greater than 40% of the boundary layer height the overall peak tones measured on the aft wall were effectively reduced and in general, the larger the rod the better the suppression though the differences were small. The most notable difference in the effect of rod diameter was on the fluctuating surface pressure measured on the cavity aft wall and floor. The most effective sized rod was found to be $d^* = 0.43$ when considering the combines suppression on the aft wall and floor measurements. Rods with larger diameters were not as effective at suppressing the fluctuating pressures on the cavity floor. Figure 6-8(a) through 6-7(j) are added for completeness where the power spectral density and p_{rms} plots for each rod diameter at each placement in the boundary layer are illustrated.

The finding that a rod sized approximately 50% of the boundary layer height and placed such that the top of the rod is near the edge of the boundary layer, provides the most effective suppression is consistent with the subsonic experiments by Stanek (2005), Smith *et al.* (2002) and both subsonic and supersonic experiments conducted by Ukeiley *et al.* (2004*a*). They each concluded that a rod on the order of 50%δ was recommended for effective suppression characteristics. Each rod (other than the smallest rod) examined demonstrated the ability to effectively lower the resonant tones to near the broadband levels as shown in Figure 6-7. The overall surface pressure reduction on the aft wall reached over 60% for the most effective cases while the least effective cases still exhibited reductions of just over 50%.

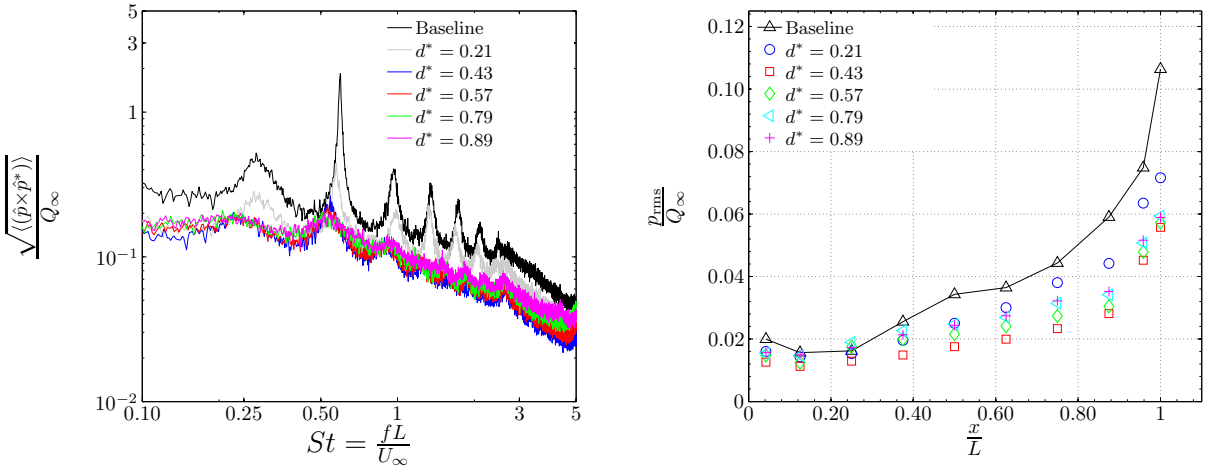

(a) PSD (b) $p_{\rm rms}$

Figure 6-7. Fluctuating surface pressures based on rod diameter with fixed gap height with the top of the rod at $\frac{y}{\delta} = 1$. PSD measured on the aft wall at $\frac{y}{D} - 0.5$ and $p_{\rm rms}$ taken on the cavity floor at various axial positions.

Further examination of the plots presented in Figure 6.2.2 allow for more trends to be observed. In general, as the rod diameter increased the peak tones were more sufficiently suppressed up to the point where the top of the rod reached the top of the boundary layer. As the rods were brought partially outside the boundary layer the reductions measured on the aft wall began to taper off. The overall suppression increased sharply between rod diameters of 20-40% of the boundary layer thickness. The effectiveness of the rods for

reducing the fluctuating surface pressures on the aft wall remained largely insensitive to rod diameter thereafter. The notable difference was measured on the cavity floor where rods exceeding 50% of the boundary layer thickness were not capable of reducing the floor pressure fluctuations as efficiently. It should be noted that due to the limited sampling rate of the A/D converter the pressure signal was not recorded at a frequency where pressure fluctuations associated with the rod shedding could be resolved. This may slightly bias the results as the self noise of the control actuation is not included. However one would not expect the distinct tones from the shedding to have a strong presence in the spectra all the way to the aft wall and is demonstrated with the numerical simulations found in Chapter 8.

Correlation plots for the suppressed cases are presented in Figure 6-8(a) through Figure 6-8(f). The baseline correlation is also repeated for convenience. Examining the autocorrelation for each case it is easily noted that the maximum correlation coefficient occurs at zero time lag whereas for other time lags the correlation is much weaker, particularly for rods greater than $d^* = 0.21$. The moderate negative correlation that exists for the $d^* = 0.21$ rod near the cavity leading edge indicated the pressure signals are inversely related. This indicates that for a pressure rise on the cavity aft wall there tends to be a drop in pressure towards the leading edge of the cavity and vice-versa. For rods where $d^* \geq 0.43$ the correlation becomes poor and the oscillations have nearly completely damped except at zero lag for the autocorrelation.

The coherence function of the pressure signals for the baseline and suppressed cavities are presented in Figure 6-9(a) through Figure 6-9(f). The aft wall spectra is superimposed on each figure for convenience. The coherence plot for the $d^* = 0.21$ case shows relatively strong coherence with coefficients exceeding 0.80 for most resonant tones evident in the spectra even as one progress towards the cavity leading edge. This is consistent with what was previously illustrated with the cross-correlation plots. The tones measured on the aft wall were not effectively reduced for this configuration which suggests little was

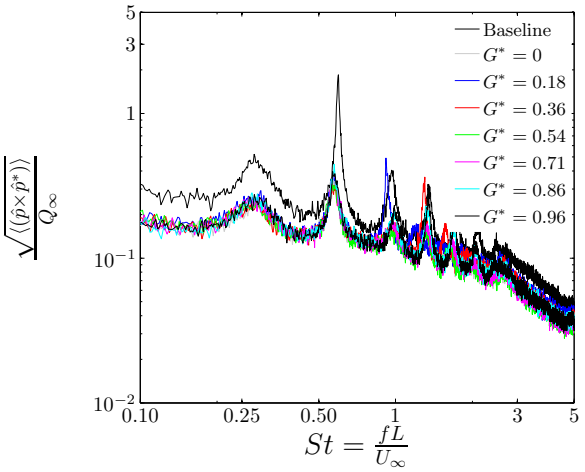

(a) $d^* = 0.21$

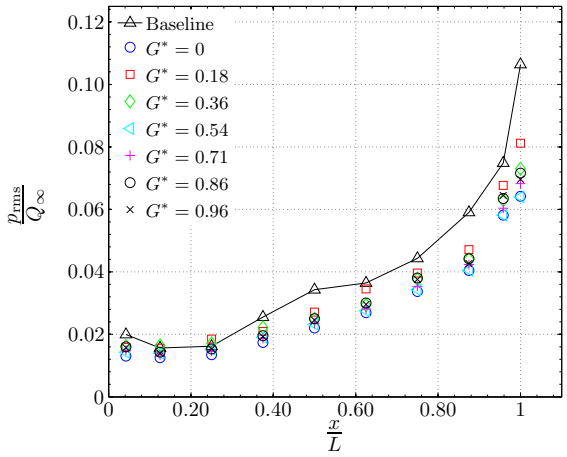

(b) $d^* = 0.21$

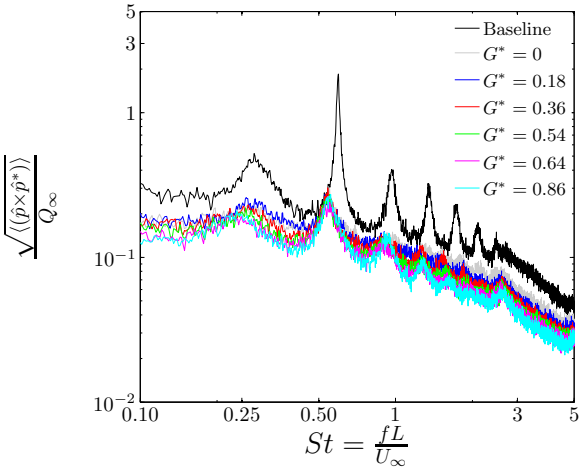

(c) $d^* = 0.43$

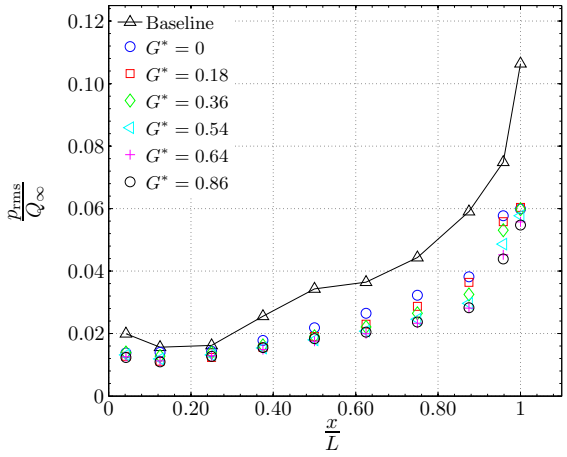

(d) $d^* = 0.43$

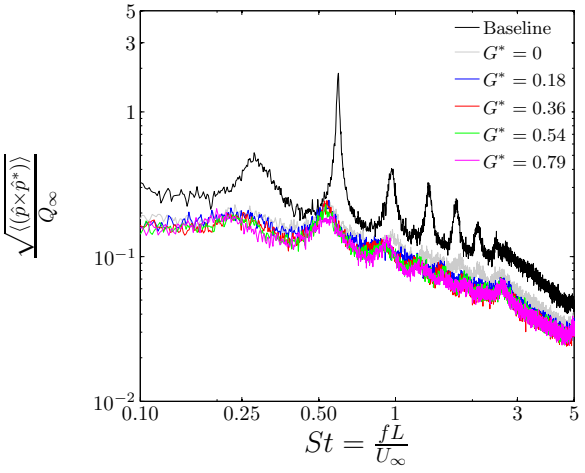

(e) $d^* = 0.57$

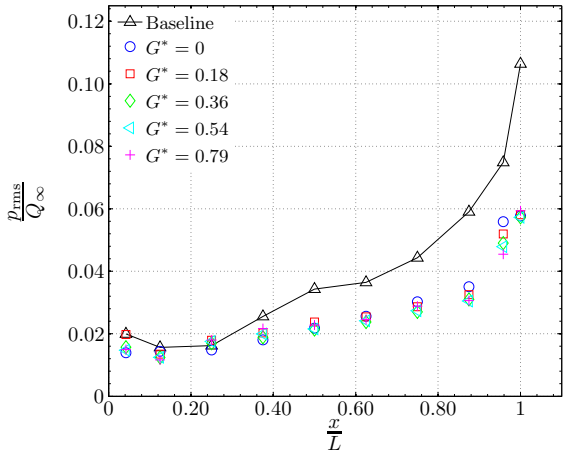

(f) $d^* = 0.57$

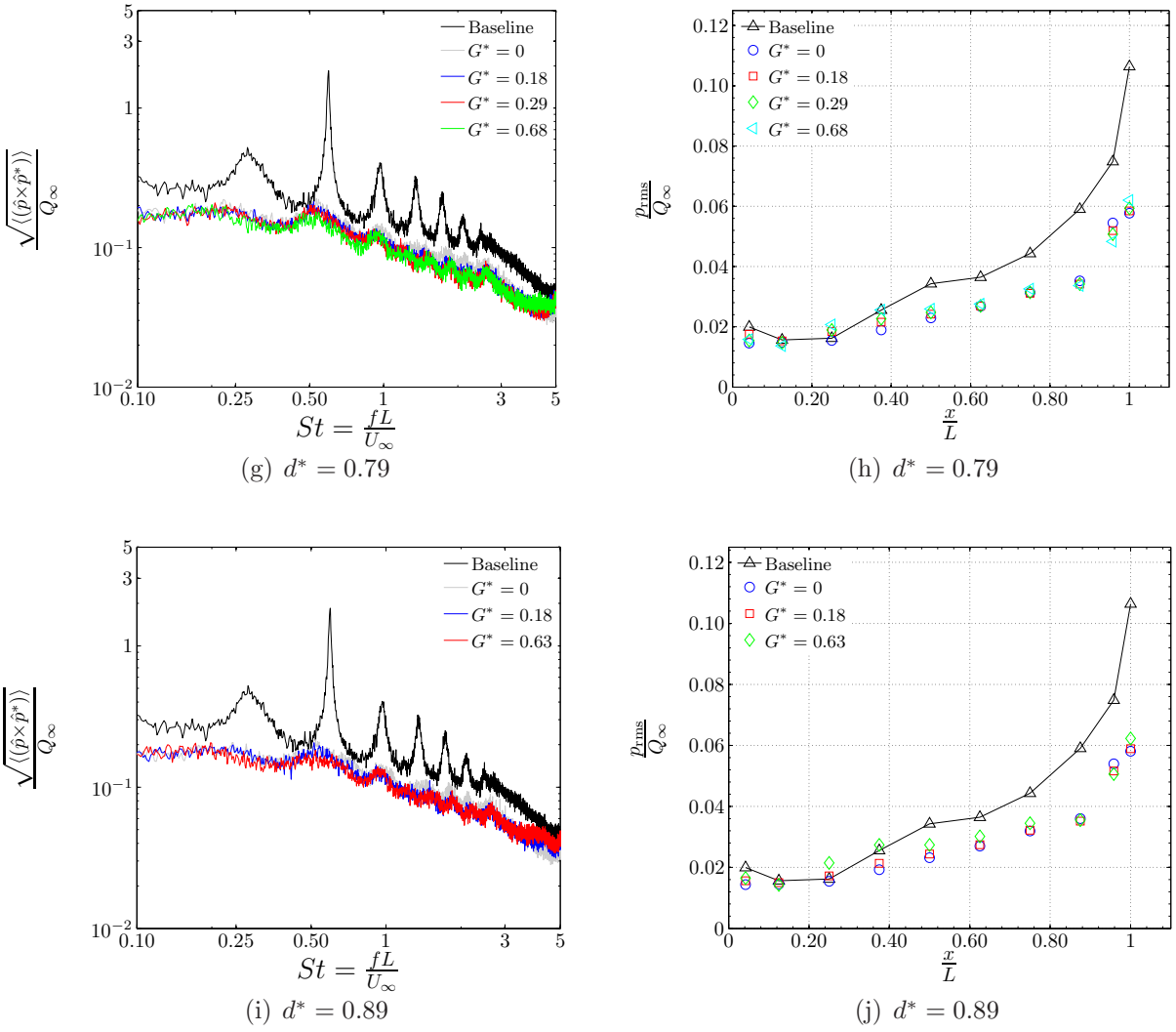

Figure 6-7. Fluctuating surface pressures based on rod diameter and gap height. First column is aft wall PSD measured at $\frac{y}{D} = -0.5$. Second column is p_{rms} taken on the cavity floor.

done to disturb the feedback mechanism. As the rod diameter increased to $d^* \geq 0.43$ the magnitudes of the coherence fall significantly coinciding with a broadening and lowering of the peaks measured on the cavity aft wall spectra. In contrast to the small diameter rod, this strongly supports that feedback mechanism or even the receptivity of the shear layer itself, has been disturbed thereby reducing the amplification of the resonant tones realized on the aft wall.

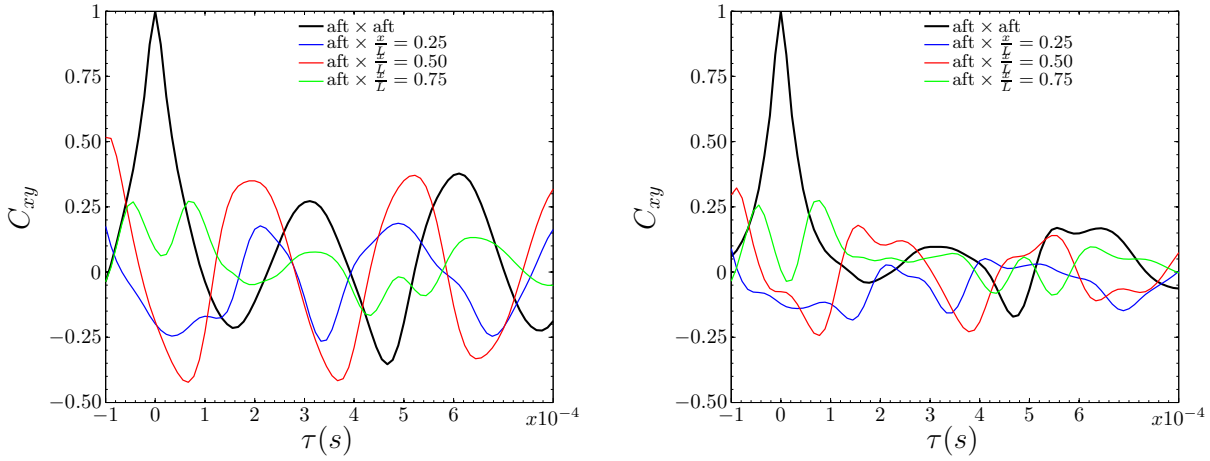

(a) Baseline

(b) $d^* = 0.21$

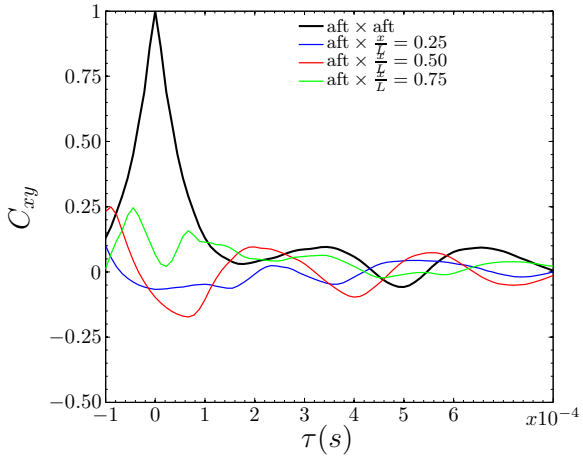

(c) $d^* = 0.43$

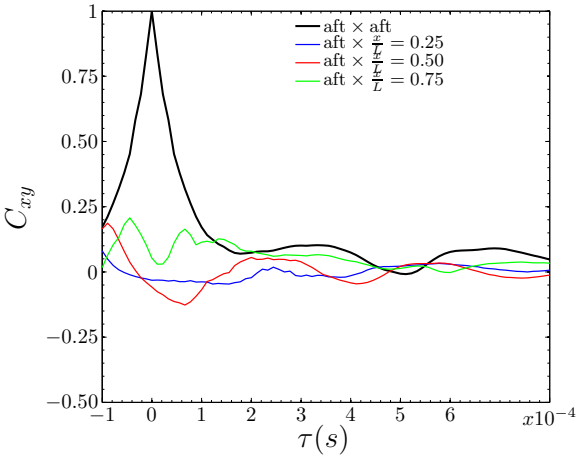

(d) $d^* = 0.57$

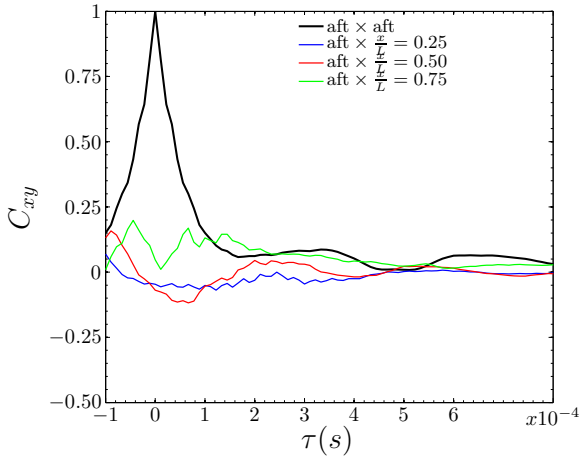

(e) $d^* = 0.79$

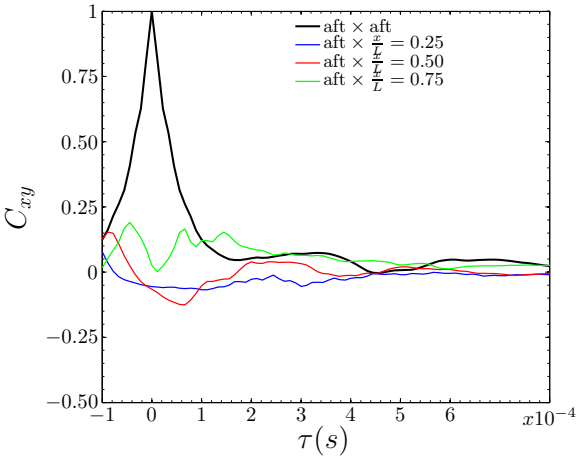

(f) $d^* = 0.89$

Figure 6-8. Cross-correlation coefficient for top of rod near top of boundary layer at selected axial positions on the cavity floor. Reference signal is taken from aft wall sensor.

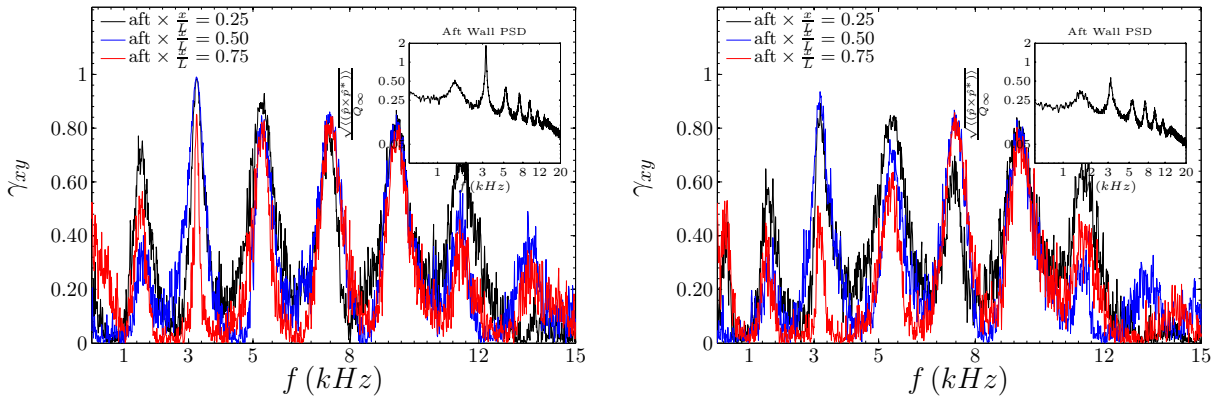

(a) Baseline

(b) $d^* = 0.21$

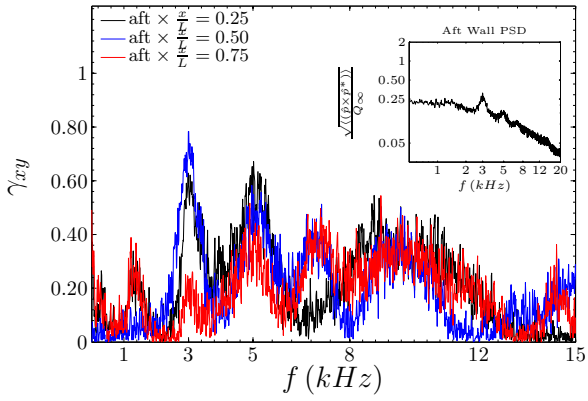

(c) $d^* = 0.43$

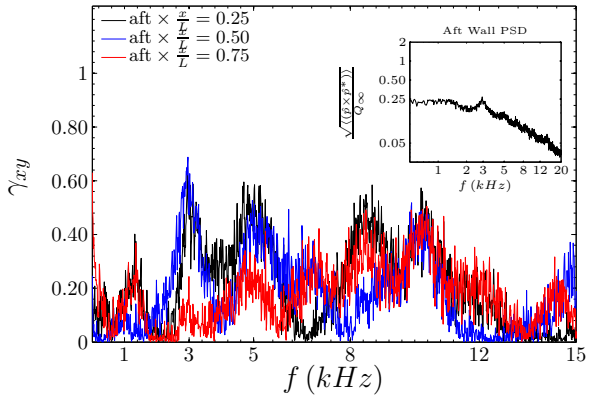

(d) $d^* = 0.57$

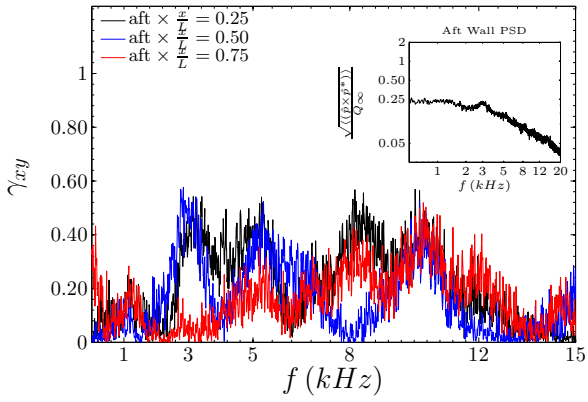

(e) $d^* = 0.79$

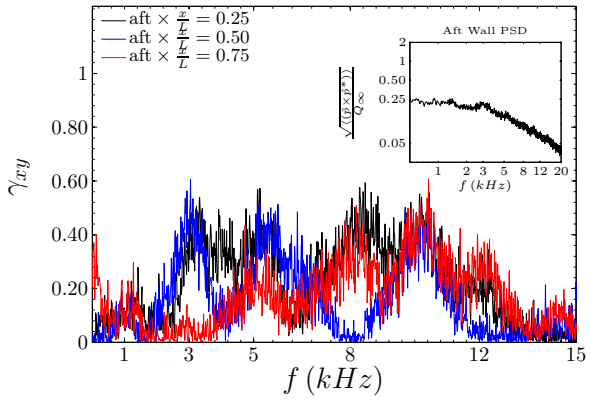

(f) $d^* = 0.89$

Figure 6-9. Cross-coherence coefficient for top of rod near top of boundary layer at selected axial positions on the cavity floor. Reference signal is taken from aft wall sensor.

The spectrogram for the most effective rod diameter is plotted at selected gap heights in Figure 6-10(a) − 6-10(d). The presence of the rod lowered the highest resonant tone to near the broadband levels throughout the entire time domain independent of gap height. Resonant tones three through six were drastically lowered when the rod was resting on the floor. The second tone still was still apparent for the suppressed configurations at lower magnitude and slightly more intermittently with time. Examining the spectrogram at any gap height, the power appears to be dispersed between frequency bands with the presence of the rod. Based on these results, how effectively the power is dispersed appears to be a function of the rod gap height.

6.3 Full Span Cavity with Suppression

The controlled full span cavity experiments were run with two gap heights for two rod diameters corresponding to $d^* = 0.21$ with $G^* = 0.08, 0.79$ and $d^* = 0.43$ with gap heights $G^* = 0.08, 0.59$. The two gap heights selected were based on the least and most effective placements of the rods from the finite span pressure measurements. The first position was such that the bottom of the rod was near the floor and the second was placed such that the top of the rod was near the top of the boundary layer. Some care was taken when considering the selection of rod length and material for the full span cavity. The method determining the selection of the rod material, cross-section and length followed suit with what was previously done for the finite span cavity. The length of the rod was increased by 12.7mm in an attempt to maintain the full span effect as best as possible. This reduced the deflection resistance of the rod when compared with the finite span cases. A thick wall 38mm long hollow cylinder made of 304 stainless steel was selected. A maximum length rod that minimized bending was preferred to reduce mounting and deflection effects. The minimum deflection based on elastic beam bending analysis for the smallest rod was $< 25\%$ of δ (roughly one rod diameter) and under 5% of δ for the large diameter rod based on freestream loading conditions. The hollow cross section was selected to ensure the natural frequency of the rods were above the dominant peaks realized in the baseline

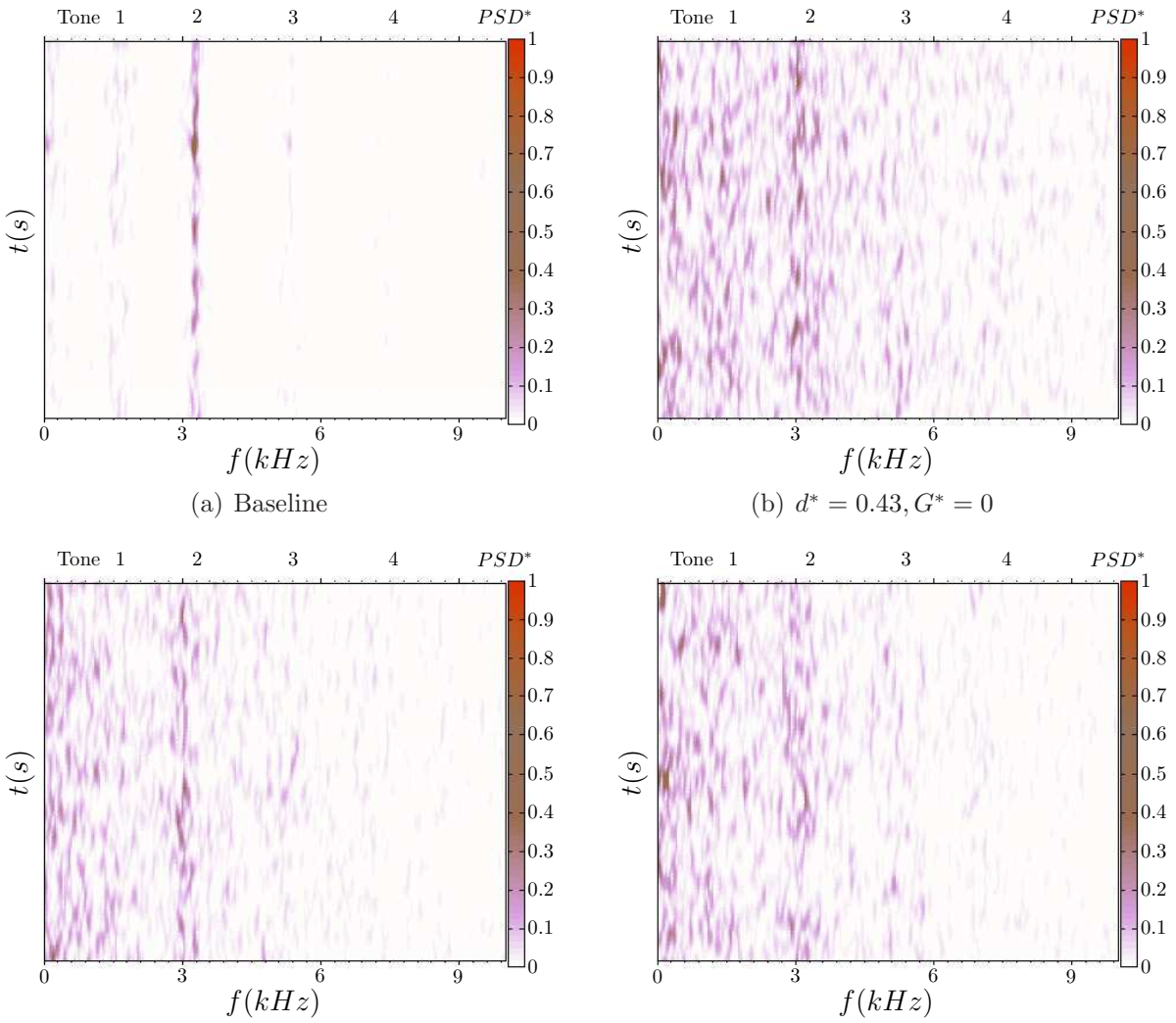

(a) Baseline

(b) $d^* = 0.43, G^* = 0$

(c) $d^* = 0.43, G^* = 0.36$

(d) $d^* = 0.43, G^* = 0.64$

Figure 6-10. Finite span cavity aft wall spectrogram for $d^* = 0.43$ at selected G^* values.

spectra. The full calculations, equations, geometric and material properties of each rod can be found in Appendix B.

The fluctuating surface pressured measured on the full span cavity aft wall and floor are presented in Figure 6-11(a) and Figure 6-11(b) respectively. The results are analogous to the finite span cavity presented above where the most effective placement of the rod was at the top of the boundary layer and the larger diameter rod outperformed the smaller rod. Both peak and broadband suppression levels were increased with the full span cavity

which is likely an effect of a better established feedback mechanism in the baseline cavity.

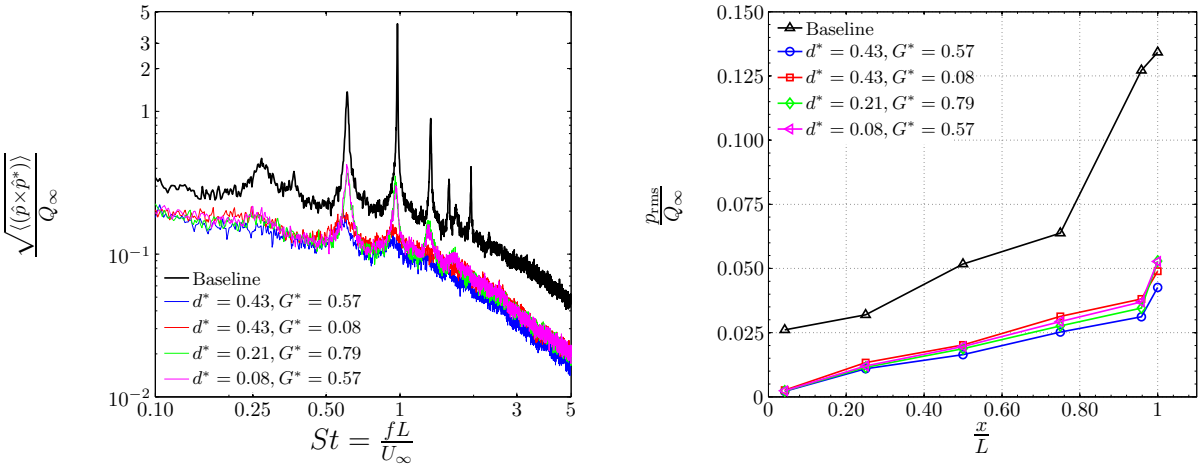

(a) PSD (b) Floor

Figure 6-11. Full span baseline and controlled fluctuating surface pressures measured where the PSD is measured on the aft wall at $\frac{y}{D} = -0.5$ and $p_{\rm rms}$ is measured at various streamwise locations on the cavity floor.

Plots of the cross-correlation for the suppressed cases are presented in Figure 6-12(a) through Figure 6-12(e). Comparing the baseline and controlled cases the findings are nearly identical with the finite span cavity. The full span cavity showed increased correlation levels at each $\frac{x}{L}$ position inside the cavity likely due to the absence of the flow entering the cavity from the sidewalls. The correlation and coherence plots indicate a larger disruption of the feedback loop as the rod increases in size.

Plots for the cross-coherence coefficient are illustrated in Figure 6-13(a) through Figure 6-13(e). Comparing the baseline and controlled cases for the cross-coherence coefficient the findings are again nearly identical as reported for the finite span cavity. The baseline plot shows well correlated peaks at each resonant tone found on the aft wall PSD figure as expected. The split tone found at the fifth peak (located at $9 - 10$kHz) from the PSD plots stands out clearly in the coherence plot. Larger diameter rods again appear to disrupt the feedback loop with decreased correlations with increasing diameter. There were only minor changes based on the rod gap height.

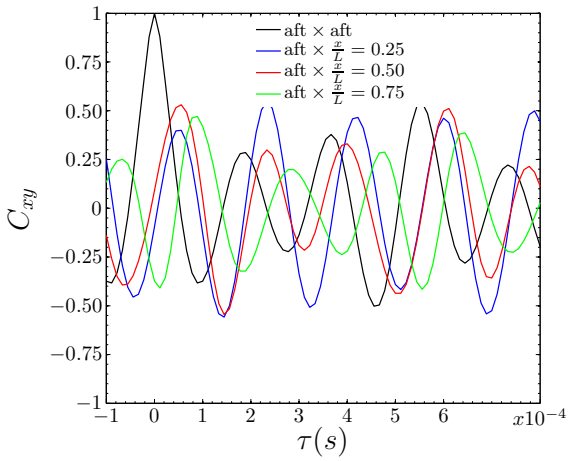

(a) Baseline

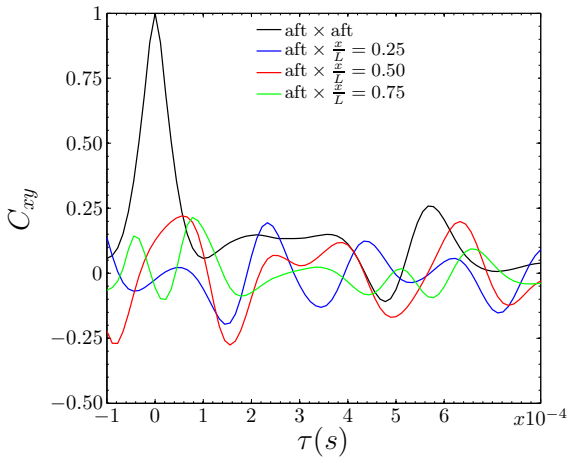

(b) $d^* = 0.21, G^* = 0.08$

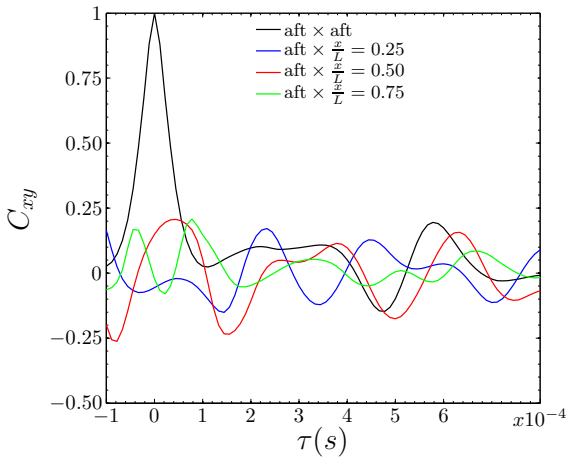

(c) $d^* = 0.21, G^* = 0.79$

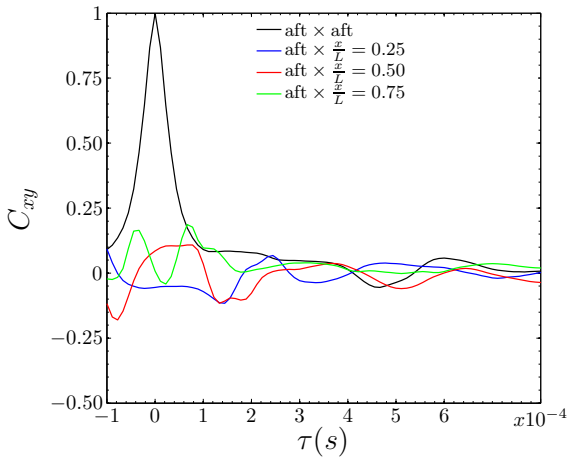

(d) $d^* = 0.43, G^* = 0.08$

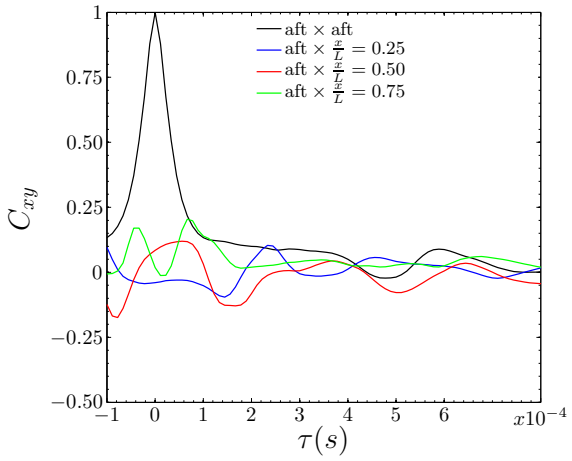

(e) $d^* = 0.43, G^* = 0.57$

Figure 6-12. Full span cavity cross-correlation at selected axial positions on the cavity floor. Reference signal is taken from aft wall sensor.

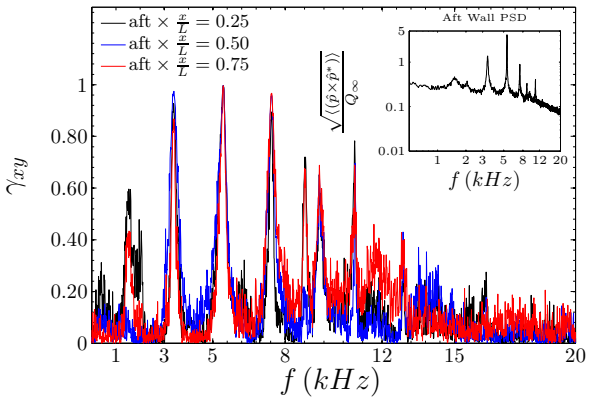

(a) Baseline

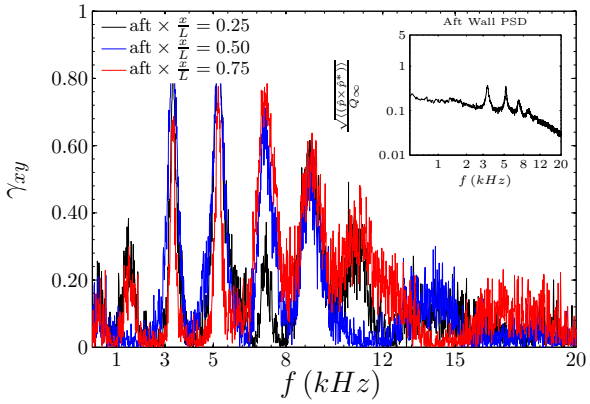

(b) $d^* = 0.21, G^* = 0.08$

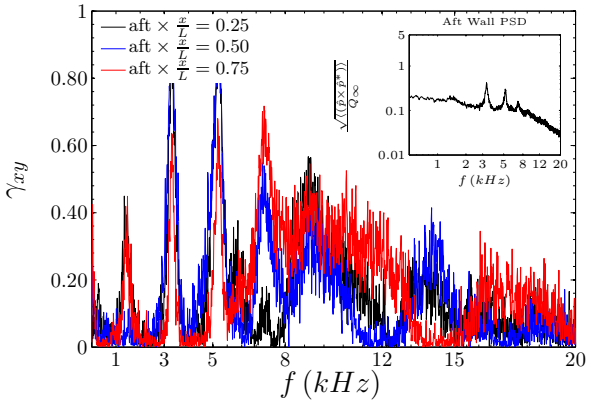

(c) $d^* = 0.21, G^* = 0.79$

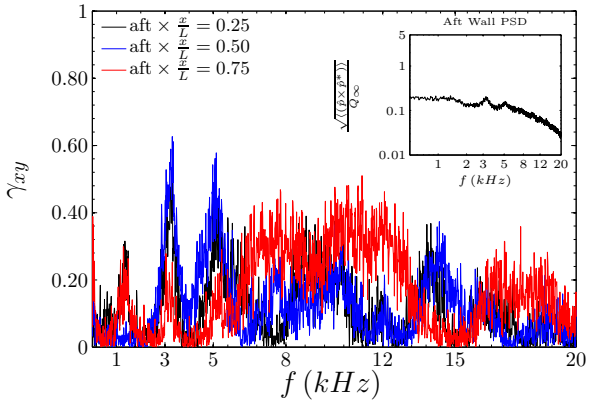

(d) $d^* = 0.43, G^* = 0.08$

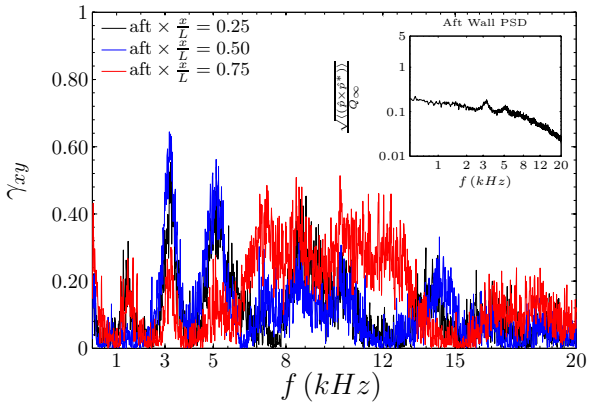

(e) $d^* = 0.43, G^* = 0.57$

Figure 6-13. Full span cavity cross-coherence at selected axial positions on the cavity floor. Reference signal is taken from aft wall sensor.

The spectrogram of each rod and gap height for the full span cavity are plotted in Figure 6-14(a) through Figure 6-14(e). The same tends noticed for the finite span cavity are realized in the full span cavity. This indicates the suppression mechanisms are likely identical in each cavity. It is apparent the larger diameter better suppresses all resonant tones in the cavity. The effect of the gap height on the rod suppression efficacy seems to be secondary to the selection of the rod diameter if only considering aft wall reductions. As indicated previously, the effect of gap height seems to play a more dominant role in the suppression of the fluctuating surface pressures on the cavity floor. This again seems to point that there likely exists at least two suppression mechanisms for the controlled cavity.

6.4 Summary

In this section the results of the suppression on the fluctuating surface pressures will be summarized for both the full and finite span cavities. Figure 6-15 summarizes the reduction of p_{rms} measured on the aft wall for each cavity and rod diameter and gap height. The full span cavity exhibited suppression levels that were roughly 15% greater than that of the finite span cavity at similar gap heights. This is not completely unexpected due to the findings of previous research such as that presented by Ahuja & Mendoza (1995). A rod sized roughly 40% of the approaching boundary layer thickness was the most effective at suppressing the fluctuating surface pressures on both the aft wall and floor when placed appropriately inside the boundary layer. The smallest rod exhibited the greatest sensitivity to placement within the boundary layer and was the least effective rod at any position. The most effective off-wall placement of the rod neglecting streamwise location variation, appears to occur when the top of the rod is placed near the top of the boundary layer. Similar results were previously reported in Ukeiley *et al.* (2004*a*).

Figure 6-15(a) and Figure 6-15(b) clearly indicate that as the rod is brought at least partially outside the boundary layer (for the finite span cavity the last point is located with the rod centerline near the top edge of the boundary layer) the suppression efficacy begins to drop off. The most effective configuration selected was $d^* = 0.43, G^* =$

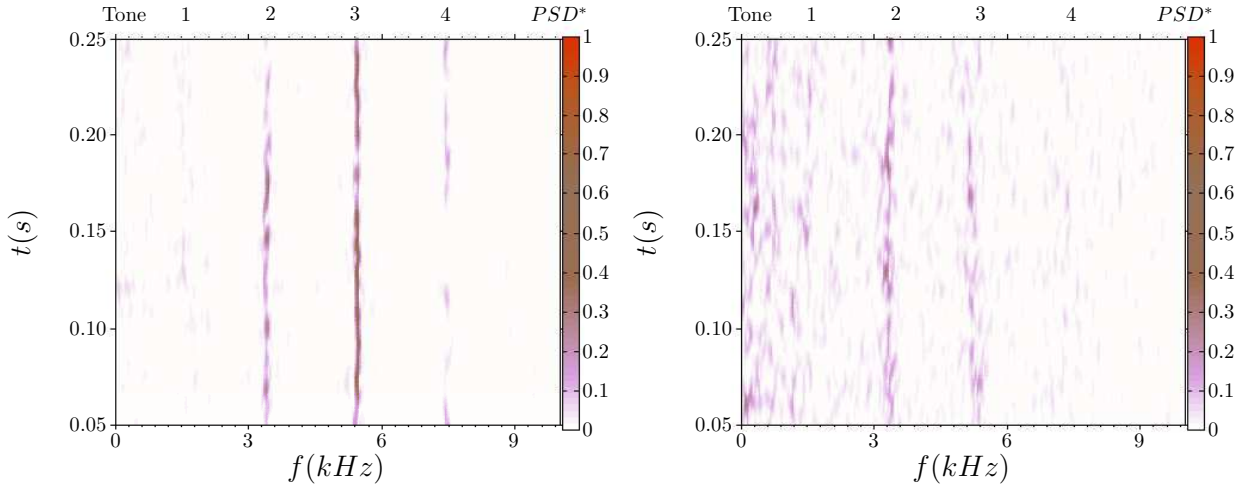

(a) Baseline

(b) $d^* = 0.21, G^* = 0.08$

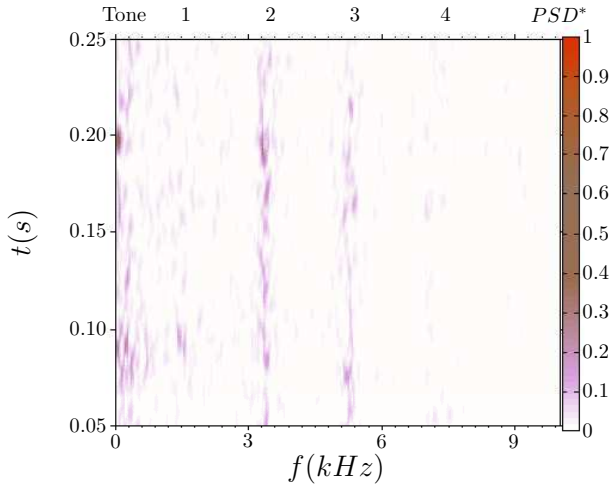

(c) $d^* = 0.21, G^* = 0.79$

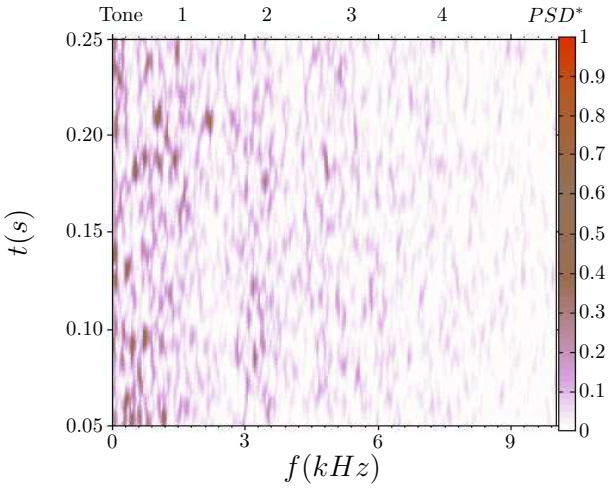

(d) $d^* = 0.43, G^* = 0.08$

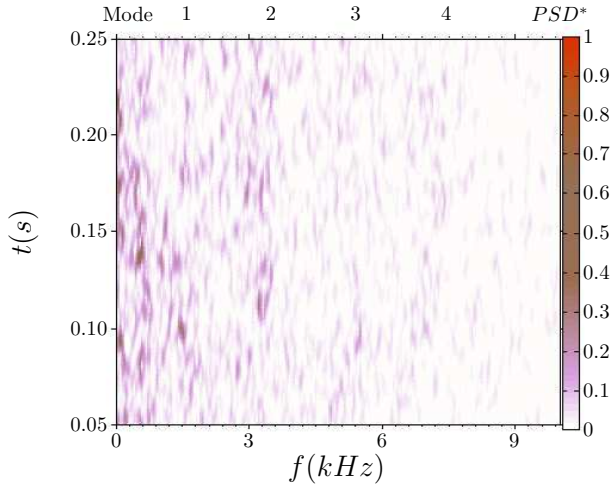

(e) $d^* = 0.43, G^* = 0.57$

Figure 6-14. Full span cavity aft wall spectrogram for given d^* and G^* values.

0.64 which places the top of the rod just below the reported boundary layer edge even though the aft wall p_{rms} reductions were not the highest as illustrated in Figure 6-15(b). Considering that the boundary layer will exhibit slightly different thicknesses based on the operating temperature (there is no temperature control in the facility) the critical point is that the best overall suppression was achieved when the top of the rod was near the top of the boundary layer. The numerical simulations presented in the previous

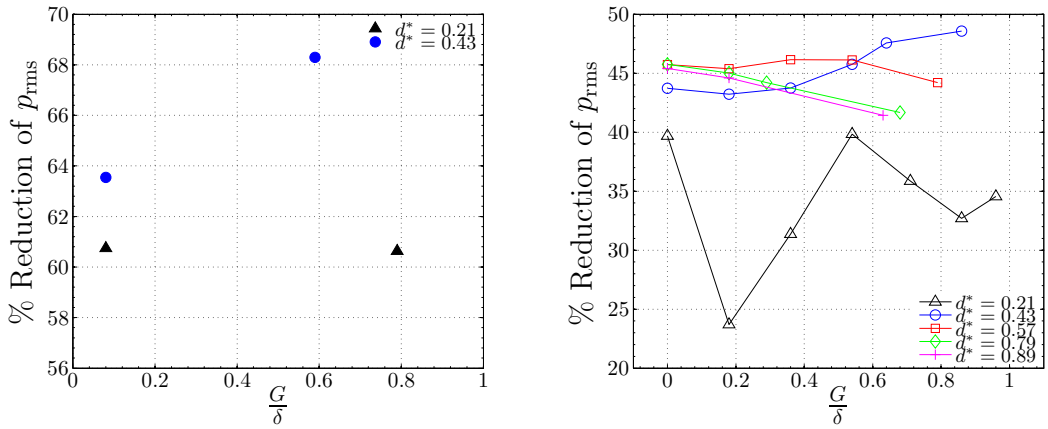

(a) Full Span (b) Finite Span

Figure 6-15. Percent reduction of p_{rms} measured on the aft wall at $\frac{y}{D} = -0.5$.

chapter indicated that as the rod was raised above the sonic line in the boundary layer there appeared to be cessation of the organized vortex shedding. Evidence was presented concurrently that the flow was more aggressively turned away from the floor as the separation bubble downstream of the cylinder grew. This was achieved as the top of the rod was brought near the top of the boundary layer. This suggests the rod may be able to loft the near body flowfield away from the wall which could in turn alter the shear layer aft wall impingement point. An upstream propagating pressure disturbance is generated by the shear layer flapping into the cavity impinging on the aft wall. The fact that the correlation time scales are the same and the correlation strengths are lowered likely indicates that the originating wave at the aft wall is weaker.

CHAPTER 7
FLOWFIELD MEASUREMENTS

This chapter is divided into two main sections based on the full and finite span cavity which both will include results from the baseline and controlled cases. Detailed analysis of the flowfield associated with the full span cavity including results where the field of view was focused on the leading edge of the cavity will be presented first. This will be followed by a more limited analysis of the finite span cavity due to difficulties encountered with obtaining high quality flow vectors throughout the shear layer. The finite span cavity analysis will be further expanded upon with computational fluid dynamics presented in the following chapter.

The configurations examined here were selected based upon the findings of the pressure measurements presented in the previous chapter. These include a baseline configuration for each cavity and configurations where the control was the most and least effective were selected for detailed analysis. The most effective case corresponded to a rod $d^* = 0.43, G^* = 0.57$ where the top of the rod was placed near the top of the boundary layer. The least effective case was $d^* = 0.21, G^* = 0.08$ where the smallest rod was placed near the floor. All of the experiments were conducted at a freestream Mach number of 1.44 with the standard operating conditions as described in Chapter 3. The detailed description of the PIV arrangement and vector processing can also be found in Chapter 3.

7.1 Full Span Cavity

In this section a detailed analysis of the full span cavity with and without control is presented. Mean flowfield, mean turbulent flowfield, two point spatial velocity correlations and Proper Orthogonal Decomposition results will be discussed.

7.1.1 Mean Flowfield

The convective velocity of the shear layer as defined by Papamoschou & Roshko (1987) is given by Equation 7–1. The convective velocity is U_c, the free stream velocity is given by U_∞, a is the speed of sound and the subscripts ∞ and 2 indicate the freestream

and low speed streams respectively.

$$U_c = \frac{a_\infty U_\infty + a_2 U_2}{a_\infty + a_2} \approx \frac{(U_\infty + U_2)}{2} \tag{7–1}$$

Assuming negligible variation of the local and freestream speed of sound (temperature variation is negligible) the equation simplifies to the approximate relation given in Equation 7–1. Detailed examination of the mean flow illustrated in Figure 7-1 for the baseline cavity showed that the shear layer flow penetrated roughly 20% of the cavity depth. The convective velocity was found to be roughly 45% of the freestream velocity. The lower stream velocity U_2 was evaluated at $\frac{x}{L} = 0.875$ and $\frac{y}{D} = 0.25$. In contrast, the

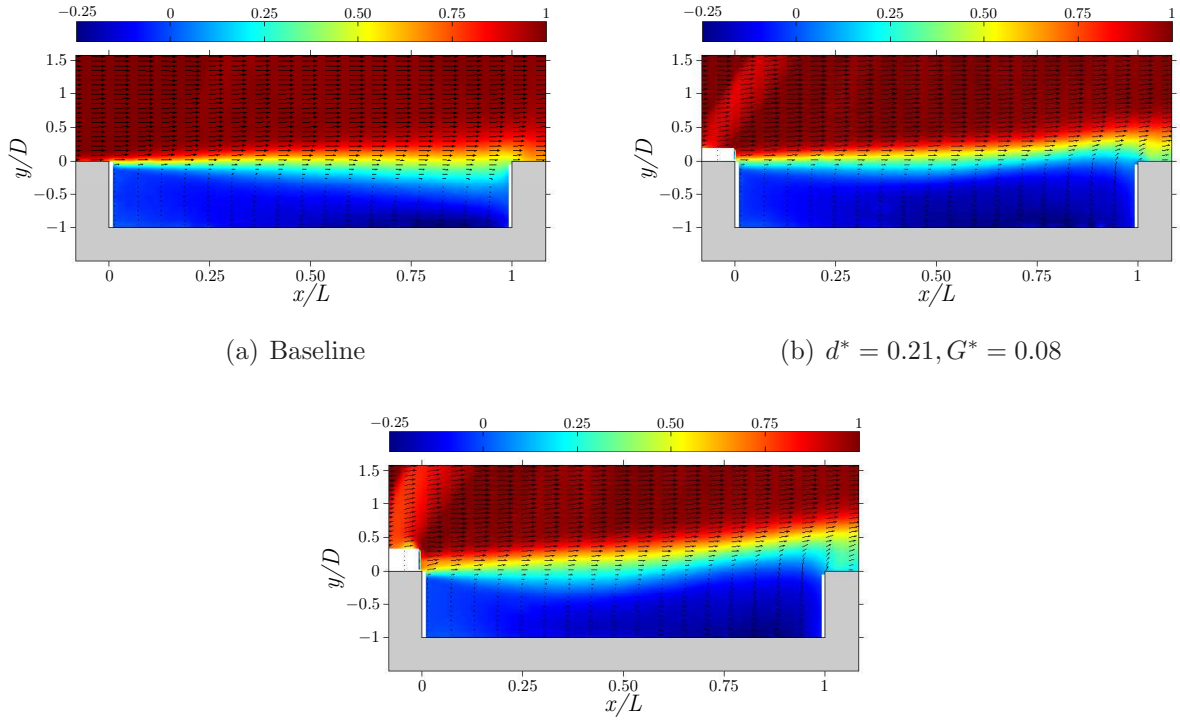

(a) Baseline

(b) $d^* = 0.21, G^* = 0.08$

(c) $d^* = 0.43, G^* = 0.57$

Figure 7-1. Full span mean streamwise velocity contours with vectors.

suppressed cavity mean streamwise flowfield indicates much lower streamwise velocities impinging on the aft wall. The shear layer and impingement point is clearly raised above the aft wall. Comparing the two controlled cases it is noted the larger diameter rod more

effectively spread the shear layer causing slower flow to impinge on the aft wall. This cases also exhibited larger recirculation velocities inside the cavity. The main recirculation inside the cavity also exhibited slightly elevated upstream velocities.

Figure 7-2 shows the results of an experiment conducted with the 2X teleconverter narrowing the field of view to approximately the first 25% of the cavity as shown in Figure 7-2. The experiment was conducted to increase the spatial resolution of the cylinder near field and better understand the interaction of the cylinder wake and cavity shear layer. The introduction of the rod leads to a cavity shear layer which is substantially spread and more effectively deflected as evident by close examination of the velocity vectors. The results presented in Chapter 5 indicated the cylinder wake was not deflected away from the wall as shown in the experimental observations here. The simulations did illustrate that the normal velocity was increased with a larger separation bubble downstream of the cylinder which deflects the flow more aggressively away from the wall for the most effective cases. Each of these conditions may lead to a shear layer that is deflected away from the wall, as shown here, especially near the cavity leading edge. It is also important to consider the effect the alternate geometry may have on the results of Chapter 5 where the rod was placed above a extended flat plate compared to the back step in the current study. Examining the two control cases it is evident the larger diameter rod exhibited a larger normal velocity component especially at the cavity leading edge.

Figure 7-3 illustrate the streamlines for each cavity. The baseline cavity is dominated by a large clockwise rotating recirculation region that stretches the whole cavity and is centered at $\left(\frac{x}{L}, \frac{y}{D}\right) = (0.85, -0.50)$. The maximum recirculation velocity was found to be nearly 25% of the free stream velocity which was located near the cavity floor. The cavity center-point (both axially and normal) showed recirculation velocities near 10% of the freestream values. The streamlines clearly indicate a secondary counter-rotating recirculation which is much smaller and located in the leading edge corner of the cavity. These findings are consistent with subsonic experiments conducted by Murray *et al.* (2009)

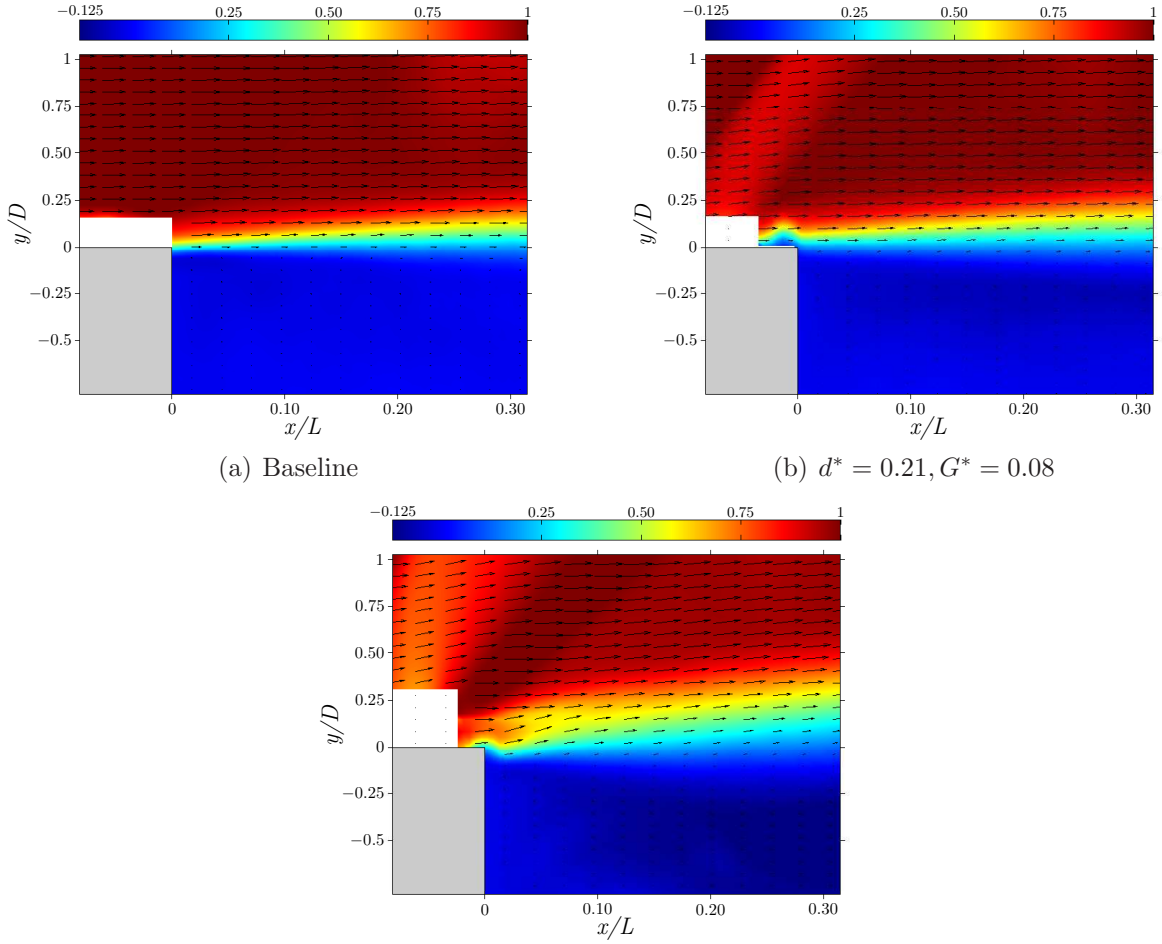

(a) Baseline

(b) $d^* = 0.21, G^* = 0.08$

(c) $d^* = 0.43, G^* = 0.57$

Figure 7-2. Zoomed cavity streamwise mean velocity contours with vectors.

for a cavity with a length to depth ratio of 6. The suppressed recirculation velocities near the floor on the aft end of the cavity where somewhat insensitive to the presence of the rod. Figure 7-4 plots the velocity profiles as a function of $\frac{y}{D}$ for various streamwise locations along the cavity length. Examining this figure it is seen that the recirculation velocity was notably increased at the cavity center-point and near the leading edge. The effect of the rod on the interior cavity flow is evident with examination of the streamline plots. The primary clockwise rotating recirculation was moved near the center-point of the cavity. The larger diameter rod exhibited a more organized and broader (attached to the cavity floor further upstream) recirculation region than noticed with the smaller diameter rod. The counter-rotating bubble at the cavity leading on the floor was still present for

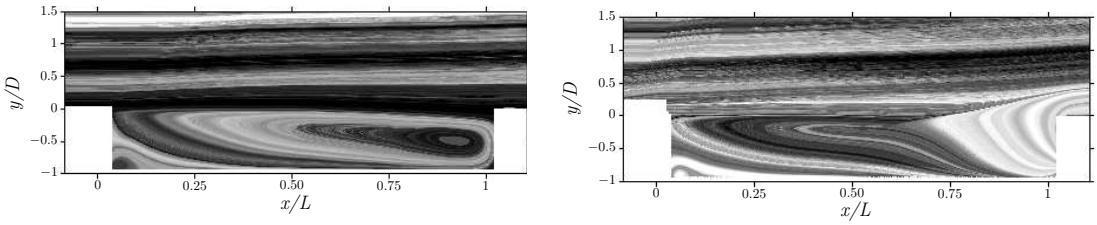

(a) Baseline

(b) $d^* = 0.21, G^* = 0.08$

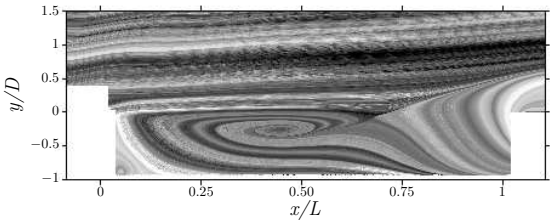

(c) $d^* = 0.43, G^* = 0.57$

Figure 7-3. Full span cavity streamlines.

each rod. The larger rod streamlines in this region indicate flow that does not impinge on the leading edge until near the cavity lip. The small diameter rod streamlines at the cavity leading edge are very similar to the baseline flow. The intricacies of the trailing edge streamlines are not fully understood and is believed to be an artifact of the partial spanwise coverage of the rod spoiler by the introduction of end effects. The rod only alters the portion of the shear layer which it spans. The area the rod spans likely lifts the shear layer creating an outflow at the center and an inflow near the walls.

Figure 7-4 illustrates the velocity profiles at various axial positions along the cavity length. Examining Figure 7-4(a) and Figure 7-4(b) it is apparent the profile has been deflected away from the wall more aggressively for the large diameter rod. The figure shows clear evidence the shear layer is broadened in the controlled cavities as one progresses downstream. The shear layer appears to spread more effectively with the larger diameter rod. The controlled cavities also exhibited increased levels of reversed flow inside the cavity.

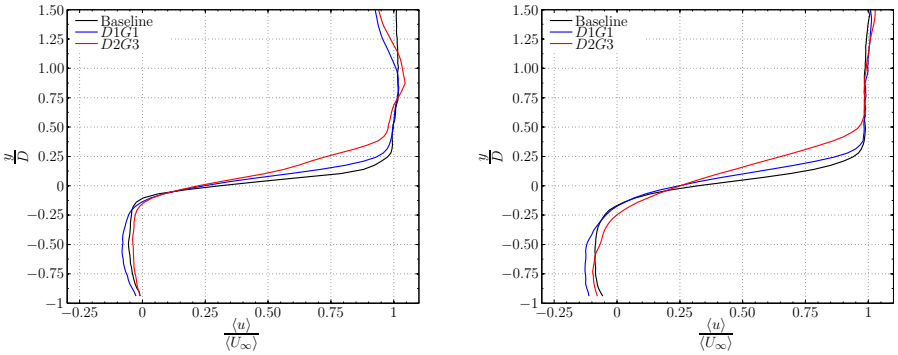

(a) $\frac{x}{L} = 0.125$ (b) $\frac{x}{L} = 0.25$

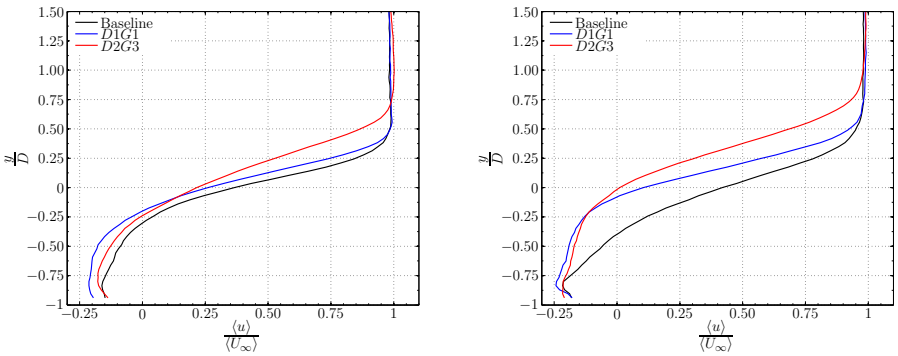

(c) $\frac{x}{L} = 0.50$ (d) $\frac{x}{L} = 0.75$

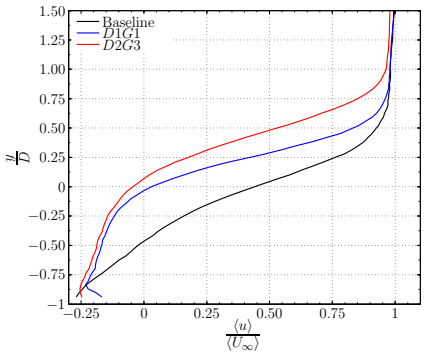

(e) $\frac{x}{L} = 0.875$

Figure 7-4. Full span cavity mean streamwise velocity profiles.

7.1.2 Turbulent Flowfield

The effect of the rod's presence on the turbulent flowfield determined by the velocity fluctuations are presented next. Figure 7-6(a) and Figure 7-7(a) show that for approximately the first 10-15% of the cavity leading edge unreliable vectors were calculated. This is likely attributable to the accumulation of oil on the test section sidewalls and cavity interior. This was consistently observed with the baseline cavity PIV experiments.

The mean turbulent streamwise velocity contours and profiles are illustrated in Figure 7-5 and Figure 7-6 respectively. The turbulent fluctuations had peaks approximately 30-35% of the free stream flow for the baseline cavity with slightly elevated fluctuations with each controlled cavity. Each rod increased the streamwise velocity fluctuations

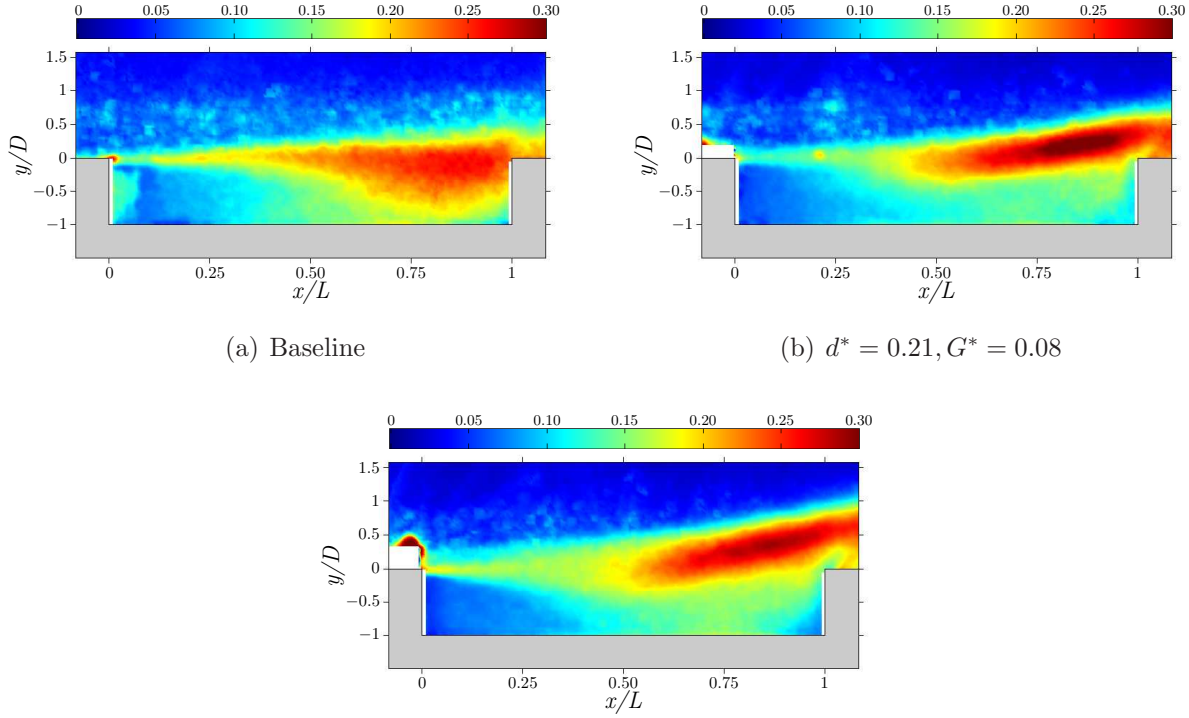

(a) Baseline

(b) $d^* = 0.21, G^* = 0.08$

(c) $d^* = 0.43, G^* = 0.57$

Figure 7-5. Full span cavity mean streamwise turbulent velocity contours.

near the trailing edge but most notably shifted the point where the maximum fluctuation levels occurred above the cavity lip. The smaller diameter rod raised the mean streamwise

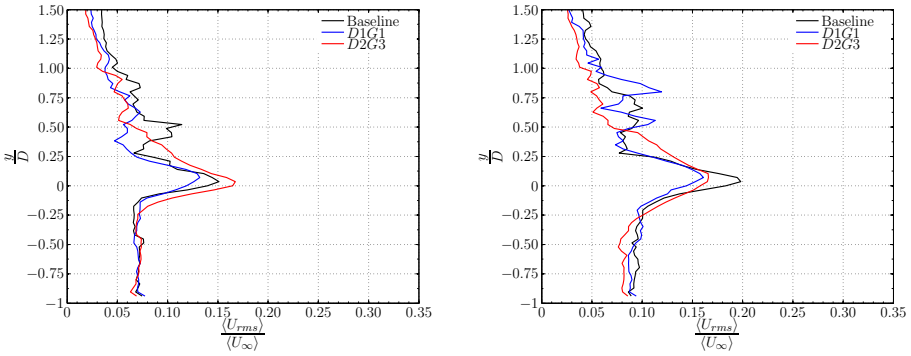

(a) $\frac{x}{L} = 0.125$ (b) $\frac{x}{L} = 0.25$

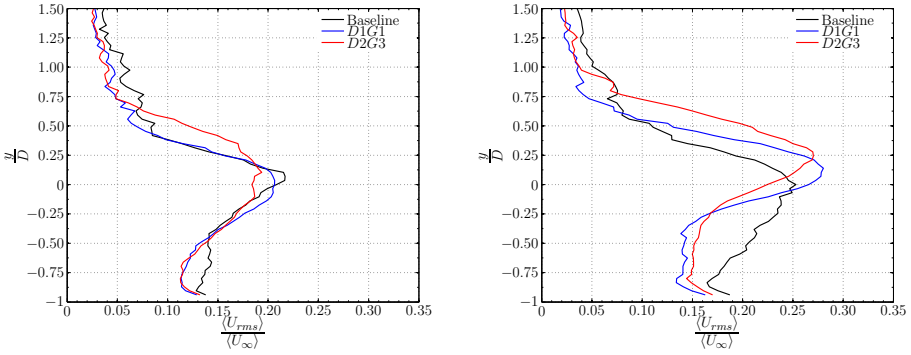

(c) $\frac{x}{L} = 0.50$ (d) $\frac{x}{L} = 0.75$

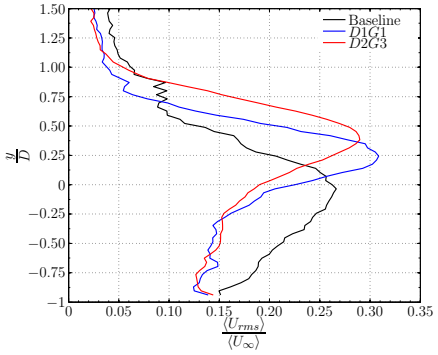

(e) $\frac{x}{L} = 0.875$

Figure 7-6. Full span cavity mean streamwise turbulent velocity profiles.

turbulent fluctuations slightly more than the large diameter rod at the trailing edge. It should be noted these differences are within measurement uncertainty ranges that were discussed in Chapter 3. The large diameter rod exhibited a greater displacement of the peak RMS values which becomes more evident as one progresses downstream in the cavity. This suggests the rod is able to alter the aft wall impingement point likely by lifting the shear layer (as shown in Figure 7-4) or by altering the flapping motion of the shear layer. The leading edge magnitude and displacement exhibited only slight variations up where $0 \leq \frac{x}{L} \leq 0.50$.

The mean normal turbulent velocity component is illustrated in Figure 7-7 where the turbulent fluctuations were roughly 15-20% of the free stream flow for the baseline cavity. The controlled cavities again exhibited elevated fluctuations near the trailing edge. The zoomed field of view for the cavities normal fluctuating velocities are presented in

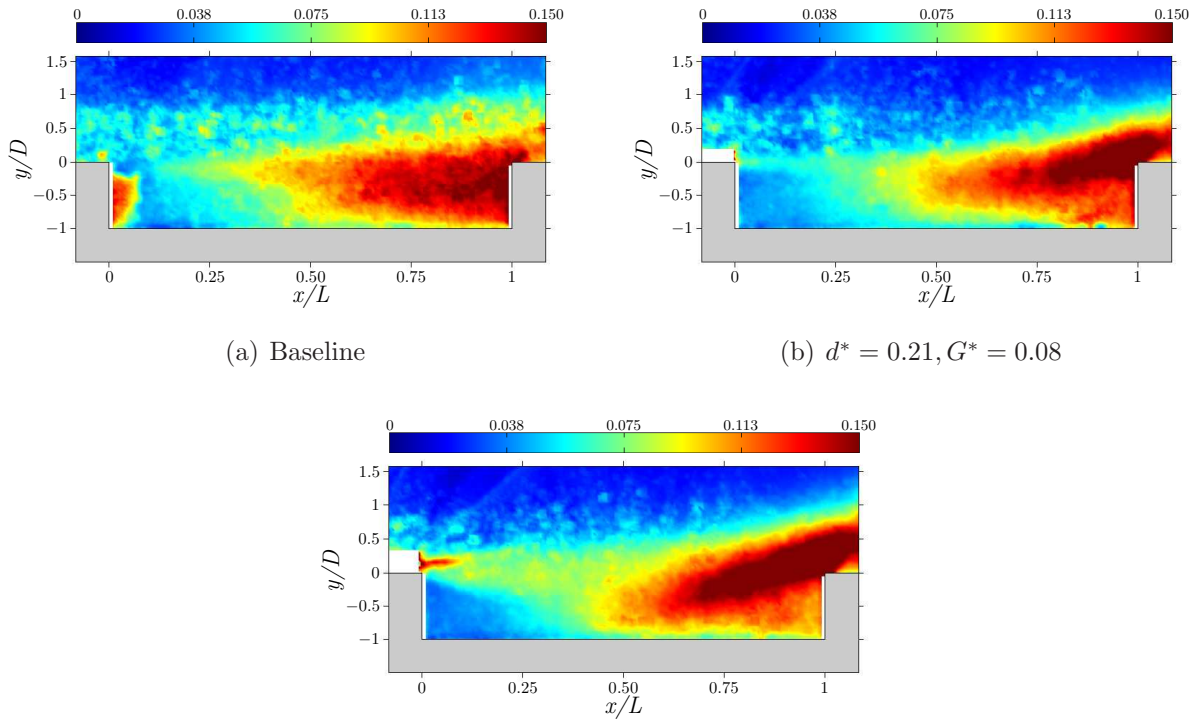

(a) Baseline

(b) $d^* = 0.21, G^* = 0.08$

(c) $d^* = 0.43, G^* = 0.57$

Figure 7-7. Full span cavity mean normal turbulent velocity contours.

Figure 7-8. The wake of the cylinder is only present in the plots for the large diameter rod clearly indicating the normal velocity of the flow is greatly enhanced by the increased rod diameter and gap height. This was expected and also reported in the numerical simulations of Chapter 5. The shear layer is intensified and spread more effectively with the presence of the large diameter rod.

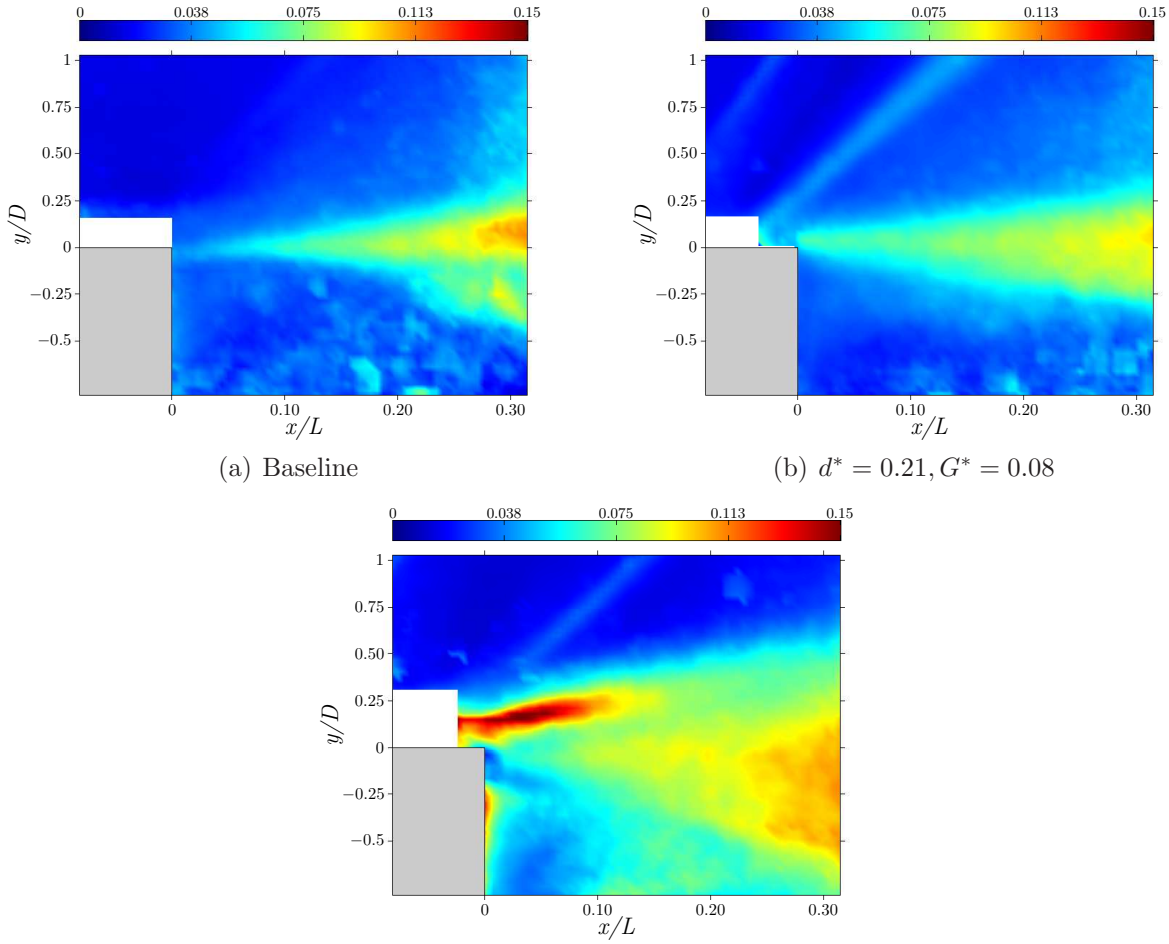

(a) Baseline

(b) $d^* = 0.21, G^* = 0.08$

(c) $d^* = 0.43, G^* = 0.57$

Figure 7-8. Zoomed cavity normal turbulent velocity contours.

The shear component ($u'v'$) of the Reynolds stress contours and profiles are given in Figure 7-9 and Figure 7-10 respectively. The shear stress at the leading edge of the cavity was slightly elevated for each controlled case as one might expect due to the interaction with the cylinder wake. From $0.125 \leq \frac{x}{L} \leq 0.5$ the peak RSS decreased for the suppressed cavities with little change in it's location relative to the cavity lip line. As one progresses

further downstream the location of the peak RSS begins to shift above the cavity lip line and near the cavity trailing edge there is a notable increase in peak RSS levels.

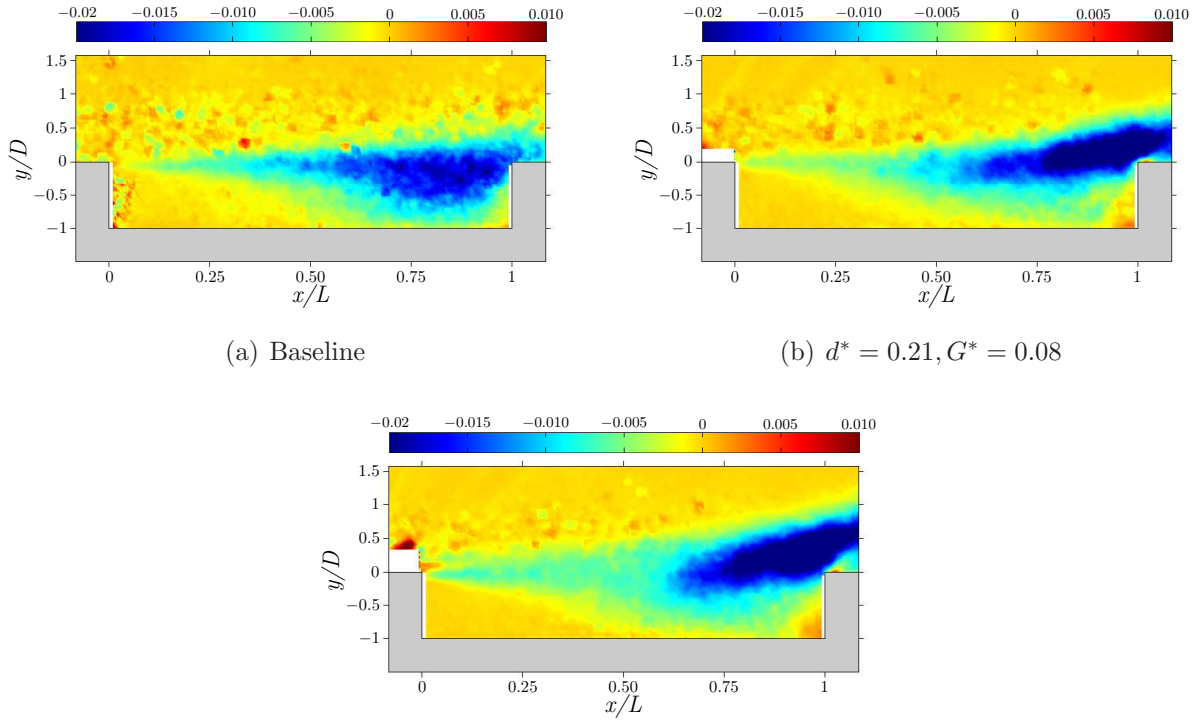

(a) Baseline

(b) $d^* = 0.21, G^* = 0.08$

(c) $d^* = 0.43, G^* = 0.57$

Figure 7-9. Mean RSS flow contours for the full span cavity.

The overall effect of the cylinder on the mean turbulent flowfield are quite similar for each controlled cavity which varied mostly in magnitudes. The quantities considered exhibited the same tendencies with a shift in the peak location by the cavities trailing edge and marked increase in magnitudes. The larger diameter rod seemed to exhibit the largest displacement of peak magnitudes which is an indication of it's capability to more effectively loft or alter the flapping of the shear layer.

Shear layers developed by flow over cavities differ slightly from that of a conventional single stream free mixing layer. The Kelvin-Helmholtz instabilities are constantly excited by the feedback mechanism and the entrainment of fluid is modified by the presence of the cavity. The spreading rate has been reported using both the momentum (θ) and vorticity

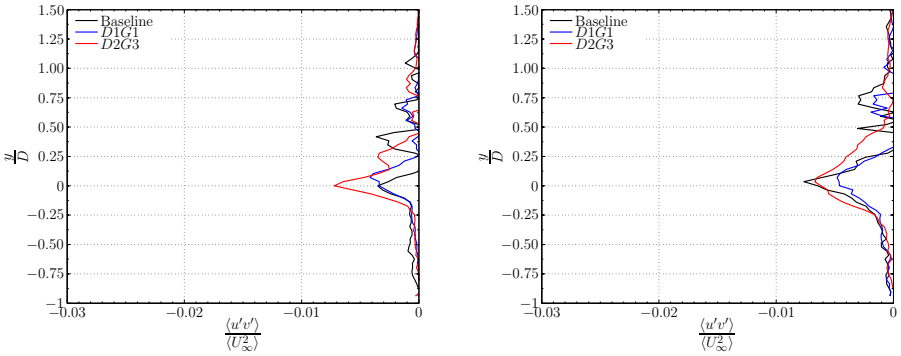

(a) $\frac{x}{L} = 0.125$ (b) $\frac{x}{L} = 0.25$

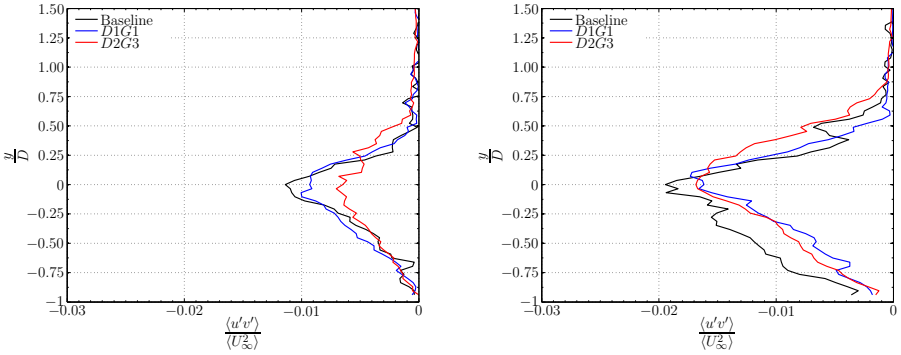

(c) $\frac{x}{L} = 0.50$ (d) $\frac{x}{L} = 0.75$

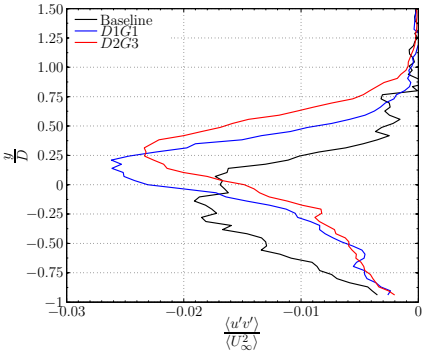

(e) $\frac{x}{L} = 0.875$

Figure 7-10. Full span mean RSS profiles.

thickness parameters (δ_w). The primary limitation when using the momentum thickness as a measure is that the variation caused by the recirculating region inside the cavity leads to some arbitrary bounds on the integration domain. The vorticity thickness, as given in Equation 7–2, is a local measure of the maximum shear which may be argued to better determine the instability properties of the shear layer. To this end, the vorticity thickness is chosen as the parameter to measure the growth of the shear layer in this research.

$$\delta_w = \frac{U_\infty}{\left(\frac{\partial U}{\partial y}\right)_{\max}} \tag{7–2}$$

It has been found that shear layers over cavities closely resemble turbulent free shear layers in that each exhibit nearly linear spreading rates. The spreading rates of shear layers with upstream laminar boundary layers was studied by Sarohia (1975) and found to be nearly linear and increased as $\frac{L}{\theta_0}$ increased where θ_o is the initial momentum thickness of the shear layer. Turbulent mixing layers generally exhibit spreading rates where $\frac{d\delta_w}{dx} = 0.162$ as reported by Brown & Roshko (1974). Cavity flow with a turbulent boundary layer at subsonic speeds was reported to exhibit linear spreading rates by Cattafesta III *et al.* (1997) with values near those reported by Brown & Roshko (1974).

To estimate the effect the rods had on the growth and mean shear rate of the cavity the vorticity thickness is plotted as a function of cavity length in Figure 7-11(a). The ordinate plot is normalized by the vorticity thickness computed as near to the leading edge as possible. The cavity length to momentum thickness ratio is approximately 140. The x-axis scales linearly from $0 \leq \frac{x}{\delta_0} \leq 40$ where 0 represents $\frac{x}{L} = 0$ and 40 is $\frac{x}{L} = 0.875$. Gharib & Roshko (1987) conducted experiments with incompressible cavity flows with $85 \leq \frac{L}{\theta_0} > 130$ and reported that the momentum growth rate was nearly constant at 0.032. Rowley (2002) gave the vorticity growth rate as four times the momentum growth rate implying the vorticity growth rate for the work conducted by Gharib & Roshko (1987) is approximately 0.12. The baseline cavity shear layer growth rate is lower than the spreading rate of turbulent free shear layers and was found to equal 0.10. The small

diameter rod exhibited a growth rate slightly less than the baseline cavity at 0.09 but started with a thicker vorticity thickness due to the presence of the rod. The larger diameter rod spread more rapidly at a rate of 0.37 until the shear layer could no longer maintain that growth rate and subsequently crossed back over the baseline rate near the cavity trailing edge. Incidentally, this is also where the magnitude of the RSS for the suppressed configurations dips below the baseline case. Near the cavity trailing edge the RSS increases drastically for the suppressed configurations which is also noticed in the vorticity spreading rate. The elevated growth rate of the shear layer is also demonstrates the rod's ability to alter the mean shear throughout the cavity shear layer. The maximum mean shear experienced by the shear layer, as estimated by the denominator of Equation 7–2, is also shown to be more effectively reduced by the larger diameter rod.

Figure 7-11(b) illustrated the location of the maximum shear as a function of vertical displacement above the cavity lip marked by $\frac{y}{D} = 0$. The location and the rate of change of the maximum shear rises above the aft wall with the larger diameter rod. It appears as the shear layer is lofted above the aft wall the maximum mean shear decreases with the added benefit of raising the location of the remaining maximum shear far away from the aft wall.

7.1.3 Evolution of Two-Point Statistics

In this section the two-point turbulent velocity statistics throughout the measurement region are presented. The two point statistics are included to help describe properties of the high Reynold's number flow where the magnitude of the feedback source in the cavity is believed to be linked to the highly correlated fluctuating velocity regions interacting with the aft wall. In all of the plots presented in this section the correlation coefficients will be presented normalized by the appropriate RMS velocity. In Figure 7-12 through Figure 7-15, the baseline cavity is represented in the first column of images followed by the small diameter rod and lastly the large diameter rod. Reading up and down the page

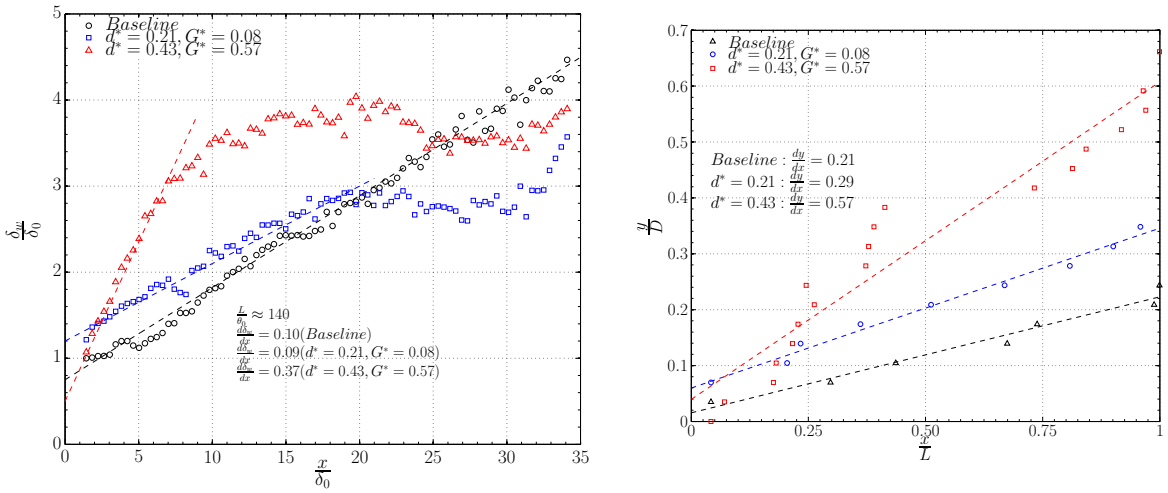

(a) Vorticity thickness (b) Location of maximum shear

Figure 7-11. Vorticity thickness of the full span cavity. Dashed lines represent calculation for $\frac{d\delta_w}{dx}$ and $\frac{dy}{dx}$.

corresponds to advancing spatially either increasing $\frac{x}{L}$ or increasing $\frac{y}{D}$. The exact origin of the correlation is given in each figure caption.

The normal direction (constant streamwise direction) spatial evolution near the cavity trailing edge are illustrated in Figure 7-12 and Figure 7-13 for the normal and axial turbulent velocity correlations respectively. Only one location is presented as similar behaviors were observed at each streamwise position. Examining this figure it becomes apparent the area of highly correlated fluid decreases for the baseline case as the origin is moved away from the cavity lip. The controlled cavities maintain higher levels of correlation as one moves away from the cavity lip. The large diameter rod exhibited the best overall correlation at $\frac{y}{D} = 0.5$ suggesting the cavity has been altered such that it now lies higher above the lip-line. It has been previously demonstrated the larger diameter rod more effectively spread the shear layer than the smaller diameter rod. Therefore, this correlation behavior is expected as one would expect the correlations to follow the spread of the shear layer fairly closely.

The correlation of the streamwise turbulent velocity indicates a skewed correlation region which may be due to a straining effect (due to raised shear stresses in the aft of the

cavity) of the large scale turbulent structures in this region. A similar trend is observed for the normal velocity based on v' illustrated in Figure 7-13. The correlations became elongated in the direction of the velocity for each figure where the suppressed cavities exhibited much higher aspect ratio regions than the baseline cavity. The larger diameter rod again maintained fairly well defined correlations higher above the lip of the cavity which is believed to be due to the spreading of the shear layer as previously mentioned.

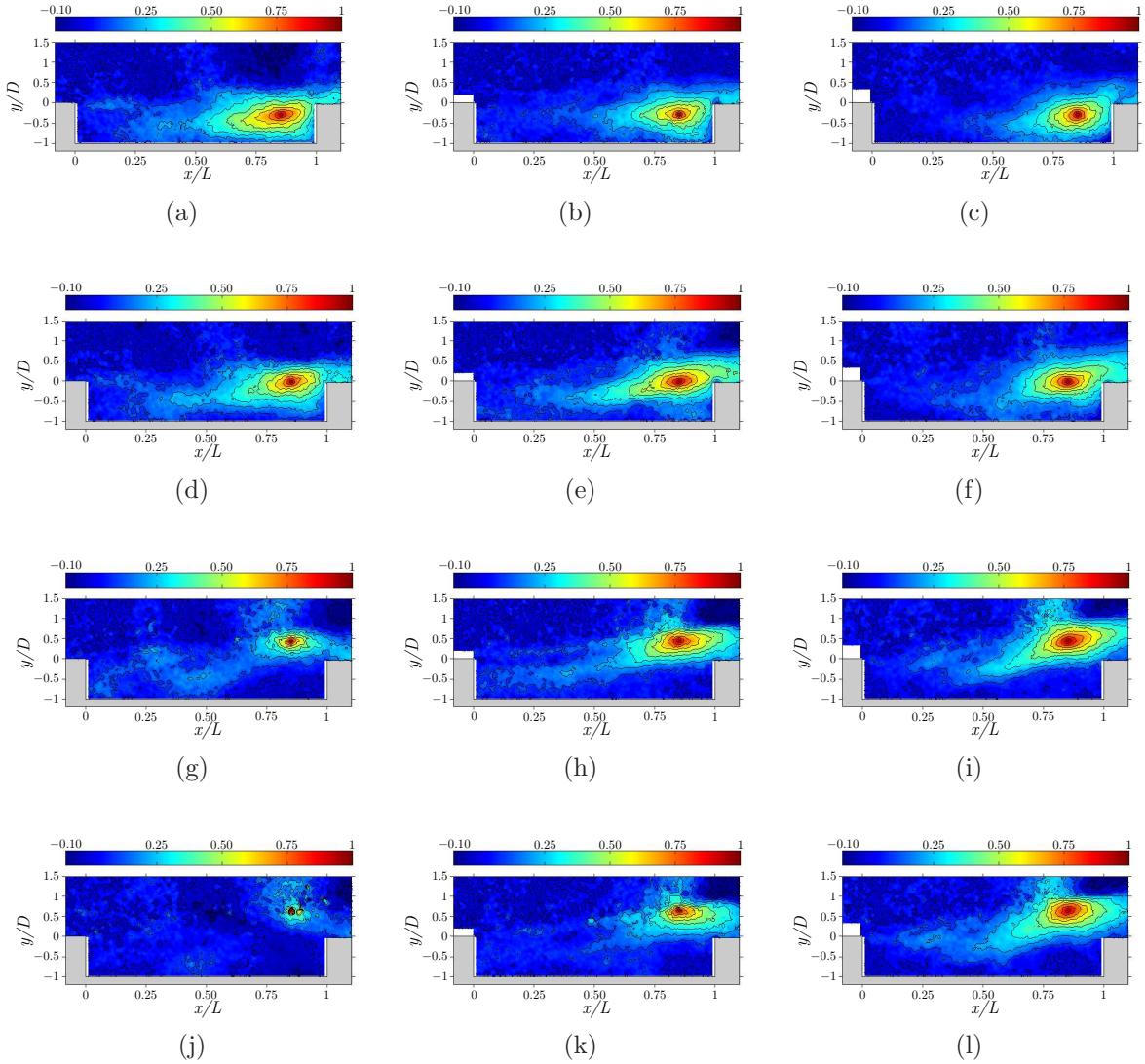

Figure 7-12. Evolution of two-point spatial axial turbulent velocity correlation centered at $\frac{y}{D} = (-0.5, 0, 0.5, 0.75)$. Columns: (a) Baseline (b) $d^* = 0.21, G^* = 0.08$ (c) $d^* = 0.43, G^* = 0.57$. $\frac{x}{L}$ position runs top to bottom in figure with axial origin located at $\frac{x}{L} = (0.25, 0.50, 0.75, 0.875)$

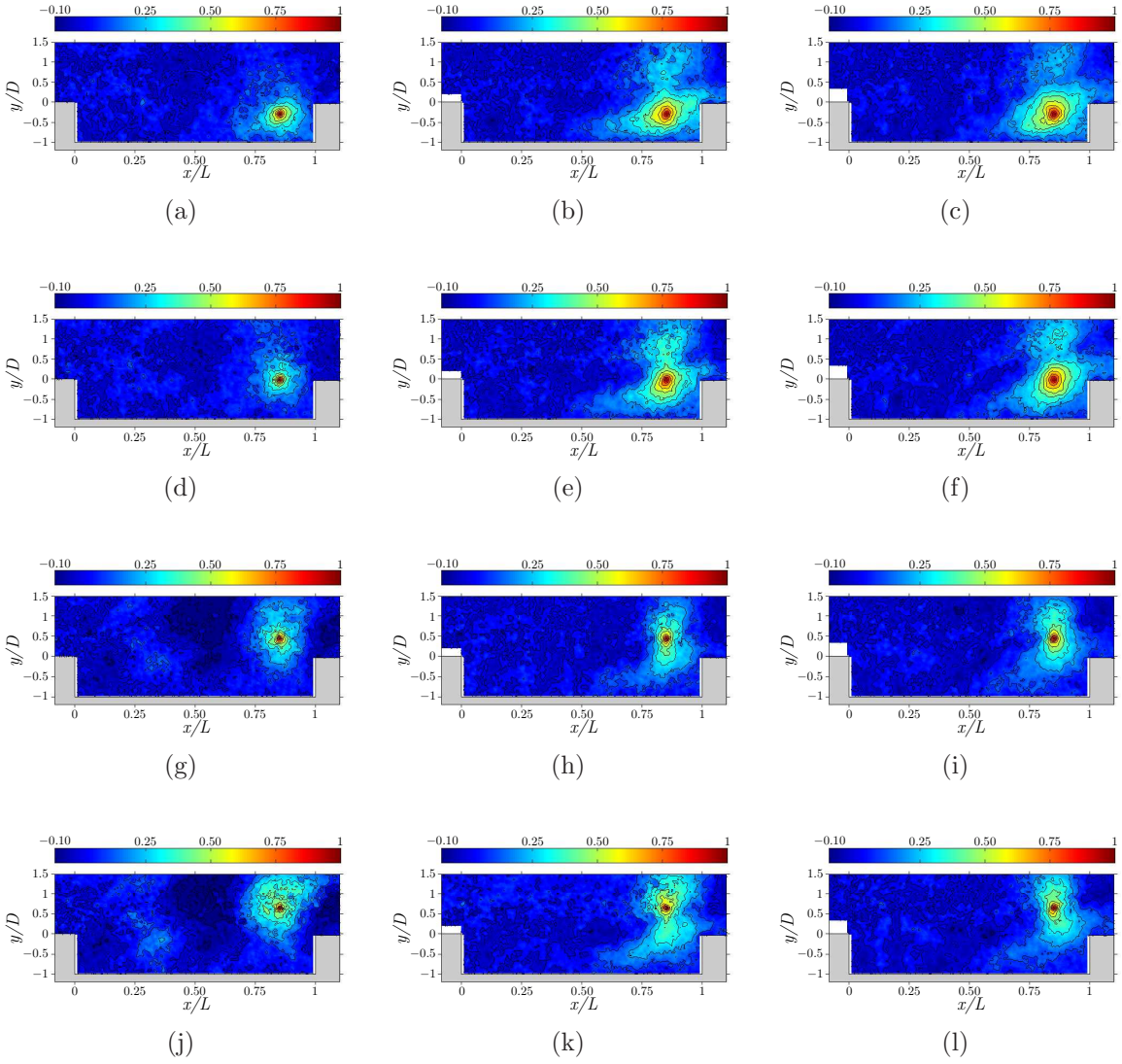

Figure 7-13. Evolution of two-point spatial normal turbulent velocity spatial correlation centered at $\frac{y}{D} = (-0.5, 0, 0.5, 0.75)$. Columns: (a) Baseline (b) $d^* = 0.21, G^* = 0.08$ (c) $d^* = 0.43, G^* = 0.57$. $\frac{x}{L}$ position runs top to bottom in figure with axial origin located at $\frac{x}{L} = (0.25, 0.50, 0.75, 0.875)$

The streamwise spatial evolution of the $u'u'$ and $v'v'$ component of the normal stress near the cavity trailing edge are illustrated in Figure 7-14 and Figure 7-15 respectively. Examining these correlations the developing elongation with cavity span becomes apparent. For the controlled cavities it is apparent the correlation region is tilted with respect to the cavity lip-line near the cavity leading edge which is believed to be an indication of the rods ability to loft the shear layer. The small and large diameter rod exhibit similar behavior at each spatial location though the larger diameter rod tends to exhibit slightly more elongated with larger tilt angles for the correlated regions. The normal direction correlation exhibits similar overall behavior at each spatial location. The correlation becomes more elongated in the normal direction as one progresses towards the cavity aft wall where this effect is magnified for the controlled cavities. The correlated regions for the larger diameter rod tend to be slightly larger than those of the smaller diameter rod. The controlled cavities show a greater propensity for the correlated region to evolve in the direction of the stress when compared with the baseline cavity.

The elongation of the correlated regions in the direction of the normal velocity is expected for a turbulent mixing layer. The general shapes of the correlation areas are quite similar with only slight alterations of the maximum correlation angles for the controlled cases.

7.1.4 Proper Orthogonal Decomposition

It can be advantageous to extract the most energetic features of the flow from the background turbulence in the shear layer in order to gain insight. Several techniques exist for identifying large scale structures in a turbulent flowfield which are summarized by Bonnet *et al.* (1998). The use of Proper Orthogonal Decomposition (POD) is well suited for such analysis since the POD modes in this research are written such that the optimal decomposition is found for the turbulent kinetic energy. Typically only the first few modes are needed to capture a majority of the large scale behavior and energy.

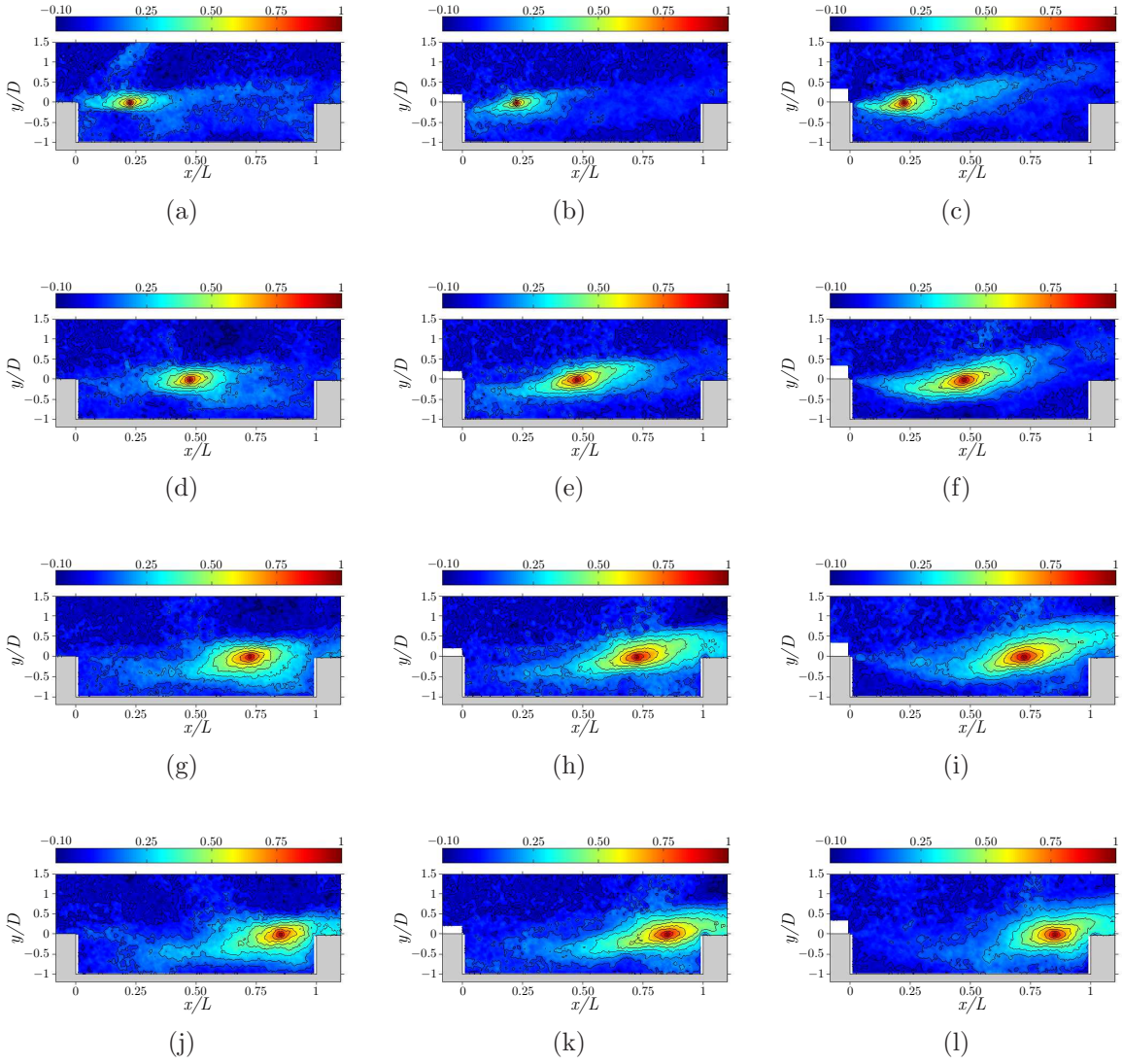

Figure 7-14. Evolution of two-point spatial axial turbulent velocity correlation centered at $\frac{y}{D} = 0$. Columns: (a) Baseline (b) $d^* = 0.21, G^* = 0.08$ (c) $d^* = 0.43, G^* = 0.57$. $\frac{x}{L}$ position runs top to bottom in figure with axial origin located at $\frac{x}{L} = (0.25, 0.50, 0.75, 0.875)$

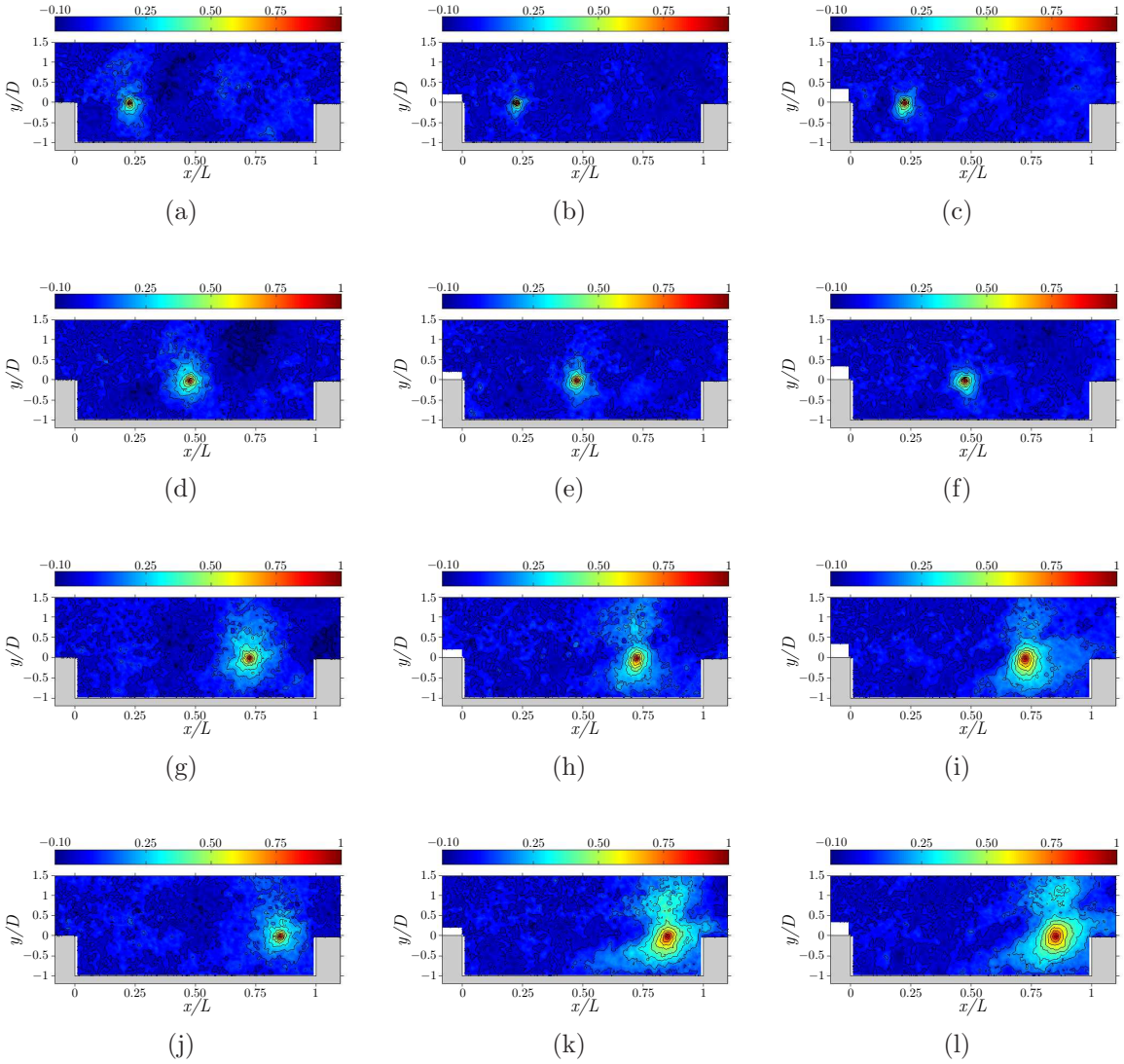

Figure 7-15. Evolution of two-point spatial turbulent velocity correlation centered at $\frac{y}{D} = 0$. Columns: (a) Baseline (b) $d^* = 0.21, G^* = 0.08$ (c) $d^* = 0.43, G^* = 0.57$. $\frac{x}{L}$ position runs top to bottom in figure with axial origin located at $\frac{x}{L} = (0.25, 0.50, 0.75, 0.875)$

Studies were conducted to ensure that enough snapshots were used in order to verify that the dominant modes were sufficiently resolved. This was accomplished by applying a varying number snapshots as illustrated in the contour plots of selected POD modes in Figure 7-16 and Figure 7-17 to access the sensitivity of the POD characteristics. Figure 7-17 shows the convergence of the turbulent kinetic energy captured per POD mode and the cumulative captured turbulent kinetic energy as a function of the number of snapshots. Though all available snapshots were used throughout this research it is noted that it appears 300-500 would be sufficient if one were interested in reconstructing the flowfield.

The amount of turbulent kinetic energy represented by each mode is determined by the magnitude of the eigenvalues and is plotted for each configuration in Figure 7-18. It is seen that there was little change in the first twenty modes between baseline and suppressed cavities with the exception of the first two modes. The fairly rapid convergence of the basis set is realized where the capture of 50% of the total turbulent kinetic energy for the controlled cavities required less than 2% of the total snapshots while the baseline required slightly more around 4%. The lag of the baseline cavity is due to the amount of energy captured in the first POD mode. The first mode of each cavity captured between 13-17% of the total turbulent kinetic energy where the suppressed cases captured more kinetic energy in the first mode which is consistent with the numerical results of Arunajatesan *et al.* (2009).

The first five POD modes associated with the streamwise and normal component of velocity for each configuration is displayed in Figure 7-19 and 7-20 respectively. In each of these figures the columns represent the cavity configuration while the rows represent the POD mode. There are several interesting qualitative features of these modes that will be highlighted. For each component of the POD modes the presence of the rod did not have a profound effect on the streamwise organization of the resolved modes. The first mode of each cavity exhibited one elongated feature which is consistent with the subsonic results

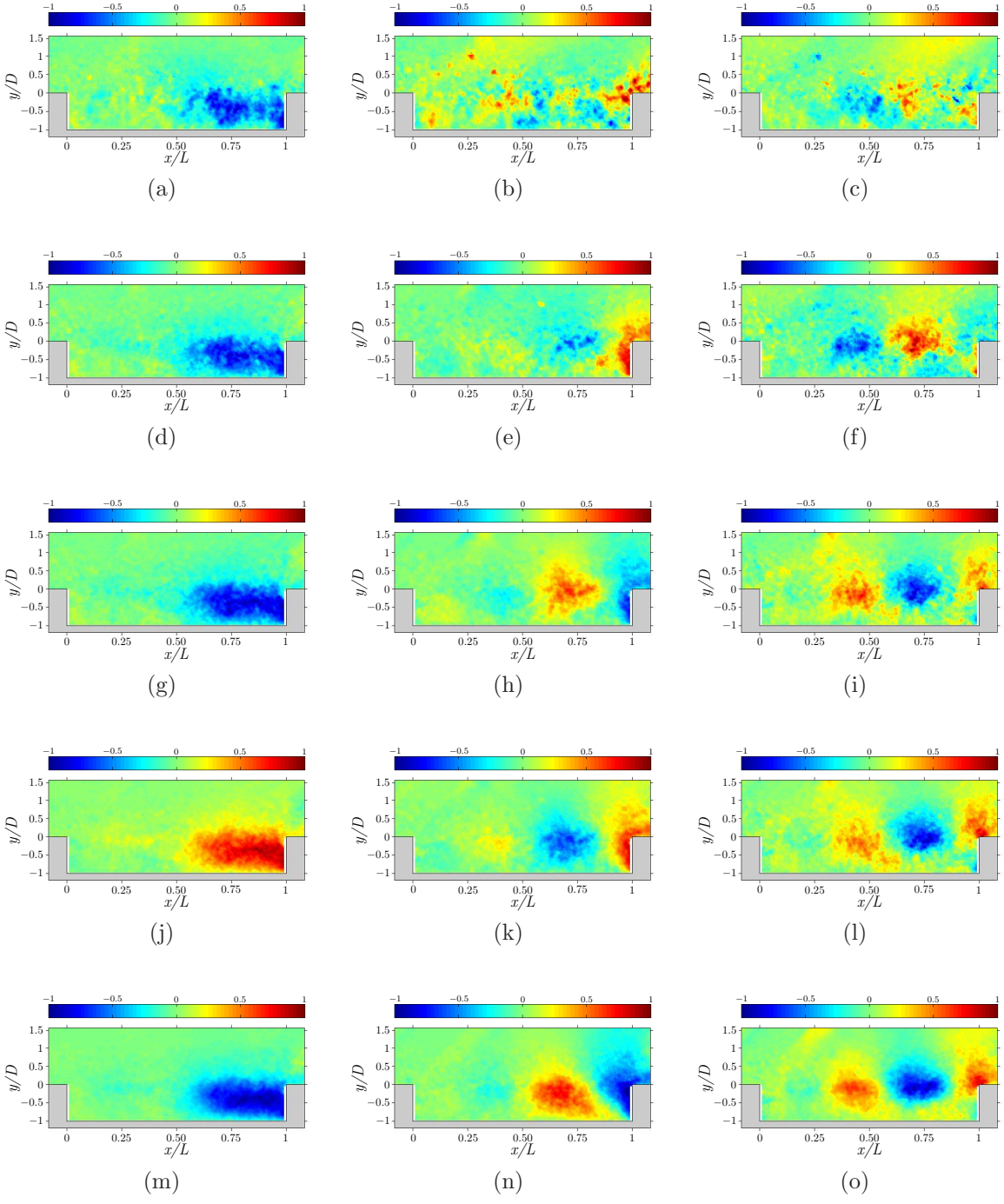

Figure 7-16. Normal direction POD modes 1,3 and 5 convergence based on the number of snapshots for the full span cavity. Columns: (a) Baseline (b) $d^* = 0.21, G^* = 0.08$ (c) $d^* = 0.43, G^* = 0.57$. Rows represent differing number of snapshots in ascending order (Snapshots = 50,200,350,500,1000)

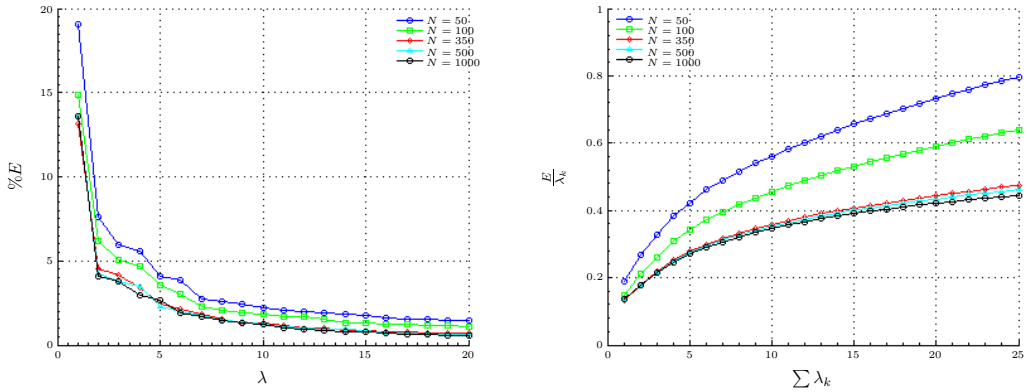

(a) Energy per POD Mode (b) Cumulative Energy Distribution

Figure 7-17. Convergence of POD energy at each mode and convergence of cumulative energy based on number of snapshots.

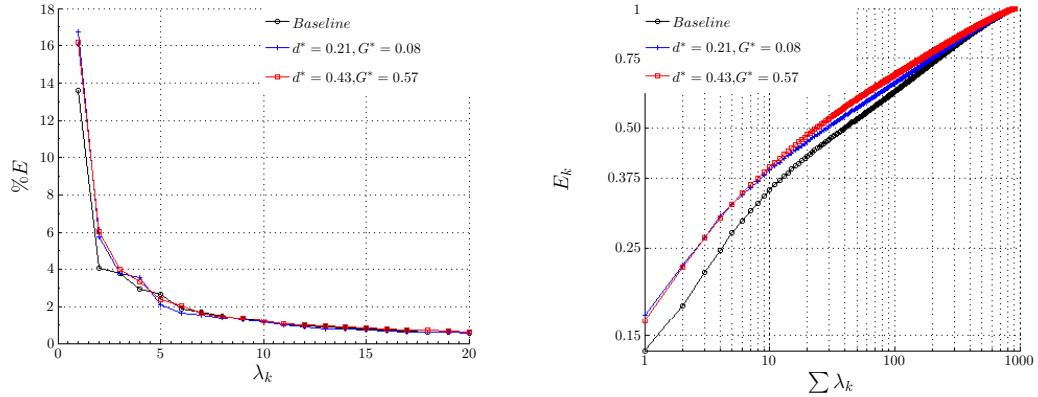

(a) Energy per POD Mode (b) Cumulative Energy Distribution

Figure 7-18. Full span cavity POD temporal convergence and energy distribution.

of Murray *et al.* (2009) The orientation and vertical location of this mode was largely influenced by the selection of rod diameter. The mode is also well organized under the cavity lip for the baseline cavity. In contrast, the suppressed cavities have been further elongated in the streamwise direction and become more compact in the normal direction. The mode has been lifted outside the cavity and turned in a counterclockwise manner which is consistent the recirculation region at the aft wall clearly shown in the streamlines of the suppressed cavities illustrated in Figure 7-3. In general, the suppressed cavities exhibited less energetic regions found under the cavity lip as seen in POD modes 2,3 and

5. It should be noted that in general the modes from the POD analysis seem aligned with the outline of the cavity mean shear layer as one would expect since this is where the dominant amount of turbulent energy resides.

It is interesting to note the suppressed cavities seem to exhibit a tendency to swap behaviors between the third and fourth modes. An well organized structure is found under the cavity lip for the fourth mode of the small diameter rod whereas a similar trend is observed for for the third mode of the larger diameter rod. The dominant mode of the cavity seems to establish itself when the flow switches between the multiple resonant peaks observed in the pressure spectra. The spectrograms presented in Chapter 6 indicate the dominant resonant tone was present nearly all the time whereas the smaller resonant peak occurred more intermittently. This view is consistent with that of the POD modes extracted from the flow which demonstrate flow features consistent with multiple Rossiter modes.

In order to quantitatively assess the similarity of the POD modes for each cavity a method defined by Rempfer & Fasel (1994) was employed where the similarity variable was calculated according to Equation 7–3 .

$$\gamma_{ij} = \left| \left(\vec{\Phi}_1^i \right) \left(\vec{\Phi}_2^j \right) \right| \tag{7–3}$$

The subscripts one and two refer to alternate cavity configurations while the superscript i,j refer to the POD mode. The similarity will be equal to one if the compared modes are identical or zero if completely dissimilar due to the orthogonality of the POD modes. Figure 7-21 illustrates the similarity computed for the baseline and suppressed cases along with the suppressed cases compared to one another. Comparing the unsuppressed and suppressed modes it is evident the best similarity occurs at the first mode with the larger diameter rod correlating significantly better. There is evidence of relatively weak correlation off the diagonals particularly under the first five modes for each suppressed case. For modes greater than five the similarity is weak or even non-existent in most cases.

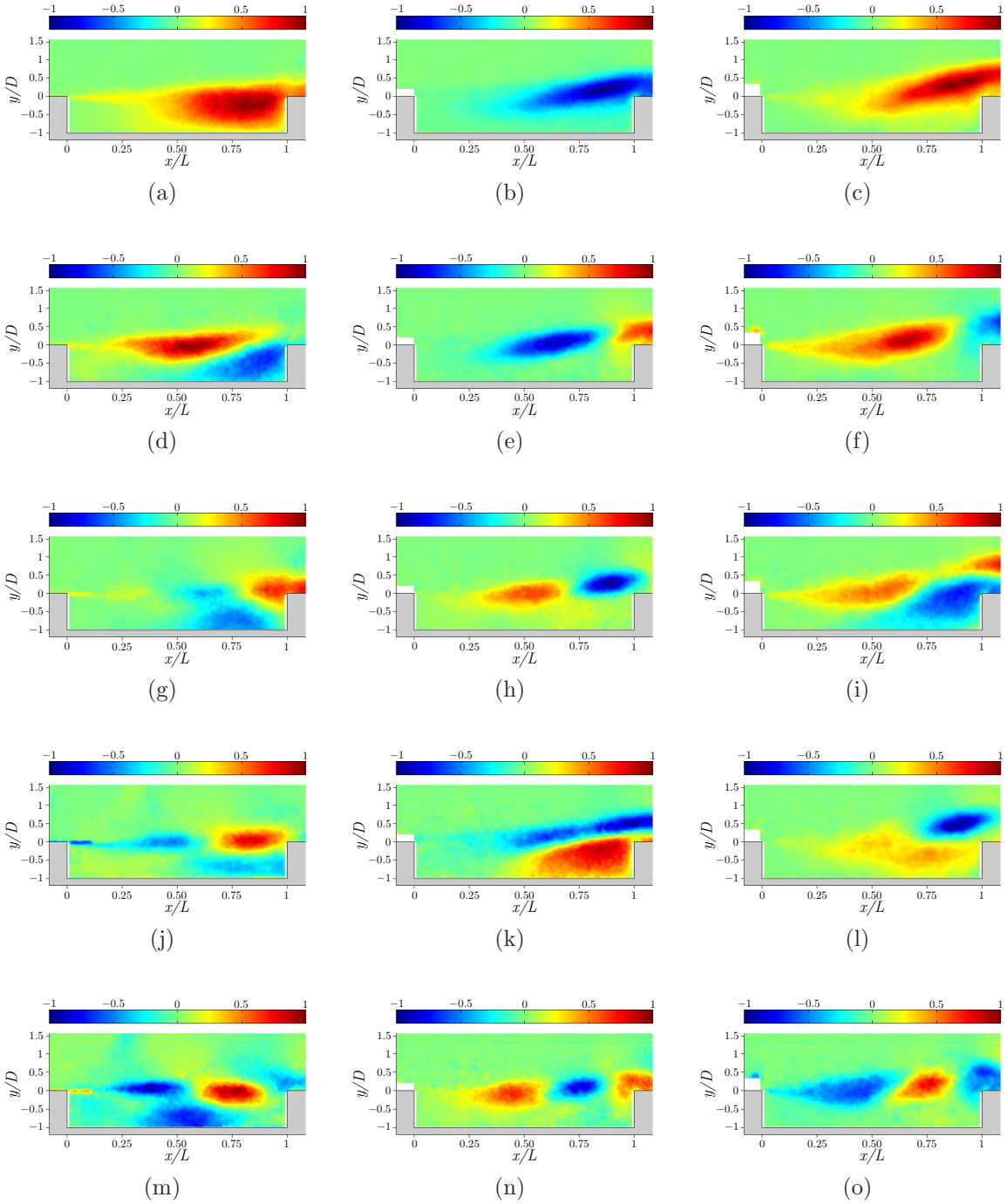

Figure 7-19. First five POD modes based on the streamwise fluctuating velocity for the full span cavity. Columns: (a) Baseline (b) $d^* = 0.21, G^* = 0.08$ (c) $d^* = 0.57, G^* = 0.57$. POD modes are sequential from top of page down.

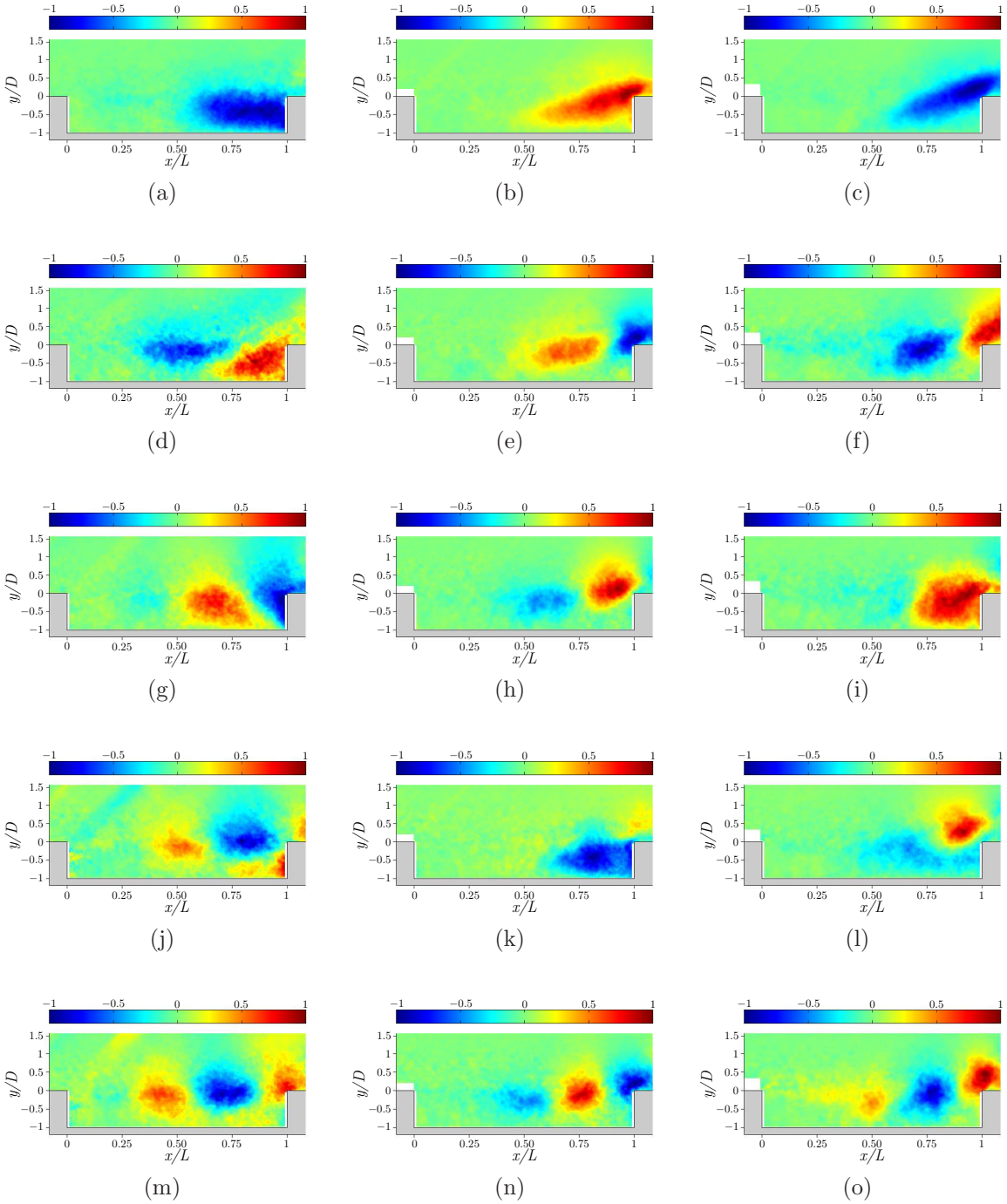

Figure 7-20. First five POD modes based on the normal fluctuating velocity for the full span cavity. Columns: (a) Baseline (b) $d^* = 0.21, G^* = 0.08$ (c) $d^* = 0.57, G^* = 0.57$. POD modes are sequential from top of page down.

A comparison of the similarity between the large and small diameter rod shows a better established correlation pattern on the diagonals. This indicates the resolved features exist in nearly the same spatial reference between the two rods. This implies each rod effects the shear layer in a similar manner.

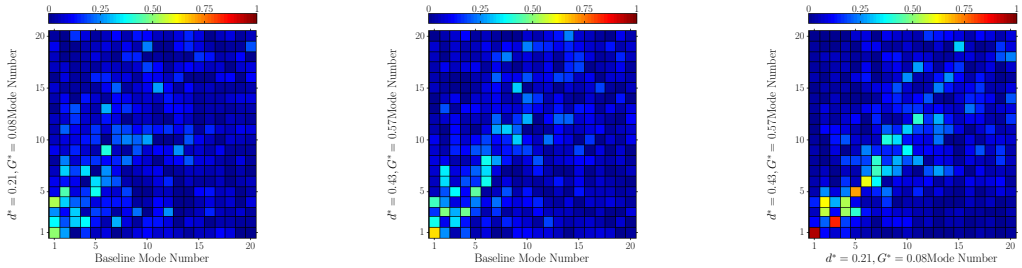

(a) (b) (c)

Figure 7-21. Full span POD spatial correlation map for the first 20 modes.

7.2 Finite Span Cavity

This section will present flowfield measurements which will be focused primarily on the finite span cavity configurations. The baseline cavity and two suppressed configurations which are identical to the full span cavity will be discussed. A brief discussion regarding the flowfield differences in the finite and full span cavity is included to further contrast the two cavities.

It should be noted that for all plots presented the vectors falling in close proximity to the edge of the cavity sidewall have been removed. This was necessary due to glare at the side lip of the cavity. Figure 7-22 shows a raw image of an instantaneous seeded flowfield for the baseline cavity highlighting the illuminated tracer particle and the edge of the cavity sidewall. The masked regions were determined by averaging the mean intensity of the unprocessed tracer-images. Appropriate threshold values where applied to clearly identify high intensity pixels and subsequently "masked" for the PIV vector calculations.

7.2.1 Full and Finite Span Flowfield Comparison

A comparison of the full and finite span cavity mean flowfields are presented in Figure 7-23. The finite span cavity shear layer penetrates much deeper inside the cavity which

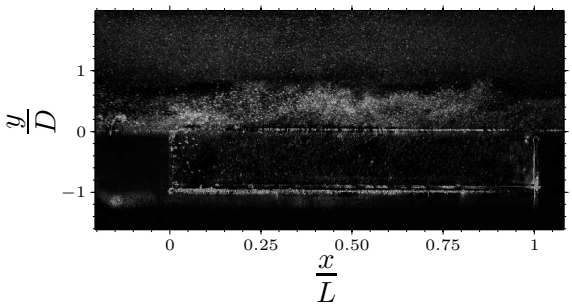

Figure 7-22. Example of seeded flowfield illustrating edge of cavity sidewall.

is apparent by the more aggressively turned velocity vectors. The flow is likely forced into the cavity due to the flow spillage over sidewalls. The primary recirculation region has been forced towards the center of the cavity with the origin located approximately at the midpoint. The increased crossflow inside the finite span cavity is believed to be the primary factor leading to the reduced pressure fluctuations.

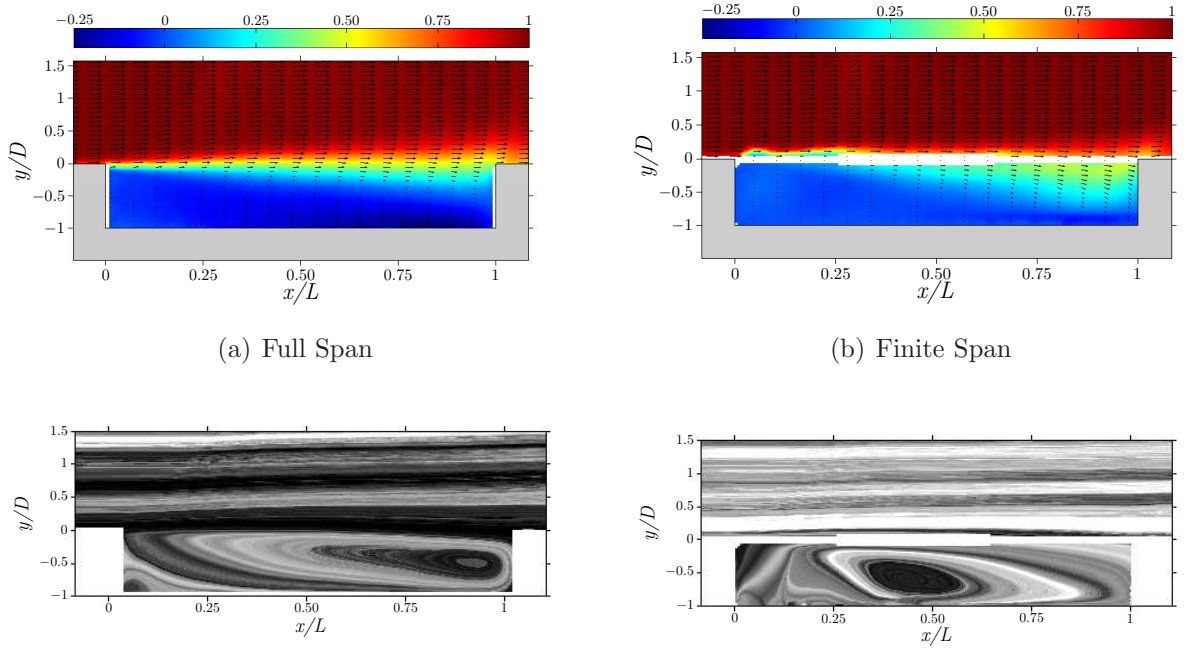

(a) Full Span

(b) Finite Span

(c) Full Span

(d) Finite Span

Figure 7-23. Comparison of full and finite span cavity streamwise velocity contours.

7.2.2 Mean Flowfield

Figure 7-24 illustrates the contours of the mean streamwise flowfield for the baseline and two controlled cases. The baseline cavity flow shows a shear layer that penetrates deep inside the cavity roughly $\frac{y}{D} = 0.75$ with velocities on the order 45% of the freestream velocity. As the rod diameter and gap height are increased the streamwise velocity inside the cavity decreases while the reversed flow becomes more prominent and is easily seen when examining the velocity vectors for each configuration. The streamlines and velocity vectors in and immediately surrounding the shear layer remain nearly parallel to the streamwise flow initially then turn into the cavity around $\frac{x}{L} = 0.5$. Examining Figure 7-24 it is easy to see the shear layer has been broadened by the trailing edge and the penetration of the streamwise velocity has been largely reduced for the suppressed cavities. As the rod diameter and gap height is increased ($d^* = 0.43, G^* = 0.57$) it also becomes apparent that the shear layer is further broadened and lower streamwise velocity flow impinges on the aft wall. Figure 7-25 illustrates the streamlines for each cavity. Due to the missing data around the cavities lip line these plots appear disjoint and it is hard to follow some of the recirculation patterns. The baseline cavity interior flow is dominated by a single clockwise rotating recirculation bubble that spans 75% of the cavity length and is centered at $\left(\frac{x}{L}, \frac{y}{D}\right) = (0.5, -0.5)$. The primary clockwise rotating recirculation bubble inside the cavity is moved near the cavity trailing edge for the large diameter rod when compared with the baseline or small rod cavity. The vertical location of the origin of this recirculation region remains insensitive to the baseline or suppressed cavity configuration. The maximum recirculation velocity was found to be nearly 10% of the free stream velocity for the baseline cavity and up to 20% for the suppressed cavities which was located near the cavity floor. The cavity midpoint showed recirculation velocities near 5% and 10% of the freestream values for the baseline and suppressed cavities respectively. The streamlines indicate what appears to be a secondary counter-rotating recirculation

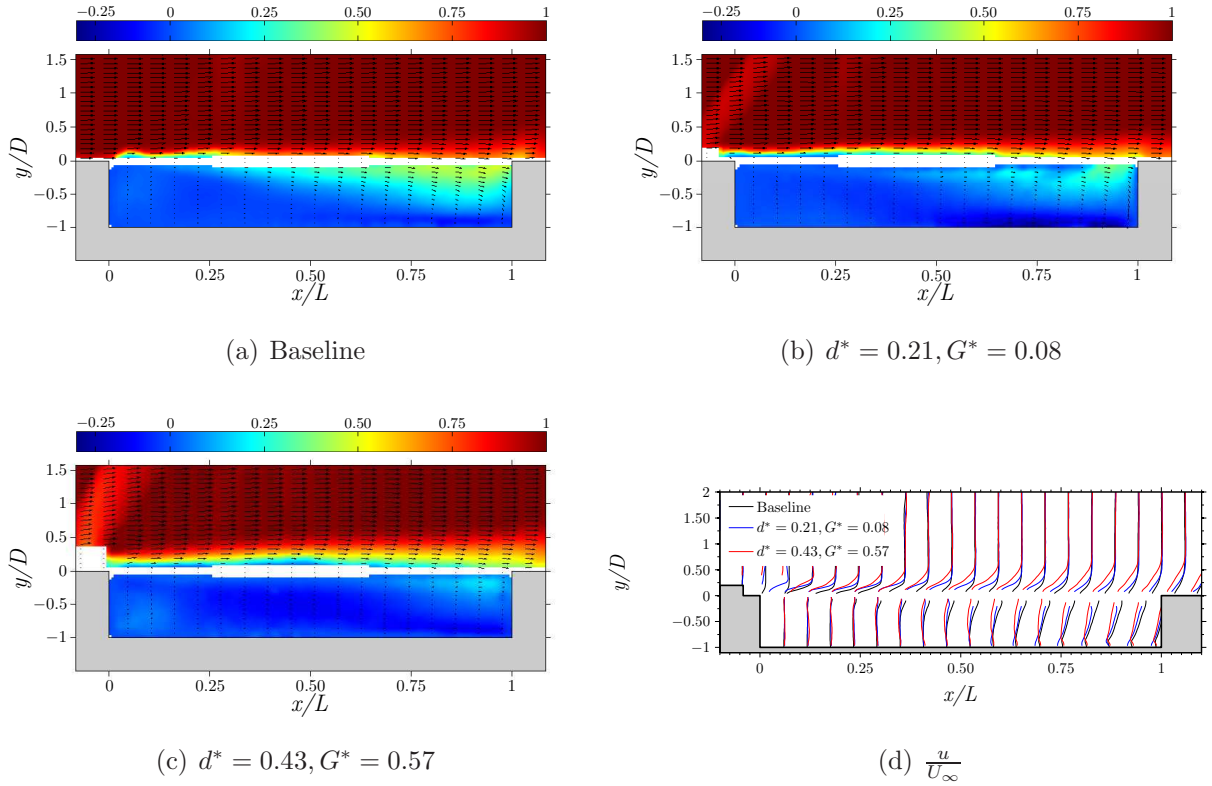

(a) Baseline

(b) $d^* = 0.21, G^* = 0.08$

(c) $d^* = 0.43, G^* = 0.57$

(d) $\frac{u}{U_\infty}$

Figure 7-24. Finite span cavity mean streamwise velocity contours and profiles.

region that spans $0 \leq \frac{x}{L} \leq 0.25$ of the cavity for each cavity which is more prominent than what was previously shown for the full span cavity.

7.2.3 Turbulent Flowfield

The effect of the rods presence on the turbulent flowfield for the finite span cavities are presented in this section. Figure 7-26 through Figure 7-28 show the contours and profiles for the mean and turbulent flowfields respectively. The fluctuations are on the same order as the full span cavity nearly 35% and 15% of the free stream flow for the streamwise and wall normal fluctuating velocities respectively for the baseline cavity. Examining the profiles it is seen that the estimated point of maximum streamwise fluctuation appears to shift downward into the cavity. Each rod seemed to have little effect on the overall magnitude of the streamwise or normal RMS velocity fluctuations though it should be noted this effect could be hidden by the missing vectors through the shear layer.

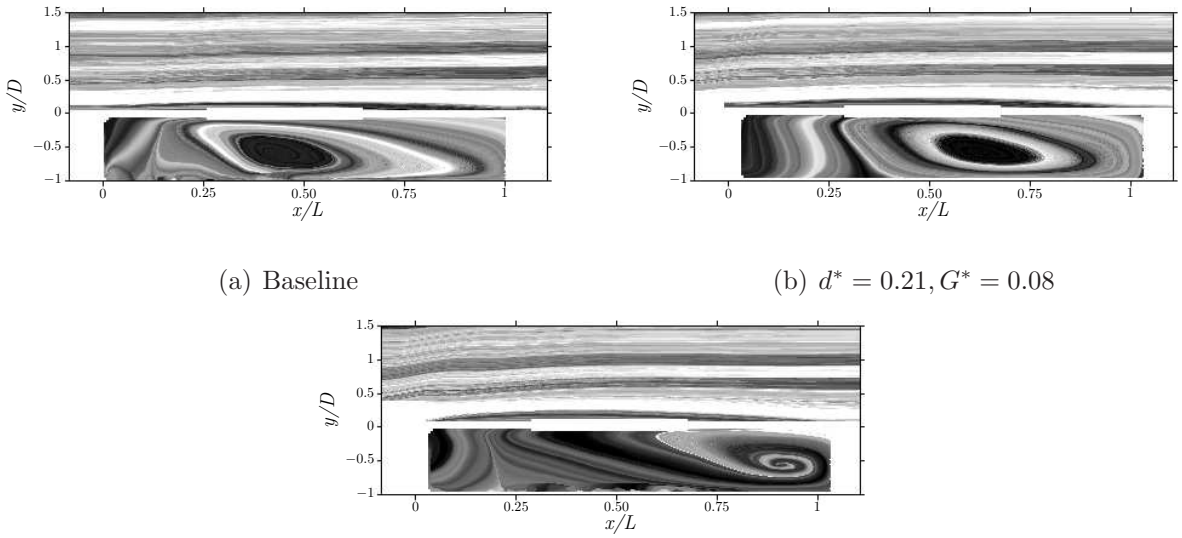

(a) Baseline

(b) $d^* = 0.21, G^* = 0.08$

(c) $d^* = 0.43, G^* = 0.57$

Figure 7-25. Full span cavity mean streamlines.

Most notably the rods exhibited the capability to shift the point where the maximum fluctuation above the cavity lip consistent with full span cavity though not as drastically. For the finite span cavity the potential lifting of the shear layer is in constant battle with the flow spilling into the cavity from the sidewalls tending to inhibit the overall lofting effect. The larger diameter exhibited a greater displacement of the peak RMS values which becomes more evident as you progress towards the leading edge of the cavity.

Instantaneous images of the density gradient for the baseline and suppressed cavity are illustrated in Figure 7-29. The images clearly show the shear layer lifted above the aft wall which results in reduced gradients inside the cavity. It should be noted that although this is only one single representation of this phenomena, each snapshot illustrated similar behavior. This supports the notion of the feedback mechanism being disrupted inside the cavity by altering the aft wall impingement location. Furthermore, this supports the discussion based on the pressure correlation analysis presented in Chapter 6.

Arunajatesan *et al.* (2002, 2003) performed high fidelity numerical simulations using a rod as a suppression device for subsonic flow. Through an analysis of the turbulent

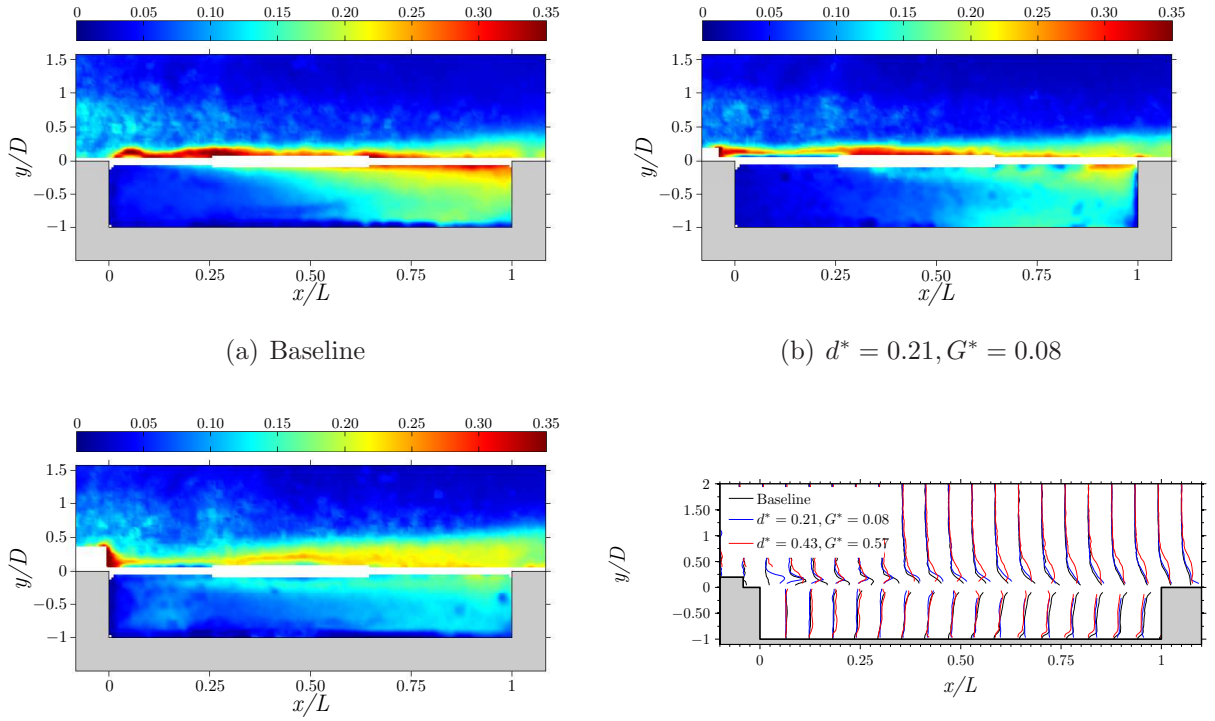

(a) Baseline

(b) $d^* = 0.21, G^* = 0.08$

(c) $d^* = 0.43, G^* = 0.57$

(d) $\langle u_{\mathrm{rms}} \rangle$ profiles

Figure 7-26. Finite span mean streamwise turbulent velocity contours.

kinetic energy budget they report the addition of negative production alters the balance of production and dissipation commonly found in free shear flows (or in this case, similar to baseline cavity flows). They explained the energy budget was dominated by dissipation rates due to the small scale structures in the shear layer. There existed lower production rates due to the addition of the negative production a direct artifact of the turbulence generated by the oscillating rod wake. These coupled events, they argue, are likely the driving mechanism for the reduction of the resonance in the cavity. Although the energy budgets could not be extracted from the measurements the decreased mean shear throughout the shear layer $\left(\frac{\partial U}{\partial y}\right)$ is consistent with this notion.

7.3 Summary

Flowfield measurements for the full and finite span cavities with and without suppression were presented in this chapter. The flow spilling into the cavity for the finite

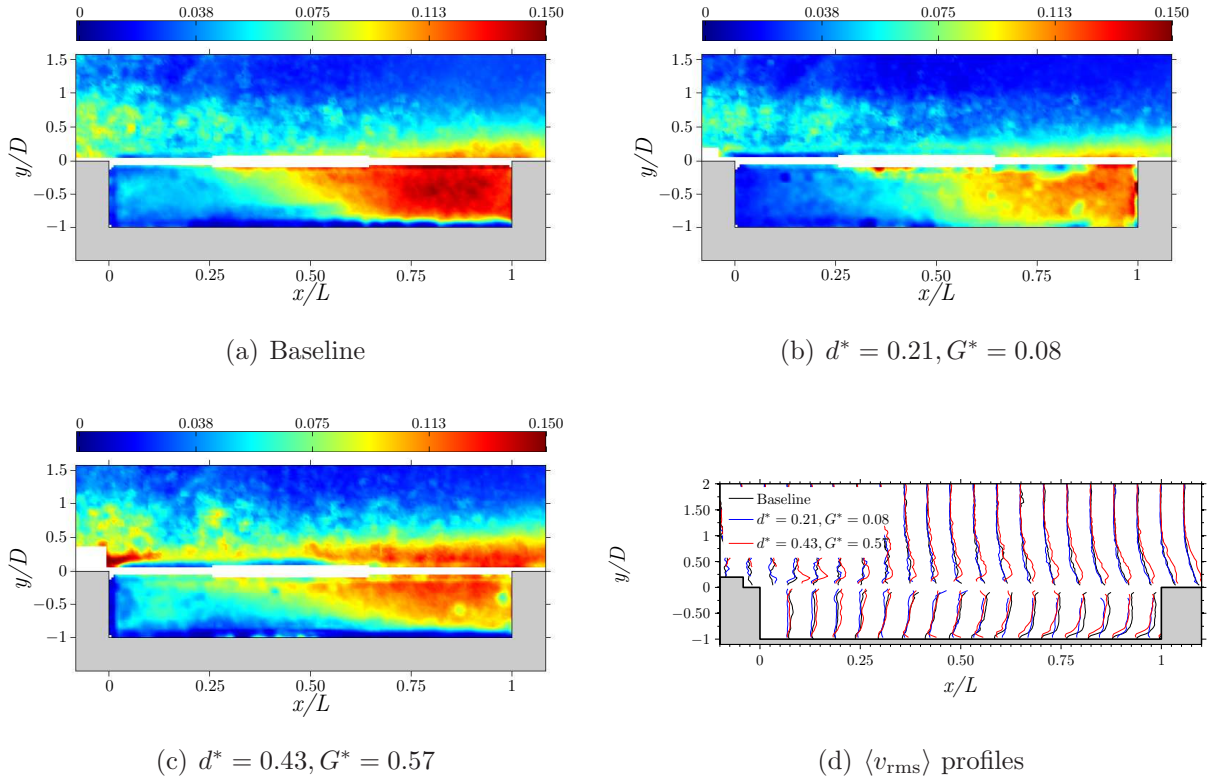

(a) Baseline

(b) $d^* = 0.21, G^* = 0.08$

(c) $d^* = 0.43, G^* = 0.57$

(d) $\langle v_{\text{rms}} \rangle$ profiles

Figure 7-27. Finite span mean normal turbulent velocity contours.

span case is believed to result in a different baseline interior cavity flow. The primary recirculation region is shortened and shifted towards the center of the cavity for the finite span cavity. The mean turbulent flow fields for these two cavities share similar intensities albeit the flow penetrated deeper into the finite span cavity. The enhanced mixing of the finite span cavity leads to slightly elevated fluctuating velocities and counter-intuitively, lowers the pressure fluctuations inside the cavity. The enhanced mixing on the cavity floor likely hinders and dampens the propagation of disturbances inside the cavity which leads to a disrupted feedback mechanism thus lowering the magnitudes of the resonant tones. To this end, the suppression levels realized appear to be driven by the same mechanism for each cavity as the observed turbulent field reductions and trends were very similar.

The use of two-point statistics revealed the normal or axial turbulent velocity evolution became elongated in the direction examined. These regions were aligned with

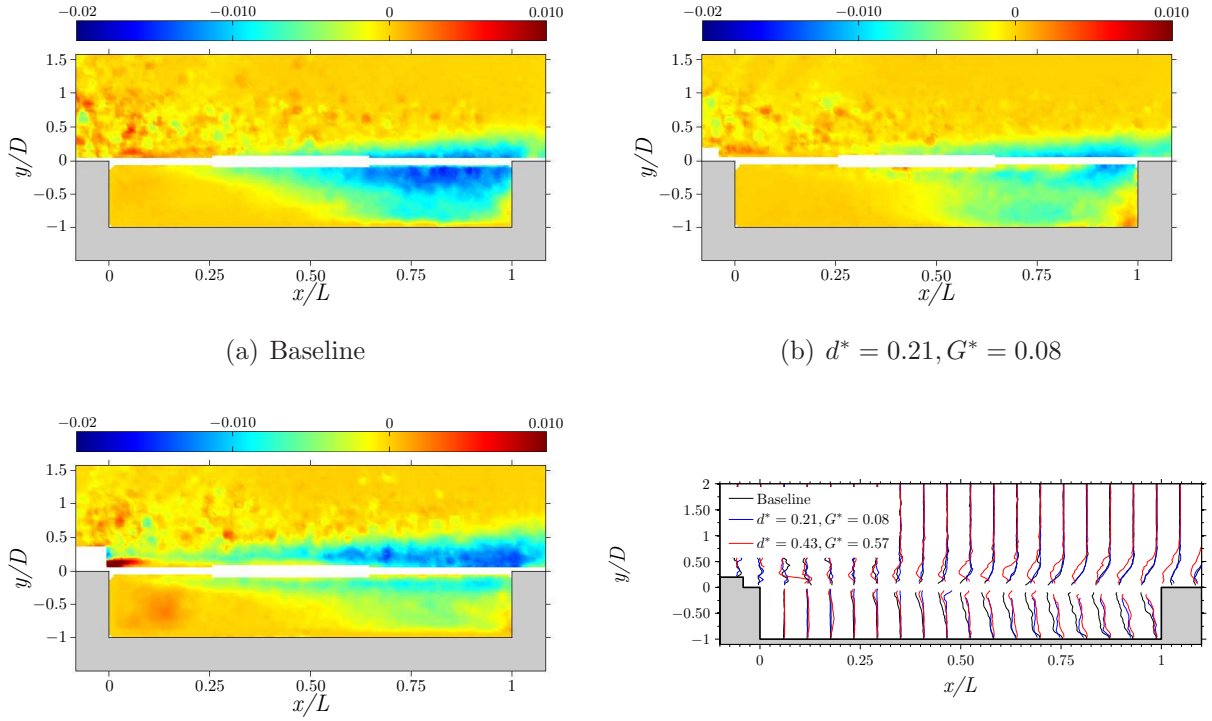

(a) Baseline

(b) $d^* = 0.21, G^* = 0.08$

(c) $d^* = 0.43, G^* = 0.57$

(d) RSS profiles

Figure 7-28. Finite span mean streamwise RSS contours.

or slightly turned into the cavity for the baseline cavity whereas the suppressed regions were deflected away from the cavity lip immediately at the leading edge of the cavity and lifted above the aft wall by the trailing edge. The examination of POD modes further supported that the spatial streamwise organization of the turbulent structures was altered when controlled. The well established structures that were identified inside the cavity for the baseline cavity where typically not present with the controlled cavities and tended to be lifted higher above the cavity lip line.

The presence of the rod was shown to decrease the mean shear gradient (more effectively for the large rod placed at the top of the boundary layer) in the shear layer. The rod was also able to shift the point of maximum shear away from the aft wall. A weaker wave originating at the aft wall as explained in the summary of Chapter 6 coupled with the flowfield visualization presented in this chapter, clearly demonstrate the

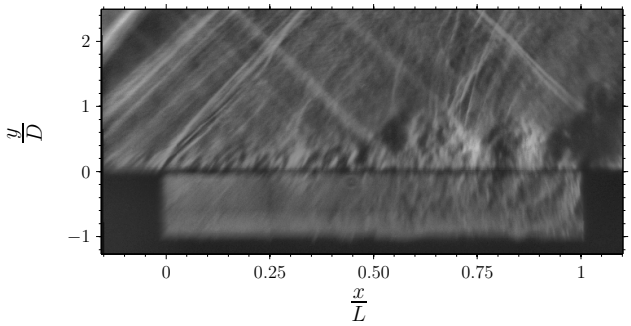

(a) Baseline

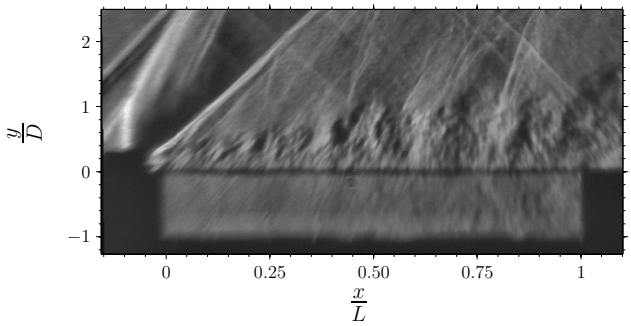

(b) $d^* = 0.41, G^* = 0.57$

Figure 7-29. Selected instantaneous Schlieren images for baseline and suppressed ($d^* = 0.43, G^* = 0.57$) configurations from the finite span cavity.

impingement point on the aft wall of the cavity has been drastically altered. It is plausible to associate the reduced pressure fluctuations with the suppression of the flapping motion of the shear layer or the lofting of the shear layer which would in turn flap above the cavity lip line. This would result in lower speed flow impinging on the cavity aft wall relative to the baseline case. The suppression of the flapping motion could also be linked to the increased thickness of the shear layer. The increased thickness could be tied to increased turbulence levels in the approaching boundary layer at the leading edge as reported in Ukeiley *et al.* (2004*b*).

CHAPTER 8
SIMULATION OF BASELINE AND CONTROLLED CAVITY

This chapter will focus on discussing the results of the CFD simulations using the methods outlined in Chapter 4. The simulations were run for the baseline and controlled cavity with $d^* = 0.43, G^* = 0.58$. This configuration was previously shown (Chapter 6) to be the most effective control arrangement. The chapter will start with a discussion on the validation effort for the simulations and will then progress similarly through the data analysis as was performed in Chapter 6 and Chapter 7. Results will be presented for fluctuating pressure measurements, mean flowfield and mean turbulent flowfield in conjunction with two-point statistics and POD.

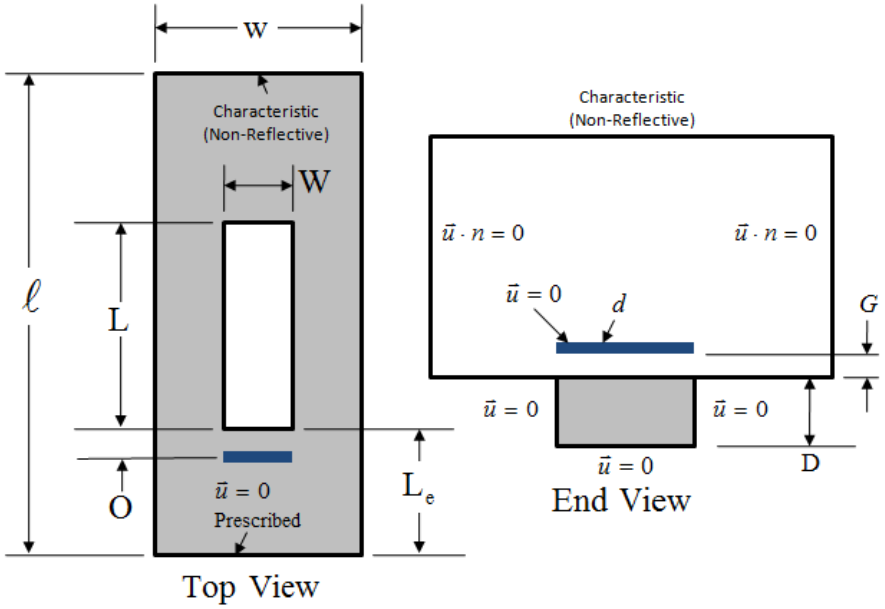

Figure 8-1. Geometry and boundary conditions for the numerical simulations.

The geometry and boundary conditions are illustrated in Figure 8-1 with the physical parameters listed in Table 8-1. All solid surfaces used a classical no-slip boundary condition except the test-section side walls where a slip boundary condition was applied. More details of the prescribed boundary condition are found in Chapter 4. The remaining boundary conditions applied were non-reflecting characteristic boundaries. A representation of the overset structured mesh is given in Figure 8-2 with the approximate point

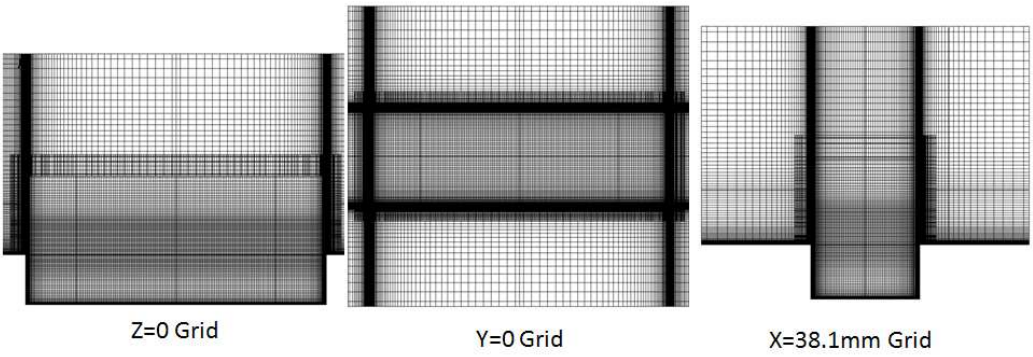

Figure 8-2. Structured overset grid.

count for the grid system given in Table 8-2. The baseline grid system consisted of three block to block superblocks. The cavity grid was overset with the test-section grid which required a collar grid for proper communication. The controlled configuration added a overset cylinder superblock which followed the grid refinement and topology outlined in Chapter 5. The solution was run on 60 Opteron 2.8GHz Central Processing Units (CPU) and each simulation required on average 8.6×10^4 CPU hours of computation time.

The selected baseline cavity mesh (fine grid) consisted of ten million nodes (16 million for the controlled configuration) including the collar grid. The distribution of points were maximized inside the cavity and shear layer region in hopes of lowering the overall eddy viscosity introduced by the turbulence model. The maximum length of a cell in any coordinate direction, given by Δ, did not exceed $\Delta \approx 0.10L$. This constraint was applied within the cavity and for a distance D outside and around the cavity to adequately resolve the shear layer. There were a total of 51 points located in approaching boundary layer with a first wall spacing of $\frac{y}{\delta} = 4 \times 10^{-4}$ leading to a $y^+ < 2$. The point distribution in the normal direction was specified using a hyperbolic tangent profile and the cell stretching ratio in any coordinate direction was kept under 20%.

Table 8-1. List of dimensions (mm) referring to Figure 8-1.

L	D	W	ℓ	w	L_e	h	δ	O	d	G
76.2	12.7	25.4	152.4	76.2	38.1	50.8	3.8	3.2	1.5	2.0

Table 8-2. Computational grid sizes for the baseline cavity.

Grid	Points	i	j	k
Cavity (Fine)	$7.2x10^6$	322	121	111
Cavity (Coarse)	$3.5x10^6$	151	51	51
Test-Section	$2.8x10^6$	251	71	151

Each simulation was run at a constant physical time step of $dt = 5 \times 10^{-7}$s which was corresponded to the physical time step used in the simulations presented in Chapter 5. The solution was marched forward sixteen periods based on the lowest predicted Rossiter tone to allow the flow to achieve statistical stationarity. PSD plots were computed with a record length of 2^{14} using 75% overlap which resulted in a PSD frequency resolution of $f_r = \frac{f_S}{nfft}$ =122Hz. Ensemble averaging was used for mean flow and turbulent flowfield calculations where complete solution files were output every 20 iterations over the next 16 flow periods.

8.1 Validation of Cavity Simulations

A limited grid refinement study was conducted to evaluate how cell size effected the performance of both the solver and selected turbulence model. As a result of this study, it was also found that the original prescribed boundary layer (BL_1) velocities were not in good agreement with the typical experimental boundary layer. The original nozzle solution was choked at stagnation conditions that were not consistent with what was observed in the experimental observations. This led to velocities in the boundary layer that were on the order of 20% higher than expected and is consistent with the higher resonant tones observed in Figure 8-4(a). This error was resolved for the fine grid simulations only (BL_2). This leads to the grid resolution studies being conducted with different inlet profiles for the different grids however the results of the grid resolution studies are still believed to be valid.

Figure 8-3 illustrates random instantaneous snapshots of the Z-vorticity component for the baseline cavity with both the coarse and fine grids. The fine grid resolved structures on a smaller spatial scale indicative of the enhanced overall spatial resolution. Figure

8-4 illustrates the sensitivity of the fluctuating surface pressures measured on the cavity floor based on the selected approaching boundary layer and level of grid refinement. As expected, Figure 8-4(a) indicates the solution is equally sensitive to both the level of grid refinement and the approaching boundary layer. The aft wall spectra is compared in Figure 8-4(b) where the most notable differences are found in the frequencies of the resonant tones. Higher velocities in the approaching boundary layer resulted in higher resonant tones due to the increased convective velocity in the shear layer. The magnitudes of the higher frequency resonant tones were slightly exaggerated when compared with the corrected boundary layer. It should be noted that only the aft wall and floor were considered but the forward wall exhibited similar behaviors as well. Subsequently, it was decided to go with the the finer of the two grids for all of the analysis presented here.

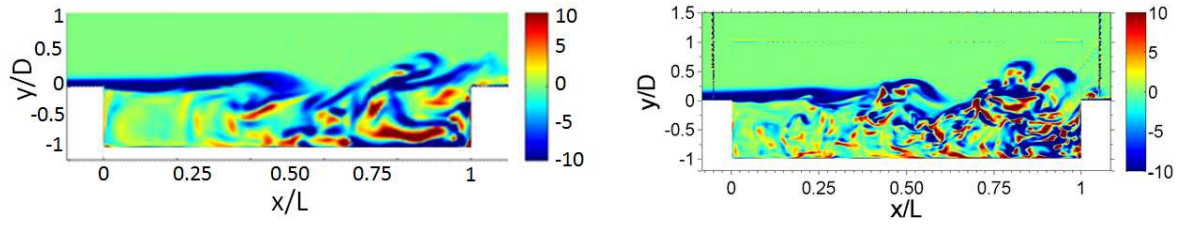

(a) Coarse (BL_1)

(b) Fine (BL_2)

Figure 8-3. Instantaneous snapshots of ω_z vorticity contours illustrating the combined grid refinement and corrected boundary layer effects.

Figure 8-5 illustrates a qualitative assessment of the flowfield based on the controlled cavity leading edge near-field. Figure 8-5(b) illustrates a random instantaneous snapshot of the tracer particle in the flowfield for the $d^* = 0.40, G^* = 0.57$ while Figure 8-5(a) illustrates a ω_z vorticity contour plot taken from a random snapshot of the simulation. Each image illustrates the complex interaction of the separated boundary layer aft of the cylinder and the wake of the cylinder. The general behavior of the cylinder interaction with the shear layer appears to be in fair agreement between the experimental observations and simulations.

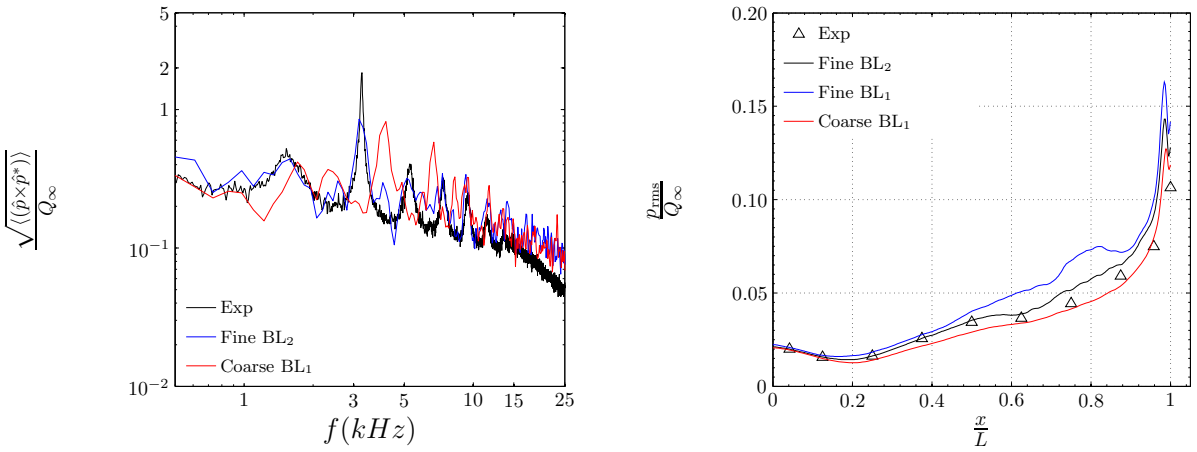

(a) PSD (b) p_{rms}

Figure 8-4. Effect of grid refinement on cavity fluctuating surface pressures. PSD plot measured on the aft wall at $\frac{y}{D} = -0.5$ and p_{rms} taken on the cavity floor at various axial positions

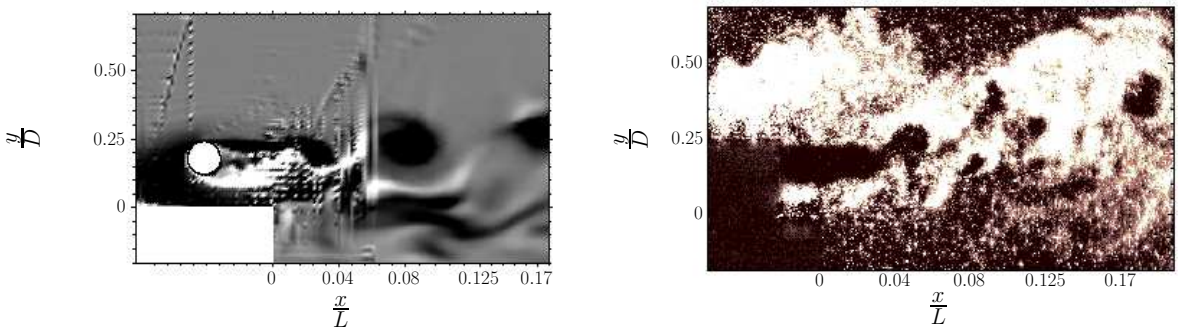

(a) CFD (b) Experiment

Figure 8-5. Instantaneous snapshot of tracer particle in the cylinder near field and CFD vorticity illustrating the near field cylinder flow dynamics.

The simulations were further validated with experimental pressure and velocity field measurements that were presented in Chapter 6 and Chapter 7. The mean streamwise velocity contours with vectors are qualitatively compared in Figure 8-6(a) and Figure 8-6(b) respectively. There is good agreement between the simulation and experimental measurements for the baseline cavity which is illustrated here. The mean streamwise velocity in the shear layer and the mean streamwise turbulent velocity along with the flow penetration depth are in good agreement as demonstrated by Figure 8-6 and Figure 8-7.

The mean streamlines for the CFD simulation and experimental measurements are shown in Figure 8-6(c) and Figure 8-6(d). Each figure shows a primary recirculation bubble located near the center of the cavity though the numerical simulations have this bubble located slightly farther downstream. It should be noted that some error is anticipated in the experimental streamlines near the leading edge due to oil build up and difficulty in adequately seeding this region.

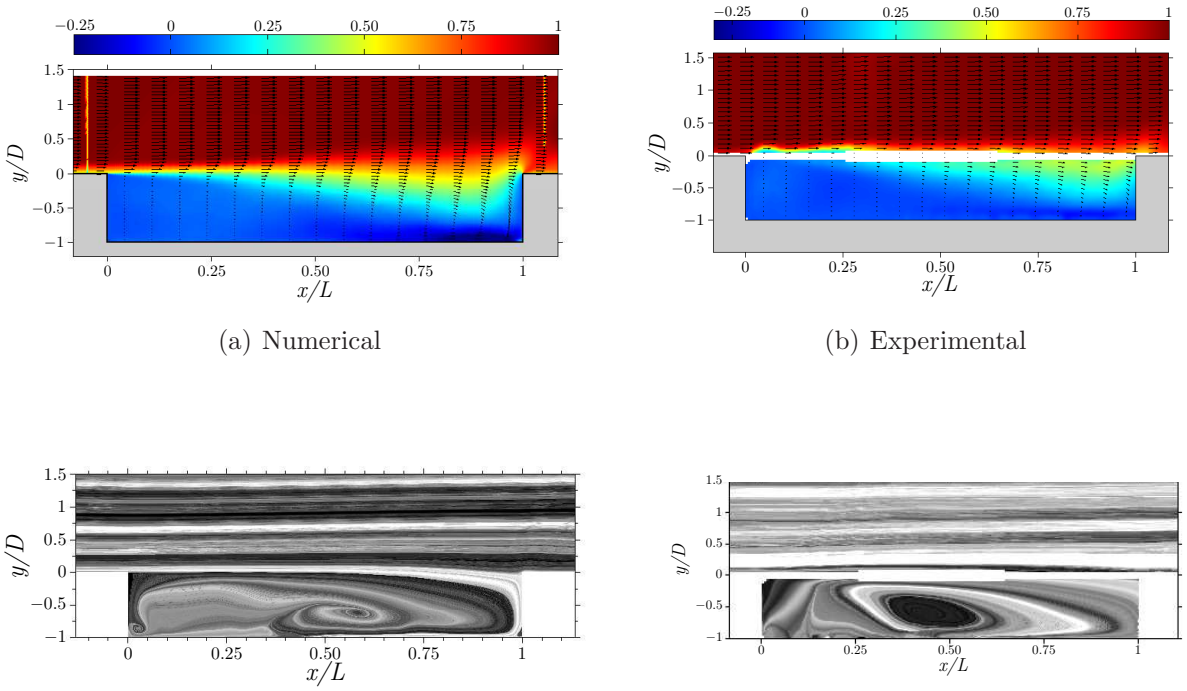

(a) Numerical

(b) Experimental

(c) Numerical

(d) Experimental

Figure 8-6. Experimental and numerical mean streamwise velocity contours and mean streamlines.

Mean streamwise velocity profiles and mean streamwise turbulent velocities are quantitatively compared in Figure 8-7 at select streamwise locations for the baseline cavity. The simulations and experimental observations are in good agreement with the differences found near the cavity floor near the trailing edge. The increased error in

these regions are likely attributable to the difficulties encountered in the experiment with measurements close to the wall (laser bloom) and inadequate seeding.

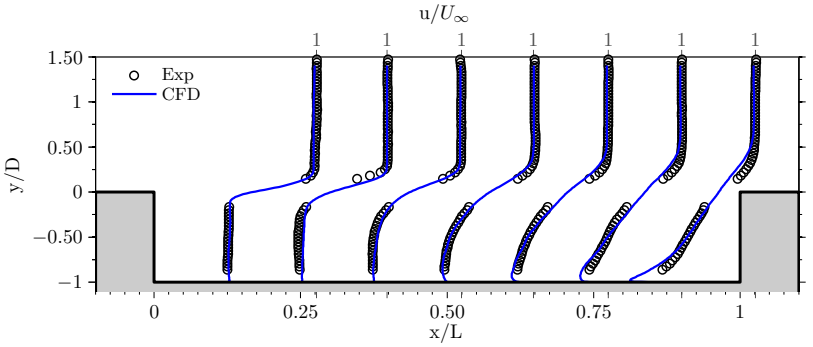

(a) Mean streamwise velocity

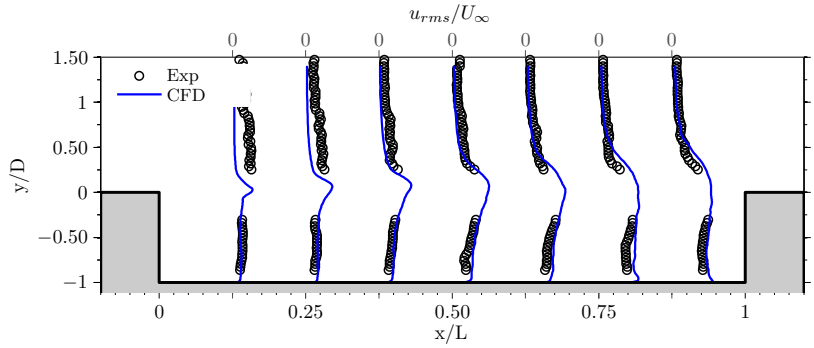

(b) Mean streamwise turbulent velocity

Figure 8-7. Experimental and numerical mean streamwise and turbulent velocity comparison.

A comparison of the aft wall spectra for the baseline and controlled cavity are presented in Figure 8-8(a) and Figure 8-8(b) respectively. The computational spectra agrees favorably with the experimental data for both cavities. The largest discrepancy is found in the magnitude of the dominant resonant tone and at decreased broadband accuracy at higher frequencies. The resolution of the peak tone magnitude is a function of the frequency resolution difference between the data where the experimental resolution was 11Hz and the numerical could only be resolved to 122Hz. The divergence of the solution at higher frequencies is likely attributable to the lack of spatial resolution, turbulence model limitations and implicit methods in the numerical scheme. In particular,

to fully resolve the broadband behavior at higher frequencies, one would need to approach resolution on the order of the Kolomogorov scale and RANS solutions are not capable of this due to the limitations discussed in Chapter 4. Figure 8-9(a) again shows good

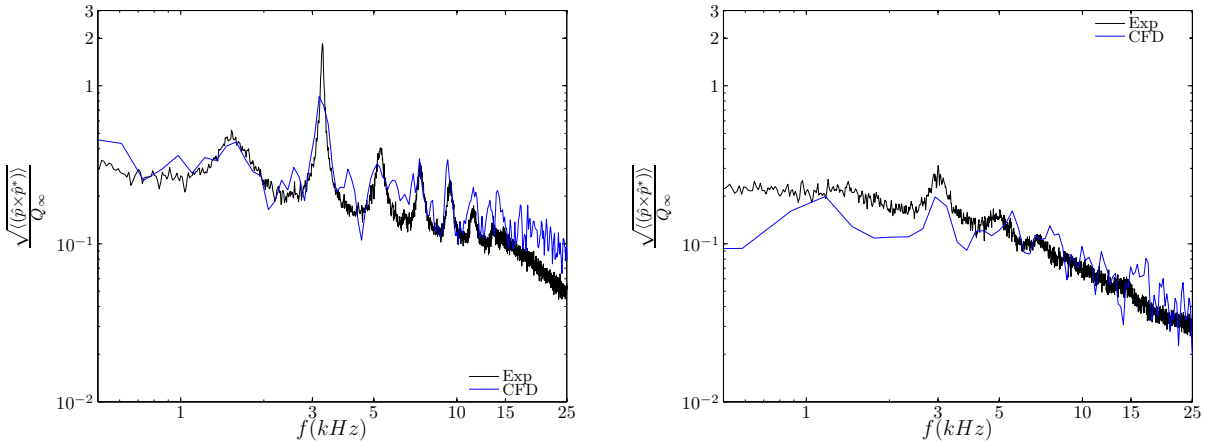

(a) Baseline (b) Controlled

Figure 8-8. Comparison of computational and experimental aft wall spectra taken at $\frac{y}{D} = -0.5$.

agreement in both trend and magnitude with the fluctuating surface pressures measured on the cavity floor for both baseline and suppressed cavities.

8.2 Instantaneous Flowfield and Pressure Measurement

Unsteady pressure measurements extracted from the cavity centerline at $z = 0$ are presented in Figure 8-9. The effectiveness of the rod as a passive suppression device is clearly evident where both resonant tones and broadband levels were reduced by similar levels to those observed in the experimental measurements. The spectra on the aft wall for the controlled case indicated a broad peak near 50kHz associated with the shedding of the rod which is in good agreement with PSD peaks illustrated in Chapter 5 for this size rod and gap height. It should be noted this peak has an amplitude an that is an order of magnitude lower than the dominant resonant frequency of the baseline cavity. This suggests the A/D limitation (45kHz) presented in Chapter 6 will only slightly effect the results of percent reductions for the experimental results. Cross and auto-

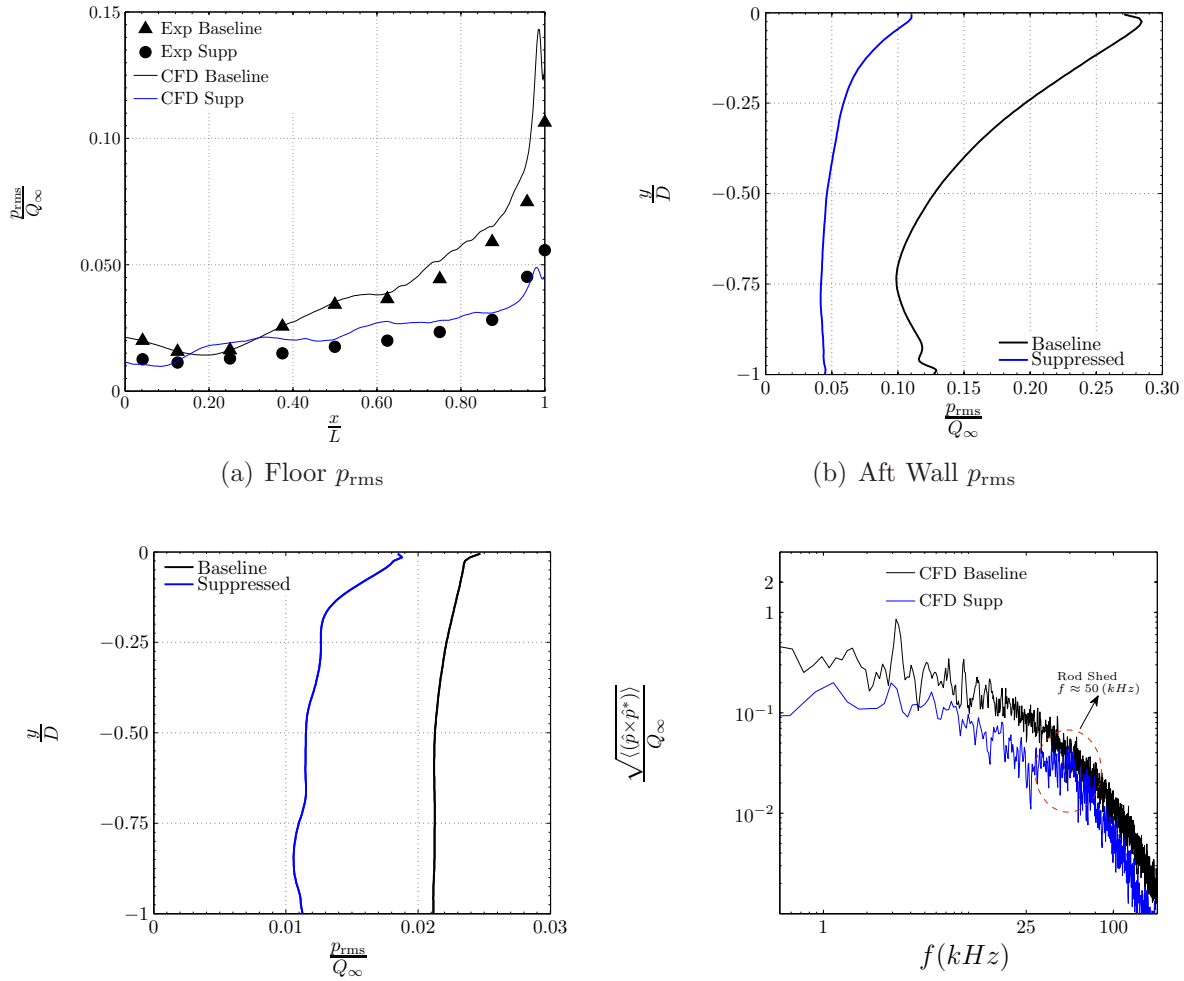

(a) Floor p_{rms}

(b) Aft Wall p_{rms}

(c) Forward Wall p_{rms}

(d) Aft Wall PSD

Figure 8-9. Baseline and controlled cavity fluctuating surface pressures on the aft wall, leading edge wall and floor. Spectra measured on the aft wall is at $\frac{y}{D} = -0.5$

correlations of the pressure for the aft wall at select locations on the floor and upstream wall are illustrated in Figure 8-10. Both the baseline and controlled cavity are in close agreement with the correlations presented in Chapter 6 for the finite span cavity. Table 8-3 contains the time lags, distance between correlated points and the calculated speed of the disturbance propagating upstream inside the cavity. The calculated disturbance propagates upstream nearly at the local speed of sound implying that the correlation is picking up the acoustic feedback traveling through the cavity for both the baseline and controlled configurations.

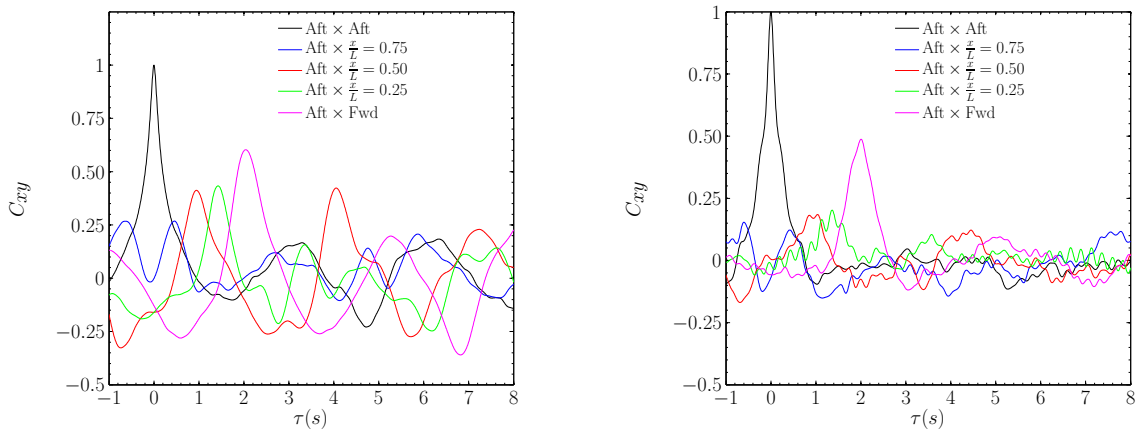

(a) Baseline

(b) Controlled

Figure 8-10. Baseline and controlled cavity auto and cross correlations.

Table 8-3. Cavity wave speed, time lags and distances.

Case	τ(s) $\times 10^{-4}$	$\Delta\frac{x}{L}$	a(m/s)
CFD Base	2.04	1	374
CFD Supp	2.00	1	381
Exp Base	2.11	0.75	361
Exp Supp	2.11	0.75	361

Though the correlations clearly demonstrate the rod's ability to effectively disrupt the feedback mechanism of the cavity flow as explained in Chapter 6, there was little effect on the speed at which these disturbances occur. The highly resonant phenomena of the baseline cavity which manifests itself as fairly smooth nearly sinusoidal oscillations is apparent in these plots. There is a notable lack of smoothness to the correlation profiles which tend to exhibit sharper peaks with finer scale noise for the controlled cavity. The levels of the correlated signal which are propagating upstream are being reduced closer to the background turbulence levels hence the correlations are noisier.

The shear layer of the controlled cavity is dominated by small scale structures which is qualitatively verified by examination of the baseline and controlled cavity instantaneous vorticity contours presented in Figure 8-11. It is evident from these figures that the wake of the cylinder appear to be rolling up after approximately two diameters and is clearly pulling in some of the fluid from the cavity shear layer. This interaction tends to tear off

clockwise rotating structures from the cylinder upper shear layer. There is no apparent alternate shedding from the upper and lower cylinder shear layer. These structures are introduced into the cavity shear layer in a periodic fashion similarly to that predicted by the vorticity contours illustrated in Chapter 5 for the $d^* = 0.41, G^* = 0.64$ simulation. The addition of these structures into the shear layer curbs the spanwise organization of the shear layer.

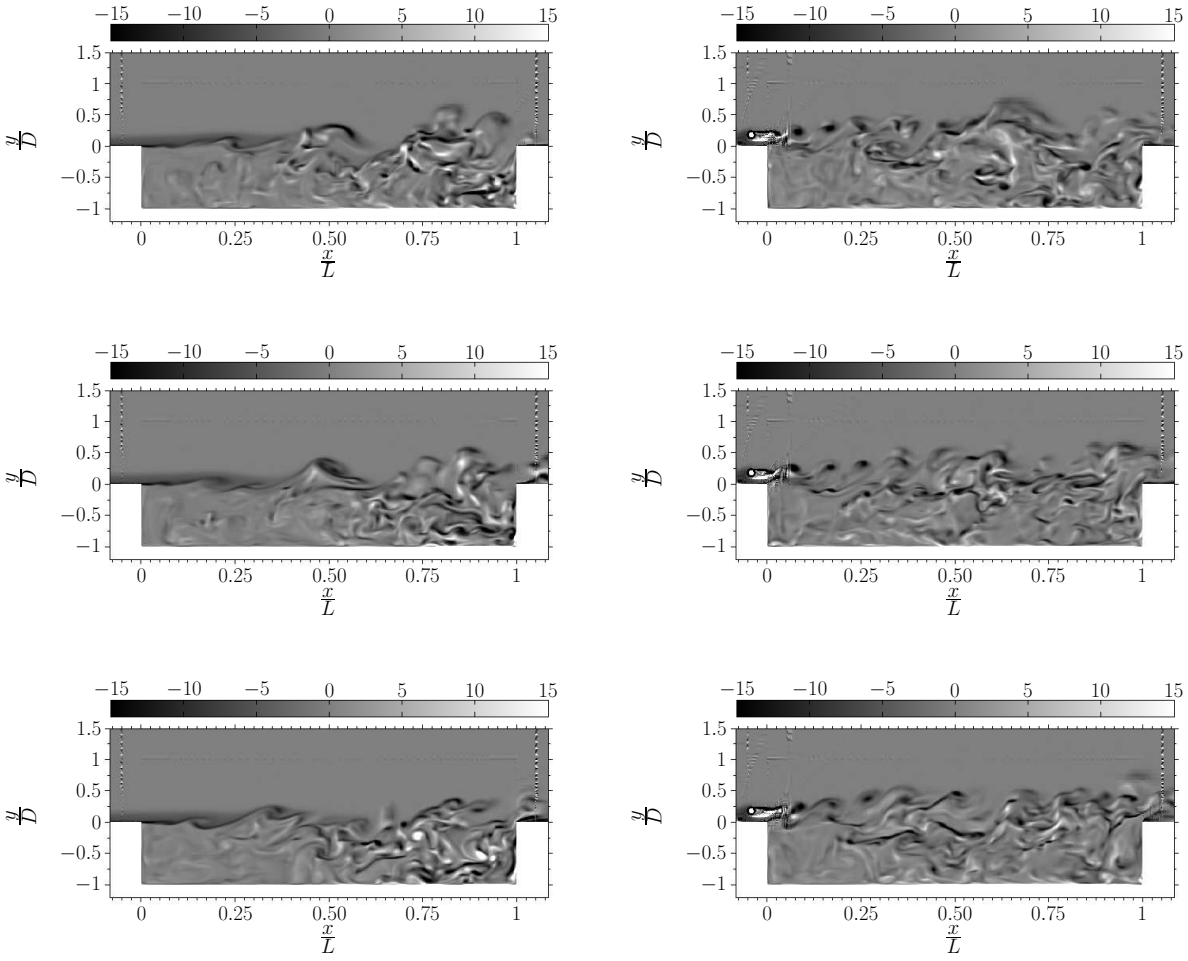

Figure 8-11. Instantaneous non-dimensional vorticity contours for the baseline and controlled cavity taken at 5×10^{-7}s intervals. The baseline cavity is shown in the first column and the controlled cavity in the next column.

8.3 Mean Flowfield

In this section the ensemble averaged mean flowfield will be analyzed and discussed. Mean streamlines for both cavities are presented in Figure 8-12. The baseline cavity is dominated by a large clockwise rotating recirculation region which covers from $0.35 \leq \frac{x}{L} \leq 1$. A much smaller localized counter-rotating recirculation bubbles is found on the cavity floor at the leading edge. The suppressed cavity exhibits a single dominant recirculation bubble as well which is centered near $\left(\frac{x}{L}, \frac{y}{D}\right) = (0.95, -0.375)$. The counter-rotating leading edge bubble has been enlarged and the the streamlines inside the bay indicate an aggressive upward trend off the cavity floor not realized in the baseline cavity. The freestream streamlines are slightly deflected away from the cavity in the normal direction for the controlled case.

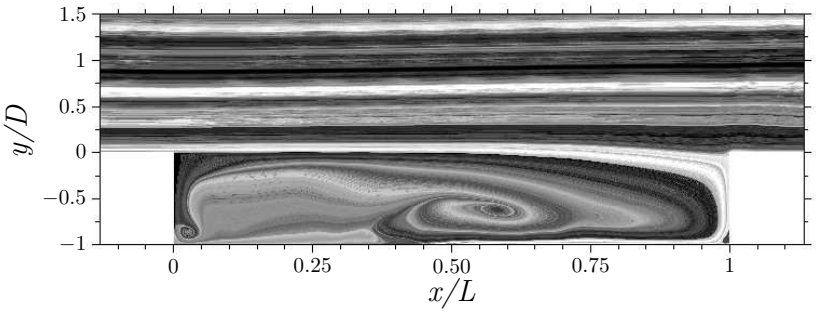

(a) Baseline

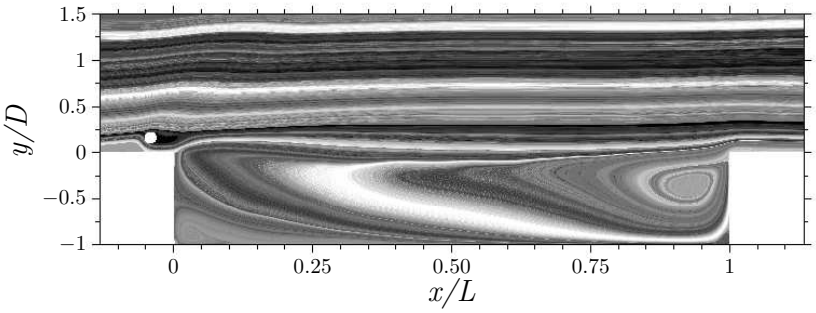

(b) Controlled

Figure 8-12. Baseline and controlled mean streamlines.

Each component of the mean velocity field is illustrated in Figure 8-13. Referring to Figure 8-13(a) and 8-13(b) the shear layer is clearly spread, most obviously near the leading edge, and lifted above the aft wall. The presence of the rod results in a stronger recirculation region inside the cavity. Examining the mean streamwise velocity contours and profiles the wake of the cylinder in the near field (blue in the contour plots) appears to be slightly deflected towards the wall similar to the simulations of Chapter 5.

Examining the vertical velocity component it is immediately noticed that the rod reduces the amount of inflow in the downstream portion of the cavity. The lifting of the shear layer results in a mean positive normal velocity field throughout the majority of the cavity not observed in the baseline cavity. Figures 8-13(e) and 8-13(f) show the mean span-wise velocity contours where it is apparent that the presence of the rod enhances the three-dimensionality of the flowfield inside of the cavity most notably at the leading and trailing edges.

The mean streamwise and normal velocity profiles are illustrated in Figure 8-14 at select axial positions. The presence of the rod wake is still clearly visible in the inflected velocity profile found near the leading of the cavity. The inflection clearly occurs below the rod centerline and is still has a strong presence at 3d downstream. This is consistent with results from Chapter 5 where the mean streamwise velocity profiles were also deflected towards the wall. The profiles still had a presence roughly 3d downstream with the inflection occurring at roughly $\frac{y}{\delta} = 0.60$ or near the bottom of the cylinder for each simulation. The mean streamwise velocity profile is effectively spread out through the entire shear layer while the recirculation velocity inside the cavity in the downstream portion is increased. The effect of the control on the mean normal velocity is visible where the flow direction in the downstream portion of the cavity is reversed between $0.50 \leq \frac{x}{L} \leq 0.875$. The flow influx at the trailing edge is vastly reduced with flow control. There is a notable increase the mean normal velocity immediately downstream of the

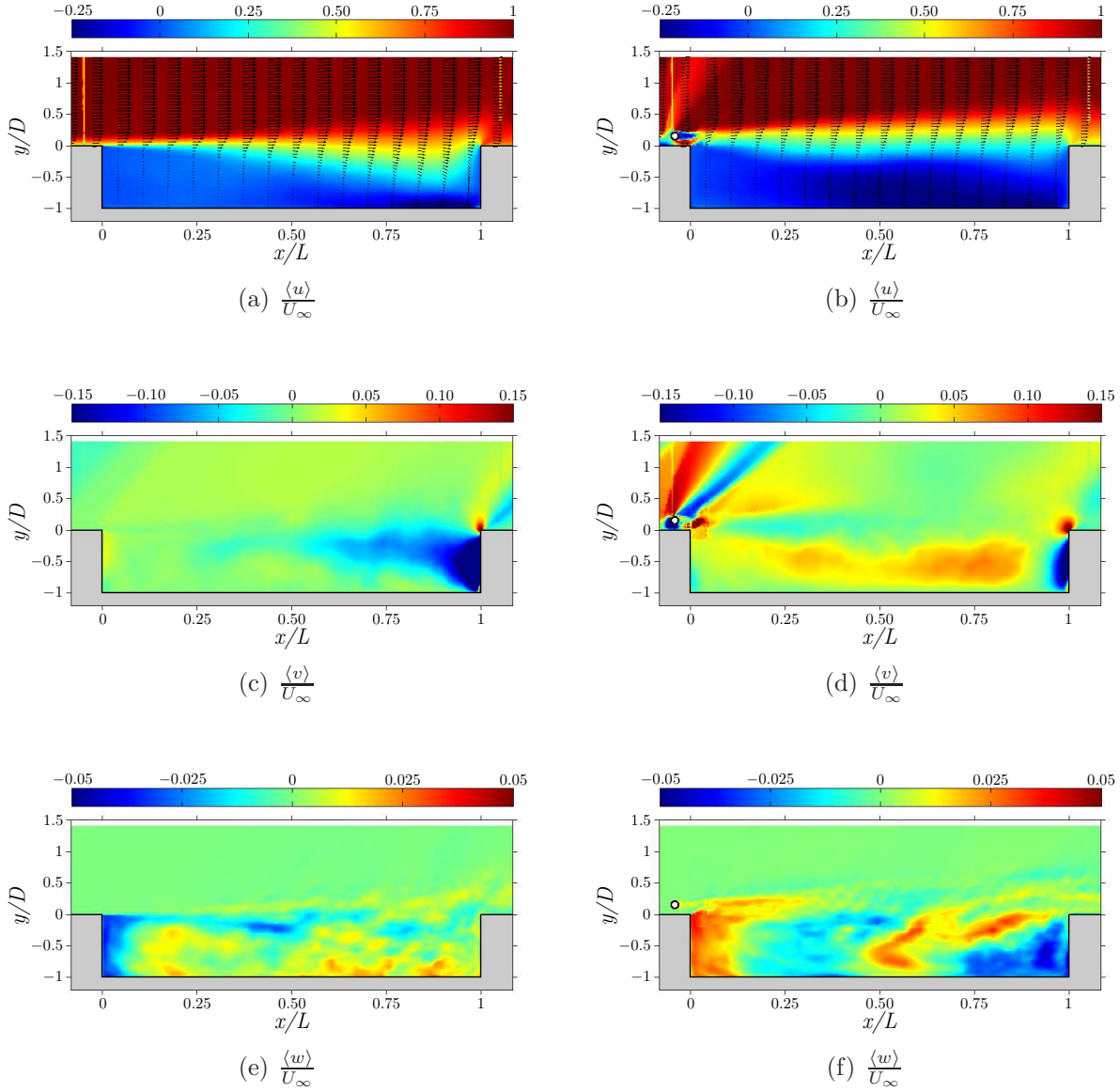

(a) $\frac{\langle u \rangle}{U_\infty}$ (b) $\frac{\langle u \rangle}{U_\infty}$

(c) $\frac{\langle v \rangle}{U_\infty}$ (d) $\frac{\langle v \rangle}{U_\infty}$

(e) $\frac{\langle w \rangle}{U_\infty}$ (f) $\frac{\langle w \rangle}{U_\infty}$

Figure 8-13. Mean velocity flowfield contours. Column (a) and (b) are the baseline and controlled cavity respectively.

cylinder, consistent with findings from Chapter 5, which is believed to initially deflect the shear layer away from the cavity lip line.

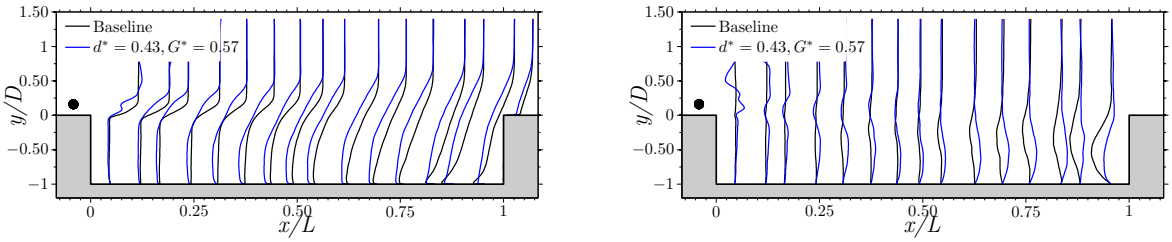

(a) $\frac{\langle u \rangle}{U_\infty}$ (b) $\frac{\langle v \rangle}{U_\infty}$

Figure 8-14. Mean streamwise and normal velocity profiles at various axial locations.

Contours of the mean vertical velocity component with velocity vectors at select streamwise locations on the yz plane are illustrated in Figure 8-15 and Figure 8-16 for the baseline and controlled cavity respectively. The three dimensionality of the cavity flow becomes clearer when examining these figures. The cavity flow is not only dominated by the main streamwise recirculation bubble as illustrated by the streamlines of Figure 8-12 but also exhibit two opposing rotating regions divided near the cavity centerline. These regions become more intense as the flow progresses towards the trailing edge of the cavity leading to more flow being pulled inside the cavity and increased mixing. The existence and consequence of these recirculation regions is what is believed to be the major difference when comparing the full and finite span cavities. The controlled cavity shows a similar trend where these two opposing recirculation regions gain intensity as one progresses towards the aft wall. The major difference is the direction of rotation, i.e., the presence of the rod reverses the direction of each recirculation region. When the cavity is controlled the shear layer is lifted above the cavity lip-line. This results in an altered pressure gradient which draws the flow into the cavity over the sidewalls and forces it out over the cavity lip near the centerline.

The vorticity thickness and location of maximum shear, calculated in a similar manner to the experimental data, is plotted in Figure 8-17(a) and 8-17(b) for each cavity.

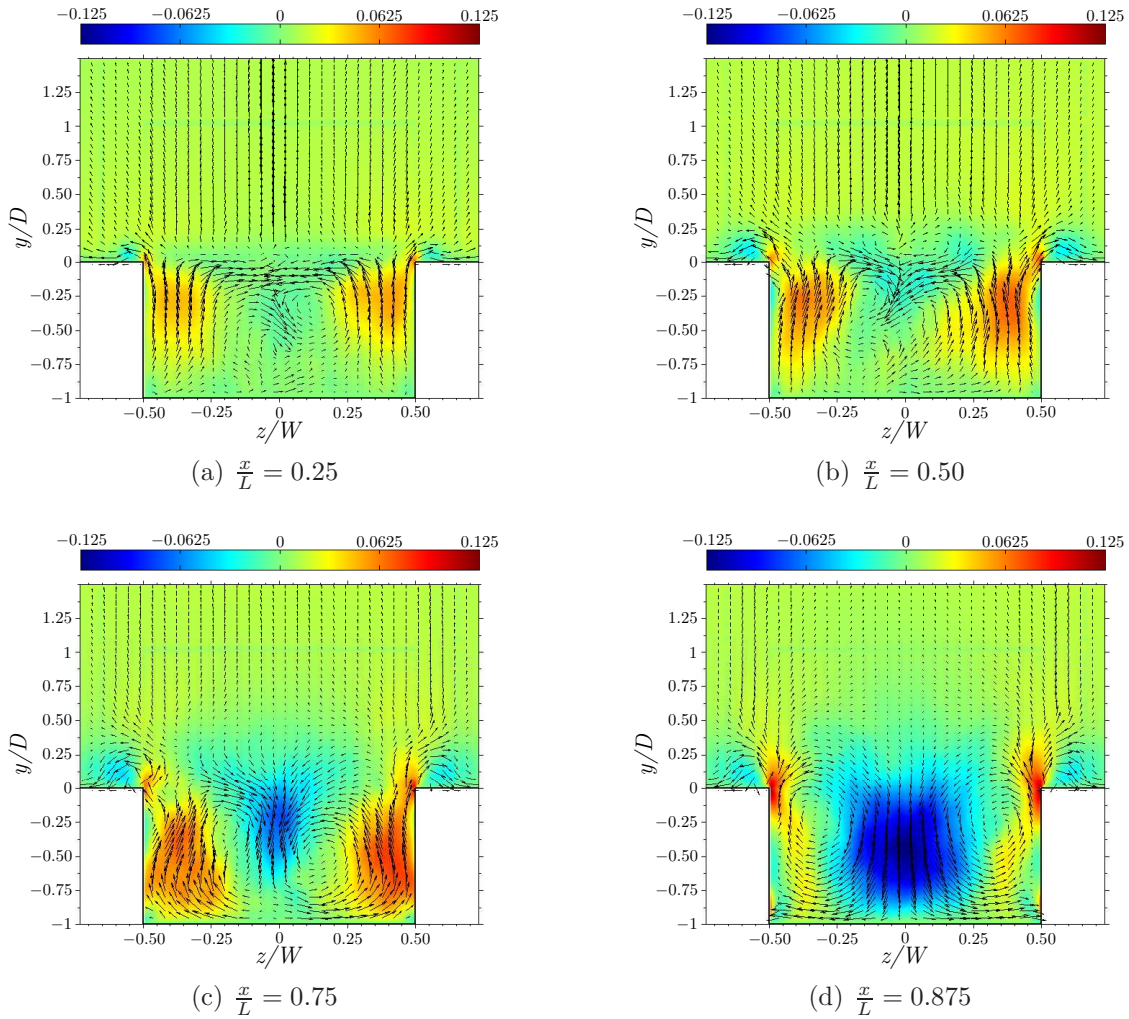

(a) $\frac{x}{L} = 0.25$ (b) $\frac{x}{L} = 0.50$

(c) $\frac{x}{L} = 0.75$ (d) $\frac{x}{L} = 0.875$

Figure 8-15. Baseline cavity mean normal velocity contours on the yz plane at various axial locations showing opposing recirculation regions.

The growth rate is seen to behave linearly with varying slopes that seem dependent on axial location. The baseline cavity exhibited growth rates of 0.22 over the first 5% of the cavity and dropped off to 0.08 over the next 30% of the cavity length. The shear layer appears to grow very aggressively over the next 60% of the cavity where rates approached the initial growth. The controlled cavity exhibited similar behavior with three fairly distinct linear growth rate ranges identifiable although their extent and rates were significantly different. The ranges were considerably longer than the baseline cavity and regions I and II grow more aggressively than the baseline cavity. The trends observed are

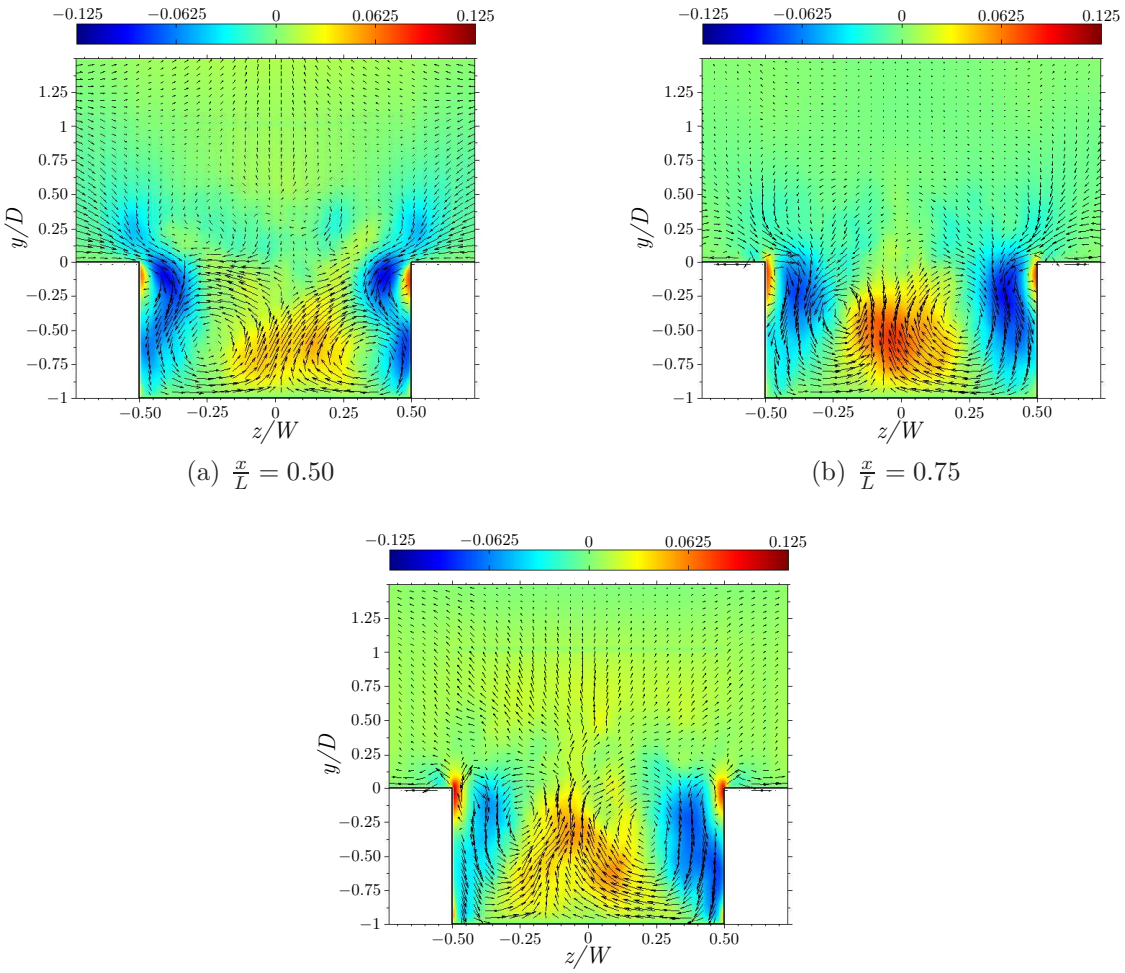

(a) $\frac{x}{L} = 0.50$

(b) $\frac{x}{L} = 0.75$

(c) $\frac{x}{L} = 0.875$

Figure 8-16. Controlled cavity mean normal velocity contours on the yz plane at various axial locations showing opposing recirculation regions rotating in opposite direction of baseline cavity.

in good agreement with the experimental data where the controlled cavity growth rate exceeds the baseline rate until the streamwise position $\frac{x}{L} \approx 0.50$. The growth rates then continually taper off towards the trailing edge of the cavity eventually falling below rates observed in the baseline. The location of maximum shear also rises above the aft wall consistent with the experimental observations. This is a clear indication the maximum shear is decreased and lifted above the cavity lip when the rod is present. The reduced shear is believed to be a key contributor to the smaller less organized structures presented in Figure 8-11.

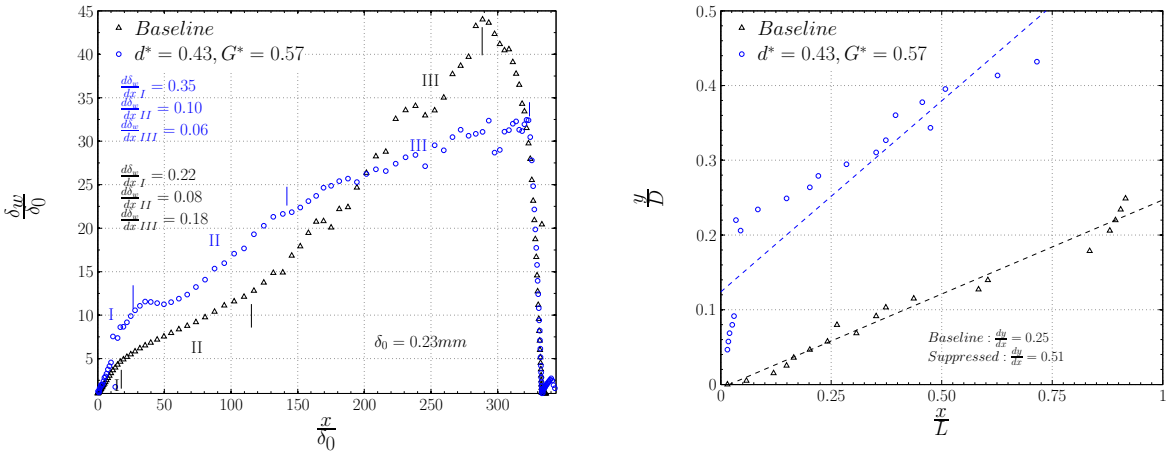

(a) Vorticity Thickness

(b) Location of max $\left(\frac{dU}{dy}\right)$

Figure 8-17. Baseline and controlled cavity vorticity growth rate and location of maximum shear.

The growth rate of the shear layer is further substantiated with a qualitative assessment of the mean vorticity contours shown in Figure 8-18 for each cavity. It is apparent that the mean vorticity over the first 25% of the cavity shear layer is drastically reduced and broadened. The magnitude of the mean vorticity inside the cavity has also been reduced most notably at the trailing edge.

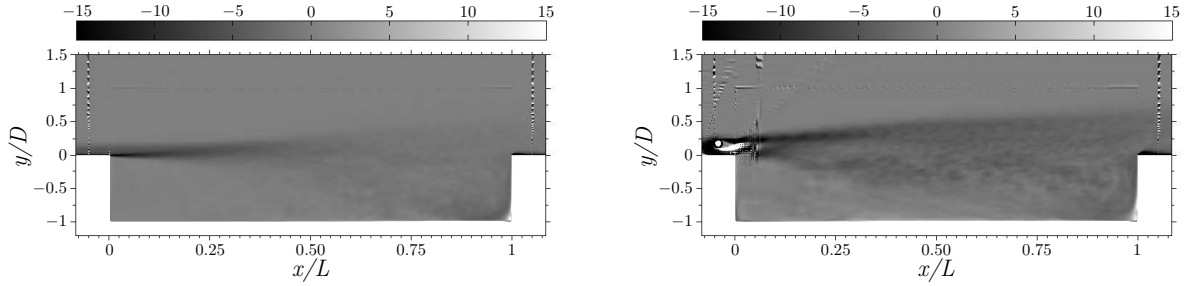

(a) Baseline

(b) Controlled

Figure 8-18. Mean vorticity (ω_z) contours for the baseline and controlled cavity.

8.4 Mean Turbulent Flowfield

The turbulent features of the cavity flowfield will be discussed in this section and contour plots of them can be found in Figure 8-19. The turbulent velocities from the

simulations are in good agreement with what was observed in the experiments with the peak turbulence levels generally within 5%. The rods ability to pull the streamwise velocity fluctuations above the cavity lip are seen in Figure 8-19(b). A similar trend is observed for the normal and spanwise turbulent velocities where the rod was able to reduce the velocity fluctuations inside the bay.

The turbulent velocities, RSS and TKE profiles are plotted at various axial locations in Figure 8-20. Examination of the streamwise and normal components of the turbulent velocity profiles illustrates the spreading of the shear layer in greater detail for the controlled cavity. The point where the maximum turbulent fluctuation exists (for each component) is raised above the lip of the cavity as one progresses downstream which is consistent with experimental observations. The profiles also clearly show the reduced turbulent fluctuations inside the cavity for both the axial and normal velocities. With the lifting and broadening of the shear layer the turbulent kinetic energy and turbulent shear stress at the trailing edge of the cavity have been substantially reduced. The rod caused a similar reduction of maximum fluctuation levels for each velocity component. This is again an indication of the rods ability to interfere with the coherence of the baseline shear layer leading to smaller less energetic turbulent structures.

8.4.1 Evolution of Two-Point Velocity Correlations

In this section the evolution of the two-point turbulent velocity statistics are presented. In all of the plots presented in this section the correlation coefficients will be presented normalized by the appropriate turbulent velocity as defined in Chapter 2. For Figure 8-21 and Figure 8-22 the baseline cavity is represented in the first column of images followed by the suppressed cavity. For all of these figures progressing down the column corresponds to advancing in the streamwise direction.

Figures 8-22(a) $-$ 8-22(j) illustrates the streamwise evolution of the streamwise component of the turbulent velocity correlations for the baseline and controlled cavity with the origin located at $\frac{y}{D} = 0$. The highly correlated regions for each cavity are

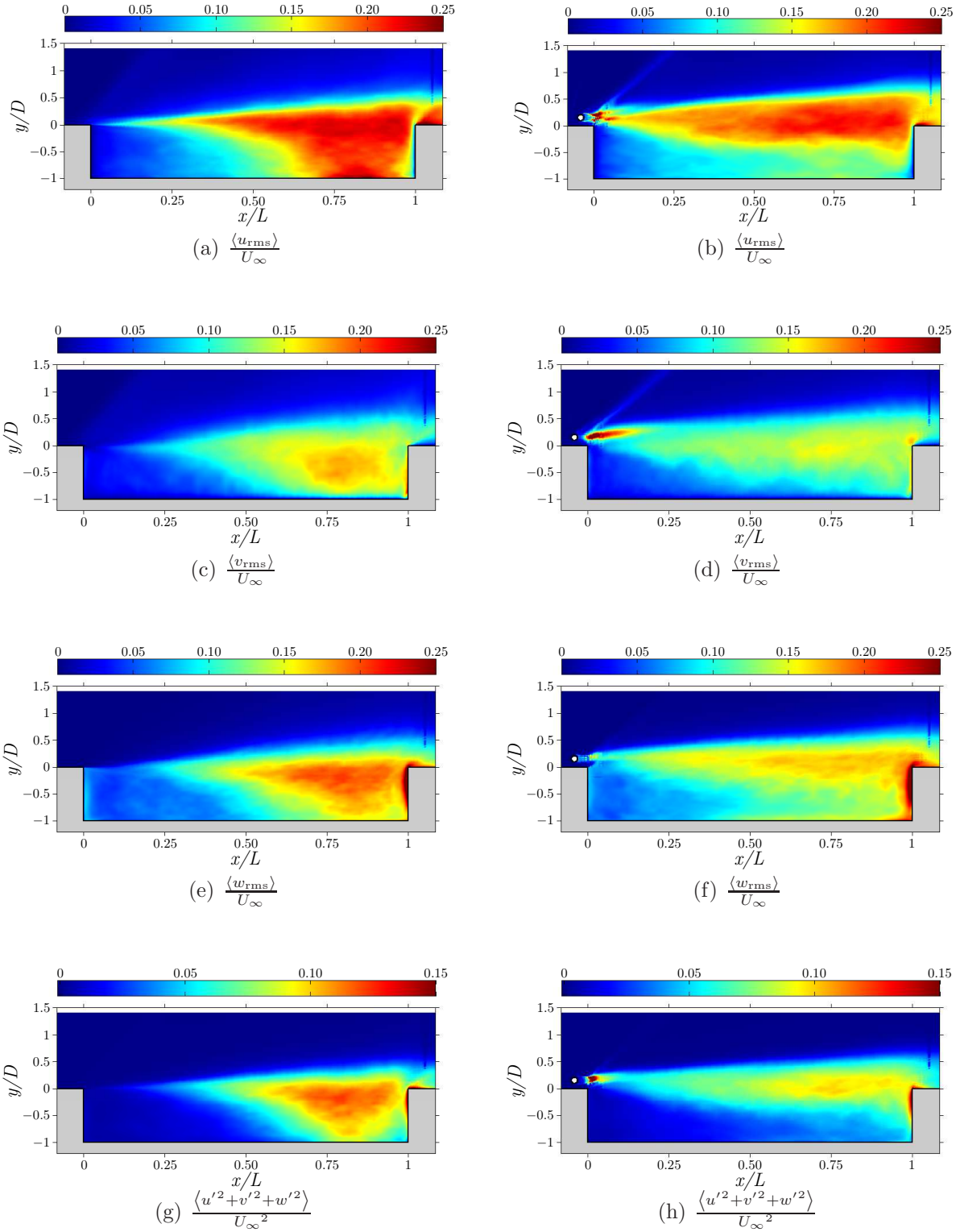

Figure 8-19. Mean turbulent flowfield contours. Column (a) and (b) are the baseline and controlled cavity respectively.

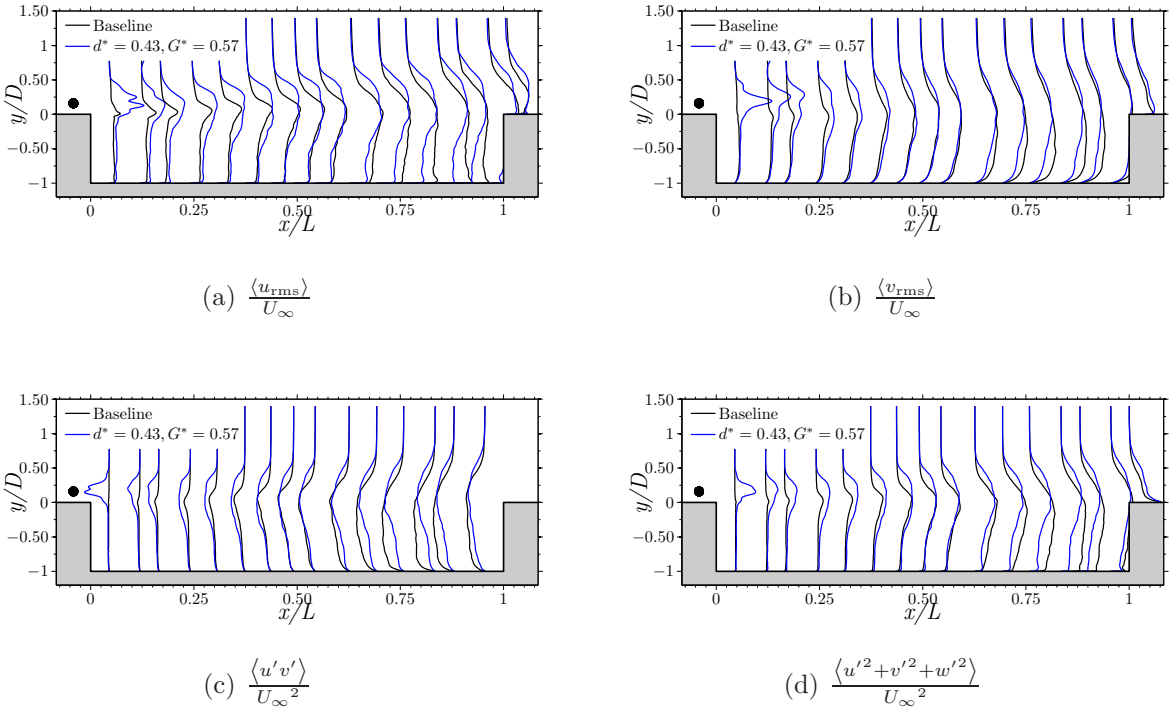

(a) $\frac{\langle u_{\text{rms}} \rangle}{U_\infty}$

(b) $\frac{\langle v_{\text{rms}} \rangle}{U_\infty}$

(c) $\frac{\langle u'v' \rangle}{{U_\infty}^2}$

(d) $\frac{\langle u'^2+v'^2+w'^2 \rangle}{{U_\infty}^2}$

Figure 8-20. Mean flowfield and mean turbulent flowfield profiles.

elongated in the streamwise direction. The baseline cavity exhibits larger well correlated regions while the controlled case exhibits more compact correlated regions most notably at $\frac{x}{L} = 0.5$. Upon inspection, the correlations clearly indicate that the turbulent length scale (if one were to integrate the correlation region) is lengthened in the axial direction for the baseline cavity. This suggests that the controlled cavity shear layer will only be capable of containing smaller turbulent structures.

Figure 8-22 illustrates the evolution of the normal component of the turbulent velocity correlation for the baseline and controlled cavity with the origin located at $\frac{y}{D} = 0$. The highly correlated regions are again elongated in the direction of the turbulent velocity, i.e., the vertical direction. The baseline cavity exhibits larger well correlated regions while the controlled cavity exhibits more compact correlated regions. Examining Figure 8-22 one can see an alternating pattern of low and high correlation areas throughout the baseline

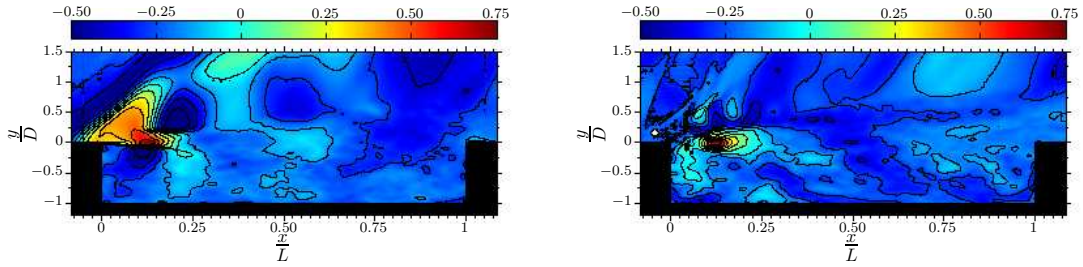

(a) Origin at $\left(\frac{x}{L}, \frac{y}{D}\right) = (0.125, 0)$

(b) Origin at $\left(\frac{x}{L}, \frac{y}{D}\right) = (0.125, 0)$

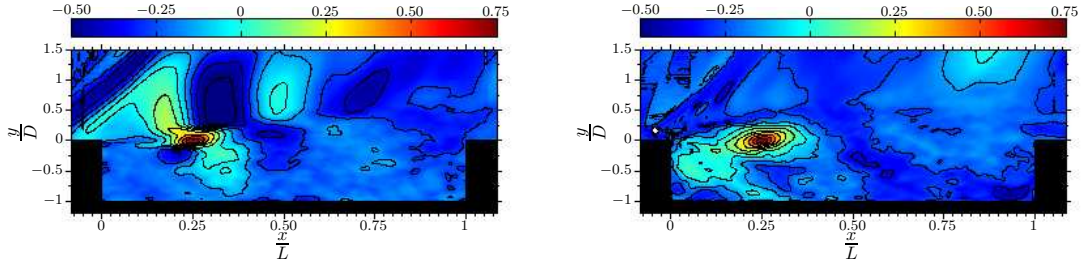

(c) Origin at $\left(\frac{x}{L}, \frac{y}{D}\right) = (0.25, 0)$

(d) Origin at $\left(\frac{x}{L}, \frac{y}{D}\right) = (0.25, 0)$

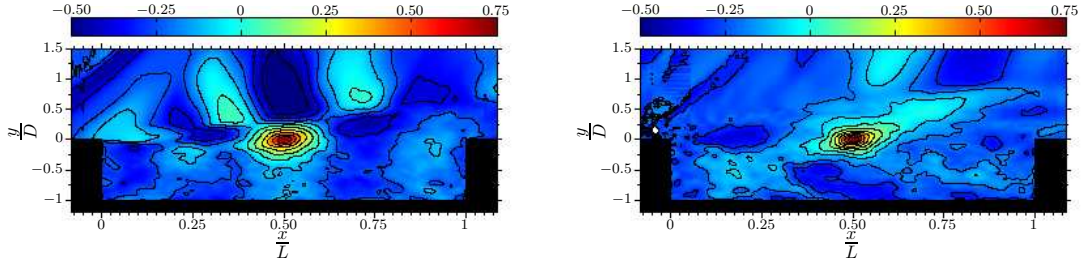

(e) Origin at $\left(\frac{x}{L}, \frac{y}{D}\right) = (0.50, 0)$

(f) Origin at $\left(\frac{x}{L}, \frac{y}{D}\right) = (0.50, 0)$

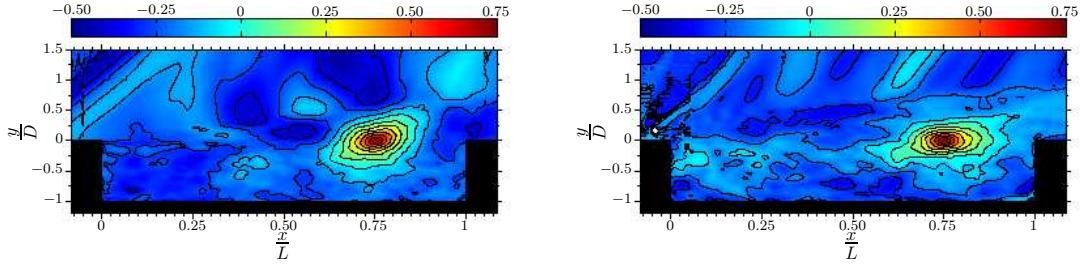

(g) Origin at $\left(\frac{x}{L}, \frac{y}{D}\right) = (0.75, 0)$

(h) Origin at $\left(\frac{x}{L}, \frac{y}{D}\right) = (0.75, 0)$

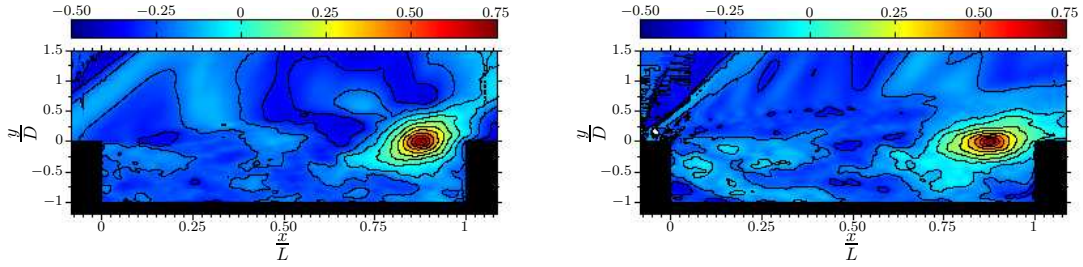

(i) Origin at $\left(\frac{x}{L}, \frac{y}{D}\right) = (0.875, 0)$

(j) Origin at $\left(\frac{x}{L}, \frac{y}{D}\right) = (0.875, 0)$

Figure 8-21. Evolution of streamwise spatial velocity correlation. Columns (a) and (b) are the baseline and controlled cavity respectively.

shear layer which do not exist for the controlled cavity. This behavior is indicative of is a periodic nature of the turbulent structures in cavity shear layer for the baseline case.

Figure 8-23(a) and Figure 8-23(b) illustrate spatial correlation plots of the fluctuating surface pressure as a function of separation with the origin located at the center point of the aft wall for each cavity. Similar to the spatial velocity correlations reported in Figure 8-22, the pressure correlation regions tend to be elongated in the normal direction for each cavity. The baseline cavity exhibits a much larger highly correlated region that extends from just below the origin to the top of the aft wall. The controlled cavity's well correlated region is noticeably more compact which suggests that smaller scale structures have impacted the aft wall. This is consistent with the argument that the control is breaking up the organized turbulent features impacting the aft wall thus reducing the source of the upstream propagating wave.

8.4.2 POD

Results from the application of the Proper Orthogonal Decomposition to velocity field snapshots from the finite span cavity is presented in this section in the same manner as was done for the full span cavity in Chapter 7. As mentioned in Chapter 7, it is advantageous to extract events which contain large amounts of turbulent kinetic energy.

Figure 8-24(a) and Figure 8-24(b) represent the turbulent kinetic energy distribution and cumulative energy for the extracted POD modes respectively. The baseline cavity exhibited slightly more energy in the first five modes however there was little difference thereafter up to the first twenty modes considered. The fairly rapid convergence of the basis set is observed where 50% of the total turbulent kinetic energy of for the baseline cavity required approximately 2% of the total snapshots while the suppressed cavity required slightly more at approximately 2.5%. The energy captured in the first mode was roughly 8% for each cavity while the next three modes differed by as much as 1.5% but captured under 5% of the total turbulent kinetic energy per mode. Only the first five modes are considered in the following discussion for two reasons. The first is for

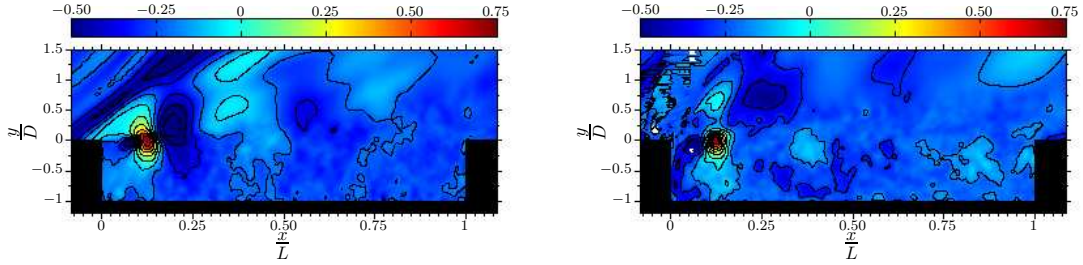

(a) Origin at $\left(\frac{x}{L}, \frac{y}{D}\right) = (0.125, 0)$

(b) Origin at $\left(\frac{x}{L}, \frac{y}{D}\right) = (0.125, 0)$

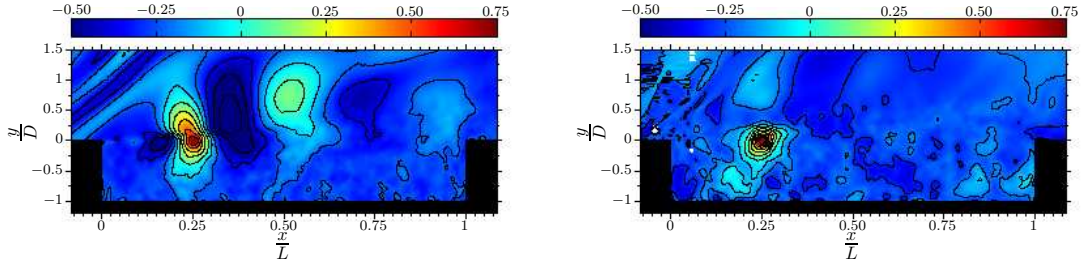

(c) Origin at $\left(\frac{x}{L}, \frac{y}{D}\right) = (0.25, 0)$

(d) Origin at $\left(\frac{x}{L}, \frac{y}{D}\right) = (0.25, 0)$

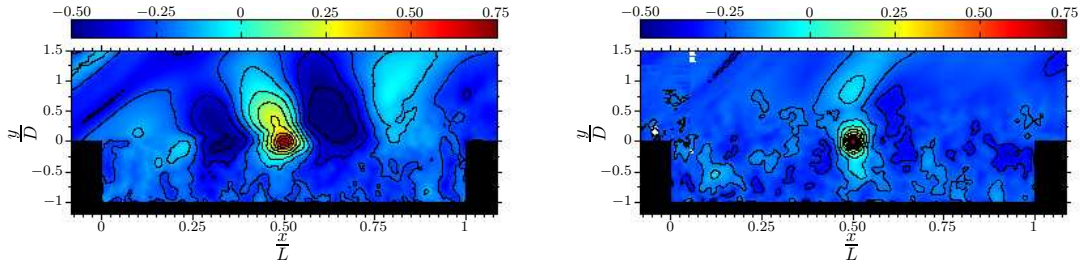

(e) Origin at $\left(\frac{x}{L}, \frac{y}{D}\right) = (0.50, 0)$

(f) Origin at $\left(\frac{x}{L}, \frac{y}{D}\right) = (0.50, 0)$

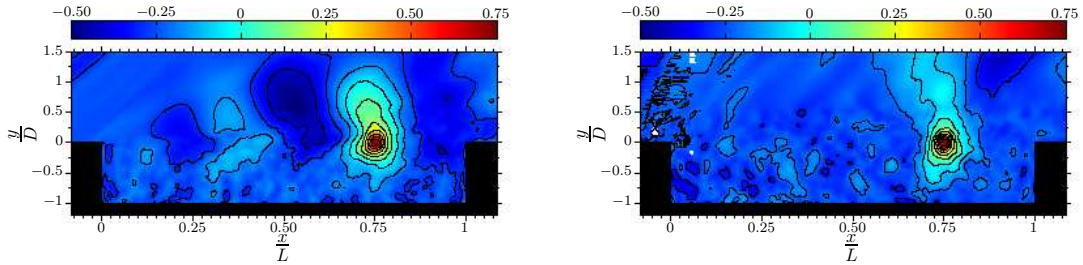

(g) Origin at $\left(\frac{x}{L}, \frac{y}{D}\right) = (0.75, 0)$

(h) Origin at $\left(\frac{x}{L}, \frac{y}{D}\right) = (0.75, 0)$

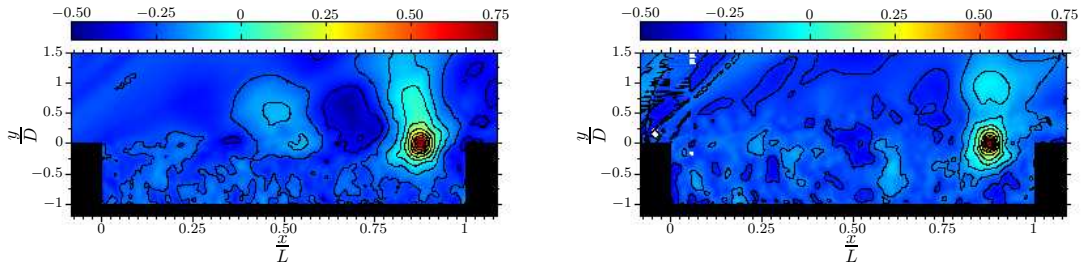

(i) Origin at $\left(\frac{x}{L}, \frac{y}{D}\right) = (0.875, 0)$

(j) Origin at $\left(\frac{x}{L}, \frac{y}{D}\right) = (0.875, 0)$

Figure 8-22. Evolution of normal spatial velocity correlation. Columns (a) and (b) are the baseline and controlled cavity respectively.

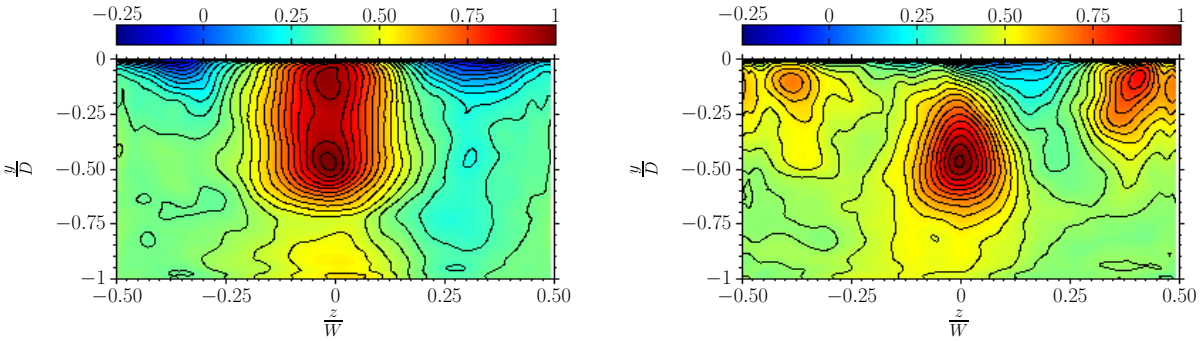

(a) Baseline (b) Controlled

Figure 8-23. Fluctuating surface pressure correlation on the aft wall with the origin located at the center point.

conciseness, as higher modes demonstrated similar trends. The second reason is because for increasing mode numbers the energy should occur at smaller spatial scales and it is likely they will become unimportant (say beyond the first 10-20 modes) for modeling or reconstructing the overall global behavior of the cavity. To this end, it is understood that it is not clear that the modes with the most kinetic energy should be uniquely targeted for flow control purposes.

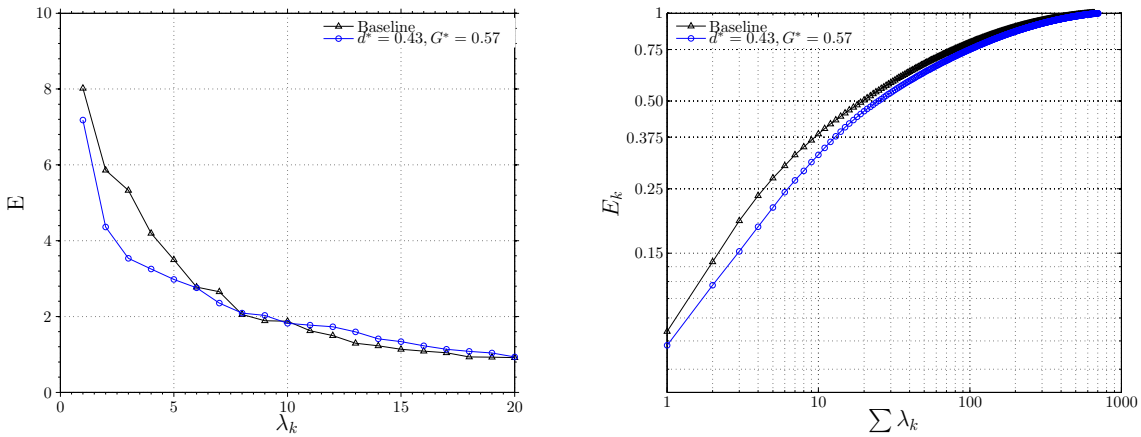

(a) TKE Distribution per Mode (b) Cumulative TKE

Figure 8-24. Energy distribution of POD modes.

Figure 8-25(a) and Figure 8-25(j) represent the first five POD modes based on the normal component of the turbulent velocity for the baseline and controlled cavities. It should be noted that only the POD modes associated with the vertical velocity component is shown as those associated with the streamwise velocity component exhibited similar behavior. The first mode of the baseline cavity exhibited one elongated feature which is consistent with the subsonic results of Murray *et al.* (2009) and those presented in Chapter 7. The POD mode fluctuations for the baseline cavity are in-phase across the length of the cavity and represents the oscillation of the shear layer. The suppressed cavity POD mode fluctuations are no longer in phase as illustrated by the alternating negative and positive regions located throughout the shear layer region. In contrast to the full span cavity POD results discussed in Chapter 7, the presence of the rod did have a profound effect on the streamwise organization of the resolved modes for the finite span cavity. The large scale well organized nature of the baseline cavity shear layer is reflected in the POD modes where alternating positive and negative regions apparently resemble locations where highly energetic turbulent structures could reside. This is clearly missing in the suppressed cavity POD modes, particularly evident in the odd numbered modes. Here, small compact regions of highly energetic flow are located in the cylinder near field and is expected due to the turbulent fluctuations of the cylinder wake. The regions with high turbulent kinetic energy found under the cavity lip of the baseline cavity for modes three and four are not present in the suppressed cavity modes. The even numbered modes for the suppressed cavity are generally elongated in the streamwise direction while compacted in the vertical direction when compared to the baseline cavity modes. Comparing the modes for the baseline and controlled cases, primarily for even numbered modes, one sees the highly energetic regions are better aligned in the streamwise direction for the suppressed cavity. This is believed to be a consequence of the altered behavior of the shear layer oscillations where the baseline cavity shear layer exhibits a strong tendency to flap into and out of the cavity at the trailing edge. The controlled cavity POD modes seem to indicate this

flapping nature of the shear layer has been drastically altered. In general, there is good agreement in the observed behavior of the POD modes with the evolution of the two point statistics discussed above. The cavity shear layer consists of smaller less organized regions in space where highly energetic flow structures would be found.

Recent work by Arunajatesan *et al.* (2009) has found that the spanwise velocity component modes show smaller scale structures with the cavity controlled by micro-jets. They state the major effect of control is the change, or disorganization, in spanwise structure of the shear layer when control is present. The found that a two-dimensional (streamwise and normal velocities) POD of the velocity field did not correlate well with the modes of pressure. A three-dimensional POD, on the other hand, correlated well. They observed that by neglecting the spanwise velocity in the POD analysis the physical interpretation of what the POD modes represent are likely skewed especially in the case of the controlled cavity because of the increased three dimensionality of the flow. They further surmise that since the pressure field in the cavity is more or less two-dimensional, the two-dimensional POD of the pressure can be a good representation of the flow. In light of this observation, it is acknowledged this is a potential short-coming of the POD work in this research and will warrant more detailed investigation in the future.

8.5 Summary

Simulations using a second-order time and space solver utilizing a DES approach with a one equation turbulence model were performed. There was good agreement between the simulations and experimental observations in examining overall trends and magnitudes. The comparisons included fluctuating surface pressures measurements, mean flowfield analysis, turbulent fluctuation intensities and the growth rate of the cavity shear layer. The ability to visualize all three dimensions gave insight into the effect the rod had on the interior cavity flow. Looking at the $z = 0$ plane revealed a dominant clockwise rotating recirculation pattern with the origin located near the cavity center point. There were also smaller counter rotating bubbles located on the floor at the cavity leading and trailing

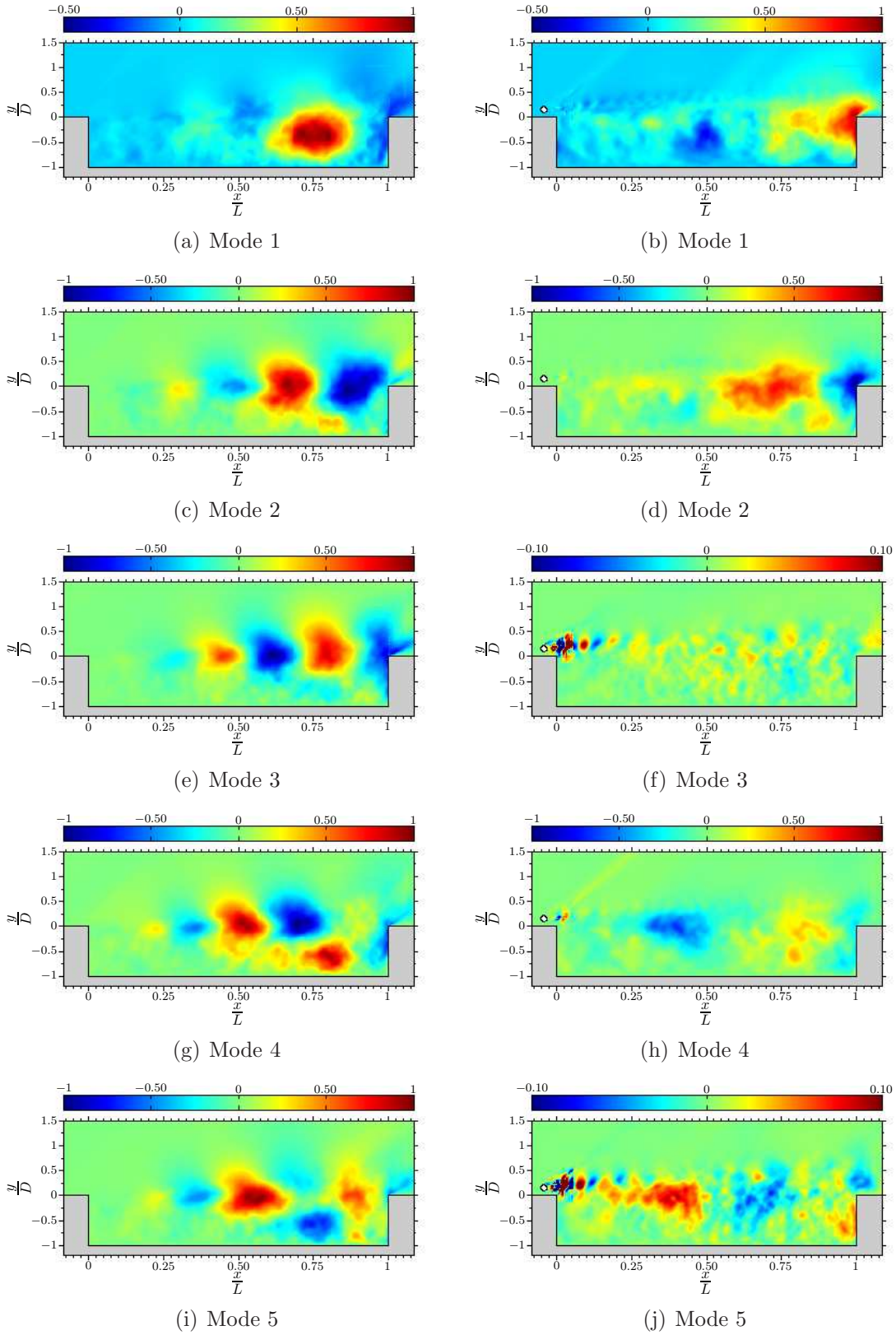

(a) Mode 1

(b) Mode 1

(c) Mode 2

(d) Mode 2

(e) Mode 3

(f) Mode 3

(g) Mode 4

(h) Mode 4

(i) Mode 5

(j) Mode 5

Figure 8-25. POD modes based on the normal fluctuating velocity. Columns (a) and (b) are the baseline and controlled cavity respectively.

edges. The controlled cavity shifted the dominant recirculation region center near the trailing edge of the cavity. The interior flow of the cavity was more aggressively swept upwards when controlled. An examination of the mean normal velocity on the selected yz planes indicated two opposing recirculation regions split by the cavity centerline for the each cavity. These regions intensified as one progressed towards the trailing edge. The baseline cavity rotated in such a way as the centerline of the cavity was drawing fluid into the cavity and fluid was expelled outside the cavity at the sidewalls. The presence of the rod reversed the rotation of these regions where the mean normal velocity at the centerline was now out of the cavity and fluid was drawn into the cavity at the sidewalls. This is believed to be the consequence of the pressure gradient generated as the shear layer is lifted above the cavity lip.

The use of two-point statistics showed the evolution of highly correlated regions became elongated in the direction of the component of the turbulent velocity considered. These regions were much more compact for the controlled cavity. Coupled with the results from the POD, it was clear the organizational behavior of these structures was highly sensitive to the presence of flow control with the rod. The POD modes clearly illustrated much smaller regions of high turbulent kinetic energy where only smaller scale structures could reside compared to the baseline cavity. Instantaneous vorticity images revealed the complex interaction of the rod wake and the separated boundary layer downstream of the rod. This interaction resulted in small scale turbulent structures injected into the shear layer in a periodic fashion typically on the upstroke of the cylinder wake even though there was no strong Von-Kármán type shedding present.

Cross and auto-correlation analysis revealed identical trends as observed with the experimental observations. The correlation levels dropped with the presence of the rod and is a strong indication of a disrupted feedback mechanism. The speed at which the disturbance propagates inside the cavity appears to be independent of the rod's presence. The lowered correlation values also suggest the upstream propagating wave

emanating from the shear layer impingement on the aft wall is weakened when the cavity is controlled.

The presence of the rod in this research leads to a thicker shear layer (most notably at the cavity leading edge) with an elevated shear layer spreading rate. The wake of the rod pulls at the shear layer leading to higher shear stresses and a thicker shear layer close to the cavity leading edge. These conditions likely inhibit the ability of the shear layer to roll-up into large scale organized structures by decreasing the receptivity and growth rate of the disturbances in the shear layer. The mean flowfield and mean turbulent flowfield examination also revealed the shear layer was lifted when controlled. The lifting of the shear layer and the flapping motion of the shear layer may be dually responsible for altering the aft wall impingement point. The penetration of the shear layer into the cavity would be reduced if the shear layer flaps above the aft wall or flaps less aggressively. It is further postulated that the flapping motion would likely be altered by the presence of the thicker shear layer. Lastly, it was observed that the mean shear was decreased in the controlled case while the point of maximum shear was shifted away from the aft wall.

CHAPTER 9
CONCLUSIONS AND FUTURE WORK

A coupled experimental and numerical investigation of the effects of control on a $M_\infty = 1.4$ supersonic flow over a open rectangular cavity with a length-to-depth ratio of six was conducted. The altering of the flow was achieved by placing a cylindrical rod in boundary near the cavities leading edge. Measurements included the fluctuating surface pressure on the cavity centerline for five rod diameters and various gap heights. It was determined that a rod sized approximately 40% of the approaching boundary layer height placed such that the top of the rod is near the top of the boundary layer, resulted in the best overall suppression (both broadband and tonal components) of the fluctuating pressures on the cavity surfaces however many other cases demonstrated significant reductions as well. The broadband levels of the baseline cavity are likely attributable to the approaching boundary layer turbulence levels and the fact the rod was able to reduce these levels in the controlled cases suggests the turbulence throughout the shear layer was slightly altered. The mean velocity and turbulent flowfield statistics for the baseline and selected control cases were acquired and analyzed on the cavity centerline using data acquired from particle image velocimetry. Computational fluid dynamics using a detached eddy simulation approach was conducted to gain further insight for measurements off of the cavity centerline and for the near body flowfield of the cylinder.

This final chapter summarizes the major findings and contributions brought out in this work which were discussed throughout this dissertation. It starts with a summary of the finite and full span cavity results which is followed by a discussion of the demonstrated accuracy of the CFD approach employed throughout this research. This is followed with a summary of the mechanisms believed to be present for the control of the cavity flow. Finally, the chapter concludes with recommendations for improvements and where this work could be extended upon.

9.1 Finite and Full Span Cavities

Flowfield measurements for the full and finite span cavities with and without control were presented. The spectra measured on the aft wall exhibited resonant tones that occurred at the same frequencies. For both configurations these frequencies were reasonably represented by Rossiter's equation with the default constants. The dominant tone switched between the second and third lowest resonant tone for the finite and full span cavities respectively and was substantially greater for the full span cavity.

The centerline velocity fields had similar overall features although there were many differences. The most significant difference observed in the flowfield measurements was that the finite span cavity allows for fluid exchange from the side walls which causes a different interior flow for the baseline case. The primary recirculation region is shortened and shifted towards the center of the cavity for the finite span cavity. The mean turbulent flowfields for these two cavities share similar intensities albeit the flow penetrated deeper into the finite span cavity. The increased cross-flow likely decreases the strength of the disturbances inside the cavity which leads to lower magnitudes of the resonant tones. When controlled, the full span cavity shear layer appeared to be lifted slightly higher above the cavity lip line with differences in the shear layer growth rate. The differences observed between the controlled cavity flowfields are believed to be a consequence of the partial coverage of the rod with the full span cavity and the differences in the interior flow as explained above. To this end, the suppression realized appears to be driven by the same mechanism for each cavity though exaggerated with the full span cavity.

9.2 Demonstration of DES

A second order (time and space) detached-eddy simulation that uses Reynolds averaging with a one equation turbulence model was found to be reasonably accurate for $M_\infty = 1.4$ cavity flow. The ability of the current technique to decently capture the relevant physics of the controlled and baseline cavity flows was demonstrated. Specifically, it was shown that there was good agreement between experimental and simulated values

of the fluctuating surface pressure on the cavity surfaces when the appropriate boundary layer was prescribed in the simulations. Additionally, the mean velocity flowfield and turbulent statistics were in good agreement. The shear layer growth rates were in good agreement when considering trends between the baseline and controlled cases. The simulations accurately predicted higher spreading rates for the controlled cavity that taper off at $\frac{x}{L} = 0.5$ eventually falling below the values realized in the baseline cavity. The magnitude of the growth rates exhibited some variance but it should be noted this was when comparing an experimental full span cavity with the simulated finite span. It is not entirely clear whether these differences are attributable to the geometry, numerical approach or combination thereof. More specifically, it is noted that most compressibility corrections to turbulence models have been applied to improve correlations with experiments for the spreading rate of free shear layers at lower speeds than the focus of this research and furthermore the shear layer spreading rate for the finite span cavity was not able to be computed accurately from the experiment. Further investigation is warranted to determine the cost/benefits of including compressibility corrections, two-equation turbulence models, numerical schemes and full LES as computational resources continue to grow. Nonetheless, it is this authors opinion that analysis using the guidelines posed in this research would be beneficial to the community and are immediately available in most modern CFD solvers. It should be noted that the a-priori knowledge of the approaching boundary layer details were pivotal in the achieved accuracy of the simulations and hence this represents a key need to match experimental data.

9.3 Cavity Control

The use of two-point turbulent velocity correlations and POD analysis illustrated the streamwise organization of the turbulent structures was altered by the control efforts. The well established structures that were identified inside the full or finite span baseline cavity where typically not present with the controlled cavities and were shown to be typically lifted above the cavity lip. The POD modes clearly illustrated much smaller

regions of high intensity turbulent kinetic energy for the controlled cases where smaller scale structures would likely reside when compared to the baseline cavity.

The ability to visualize all three velocity components by the use of CFD gave insight into the effect the rod had on the interior cavity flow. Considering the xy plane located at the center of the cavity it was seen that there existed a dominant clockwise rotating recirculation with it's origin located near the cavity center point. The presence of the rod shifted the dominant recirculation pattern closer to the trailing edge of the cavity and the interior flow was more aggressively swept upwards. An examination of the mean normal velocity on the select yz planes indicated two opposing recirculation regions split by the cavity centerline for the each cavity that increased in intensity as you progressed towards the trailing edge. The flow in the baseline cavity rotated in such a way as the centerline of the cavity was drawing fluid into the cavity and expelled it at the sidewalls. The presence of the rod reversed the rotation of these regions were the mean normal velocity at the centerline was now out of the cavity and fluid was drawn into the cavity at the sidewalls. It is likely that the lifting of the shear layer due to the rod created the pressure gradient such that the flow is drawn inside the cavity at the side walls leading to the changes in the flow pattern. In light of this observation, it is not yet determined if the fluctuating pressure on the entire cavity is effectively suppressed. In other words, has the overall loading on the cavity walls been suppressed or just re-distributed where further analysis of the results from the simulations will be required to determine this.

Previous researchers have attempted to study the linear stability analysis of the cavity shear layer when a rod in the approaching boundary layer was used as the control device. However, as Freymuth (1966) showed for a separated laminar boundary layer, the growth rates are independent of the amplitude of forcing which definitely has an analogy to the cavity flow being studied here. Direct numerical simulations were performed by Guillaume & Colonius (2008) to investigate the three-dimensional global instability of compressible flow over open cavities. They applied the so called bi-global linear stability

originally used by Theofilis & Colonius (2002) to take into account non-parallel effects and possible coupling of the shear layer with the acoustic scattering and the recirculated flow inside the cavity. They identified three-dimensional instabilities which took the form of disturbances growing in the recirculation region within the cavity. The results indicate the instability is tightly coupled with the strength of the recirculation region in the downstream portion of the cavity. They note these instabilities would not be accessible to classical linear stability of parallel flows. Furthermore, the classical stability argument has been utilized to say that control is achieved through the breakdown of a pair of opposite sign vortical structures (alternate top/bottom shedding in the case of the cylinder) which was not evident in the simulations presented in Chapter 8 severely limiting the applicability of this notion.

The coupled numerical and experimental analysis of the finite span cavity seem to point consistently to the same flowfield differences when a rod is placed at the leading edge of the cavity. The controlled cavity leads to a thicker shear layer (most notably at the cavity leading edge) with an elevated spreading rate. Referring to the simulations in Chapter 8, the structures in the wake of the rod interact with the cavity shear layer with a time periodic excitation which pulls up on the shear layer. Additionally, these structures tend to increase the entrainment of fluid inside the cavity and spread out the shear layer more rapidly. These conditions inhibit the ability of the shear layer to roll-up into large scale organized structures that impinge on the aft wall. This is illustrated in the turbulent velocity correlations and POD analysis where the organizational nature of highly energetic structures was shown to be drastically altered. This leads to smaller less organized turbulent structures throughout the shear layer as demonstrated in the vorticity plots found in Chapter 8. This is further demonstrated the decreased footprint on the aft wall fluctuating pressure correlations from the simulations presented in Chapter 8. The thicker shear layer with smaller scale turbulent structures is believed to decrease the receptivity and growth rate of the disturbances.

The mean flowfield and mean turbulent flowfield examinations also revealed the shear layer was lifted when controlled. The lifting of the shear layer and the flapping motion of the shear layer may be dually responsible for altering the aft wall impingement point. The penetration of the shear layer into the cavity would be reduced if either the shear layer is lifted or if it flaps above the cavity lip line or less aggressively. It is further postulated that the flapping motion would likely be altered by the presence of the thicker shear layer. This is believed to lead to a weakened upstream propagating disturbance due in part to the decreased flow velocity impinging on the cavity aft wall. This in turn, results in the reduced peaks observed in the resonant tones for the controlled cases. The key points regarding the control of the cavity are summarized below.

- The rod leads to a thicker shear layer that initially spreads more rapidly because the structures in the wake of the rod interact with the cavity shear layer with a time periodic excitation which lifts the shear layer near the cavity leading edge. The structures are smaller and less organized which is believed to lead to a shear layer that is less receptive to the upstream disturbances inside the cavity.
- The rod is able to alter the aft wall impingement point due to the lifting and altered flapping nature of the shear layer. This results in lower speed flow impinging on the aft wall.
- The upstream propagating disturbance emanating from the aft wall is weakened in part due to the lowered velocity flow impinging on the aft wall. These coupled events lead to drastically reduced fluctuating pressures measured on the cavity surfaces and thus lowered magnitudes of the resonant tones (near broadband levels). The fact that broadband levels are slightly lowered, indicates the control was able to alter the turbulence levels throughout the shear layer.

9.4 Future Work

Based upon the findings in the current work there are several areas of research offered as possible suggestions for further inquiry and are broken into numerical and experimental sections accordingly.

9.4.1 Computational Fluid Dynamics

Due to the good agreement of the numerical simulations with observed experimental observations further investigation has already been undertaken though the completion

is further down the road. Similar to the zoomed PIV efforts, numerical simulations have been initiated using block to block grids (eliminating overset boundaries) to investigate the cylinder wake near field flow features at various gap heights and rod diameters. The use of higher order numerical schemes and turbulence models is also being investigated in attempt to quantify turbulent production and dissipation rates. The streamwise location of the rod will likely be investigated to study the effects on the cavity shear layer. Investigating the effects of turbulent intensities in the approaching boundary layer using techniques similar to that presented in Comte *et al.* (2008) and Levasseura *et al.* (2008) could be pursued. As discussed briefly in Chapter 8, the POD analysis could be further expanded to include all three velocity components over the entire computational domain. Additionally, the POD analysis could be performed based on the pressure field as an input. Compressibility effects could be investigated using techniques such density weighted averaging for the current data set or codes that include compressibility corrections in the turbulence model or use Favre averaging.

9.4.2 Experimental

Further work is recommended in the PIV analysis of the finite span cavity to minimize the bloom realized in this work. A very similar analysis would be proposed but the design of the finite cavity would be altered. More specifically, one should ensure all surfaces of the glass cavity sidewall would be polished. It is believed this alone would drastically reduce the bloom experienced in this research. Furthermore, the use of three-component PIV could be used to extract useful information regarding the span-wise cavity flowfield. Synchronized surface pressure measurements and velocity field measurements can be obtained. Not only would this allow one to investigate reconstruction of the flowfield using reduced order models obtained via POD but would also allow one to more thoroughly investigate the correlation between structures observed in the shear layer and the surface pressure measurements. An extensive literature review of suppressed cavities using a rod suppression device also reveals experimental flowfield measurements are lacking

at subsonic and transonic Mach numbers. A purely subsonic flowfield could be studied with minimal effort requiring only the design of a new nozzle to achieve the desired flow conditions. A detailed investigation of the turbulent intensities measured in the approaching boundary layer and a re-characterization of the test-section flow conditions would be required. Transonic Mach numbers might require a more intricately designed test section to bleed the boundary layer as well.

9.4.3 Future Consideration

The research presented could be further extended by studying the fundamental flow phenomena regardless of whether it is numerical or experimental. Some key topics to be further investigated could include energy balances from the turbulent kinetic energy equation and a more detailed analysis of pressure correlations on all of the cavity surfaces to quantify the reduction of magnitude of the sources. Lastly, one could consider the dynamics phenomena to further try to identify what truly is the source in the flow field for both the suppressed and baseline cavities.

APPENDIX A
TURBULENCE MODEL FORMULATION

A discussion of the transition from the compressible Navier-Stokes equations to the RANS equations and subsequent one equation SA turbulence model are offered in this appendix for convenience to the interested reader. The appendix begins with a detailed review of the compressible Navier-Stokes equations and is followed by the derivation of the RANS equations. The discussion is ended with a detailed explanation of the SA turbulence model with all of the variables and coefficients listed for the selected CFD solver.

A.1 Compressible Navier-Stokes Equations

The governing equations for the current research are derived from the general instantaneous compressible Navier-Stokes equations written in cartesian coordinates. The continuity equation may be written as

$$\frac{\partial \rho}{\partial t} + \frac{\partial \left(\rho u_i\right)}{\partial x_i} = 0 \tag{A–1}$$

where ρ is the fluid density, u_i is the tensor form of the velocity vector and t is time. The momentum equation may be written as

$$\frac{\partial \left(\rho u_i\right)}{\partial t} + \frac{\partial \left(\rho u_i u_j\right)}{\partial x_j} = \frac{\partial \tau_{ij}}{\partial x_j} - \frac{\partial p}{\partial x_i} + \rho f_i \tag{A–2}$$

where p is the fluid pressure and f_i represents body forces. The viscous stress tensor is given as

$$\tau_{ij} = \mu \left[\left(\frac{\partial u_i}{\partial x_j} + \frac{\partial u_j}{\partial x_i} \right) - \frac{2}{3} \delta_{ij} \frac{\partial u_k}{\partial x_k} \right] \tag{A–3}$$

where μ is the molecular viscosity which is calculated using Sutherland's law

$$\mu = \mu_{\text{ref}} \left(\frac{T}{T_{\text{ref}}} \right)^{\frac{3}{2}} \frac{T_{\text{ref}} + S}{T + S}. \tag{A–4}$$

The underscore 'ref' is the reference value of either the temperature, given by T, or the viscosity. The value of the Sutherland temperature is taken as $S = 110.4\text{K}$. The Kronecker

delta function is given by

$$\delta_{ij} = \begin{cases} 1 & \text{if } i = j \\ 0 & \text{if } i \neq j. \end{cases} \tag{A–5}$$

The conservation of energy may be written as

$$\frac{\partial(\rho E)}{\partial t} + \frac{\partial(\rho u_i E)}{\partial x_j} = \frac{\partial}{\partial x_j}(u_i \tau_{ij} - q_i) - \frac{\partial(p u_i)}{\partial x_i} \tag{A–6}$$

where heat flux is given by

$$q_i = -k_c \frac{\partial T}{\partial x_i} = -\frac{\mu c_p}{\mathrm{Pr}} \frac{\partial T}{\partial x_i}. \tag{A–7}$$

The ratio of momentum diffusivity (kinematic viscosity) and thermal diffusivity (α) is given by the non-dimensional Prandtl number

$$\mathrm{Pr} = \frac{\nu}{\alpha} = \frac{c_p \mu}{k_c} \tag{A–8}$$

where c_p is the specific heat at constant pressure and k_c is the fluid thermal conductivity. The total energy per unit mass is expressed as

$$E = c_v T + \frac{1}{2} u_i u_i = e + k \tag{A–9}$$

where e is the specific internal energy and k represents the kinetic energy per unit mass. The total enthalpy per unit mass (H) and pressure (p) are written as

$$H = E + \frac{p}{\rho} = E + RT \tag{A–10}$$

$$p = (\gamma - 1)\rho e \tag{A–11}$$

where R is the universal gas constant. The ratio of the specific heats, also known as the heat capacity ratio or adiabatic index, is taken as a constant for a calorically perfect gas

$$\gamma = \frac{c_p}{c_v} = 1.4 \tag{A–12}$$

where c_v is the ratio of specific heat at constant volume.

A.2 Compressible Reynolds Averaged Navier-Stokes Equations

Direct solution of these equations as described above is not yet practically feasible due to the spatial and temporal resolution requirements for solving the small scale structures found within a turbulent boundary layer. Therefore, a form of filtering is applied to capture only the scales of interest and a new set of equations is derived and subsequently solved. In 1895 Osbourne Reynolds suggested the flow variables, namely the instantaneous velocity ($\tilde{u_i}$) in the Navier-Stokes equations, could be decomposed into a fluctuating and mean component

$$\tilde{u}_i\left(x,t\right) = \overline{u}_i\left(x\right) + u_i'\left(x,t\right) \tag{A–13}$$

where the mean and fluctuating components are given by the overbar and prime notation respectively. The resulting velocities could further be temporally averaged over a large enough time scale to ensure statistical stationarity

$$\overline{u}_i = \frac{1}{2T}\int_{-T}^{T} u_i\, dt. \tag{A–14}$$

where the mean of the fluctuating velocity is defined as

$$\overline{u_i'} = \frac{1}{2T}\int_{-T}^{T} u_i'\, dt = 0. \tag{A–15}$$

Decomposing and averaging the compressible continuity equation results in

$$\frac{\partial\overline{\rho}}{\partial t} + \frac{\partial\overline{\rho u_i}}{\partial x_i} = 0. \tag{A–16}$$

The Reynolds averaged compressible momentum equation as

$$\frac{\partial\overline{\rho u_i}}{\partial t} + \frac{\partial\overline{\rho u_i u_j}}{\partial x_j} + \frac{\partial}{\partial x_j}\left(\overline{\rho u_i' u_i'}\right) = \frac{\partial\overline{\sigma_{ij}}}{\partial x_j} - \frac{\partial\overline{p}}{\partial x_i} \tag{A–17}$$

where the deviatoric stress tensor is expressed by

$$\sigma_{ij} = 2\mu\left(S_{ij} - \frac{1}{3}S_{kk}\delta_{ij}\right). \tag{A–18}$$

The Reynolds averaged energy equation is

$$\frac{\partial \overline{\rho E}}{\partial t} + \frac{\partial}{\partial x_j}\left(\overline{\rho u_i E} + \overline{H}\right) + \frac{\partial}{\partial x_j}\left(\overline{\rho u_j' e'} + \frac{1}{2}\overline{\rho u_i' u_i' u_j'}\right) = \frac{\partial}{\partial x_j}\left(\overline{u_i \sigma_{ij}}\right) + \frac{\partial}{\partial x_j}\left(\overline{u_i' \sigma_{ij}'}\right) - \frac{\partial}{\partial x_j}\left(k_c \frac{\partial \overline{T}}{\partial x_j}\right) \tag{A–19}$$

where k_c is the heat transfer coefficient. The strain rate tensor is given as

$$S_{ij} = \frac{1}{2}\left(\frac{\partial \overline{u}_i}{\partial x_j} + \frac{\partial \overline{u}_j}{\partial x_i}\right) \tag{A–20}$$

and the turbulent kinetic energy is expressed as

$$k = \frac{1}{2}\overline{u_i' u_i'}. \tag{A–21}$$

The total energy and enthalpy are expressed by

$$\overline{E} = \overline{e} + \frac{1}{2}\overline{u_i u_i} = \overline{e} + \overline{k} \tag{A–22}$$

$$\overline{H} = \overline{E} + \frac{\overline{p}}{\overline{\rho}}. \tag{A–23}$$

A set of five unknown correlations, given below, was added due to the application of the Reynolds decomposition. These correlations are typically determined empirically whenever possible and applied to achieve proper closure for the set of partial differential equations.

1. $\overline{u_i' u_j'}$ when multiplied by ρ gives the the Reynolds Stress tensor R_{ij} and is associated with the transport of momentum due to the turbulent motion of the fluid
2. $\overline{u_i' e'}$ when multiplied by ρ gives the turbulent heat flux
3. $\overline{u_i' u_i' u_j'}$ is a triple correlation representing turbulent diffusion
4. $\overline{u_i' \sigma_{ij}'}$ is the viscous dissipation due to the fluctuating velocities
5. k is the turbulent kinetic energy

The main problem in turbulence modeling involves calculating the R_{ij} from the known mean quantities. Typically, the Boussinesq approximation is applied which is based on the assumption that the momentum transfer caused by turbulent eddies can be modeled by

eddy viscosity. This idea is similar to how molecular viscosity describes the momentum transfer caused by molecular motion in a gas. The Boussinesq hypothesis therefore states that the Reynolds stresses can be calculated as the product of dynamic eddy viscosity and the strain-rate tensor (S_{ij}) of the mean flow i.e.,

$$R_{ij} = \overline{u_i' u_j'} = \mu_t \left(\frac{\partial u_i}{\partial x_j} + \frac{\partial u_j}{\partial x_i} \right) - \frac{2}{3} \rho k \delta_{ij}. \tag{A–24}$$

The eddy viscosity is a scalar and consequently the Reynolds stress components are linearly proportional to the mean strain-rate tensor. Morkovin (1962) stated that compressibility of the flow is not important unless the motion of the eddies are traveling at supersonic speeds. He further states that the local mean density is important to the determination of the turbulent structure not the fluctuating component of the density. Rumsey (2009) states that compressibility has a small effect on turbulence for wall bounded flows under $M_\infty \approx 5$. However, it is noted, most compressibility corrections have been applied to improve correlations with experiment for the spreading rate of free shear layers such as in the work of Bardina *et al.* (1997).

A.3 Spalart-Allmaras Turbulence Model

A one-equation turbulence model, such as the Spalart-Allmaras model, can be derived to account for the convection and diffusion of turbulence. This turbulence model was derived using empirical relationships with the aim of developing a turbulent transport model that was fast, robust, and accurate for both shear layers and boundary layers. This was accomplished by deriving a transport equation for the turbulent eddy viscosity $\nu_t = \frac{\mu_t}{\rho}$ where ρ and μ_t are the density and absolute turbulent viscosity of the fluid respectively. One equation models have no mechanism to compute the turbulent length scale and thus must include one to account for the geometric length scale (such as distance to the wall). The eddy viscosity is related to the Reynolds stresses by

$$\nu_t = \frac{\overline{u'v'}}{\frac{du}{dy}} \tag{A–25}$$

and is subject to conversion law described by

$$\frac{D\nu_t}{Dt} = \frac{\partial \nu_t}{\partial t} + (u \cdot \nabla)\,\nu_t = \text{Diffusion} + \text{Production} - \text{Destruction}. \tag{A–26}$$

To construct the full model for a turbulent flow, each term on the right hand side need to be defined. Defining these terms in non-dimensional form results in additional constants and non-dimensional functions for each term. The SA model uses experiments from incompressible free shear flow to correct levels of shear stress in two dimensional mixing layers and wakes. The values for the peak shear stress were taken as $0.01\Delta U^2$ and $0.06\Delta U^2$ for the mixing layer and wake respectively where the term ΔU is the peak velocity difference. The transported quantity in this model is the undamped eddy viscosity ($\tilde{\nu}$) eddy viscosity and is related to the eddy viscosity by

$$\nu_t = \tilde{\nu} f_{v1} \tag{A–27}$$

where the subscript v implies the term is viscous for the remainder of the discussion. The function f_{v1} is defined as

$$f_{\nu_1} = \frac{\chi}{\chi^3 + {c_{v1}}^3} \tag{A–28}$$

where c_{v1} is a constant. For the viscous sublayer SA introduced two variables $\tilde{\nu}$ which is equal to ν_t except in the viscous range (near the wall) and the ratio of the eddy viscosity and fluid viscosity

$$\chi = \frac{\tilde{\nu}}{\nu}. \tag{A–29}$$

For the final form of the model SA considered the classical log layer and devised near-wall damping functions determined from empirical data so that $\tilde{\nu} = \kappa y u_*$ all the way to the wall where y is the distance to the wall, u_* is the friction velocity and κ is the Kármán constant typically taken as 0.41. The model therefore solves the following transport

equation

$$\underbrace{\frac{\partial\tilde{\nu}}{\partial t}+U_j\frac{\partial\tilde{\nu}}{\partial x_j}}_{\text{Convection}}=\underbrace{c_{b1}\left(1-f_{t2}\right)\tilde{S}\tilde{\nu}}_{\text{Production}}-\underbrace{\left[c_{w1}f_w-\frac{c_{b1}}{k^2}f_{t2}\right]\left(\frac{\tilde{\nu}}{d}\right)^2}_{\text{Destruction}}+\underbrace{\frac{1}{\sigma}\frac{\partial}{\partial x_k}\left[\left(\nu+\tilde{\nu}\right)\frac{\partial\tilde{\nu}}{\partial x_k}\right]}_{\text{Dissipation}}+\underbrace{\frac{c_{b2}}{\sigma}\frac{\partial^2\tilde{\nu}}{\partial {x_k}^2}}_{\text{Diffusion}} \tag{A–30}$$

where the subscripts b, w, t stand for basic, wall and trip respectively. The term $\tilde{S}$ is the turbulent strain rate tensor and is related to the vorticity magnitude (S) by

$$\tilde{S}=S+\frac{\tilde{\nu}}{k^2d^2}f_{v2} \tag{A–31}$$

where d is the distance to the wall and k is the turbulent kinetic energy taken to be a constant. The second viscous function is related to f_{v1} by

$$f_{v2}=1-\frac{X}{1+Xf_{v1}}. \tag{A–32}$$

The function f_w is defined by

$$f_w\left(r\right)=g\left[\frac{1+c_{w3}^6}{g^6+c_{w3}^6}\right]^{\frac{1}{6}} \tag{A–33}$$

where g, r and f_{t2} are given by

$$g=r+c_{w2}\left(r^6-r\right) \tag{A–34}$$

$$r=\frac{\tilde{\nu_t}}{\tilde{S}k^2d^2} \tag{A–35}$$

$$f_{t2}=c_{t3}e^{-c_{t4}\chi^2}. \tag{A–36}$$

The trip function f_{t1} and the function f_{t2} are expressed as

$$f_{t1}=c_{t1}g_te^{-c_{t2}\frac{{\omega_t}^2}{\Delta U^2}\left(d^2+{g_t}^2+{d_t}^2\right)} \tag{A–37}$$

$$f_{t2}=c_{t3}e^{-c_{t4}\chi^2} \tag{A–38}$$

where d_t is the distance from the grid point to the trip, ω_t is the vorticity at the wall, ΔU is the difference between the field point velocity and velocity at the trip. The wall

Table A-1. SA-DES turbulence model coefficients

c_{b1}	c_{b2}	k	c_{w1}	c_{w2}	c_{w3}	c_{v1}	c_{t3}	c_{t4}	σ
0.1355	0.622	0.41	3.2391	0.3	2	7.1	1.2	0.5	$\frac{2}{3}$

boundary condition is naturally satisfied when $\tilde{\nu} = 0$. The function f_w approaches a constant value when the value r may be truncated to 10. The function g_t is

$$g_t = \min\left(0.1, \frac{\Delta U}{\omega_t \Delta x}\right) \tag{A–39}$$

where Δx is the grid spacing along the wall at the trip. Lastly, the function c_{w1} is given by

$$c_{w1} = \frac{c_{b1}}{k^2} + \frac{1 + c_{b2}}{\sigma} \tag{A–40}$$

where σ is the turbulent Prandtl number. All of the constants used in the CFD flow solver are given in Table A-1.

APPENDIX B
VIBRATION AND DEFLECTION OF SELECTED RODS

This appendix gives the details of the analytical approach for estimating the rod deflection and vibration. Consideration had to be given to this topic due to the sizing of the rods considered, i.e., because $d \leq \delta$. It was found that neither the anticipated longitudinal or transverse natural frequency of the rod were of major concern, especially for the most effective rod detailed throughout this research.

The geometry of each rod used in this study is given in Table B-1 where d_o and t_w represent the rod outer diameter and wall thickness respectively. Each rod was made of 304 stainless steel with the material density and modulus of elasticity of $\rho = 8000\text{kg/m}^3$ $E = 193\text{GPa}$ respectively.

B.1 Rod Fundamental Frequency

The natural frequency was found from a simple pin-pin constrained hollow circular cross section rod as shown in Figure B-1. Inman (2007) gives the longitudinal natural frequency for this device according to

$$\begin{aligned} \omega_n &= \frac{(n\pi c)}{L} \\ f &= \frac{\omega_n}{2\pi} \end{aligned} \tag{B–1}$$

where $c = \sqrt{\frac{E}{\rho}}$ and $n = 1, 2, ...$ represents an integer value for harmonic considerations. The fundamental frequency of the rod is expected to be $f \approx 97\text{kHz}$ for the small diameter rod which is well outside the resonant frequencies found in the cavities and the anticipated rod shedding frequency.

Table B-1. Rod geometry

d^*	0.21	0.43	0.57	0.79	0.89
d_o(mm)	0.75	1.53	2.02	2.81	3.16
t_w(mm)	0.15	0.25	0.25	0.30	0.50

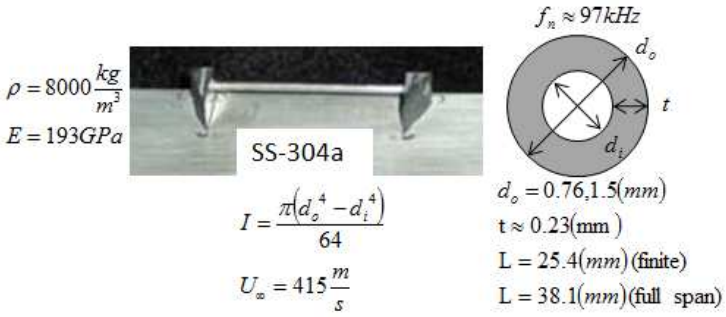

Figure B-1. Suppression device properties.

Table B-2. Transverse fundamental vibration of rod

d^*	d_o (mm)	d_i (mm)	f_n (kHz)
0.21	0.91	0.76	457
0.43	1.47	1.27	751

The transverse vibrational fundamental frequency was calculated using

$$\omega_n = (\beta_1 L)\sqrt{\frac{c}{L^4}} \tag{B–2}$$

where $(\beta_1 L) = 4.73$, $c = \frac{EI}{\rho A}$, A is the rod cross sectional area and the moment of inertia is $I = \frac{\pi\rho L}{4}(d_o^4 - d_i^4)$. Table B-2 illustrates the computed fundamental frequency for the two smallest rods considered throughout this research. It should be noted the larger rods considered would exhibit progressively higher fundamental frequencies and less deflection due to the increased stiffness and wall thickness.

B.2 Deflection of Rod

A conservative estimate of the expected deflection of the rod based on the freestream velocity U_∞ was calculated using the continuity equation. The loading was assumed uniformly distributed over the cylinder

$$\sum F_x = \rho U_\infty^2 A \tag{B–3}$$

where $A = \frac{\pi d_o L}{2}$. The deflection was then computed from beam bending theory where

$$\delta = \frac{5}{384}\frac{FL^3}{EI}. \tag{B–4}$$

The results are shown in Figure B-2 where δ, for the purpose of this appendix, represents the calculated deflection and δ_0 is the thickness of the approaching boundary layer. The largest anticipated rod deflection (for the smallest diameter and longest rod) was on the order of 50% of the boundary layer height and less than 5% for the most effective rod.

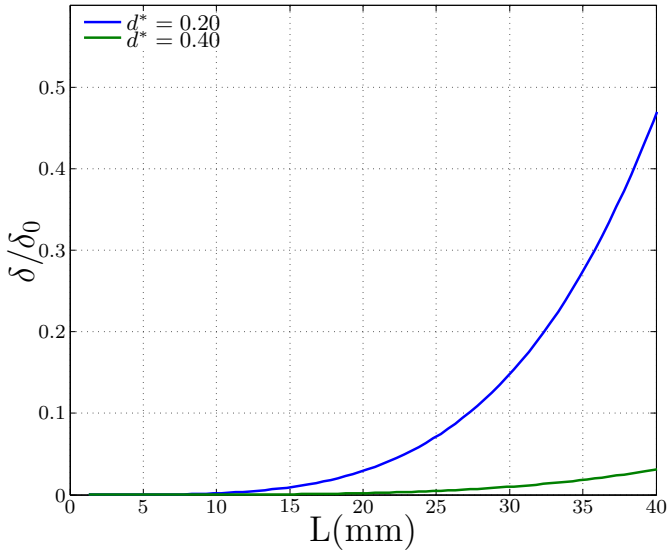

Figure B-2. Estimated rod deflection based on diameter and L for a given U_∞.

REFERENCES

Adrian, R. J. 1991 Particle-imaging techniques for experimental fluid mechanics. *Annu. Rev. Fluid Mech.* **23**, 261–304.

Ahuja, K. K. & Mendoza, J. 1995 Effects of cavity dimensions, boundary layer, and temperature on cavity noise with emphasis on benchmark data to validate computational aeroacoustic codes. *Tech. Rep.* CR-4653. NASA.

Alvi, F. S., Elavarasan, R., Shih, C., Garg, G. & Krothapalli, A. 2003 Control of supersonic impinging jet using microjets. *AIAA J.* **41**, 1347–1355.

Arunajatesan, S., Kannepalli, C., Sinha, N., Sheehan, M., Alvi, F. S., Shumway, G. & Ukeiley, L. S. 2009 Suppression of cavity loads using leading–edge blowing. *AIAA J.* **47**, 1132–1144.

Arunajatesan, S., Shipman, J. & Sinha, N. 2002 Hybrid RANS-LES simulation of cavity flow fields with control. *AIAA Paper* 2002-1130.

Arunajatesan, S., Sinha, N. & Seiner, J. M. 2003 Mechanisms in high-frequency control of cavity flows. *AIAA Paper* 2003-0005.

Bardina, J. E., Huang, P. G. & Coakley, T. J. 1997 Turbulence model testing, and development. *Tech. Rep.* TM-110446. NASA.

Bashkin, V., Vaganov, V., Egorov, I., Ivanov, D. & Ignatova, G. 2002 Comparison of calculated and experimental data on supersonic flow past a circular cylinder. *J. of Fluid Mech.* **37**, 473–483.

Bastrzyk, M., Ramen, G. & Das, K. 2009 Cavity noise suppression through shear layer liftoff. *AIAA Paper* 2009-3203.

Bearman, P.W. & Zdravkovich, M.M. 1978 Flow around a circular cylinder near a plane boundary. *J. Fluid Mech.* **89**, 33–47.

Bendat, J.S. & Piersol, A.G. 1986 *Random Data Analysis*, 2nd edn. New York, NY: John Wiley and Sons, Inc.

Berkooz, G., Holmes, P. & Lumley, J.L. 1993 The proper orthogonal decomposition in the analysis of turbulent flows. *J. Fluid Mech.* **25**, 539–575.

Bilanin, A.J. & Covert, E.E. 1973 Estimation of possible excitation frequencies for shallow rectangular cavities. *AIAA J.* **11**, 347–351.

Block, P. 1976 Noise response of cavities of varying dimensions at subsonic speeds. *Tech. Rep.* TN-D8351. NASA.

Bonnet, J.P., Delville, J., Glauser, M.N., Antonia, R.A., Bisset, D.K., Cole, D.R., Fiedler, H.E., Garem, J.H., Hilberg, D., Jeong, J., Kevlahan,

N.K.R., Ukeiley, L. S. & Vincendeau, E. 1998 Collaborative testing of eddy structure identification methods in free turbulent shear flows. *Exps. Fluids* **25**, 197–225.

Boydston, J., Squires, K. & Forsythe, J. 2008 Detached eddy simulation of high reynolds number flow over a retangular cavity. *AIAA Paper* 2008-606.

Brown, G.L. & Roshko, A. 1974 On density effects and large structure in turbulent mixing layers. *J. Fluid Mech.* **64**, 775–816.

Buresti, G. & Lanciotti, A. 1979 A vortex shedding from smooth and roughed cylinders in cross flow near a plane surface. *Aeronautical Quarterly* **30**, 305–321.

Buresti, G. & Lanciotti, A. 1980 Pressure measurements around a circular cylinder in cross-flow near a plane boundary. *AIAA J.* **80**, 305–321.

Buresti, G. & Lanciotti, A. 2003 Mean and fluctuating forces on a circular cylinder in cross-flow near a plane surface. *J. Wind Eng. and Indus. Aerodynamics* **41**, 639–650.

Cain, A. B., Epstein, R. E. & Kerschen, E. J. 1999 Quick turnaround prediction of weapons bay cavity acoustics resonance. *AIAA Paper* 1999-1899.

Cain, A. B., Rogers, M. M. & Kibens, V. 2001 Simulations of high-frequency excitation of a plane wake. *AIAA Paper* 2001-514.

Cain, A. B., Rogers, M. M. & Kibens, V. 2003 Characterization of high-frequency excitation of a wake by simulation. *AIAA Paper* 2003-179.

Cattafesta III, L. N., Garg, S., Choudhari, M. & Li, F. 1997 Active control of flow-induced cavity resonance. *AIAA Paper* 1997-1804.

Cattafesta III, L. N., Garg, S. & Shukla, D. 2001 Development of piezoelectric actuators for active flow control. *AIAA J.* **39**, 1347–1355.

Cattafesta III, L. N., Shukla, D., Garg, S. & Ross, J. A. 1999 Development of an adaptive weapons-bay suppression system. *AIAA Paper* 1999-1901.

Cattafesta III, L. N., Song, Q., Williams, D., Rowley, C. & Alvi, F. S. 2008 Active control of flow-induced cavity oscillations. *Prog. Aerospace Sci.* **44**, 479–502.

Cattafesta III, L. N., Williams, D. R., Rowley, C. W. & Alvi, F. S. 2003 Review of active control of flow-induced cavity oscillations. *AIAA Paper* 2003-3567.

Chung, J. N. & Troutt, T. R. 1988 Simulation of particle dispersion in an axisymmetric jet. *J. Fluid Mech.* **186**, 199–222.

Colonius, T. 2001 An overview of simulation, modeling, and active control of flow and acoustic resonance in open cavities. *AIAA Paper* 2001-76.

Colonius, T., Basu, A. J. & Rowley, C. W. 1999 Numerical investigation of the flow past a cavity. *AIAA Paper* 1999-1912.

Comte, P., Daude, F. & Mary, I. 2008 Simulation of the reduction of unsteadiness in a passively controlled transonic cavity flow. *J. Fluids and Struc.* **24**, 1252–1261.

Cummings, R., Morton, S. & McDaniel, D. 2008 Experiences in accurately predicting time-dependent flows. *J. Fluids and Struc.* **44**, 241–257.

Davidhazy, A. 2009 Schlieren image of supersonic bullet. Rochester Institute of Technology.

Dix, R. E. & Bauer, R. C. 2004 Experimental and theoretical study of cavity acoustics. *Tech. Rep.* TR-99-4. AEDC.

Dudley, J. G., Shumway, G., Tinney, C. & Ukeiley, L. S. 2008 Flow characteristics of the University of Florida Mach 1.5 supersonic wind tunnel. *AIAA Paper* 200-3942.

Dusing, D., Fox, C., Tam, C., Orkwis, P., Disimile, S. & Peter, J. 1994 An experimental and computational study of unsteady supersonic 2-D open cavity flow physics. *AIAA Paper* 1994-528.

Freymuth, P. 1966 On transition in a separated laminar boundary layer. *J. Fluid Mech.* **25**, 683–784.

Gharib, M. & Roshko, A. 1987 The effect of flow oscillations on cavity drag. *J. Fluid Mech.* **177**, 501–530.

Gladstone, J. H. & Dale, T. P. 1864 Researches on the refraction, dispersion and sensitivness of liquids. *Phil. Trans. Royal Soc.* **153**, 317–343.

Götkun, S. 1975 The drag and lift coefficients of a cylinder placed near a plane surface. Master's thesis, Naval Postgraduate School, Monterey, CA.

Grace, S. 2001 An overview of computational aeroacoustic techniques applied to cavity noise prediction. *AIAA Paper* 2001-510.

Grant, I. & Owens, E. H. 1990 Confidence interval estimates in PIV measurements of turbulent flows. *J. Appl. Opt.* **29**, 1400–1402.

Green, B., Bergeron, K., Decker, R., Cureton, C., Kernazhitskiy, S., Lillian, C. & Nichols, B. 2008 Unsteady flow characteristics for external stores. In *IHAAA*.

Guillaume, B. A. & Colonius, T. 2008 Three-dimensional instabilities in compressible flow over open cavities. *J. Fluid Mech.* **599**, 309–339.

Hamed, A., Basu, D. & Das, K. 2003 Detached eddy simulations of supersonic flow over cavity. *AIAA Paper* 2003-549.

Hamed, A., Das, K. & Basu, D. 2004 Numerical simulations of fluidic control for transonic cavity flows. *AIAA Paper* 2004-429.

Heller, H. H. & Bliss, B. D. 1975 The physical mechanism of flow-induced pressure fluctuations in cavities and concepts for their suppression. *AIAA Paper* 1975-491.

Inman, D. 2007 *Engineering Vibrations*, 3rd edn. New York, NY: Prentice Hall.

John, J. & Keith, T. 2006 *Gas Dynamics*, 3rd edn. New York, NY: Prentice Hall.

Kähler, C. J. 2003 General design and operating rules for seeding atomisers. *PIV03 Paper* 3207.

Kastner, J. & Samimy, M. 2003 Effects of forcing frequency on the control of an impinging high speed jet. *AIAA Paper* 2003-0006.

Kegerise, M. A., Cabell, R. H. & Cattafesta III, L. N. 2007*a* Real time feedback control of flow induced cavity tones - part 1: Fixed-gain control. *Phys. Fluids* **307**, 906–923.

Kegerise, M. A., Cabell, R. H. & Cattafesta III, L. N. 2007*b* Real time feedback control of flow induced cavity tones - part 2: Adaptive control. *Phys. Fluids* **307**, 924–940.

Kegerise, M. A., Cattafesta III, L. N. & Ha, C. 2003 Adaptive identification and control of flow-induced cavity oscillations. *AIAA Paper* 2002-3158.

Kegerise, M. A., Spina, F. E., Garg, S. & Cattafesta III, L. N. 2004 Mode-switching and nonlinear effects in compressible flow over a cavity. *Phys. Fluids* **16**, 678–687.

Komerath, N. M., Ahuja, K. K. & Chambers, F. W. 1987 Prediction and measurement of flow over cavities - a survey. *AIAA Paper* 1987-0166.

Kompenhans, J. & Hőcker, R. 1988 Application of particle image velocimetry to high speed flows. *Particle Image Velocimetry*.

Krishnamurty, K. 1955 Acoustic radiation from two-dimensional rectangular cutouts in aerodynamic surfaces. *Tech. Rep.* CR-3487. NACA.

Krothapalli, A., Wishart, D. P. & Loureno, L. M. 1994 Near field structure of a supersonic jet. *Particle Image Velocimetry*.

Kulite 2010 XCQ-062 series pressure transducer. http://www.kulite.com.

Larcheveque, L., Sagaut, P. & Le, T. 2003 Large-eddy simulations of flows in weapon bays. *AIAA Paper* 2003-778.

Launder, B. E. 1991 An introduction to the modeling of turbulence. *VKI* N91-31551.

Lawson, S. J. & Barakos, G. N. 2010 Evaluation of DES for weapons bays in UCAVs. *J. Aerosapce Sci. and Tech.* **14**, 397–414.

Levasseura, V., Sagautb, P., Malleta, M. & Chalota, F. 2008 Unstructured large eddy simulation of the passive control of the flow in a weapon bay. *J. Fluids and Struc.* **24**, 1204–1215.

Lumley, J. 1967 The structure of inhomogenous turbulent flows. pp. 166–178. *Atm. Turb. and Radio Wave Prop.*

Lund, T. S., Wu, X. & Squires, K. D. 1998 Generation of turbulent inflow data for spatially-developing boundary layer simulations. *J. Comp. Phys.* **140**, 233–258.

Menter, F. R. 1994 Two-equation eddy-viscosity turbulence models for engineering applications. *AIAA J.* **32**, 1598–1605.

Morkovin, M. 1962 *Effects of Compressibility on Turbulent Flows*. New York, NY: Mecanique de la Turbulence.

Murray, N., Sällström, E. & Ukeiley, L. S. 2009 Properties of subsonic open cavity flow fields,. *Phys. Fluids* **21**, 95–103.

Murray, N. & Ukeiley, L. S. 2007 Modified quadratic stochastic estimation of resonating subsonic cavity flow. *J. Turb.* **8**, 1–29.

Nayyar, P., Barakos, G., Badcock, K. & Kirkham, D. 2005 Analysis and control of transonic cavity flow using DES and LES. *AIAA Paper* 2005-5267.

Nichols, B. 2005 Turbulence models and their application to complex flows. *Tech. Rep.* Revision 3. HPCMP/PET and UAB.

Nichols, R. 2006 Comparison of hybrid turbulence models for a circular cylinder and a cavity. *AIAA J.* **44**, 1207–1219.

Nichols, R. H. & Heikkinen, B. D. 2005 Validation of implicit algorithms for unsteady flows including moving and deforming grids. *AIAA Paper* 2005-683.

Nishino, T., Roberts, G. T. & Zhang, X. 2008 Unsteady RANS and detached-eddy simulations of flow around a cylinder in ground effect. *J. Fluids and Struc.* **24**, 18–33.

Panickar, P. & Raman, G. 2008*a* Cavity resonance suppression using high frequency excitation: The mystery of the cylinder-in-crossflow revisited. *AIAA Paper* 2008-2853.

Panickar, P. & Raman, G. 2008*b* Understanding the mechanism of cavity resonance suppression using a cylindrical rod in crossflow. *AIAA Paper* 2008-54.

Papamoschou, D. & Roshko, A. 1987 The compressible turbulent shear layer: An experimental study. *J. Fluid Mech.* **197**, 453–477.

Papoulis, A. 1962 *The Fourier Integral and its Applications*. New York, NY: McGraw-Hill.

Pope, S. B. 2000 *Turbulent Flows*, 1st edn. New York, NY: Cambridge University Press.

Powell, A. 1961 On the edgetone. *J. Acous. Soc. of America* **33**, 395.

Price, S. J., Sumner, D., Smith, J. G., Leong, K. & Paidoussis, M. P. 2002 Flow visualization around a circular cylinder near to a plane wall. *J. Fluids and Struc.* **16**, 175–191.

Qian, S. & Chen, C. 1996 *Joint Time-Frequency Analysis*. Englewood Cliffs, NJ: Prentice Hall.

Radhakrishnan, S. 2007 Large eddy simulation of high reynolds number flows in complex geometries. PhD thesis, University of Maryland, College Park, Md.

Raffel, M., Willert, C., Wereley, S. & Kompenhans, J. 1998 *Particle Image Velocimetry*, 2nd edn. Berlin: Springer.

Rempfer, D. & Fasel, H. F. 1994 Evolution of three-dimensional coherent structures in a flat-plate boundary layer. *J. Fluid Mech.* **260**, 351–375.

Riesz, F. & Nag, B.S. 1955 *Functional Analysis*. New York, NY: Ungar Publishing.

Rizk, M., Prewitt, N. & Ellison, S. 2002 Beggar: A store separation predictive tool. *AIAA Paper* 2002-3190.

Rizzetta, D. P. & Visbal, M. R. 1988 Numerical simulations of supersonic flow over a three-dimensional cavity. *AIAA J.* **26**, 159–167.

Rizzetta, D. P. & Visbal, M. R. 2003 Large eddy simulation of supersonic cavity flowfields including flow control. *AIAA J.* **41**, 1452–1462.

Rockwell, D. & Naudascher, E. 1979 Self-sustained oscillations of impinging free shear layers. *Annu. Rev. Fluid Dyn.* **11**, 67–94.

Roshko, A. 1955 Some measurements of flow in a rectangular cutout. *Tech. Rep.* NACA-TN-3488. NASA.

Roshko, A., Steinolfson, A. & Chattoorgoon, V. 1975 Flow forces on a cylinder near a wall or near another cylinder. In *Proc. 2nd US Conf. Wind Engeineering Research*. Paper:IV-15.

Rossiter, J. E. 1964 Wind-tunnel experiments on the flow over rectangular cavities at subsonic and transonic speeds. *Tech. Rep.* Reports and Memoranda No. 3438. Aeronautical Research Council.

Rowley, C. W. 2002 Modeling, simulation, and control of cavity flow oscillations. PhD thesis, California Institute of Technology, Pasadena, CA.

Rowley, C. W., Colonius, T. & Basu, A. 2002*a* On self-sustained oscillations in two-dimensional compressible flow over rectangular cavities. *J. Fluid Mech.* **455**, 315–346.

Rowley, C. W., Colonius, T. & Murray, R. M. 2000*a* Pod based models of self-sustained oscillations in the flow past an open cavity. *AIAA Paper* 2000-1969.

Rowley, C. W., Juttijudata, V. & Williams, D. 2000*b* Cavity flow control simulations and experiments. *AIAA Paper* 2005-0292.

Rowley, C. W., Williams, D. R., Colonius, T., Murray, R. M., MacMartin, D. & Fabris, D. 2002*b* Model-based control of cavity oscillations Part II: System identification and analysis. *AIAA Paper* 2002-0972.

Rowley, C. W., Williams, D. R., Colonius, T., Murray, R. M. & Macmynowski, D. G. 2006 Linear models for control of cavity flow oscillations. *J. Fluid Mech.* **547**, 317–330.

Rowley, C. W. & Williams, R. D. 2006 Dynamics and control of high-Reynolds-number flow over open cavities. *Annu. Rev. Fluid Mech.* **38**, 251–276.

Rumsey, C. L. 2009 Compressibility considerations for k-ω turbulence models in hypersonic boundary layer applications. *Tech. Rep.* TM-2009-215705. NASA.

Samimy, M. & Lele, S. K. 1991 Motion of particles with inertia in a compressible free shear layer. *Phys. Fluids* **3**, 1915–1923.

Sarkar, S. & Sarkar, S. 2010 Vortex dynamics of a cylinder wake in proximity to a wall. *J. Fluids and Struc.* **26**, 19–40.

Sarohia, V. 1975 Experimental and analytical investigation of oscillations in flows over cavities. PhD thesis, California Institute of Technology, Pasadena, CA.

Sarpotdar, S., Panickar, P. & Raman, G. 2009 Cavity tone suppression using a rod in cross flow: Investigation of shear layer stability mechanism. *AIAA Paper* 2009-700.

Sarpotdar, S. & Raman, G. 2009 Influence of shedding cylinder on the cavity flow dynamics. *AIAA Paper* 2009-3350.

Settles, S. G. 2001 *Schlieren and Shadowgraph Techniques: Visualizing Phenomena in Transparent Media*, 1st edn. Berlin: Springer-Verlag.

Shaw, L. 1998 Active control for cavity acoustics. *AIAA Paper* 1998-2347.

Shaw, L. & Northcraft, S. 1999 Closed loop active control for cavity acoustics. *AIAA Paper* 1999-1902.

Shih, S., Hamed, A. & Yeuan, J. J. 1994 Unsteady supersonic cavity flow simulations using coupled kappa-epsilon and Navier-Stokes equations. *AIAA J.* **32**, 2015–2021.

Sirovich, L. 1987 Turbulence and the dynamics of coherent structures. *Quarterly of Appl. Math.* **5**, 561–590.

Smith, B., Welterlen, T., Maines, B., Shaw, L., Stanek, M. J. & Grove, J. 2002 Weapons bay acoustic suppression from rod spoilers. *AIAA Paper* 2002-662.

Smith, B. R., Jordan, J. K., Rizk, S. N. & Shaw, L. L. 2000 Computational simulation of active control of cavity acoustics. *AIAA Paper* 2000-1927.

Smith, D. L. & Shaw, L. L. 1975 Prediction of the pressure oscillations in cavities exposed to aerodynamic flow. *Tech. Rep.* TR-75-34. AFFDL.

Song, Q. 2008 Closed-loop control of flow-induced cavity oscillations. PhD thesis, University of Florida, Gainesville, FL.

Spalart, P., Strelets, J. & Allmaras, S. R. 1997 Comments on the feasubility of LES for wings and on a hybrid RANS/LES approach. AFSOR Conference on DNS/LES.

Spalart, P. R. 2000 Strategies for turbulence modelling and simulations. *J. Heat and Fluid Flow* **21**, 252–263.

Spalart, P. R. & Allmaras, S. R. 1994 A one-equation turbulence model for aerodynamic flows. *La Recherche Aerospatiale* **01**, 5–21.

Stanek, M. J. 2005 A numerical study of the effect of frequency of pulsed flow control applied to a rectangular cavity in supersonic crossflow. PhD thesis, University of Cincinnati, Cincinnati, OH.

Stanek, M. J., Raman, G., Kibens, V., Ross, J. A., Odedra, J. & Peto, J. W. 2000 Control of cavity resonance through very high frequency forcing. *AIAA Paper* 2000-1905.

Stanek, M. J., Raman, G., Ross, J., Odedra, J., Peto, J. & Alvi, F. S. 2002*a* High frequency acoustic suppression - The role of mass flow & the notion of superposition. *AIAA Paper* 2002-2404.

Stanek, M. J., Raman, G., Ross, J., Odedra, J., Peto, J. & Alvi, F. S. 2003 High frequency acoustic suppression - The mystery of the rod in crossflow revealed. *AIAA Paper* 2003-7.

Stanek, M. J., Sihna, N., Seiner, J., Pearce, B. & Jones, I. M. 2002*b* Applying very high frequency excitation to the problem of tactical directed energy beam propagation. *AIAA Paper* 2002-2272.

Strelets, M. 2001 Detached eddy simulation of massively separated flows. *AIAA Paper* 2001-879.

Tam, C. K. W. & Block, P. J. 1978 On the tones and pressure oscillations induced by flow over rectangular cavities. *J. Fluid Mech.* **89**, 373–399.

Tannehill, J. C. & Anderson, D. A. 1984 *Computational Fluid Dynamics and Heat Transfer*, 2nd edn. Hemisphere, NY: Taylor and Francis.

Tennekes, H. & Lumley, J. L. 1972 *A First Course in Turbulence*, 1st edn. New York, NY: John Wiley and Sons, Inc.

Theofilis, V. & Colonius, T. 2002 An algoritihm for the recovery of 2- and 3-D bioglobal instabilties of compressible flow over 2-D open cavities. *AIAA Paper* 2003-4143.

Travin, A., Shur, M., Strelets, M. & Spalart, P. 2000 Detached-eddy simulations past a circular cylinder. *Flow, Turb. and Combustion* **63**, 293–313.

Ukeiley, L. S., Ponton, M. K., Seiner, J. M. & Jansen, B. 2002 Suppression of pressure loads in cavity flows. *AIAA Paper* 2002-661.

Ukeiley, L. S., Ponton, M. K., Seiner, J. M. & Jansen, B. 2003 Suppression of pressure loads in resonating cavities through blowing. *AIAA Paper* 2003-0181.

Ukeiley, L. S., Ponton, M. K., Seiner, J. M. & Jansen, B. 2004*a* Suppression of pressure loads in cavity flows. *AIAA J.* **42**, 70–79.

Ukeiley, L. S., Sheehan, M., Coiffet, F., Alvi, F. S. & Jansen, B. 2004*b* Control of pressure loads in complex cavity configurations. *J. Aircraft* **45**, 1014–1024.

Ukeiley, L. S., Sheehan, M., Coiffet, F., Alvi, F. S. & Jansen, B. 2007 Control of pressure loads in complex cavity configurations. *AIAA Paper* 2007-1238.

Unalmis, O. H., Clemens, N. T. & Dolling., S. D. 2004 Cavity oscillation mechanisms in high-speed flows. *AIAA J.* **42**, 2035–2041.

Vakili, A. D. & Gauthier, C. 2001 Planar velocity measurements in compressible mixing layers. *J. Fluid Mech.* **189**, 431.

Vakili, A. D. & Gauthier, C. 2004 Control of cavity flow by upstream mass injection. *J. Aircraft* **31**, 169–174.

Van-Dyke, M. 1982 *Album of Fluid Motion*, 1st edn. Stanford, Ca: Parabolic Press.

Vikramaditya, N. S. & Kurian, J. 2009 Effect of aft wall slop on cavity pressure ocscillations in supersonic flows. *Aeronautical J.* **113**, 291–300.

Welch, P. D. 1967 The use of fast fourier transforms for the estimation of power spectra: A method based on time averaging over short modified periodograms. *IEEE Trans. on Audio and Electroacoustics* **15**, 70–73.

White, F. M. 2006 *Viscous Fluid Flow*, 3rd edn. Boston, MA: McGraw-Hill.

Wilcox, D. C. 2006 *Turbulence Modeling for CFD*, 3rd edn. New York, NY: DCW Industries, Inc.

Williams, D., Cornelius, D. & Rowley, C. 2007 Closed-loop control of linear supersonic cavity tones. *AIAA Paper* 2007-4226.

Wiltse, M. & Glezer, A. 1998 Direct excitation of small-scale motions in free shear flows. *Phys. Fluids* **10**, 2026.

Zdravkovich, M. M. 1985 Forces on a circular cylinder near a plane wall. *Appl. Ocean Res.* **7**, 197–201.

Zdravkovich, M. M. 1986 A cirular cylinder partly submerged in three boundary layers. In *5th Int. OMAE Symp, in Tokyo April 1986*.

Zhuang, N. 2007 Experimental investigation of supersonic cavity flows and their control. PhD thesis, Florida State University, Tallahassee, FL.

Zhuang, N., Alvi, F. S., Alkislar, M. & Shih, C. 2003 Aeroacoustic properties of supersonic cavity flows and their control. *AIAA Paper* 2003-3101.

Zhuang, N., Alvi, F. S., Alkislar, M. & Shih, C. 2006 Supersonic cavity flows and their control. *AIAA J.* **44**, 2118–2128.

BIOGRAPHICAL SKETCH

Jonathan G. Dudley was born in Westfield, New York. He received his bachelor's degree in 2000 from the Rochester Institute of Technology in Mechanical Engineering with a concentration in Aerospace Engineering. Jonathan began work at Valeo Engine Cooling as a performance engineer utilizing finite element methods and computational fluid dynamics for automotive and heavy truck cooling system design. In 2003 he received his master's degree while studying the fluid-structure interaction of intracranial aneurysms from the University at Buffalo. He began work for the Air Force Seek Eagle Office (AFSEO) in 2003 as a computational fluid dynamics engineer. In 2005 he married his wife Megan Dudley and in 2006 he enrolled in the doctoral program at the University of Florida (UF) where he studied under the advisement of Dr. Lawrence Ukeiley. In 2010 Jon and Megan welcomed into their lives their first newborn daughter, Malia Dudley. He currently works for the Air Force Research Laboratory (AFRL/RWAVM) as a basic research scientist. He is a member of the American Institute of Aeronautics and Astronautics (AIAA).